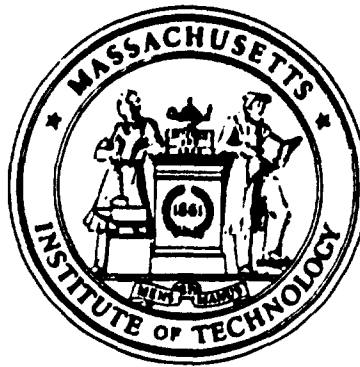


AD-A205 954



CERAMICS PROCESSING RESEARCH LABORATORY

**BASIC RESEARCH ON PROCESSING OF CERAMICS
FOR SPACE STRUCTURES**

F49620-84-C-0097 Final Scientific Report
of work conducted for Air Force Office of Scientific
Research, 31 August 1984 through 15 December 1988

H. Kent Bowen and Wendell E. Rhine

Massachusetts Institute of Technology
Materials Processing Center
77 Massachusetts Avenue
Cambridge, MA 02139

Submitted 2 February 1989

FOR UNLIMITED DISTRIBUTION

Building No. 12
Massachusetts Institute of Technology
Materials Processing Center
Cambridge, Massachusetts 02139

DISTRIBUTION STATEMENT A

DTIC
SELECTED
MAR 10 1989

H
9

UNCLASSIFIED

SECURITY CLASSIFICATION OF THIS PAGE

REPORT DOCUMENTATION PAGE				Form Approved OMB No. 0704-0188	
1a. REPORT SECURITY CLASSIFICATION Unclassified			1b. RESTRICTIVE MARKINGS		
2a. SECURITY CLASSIFICATION AUTHORITY			3. DISTRIBUTION / AVAILABILITY OF REPORT Unlimited		
2b. DECLASSIFICATION / DOWNGRADING SCHEDULE					
4. PERFORMING ORGANIZATION REPORT NUMBER(S) F49620-84-C-0097			5. MONITORING ORGANIZATION REPORT NUMBER(S) AFOSR-TR-89-0289		
6a. NAME OF PERFORMING ORGANIZATION MIT Ceramics Processing Research Laboratory		6b. OFFICE SYMBOL (If applicable)	7a. NAME OF MONITORING ORGANIZATION Air Force Office of Scientific Research		
6c. ADDRESS (City, State, and ZIP Code) Cambridge, MA 02139			7b. ADDRESS (City, State, and ZIP Code) Bolling Air Force Base, DC 20332		
8a. NAME OF FUNDING / SPONSORING ORGANIZATION AFOSR		8b. OFFICE SYMBOL (If applicable)	9. PROCUREMENT INSTRUMENT IDENTIFICATION NUMBER F49620-84-C-0097		
8c. ADDRESS (City, State, and ZIP Code) Bolling Air Force Base DC 20332			10. SOURCE OF FUNDING NUMBERS		
			PROGRAM ELEMENT NO. 61102F	PROJECT NO. 2303	TASK NO. A3
					WORK UNIT ACCESSION NO.
11. TITLE (Include Security Classification) Basic Research on Processing of Ceramics for Space Structures					
12. PERSONAL AUTHOR(S) Bowen, Rhine, Hardy, Zing, Einarsrud, Moffatt, Kamiya, Jang, Bishop, Spatz					
13a. TYPE OF REPORT final report		13b. TIME COVERED FROM 8-1-84 TO 2-15-88		14. DATE OF REPORT (Year, Month, Day) 89-1-31	
15. PAGE COUNT 295					
16. SUPPLEMENTARY NOTATION					
17. COSATI CODES			18. SUBJECT TERMS (Continue on reverse if necessary and identify by block number)		
FIELD	GROUP	SUB-GROUP	AlN Al ₂ O ₃ -Al ₂ TiO ₅ -TiO ₂ Ceramics, Organosilicon poly- Composite ceramics, meric binders, Cyclic annealing Polymer-coated SiC.		
19. ABSTRACT (Continue on reverse if necessary and identify by block number)					
<p>The hydrolysis of alkoxide emulsion droplets was investigated for preparing unagglomerated, submicrometer oxide ceramic particles with a homogeneous composition. This technique was used to prepare single- and mixed-oxide powders whose overall cation composition corresponded to the initial alkoxide cation composition. Uncalcined powders were amorphous, with high surface areas and low densities; upon calcination, powders densified and became crystalline.</p> <p>In other studies, a water-in-oil emulsion technique was investigated for preparing SrTiO₃ and BaTiO₃, and two AlN precursors were synthesized from dimethylaminoalane and NH₃. Both AlN precursors gave fine, high-purity AlN powders after heat-treatment; a colloiddally pressed sample densified to 95% of theoretical density at 1750°C.</p>					
20. DISTRIBUTION / AVAILABILITY OF ABSTRACT <input checked="" type="checkbox"/> UNCLASSIFIED/UNLIMITED <input type="checkbox"/> SAME AS RPT. <input type="checkbox"/> DTIC USERS			21. ABSTRACT SECURITY CLASSIFICATION Unclassified		
22a. NAME OF RESPONSIBLE INDIVIDUAL Donald R. Ulrich			22b. TELEPHONE (Include Area Code) (202) 767-4963		22c. OFFICE SYMBOL NL

DD Form 1473, JUN 86

Previous editions are obsolete.

SECURITY CLASSIFICATION OF THIS PAGE

UNCLASSIFIED

8. SUBJECT TERMS (cont'd)

Al_2O_3 -SiC	Emulsion techniques
Al_2O_3 -ZrO ₂	Flocculation
BaTiO ₃	SiC
	SrTiO ₃

9. ABSTRACT (cont'd)

A ceramics processing technique based on precipitating polymer-powder flocs from polymer-powder-solvent dispersions by adding a nonsolvent for the polymer was developed. For Al_2O_3 -ZrO₂ composite green bodies made using this technique, the optimal firing temperature was 1500°C.

Flocculation and cyclic annealing were studied for processing and controlling Al_2O_3 -TiO₂ composite microstructure. Homogeneous green bodies were obtained by colloid-pressing flocs of polyvinyl alcohol (PVA) and ceramic powders. Densities, which decreased during annealing, were increased by a reheat treatment. A combination of cyclic annealing and the reheating treatment produced various interesting microstructures of Al_2O_3 composites interspersed with Al_2TiO_5 and TiO₂, suggesting unique mechanical properties.

Effects of a polymer coating on the densification of a two-phase particle system were tested using SiC powder dispersed in an Al_2O_3 matrix. Composites processed with polymer coatings densified more during equivalent firing cycles than did those processed without polymer coatings.

In order to process SiC in nonaqueous solvents, dispersions of SiC in hexane were studied. The charge on β -SiC powder in low-dielectric-constant hydrocarbon media increased with OLOA®1200 concentration up to -3.2 wt% OLOA by weight of powder, and increased with the time allowed for OLOA and particle surfaces to interact.

Particle-size classification of β -SiC powder dispersions in hexane stabilized with OLOA®1200 was performed centrifugally. As-received and classified β -SiC powders were dispersed, colloidally pressed, and sintered.

Microstructures were investigated for B₄C- and C-doped β -SiC powders sintered at 2000°C and 2100°C. The average grain size for classified β -SiC powder compacts was smaller than that for as-received powder compacts when sintered at 2000°C, but on a relative scale was slightly greater.

Compacts containing β -SiC powder, B₄C, OLOA®1200 dispersant, polyphenylene, and either PMMA, polycarbosilane, or a vinylic polysilane were uniaxially pressed, pyrolyzed, and sintered at 2000-2100°C/30 min. Green pellets were subjected to a range of pressures so that sintering could be studied as a function of packing density. Organosilicon pyrolysis products did not enhance densification rates.

CONTENTS

	Page
I. BACKGROUND AND RESEARCH APPROACH.....	1
II. RESEARCH SUMMARIES.....	3
A. <u>Powder Preparation</u>	
1. Emulsions	
a. Hydrolysis of Alkoxide Emulsion Droplets.....	4
Anne Bagley Hardy	
Abstract.....	4
Introduction.....	4
Experimental Procedure.....	5
General Procedures.....	5
Alkoxides.....	6
Continuous Phase Selection.....	6
Surfactants.....	7
Preparation and Reaction of Emulsions.....	7
Alkoxide/Continuous Phase Immiscibility, Reactivity	9
Solubility of Alkoxides in Acetonitrile	
and Propylene Carbonate.....	9
Concentration Effects.....	12
Temperature Effects.....	12
Droplet- and Particle-Size Measurements.....	13
Electron Microscopy.....	14
Powder Surface Area Measurement.....	14
Density Measurement.....	15
X-Ray Diffraction.....	15
Sample Composition.....	16
Results and Discussion.....	16
System Choice.....	16
Criteria for selecting the emulsion system.....	16
Alkoxide/continuous phase immiscibility	
and reactivity.....	17
Alkoxide solubility in acetonitrile	
and propylene carbonate.....	20
Surfactant choice.....	23
Powder Formation Mechanism.....	28
Investigative approach.....	28
Variation of dispersed-phase concentration.....	29
Temperature effects.....	33
Droplet-size and particle-size distributions....	34
Proposed droplet hydrolysis mechanism.....	35
Powder Characteristics.....	38
Powder morphology.....	38
Weight loss.....	38
Crystallinity.....	41
Density and surface area measurements.....	43
Composite powders.....	45
Conclusions.....	48
References.....	51
Figures.....	55

CONTENTS (CONT'D)

	Page
A. Powder Preparation (cont'd)	
1. Emulsions (cont'd)	
b. Preparation of BaTiO ₃ and SrTiO ₃ Using a Water-in-Oil Emulsion Technique.....	75
Christophe Zing ¹	
Abstract.....	75
Introduction.....	75
Experimental Procedure.....	76
Results and Discussion.....	77
Summary.....	79
References.....	80
Figures.....	81
2. Alkoxide Precursors	
a. Synthesis of AlN Powder from Dimethylaminoalane.....	84
Mari-Ann Einarsrud ²	
Abstract.....	84
Introduction.....	84
Experimental.....	84
AlN via Precursor I.....	85
AlN via Precursor II.....	85
Powder Characterization.....	85
Sintering.....	85
Results and Discussion.....	85
Precursor Characterization.....	85
Characterization of AlN Powders.....	86
Sintering Behavior.....	86
Conclusions.....	86
References.....	87
Figures.....	88
B. Composites	
1. Al ₂ O ₃ -ZrO ₂	
a. Flocculation of Polymer-Containing Powder Dispersions by the Addition of Nonsolvents.....	90
William C. Moffatt ³	
Abstract.....	90
Introduction.....	90
Literature Review.....	91
Polymer-Solvent-Nonsolvent Phase Equilibria.....	91
Phase Separation of Polyvinyl Alcohol.....	91
Adsorption of Polyvinyl Alcohol.....	92

¹Visiting Scientist, Rhône Poulenc Inc., Paris; paper to be submitted to J. Mat. Sci. Lett.

²Visiting Scientist, Norwegian Institute of Technology, Institute of Inorganic Chemistry.

³Currently with International Superconductivity Technology Center, Tokyo; flocculation paper submitted to the American Ceramic Society.

CONTENTS (CONT'D)

Page

B. Composites (cont'd)

1. $\text{Al}_2\text{O}_3\text{-ZrO}_2$ (cont'd)

a. Flocculation of Polymer-Containing Powder Dispersions by the Addition of Nonsolvents (cont'd)

William C. Moffatt³

Phase Separation of Particle-Containing Polymer Solutions.....	93
Adsorption Isotherm.....	93
Experimental Procedure.....	93
Results and Discussion.....	94
Effect of Solution Chemistry on Apparent Particle Size.....	95
Procedure.....	95
Results and Discussion.....	96
Floc Texture Studies.....	97
Experimental Procedure.....	97
Results and Discussion.....	98
Precipitation in Nonaqueous Systems.....	99
Reversibility of Precipitation.....	99
General Discussion.....	100
Conclusions.....	101
References.....	101
Figures.....	104

b. Thermal Processing and Properties of Highly Homogeneous Alumina-Zirconia Composite Ceramics.....

William C. Moffatt³

Abstract.....	106
Introduction.....	106
Experimental.....	107
Specimen Production and Characterization.....	107
Effect of Thermal History on Properties.....	109
Effect of High-Temperature Annealing on Properties.....	112
Conclusions.....	113
References.....	114
Figures.....	116

³Currently with International Superconductivity Technology Center, Tokyo;
flocculation paper submitted to the American Ceramic Society, thermal
processing paper submitted to the Journal of Materials Science.

CONTENTS (CONT'D)

	Page
B. Composites (cont'd)	
2. $\text{Al}_2\text{O}_3\text{-Al}_2\text{TiO}_5\text{-TiO}_2$	
a. Processing and Microstructural Control of $\text{Al}_2\text{O}_3\text{-Al}_2\text{TiO}_5\text{-TiO}_2$ Composites Formed by Cyclic Annealing.....	123
Sumio Kamiya ⁴	
Abstract.....	123
Introduction.....	123
Experimental Procedure.....	124
Results and Discussion.....	126
Powder Preparation Using a Flocculation Technique.	126
Decomposition Behavior of Al_2TiO_5	129
Microstructural Control by Cyclic Annealing.....	130
Effects of Settling and Starting Composition on Annealed Materials' Properties.....	135
Conclusions.....	139
References.....	140
Figures.....	142
b. Mechanical Properties of Cyclically Annealed $\text{Al}_2\text{O}_3\text{-Al}_2\text{TiO}_5\text{-TiO}_2$ Composites.....	153
Sumio Kamiya ⁴	
Abstract.....	153
Introduction.....	153
Experimental Procedure.....	154
Results.....	155
Relation of Annealed Material Properties to Starting Powder Composition.....	155
Relation of Annealed Material Properties to Annealing Conditions.....	157
Discussion.....	160
Internal Cracks and Possible Ways to Improve Processing.....	160
Relation of Mechanical Properties to Starting Powder Composition.....	162
Relation of Strength to Grain Size.....	163
Relation of Annealing Schedule to Strength.....	163
Literature Review of $\text{Al}_2\text{O}_3\text{-TiO}_2$ Mechanical Properties and Comparison to This Study's Results.	164
Conclusions.....	165
References.....	166
Figures.....	167

⁴Visiting Scientist, Toyota Motor Corporation, Aichi, Japan; papers to be submitted to the American Ceramic Society.

CONTENTS (cont'd)

	Page
B. Composites (cont'd)	
3. Al_2O_3 -SiC	
a. Densification of Al_2O_3 -SiC Powder Composites:	
I. Effects of a Polymer Coating on SiC Particles.....	176
Hyun M. Jang ⁵	
Abstract.....	176
Introduction.....	176
Experimental Method.....	178
Powders.....	178
Processing and Characterization.....	179
Results and Discussion.....	183
Examination of Green Compacts.....	183
Effects of a Polymer Coating on Densification.....	186
Summary.....	189
References.....	190
Appendix.....	192
Figures.....	194
b. Densification of Al_2O_3 -SiC Powder Composites:	
II. Microstructural Evolution and Densification.....	200
Hyun M. Jang ⁵	
Abstract.....	200
Introduction.....	200
Experimental Methods.....	201
Results and Discussion.....	203
Summary.....	209
References.....	209
Figures.....	210
C. SiC and Polymer Studies	
1. Powder Processing and Microstructure Development	
of β -SiC.....	216
Bruce Bishop	
Abstract.....	216
Introduction.....	217
β -SiC Powder Dispersion in Low-Dielectric-Constant	
Media.....	218
Introduction.....	218
Summary of Previous Work.....	220
Experimental Background and Procedure.....	220
Results and Discussion.....	224
Conclusions.....	226
Future Work.....	226

⁵Currently at Pohang Institute of Science and Technology, Department of Metallurgy and Materials Science, Pohang, Korea; papers accepted for publication in the Journal of the American Ceramic Society.

CONTENTS (cont'd)

	Page
C. SiC and Polymer Studies (cont'd)	
1. Powder Processing and Microstructure Development of β -SiC (cont'd)	
Bruce Bishop (cont'd)	
Centrifugal Particle-Size Classification.....	227
Introduction.....	227
Experimental Procedure.....	228
Results and Discussion.....	228
Conclusions.....	236
Future Work.....	237
Microstructural Development of β -SiC.....	237
Introduction.....	237
Experimental Procedures.....	238
Results and Discussion.....	240
Conclusions.....	249
Future Work.....	250
References.....	251
Figures.....	254
2. Sintering SiC Powder Using Organosilicon Polymers as Binders.....	272
Mark Spotz	
Abstract.....	272
Introduction.....	272
Experimental Procedure.....	273
Results.....	277
Wetting and Penetration.....	277
Compaction and Pyrolysis Behavior.....	279
Sintering.....	280
Conclusions and Future Work.....	283
References.....	285
Figures.....	286
 III. RESEARCH PUBLICATIONS.....	 291

BASIC RESEARCH ON PROCESSING OF CERAMICS FOR SPACE STRUCTURES

I. BACKGROUND AND RESEARCH APPROACH

High-quality technical ceramics are capable of being tailored to have exceptional combinations of chemical and physical properties. The materials desired for aerospace structures must be lightweight, rigid, and able to withstand wide temperature excursions. Composite ceramic materials can meet these requirements and many others important to the aerospace industry. Present processing techniques, however, are unable to produce ceramic structures reliably and reproducibly due to inadequate control over material composition and microstructure.

Control is a key concept in ceramics processing. Because all steps in ceramics production (e.g., particle synthesis or preparation, dispersion chemistry and powder handling, particle packing, piece fabrication, and sintering) are strongly interdependent, ceramic pieces can be fabricated reliably and reproducibly only if every step is performed properly. Unlike the case for metals processing, mistakes in ceramics processing cannot be corrected downstream by such steps as machining, welding, and deformation.

Over the past nine years, the Ceramics Processing Research Laboratory has demonstrated the feasibility of a chemistry-based approach to ceramics powder processing -- an approach well suited to aerospace structural technology because of its applicability to a wide variety of complex materials. The diverse CPRL research team includes not only experts in conventional sintering and grain growth, but also authorities on colloid,

polymer, and organometallic chemistries, physics, and math, providing the broad base needed to explore the fundamentals of ceramics processing.

Controlled processing requires an understanding of the physical and chemical forces governing ceramic particles' behavior during each processing step; rheological behavior, polymer chemistry, and binder burnout are also considerations. Hundreds of billions of particles (crystalline or amorphous, single- or polyphase) must be manipulated successfully to produce a single satisfactory ceramic component. Because the main difficulties lie in particle packing inhomogeneities introduced prior to densification, green microstructure control is key to ceramic materials' reliability and reproducibility. The vital research in this area -- presintering science -- has attracted international attention.

Experimentation has shown it possible to prepare and control the size distribution, shape, and chemistry of ceramic particles in single-cation oxide systems. Specimens can be prepared with controlled particle packing (and therefore controlled microstructures) when colloid chemistry is understood and interparticle forces controlled. The work involved one-component systems, and also extended the current paradigms to include multi-cation and multiphase materials such as magnesium-aluminum-silicate (cordierite), alumina-titania, alumina-zirconia, and alumina-silica. Studies were also conducted on silicon carbide-alumina and non-oxide systems such as silicon carbide and aluminum nitride.

II. RESEARCH SUMMARIES

Research conducted on this contract has combined an understanding of the mechanisms of particle formation (single-component and multicomponent) and particle surface chemistry with the development of processing models. Critical experiments were carried out to test hypotheses for controlling presintered and sintered microstructures. Research utilized novel chemical preparative concepts in combination with an understanding of colloid and ceramic sciences to produce reproducible, reliable microstructures. Sintered microstructure development was studied as a function of particle packing, pressure, and temperature, with studies being made in controlling the size and distribution of pores and other minor phases, and in controlling material composition for explicit control of properties and performance (e.g., thermal, dielectric, and mechanical characteristics).

All research under AFOSR sponsorship is prepared for publication in refereed journals as soon as a study is complete. A list of papers already prepared or in preparation is included in Section III of this report. Results from eleven diverse studies conducted during this contract are described in this report, indicating the Laboratory's accomplishments.

HYDROLYSIS OF ALKOXIDE EMULSION DROPLETS

Anne Bagley Hardy

ABSTRACT

The hydrolysis of alkoxide emulsion droplets was investigated as a method for preparing unagglomerated, submicrometer oxide ceramic particles with a homogeneous composition. Appropriate alkoxide-in-solvent emulsions could be formed when the alkoxide and continuous phase were immiscible and chemically inert, and when the alkoxide had a low solubility in the continuous phase so as to minimize reaction outside the alkoxide droplet. Based on these criteria, $\text{Ti}(\text{O}-n\text{-Bu})_4$, $\text{Al}(\text{O}-\text{sec-Bu})_3$, and $\text{Zr}(\text{O}-n\text{-Pr})_4$ were selected as alkoxides; propylene carbonate was used as the continuous phase. It was demonstrated that spherical, unagglomerated hydrous oxide powders with a predominantly submicrometer diameter could be formed by hydrolyzing these alkoxides, and that the particle size and size distribution corresponded to the droplet size and size distribution. This technique was also used to prepare mixed-oxide powders having an overall cation composition corresponding to the initial alkoxide cation composition. Individual particles were shown to have a uniform, mixed-cation composition. Uncalcined powders were amorphous, with high surface areas and low densities. Upon calcination, powders densified and became crystalline. Particles retained their spherical shape after being heated to 1000°C .

INTRODUCTION

Emulsions were formed of alkoxide droplets in an immiscible, nonreactive liquid. The alkoxide droplets were then hydrolyzed to form oxyhydroxide particles. If each alkoxide droplet reacts to form a particle, then individual droplets act as microreactors, allowing particle composition, shape, size, and size distribution to be controlled through the emulsion droplet.

The emulsions studied (alkoxide droplets in an inert, continuous phase) were unusual in that they were nonaqueous; neither phase could initially contain water, because water reacts rapidly to form the metal oxyhydroxide. This necessitated finding an appropriate emulsion system, one in which the alkoxide and an inert continuous phase were immiscible. After the emulsion was formed, water was added. The water was miscible in

the continuous phase and reacted with the alkoxide droplets to form metal oxyhydroxide particles.

This approach is conceptually similar to the hydrolysis or thermal decomposition of alkoxide aerosol droplets to form metal oxyhydroxide powder. Alkoxide aerosol reaction has been used to prepare a variety of powders including TiO_2 (Visca and Matijevic, 1979), Al_2O_3 (Ingebrethsen and Matijevic, 1980), Al_2O_3 - TiO_2 (Ingebrethsen, Matijevic, and Partch, 1983), and Y_2O_3 - ZrO_2 (Ishizawa et al., 1986) powders. These researchers have shown that each droplet reacts to form a particle and that nonagglomerated, spherical, submicrometer-diameter particles with a narrow size distribution can be formed by this technique.

This report describes the selection of appropriate alkoxide/continuous phase systems and elucidates the processing variables that are important in determining the powder morphology. Physical properties of the powder prepared using this method are then described.

EXPERIMENTAL PROCEDURE

General Procedures

All glassware was cleaned with soap and water, soaked in a KOH-isopropanol bath, and then rinsed in a HNO_3 -isopropanol bath. Glassware was then rinsed repeatedly with deionized water and dried in an oven at 125°C . Distillation glassware was, in addition, flame-dried under vacuum, then back-filled with high-purity nitrogen.

Because the alkoxides are very sensitive to water, all solvents and alkoxides were handled either in a N_2 -atmosphere glove box or on a Schlenk line. Molecular sieves (used to dry solvents) were dried at 350°C for at least 10 h and stored under nitrogen before use. Filtered, deionized water was used for all reactions.

Alkoxides

Liquid aluminum and titanium alkoxides (Alfa Products, Danvers, MA) were distilled under vacuum before use [titanium ethoxide, $\text{Ti}(\text{OEt})_4$ ($110^\circ\text{C}/0.15\text{-}0.2$ mm Hg); titanium *n*-propoxide, $\text{Ti}(\text{OPr})_4$ ($69^\circ\text{C}/0.5$ mm Hg); titanium *n*-butoxide, $\text{Ti}(\text{O-}n\text{-Bu})_4$ ($145^\circ\text{C}/0.1$ mm Hg); titanium *sec*-butoxide, $\text{Ti}(\text{O-}sec\text{-Bu})_4$ ($110^\circ\text{C}/0.15$ mm Hg); and titanium 2-ethylhexoxide, $\text{Ti}(\text{O-}2\text{-EtHex})_4$ ($185^\circ\text{C}/0.2$ mm Hg)]. Yttrium isopropoxide, $\text{Y}(\text{O-}i\text{-Pr})_3$ (Alfa Products, Danvers, MA), was used as-received. Zirconium *n*-propoxide, $\text{Zr}(\text{O-}n\text{-Pr})_4$, was purchased as a $\text{Zr}(\text{O-}n\text{-Pr})_4/n$ -propanol solution (Alfa Products, Danvers, MA). The *n*-propanol was removed by distillation. The resulting product, initially very viscous, over time became a transparent solid. Hexane (20-30 vol%) was added to make the zirconium alkoxide fluid again.

Mixtures of $\text{Ti}(\text{O-}n\text{-Bu})_4$ with $\text{Al}(\text{O-}sec\text{-Bu})_3$ and of $\text{Al}(\text{O-}sec\text{-Bu})_3$ with $\text{Zr}(\text{O-}n\text{-Pr})_4$ were prepared by mixing the alkoxides, then diluting with 20 vol% hexane. Without the hexane, the mixtures formed a very viscous, almost gel-like solid; addition of the hexane made the alkoxide mixture fluid. Mixtures of $\text{Y}(\text{O-}i\text{-Pr})_3$ and $\text{Zr}(\text{O-}n\text{-Pr})_4$ were prepared by refluxing the solid $\text{Y}(\text{O-}i\text{-Pr})_3$ in an 80 vol% $\text{Zr}(\text{O-}n\text{-Pr})_4/20$ vol% hexane mixture for 30 min. After refluxing, the mixture formed a clear fluid.

Continuous Phase Selection

A variety of solvents were used as the continuous phase, including acetonitrile, butylene carbonate, nitromethane, propylene carbonate, ethylene carbonate, pyrrolidone, and formamide. Reagent-grade acetonitrile (Aldrich Chem. Co., Inc., Milwaukee, WI), from which residual water was removed with 3A molecular sieves, was used. Formamide, pyrrolidone, nitromethane, ethylene carbonate, propylene carbonate (all from Aldrich

Chem. Co., Inc., Milwaukee, WI) and butylene carbonate (Chemical Dynamics Corp., South Plainfield, NJ) were >99% pure and were dried with molecular sieves. In addition, for certain experiments, propylene carbonate was double-distilled under vacuum and stored under nitrogen over 3A molecular sieves; before use, it was filtered in a nitrogen-atmosphere glove box through a 10- μ m glass-frit filter.

Both pure solvent and solvent/surfactant solutions were used. Solvent/surfactant solutions were prepared by dissolving the surfactant in the solvent, then storing the solution over 3A molecular sieves. Typical surfactant concentrations ranged from 0 to 1.0 vol%.

Surfactants

Surfactants (Span[®]83, 80, and 20; Brij[®]35, 97, 98, and 721, and Tween[®]20), obtained as samples from ICI Americas Inc. (Wilmington, DE), were used as-received.

Preparation and Reaction of Emulsions

Emulsions were typically prepared by emulsifying 10-20 vol% alkoxide with an appropriate continuous phase (with or without surfactant) using an ultrasonic probe. The ultrasonic probe provided the mechanical energy to break the alkoxide into droplets. The same procedure was used regardless of whether a single alkoxide or an alkoxide mixture was used. Undiluted titanium alkoxides were used. Pure $\text{Zr}(\text{O-}i\text{-Pr})_4$, pure $\text{Al}(\text{O-}i\text{-Bu})_3$, and alkoxide mixtures were diluted with 20 vol% hexane to reduce the alkoxide viscosity. The alkoxides and solvents were handled in a N_2 -atmosphere glove box; ultrasonication was done in air.

A typical formulation was as follows: 3 ml alkoxide was added to 17 ml propylene carbonate in a 6-dram glass vial. The vial was capped, removed

from the glove box, and sonicated in air using a 1/2"-titanium-tip probe (Sonicator Model W-220F, Heat Systems-Ultrasonics Inc., Farmingdale, NY) for approximately 20-30 s. During sonication, the sample changed from two distinguishable, transparent layers to a uniformly turbid emulsion.

Emulsions containing continuous-phase-solvents that were more dense than the alkoxide (e.g., propylene carbonate) were more difficult to emulsify because much or all of the alkoxide layer was above the bottom of the ultrasonic probe tip and most of the probe energy is directed downwards from the tip. Therefore, to ensure better emulsification, the bottom of the tip was kept as close to the top of the sample as possible without exposing the tip to air during sonication, and narrow vials were used to maximize the amount of alkoxide below the tip. Sample turbulence caused by ultrasonication was usually sufficient to emulsify all of the alkoxide.

Immediately after emulsification, the emulsion was poured into a 30-ml centrifuge tube, and deionized water added. The emulsion rapidly changed from a uniform turbidity to a flocculated appearance as the powder formed and agglomerated. Approximately 10-molar excess of water was typically used (e.g., for 3 ml $\text{Ti}(\text{O}-n\text{-Bu})_4$, 3.0 ml H_2O was added). The samples were centrifuged at 5000-6000 rpm for about 20 min to form a powder compact. The compact was then redispersed in isopropanol and recentrifuged (volume ratio of isopropanol to powder, ~100). This washing process was typically repeated 3-6 times to remove the continuous phase and any residual surfactant.

Some powders were additionally washed using Soxhlet extraction with either tetrahydrofuran or isopropanol. The Soxhlet thimble was lined with filter paper to prevent the powder from filtering through the thimble. Typical Soxhlet washing times ranged from 12 to 30 h.

Alkoxide/Continuous Phase Immiscibility and Reactivity

A variety of solvents were combined with $\text{Ti}(\text{OBu})_4$ in one case and with $\text{Al}(\text{O-sec-Bu})_3$ in another to determine whether the solvents were immiscible with the alkoxide and to observe any reaction between the alkoxide and the solvent. Immiscibility between alkoxide and solvent was checked by mixing 2 ml alkoxide with 8 ml solvent in a 20-ml vial, vigorously shaking for ~30 s, and then leaving the sample undisturbed for several hours.

Immiscibility was assumed if, after that time, the sample had separated into two layers instead of forming a single, clear solution.

Reactivity was qualitatively noted by observing whether the nature of either phase changed (e.g., precipitate formation or liquid alkoxide solidification) after the solvent and alkoxide were mixed together. If a precipitate or gel formed, as in the $\text{Al}(\text{O-sec-Bu})_3$ -formamide case, the remaining solvent was decanted, additional alkoxide was added, and the above procedure repeated. This filtration was done to ensure that the hydrolysis was not a result of water in the solvent; the first addition of the alkoxide served to dry the solvent.

Solubility of Alkoxides in Acetonitrile and Propylene Carbonate

Solubilities of titanium alkoxides [$\text{Ti}(\text{OEt})_4$, $\text{Ti}(\text{O-n-Pr})_4$, $\text{Ti}(\text{O-n-Bu})_4$, $\text{Ti}(\text{O-sec-Bu})_4$, and $\text{Ti}(\text{O-2-EtHex})_4$], $\text{Al}(\text{O-sec-Bu})_3$, and $\text{Zr}(\text{O-n-Pr})_4$ in acetonitrile and propylene carbonate were measured. Thirty milliliters of either acetonitrile or propylene carbonate was mixed with 3 ml of alkoxide in a 40-ml centrifuge tube in a N_2 -atmosphere glove box. Undiluted titanium alkoxides were used. $\text{Al}(\text{O-sec-Bu})_3$ was used either undiluted or diluted with 20 vol% hexane. $\text{Zr}(\text{O-n-Pr})_4$ was used either as-received (in

n-propanol) or with the n-propanol distilled and the product diluted in hexane.

Samples were removed from the glove box and sonicated for 25 s with an ultrasonic probe to form emulsions. The samples were then resealed and centrifuged (2500 rpm, 1-2 h, 25°C) to separate the emulsion into two transparent layers: a solvent-rich phase (propylene carbonate or acetonitrile) and an alkoxide-rich phase. Because propylene carbonate (density = 1.19 g/cm³, per Lee, 1976) is more dense than the alkoxide (density typically ~1.0 g/cm³, per Bradley, Mehrotra, and Gaur, 1978), the alkoxide phase formed the top layer in propylene carbonate/alkoxide systems. To recover the propylene carbonate phase without introducing any alkoxide, the propylene carbonate samples were gently poured into a separatory funnel. Twenty-five milliliters of the propylene carbonate phase was collected in a volumetric flask. Because acetonitrile, on the other hand, is less dense than the alkoxide, the acetonitrile phase formed the top layer, which was pipetted directly into a 25-ml volumetric flask.

The titanium concentration in these samples was determined by ethylenediaminetetra-acetic acid (EDTA) compleximetric titration. The procedure followed one recommended in the literature (Pribil, 1982; West, 1969) with a few modifications. One to two milliliters of concentrated HNO₃ were added to dissolve the titanium hydrous oxide precipitate. To solubilize propylene carbonate samples, because propylene carbonate has a limited solubility in water, 20 ml of isopropanol was added to the 25-ml sample of propylene carbonate. All samples were then diluted to 100 ml with deionized water. An excess of 0.02-M EDTA solution was added (typically 10-35 ml), followed by several drops of 0.1-wt% xylenol orange solution and 2 ml of H₂O₂. The solution was made basic by adding NH₄OH

(solution color changed to violet), and then the pH was adjusted to 1-2 with HNO_3 (solution color changed to yellow; pH measured by pH paper). The yellow solution was titrated with 0.02-M $\text{Bi}(\text{NO}_3)_3$ to an orange-to-violet end point. EDTA solutions were standardized with a $\text{Bi}(\text{NO}_3)_3$ solution. The amount of titanium was proportional to the difference between the EDTA and $\text{Bi}(\text{NO}_3)_3$ volumes. Four measurements were made for each alkoxide-solvent combination, with a variation of approximately $\pm 5\%$ in the results.

Because the acetonitrile or propylene carbonate might possibly affect the EDTA complexation, standardization of the EDTA with $\text{Bi}(\text{NO}_3)_3$ was done in pure water, H_2O /propylene carbonate, and H_2O /acetonitrile solutions. The presence of propylene carbonate or acetonitrile was not found to affect the reaction.

Solubility measurements of $\text{Ti}(\text{O}-n\text{-Bu})_4$ in acetonitrile and propylene carbonate as a function of surfactant (Brij®35) concentration were also taken. Brij®35 solutions in propylene carbonate and acetonitrile were prepared in the range of 0-1.0 vol% surfactant, and the procedure outlined above for determining titanium was again followed.

Solubility of $\text{Al}(\text{O}-\text{sec-Bu})_3$ in propylene carbonate and acetonitrile was also determined by an indirect EDTA titration for aluminum following a recommended procedure (Pribil, 1982). A 25-ml sample of the solvent-rich portion was added to a 250-ml Erlenmeyer flask. Approximately 1 ml of HNO_3 was added to dissolve the precipitate, then an excess of 0.05-M EDTA solution was added (again, 25 ml isopropanol was added to propylene carbonate samples). The samples were boiled for ~5 min, then cooled and diluted to 100 ml with deionized water. Approximately 15 drops of 0.1 wt% xylenol orange were added, along with enough hexamine to adjust the pH to ~5.0 (resulting solution was pale yellow). The solution was then titrated

with 0.05-M $\text{Pb}(\text{NO}_3)_3$. The amount of aluminum in the continuous phase was proportional to the difference between the $\text{Pb}(\text{NO}_3)_3$ and EDTA volumes.

The concentration of $\text{Zr}(\text{O}-n\text{-Pr})_4$ in the continuous phase was measured by ICP analysis (Galbraith Laboratories, Knoxville, TN). Samples for analysis were prepared by hydrolyzing the alkoxide in the solvent-rich phase, then adding a HNO_3 solution in isopropanol to the continuous phase to dissolve the precipitate.

Concentration Effects

Emulsions of $\text{Al}(\text{O}-\text{sec-Bu})_3$, $\text{Ti}(\text{O}-n\text{-Bu})_4$, and $\text{Ti}(\text{O}-2\text{-EtHex})_4$ in propylene carbonate were prepared using alkoxide concentrations ranging from 0.1 to 10 vol%. The total volume (alkoxide plus continuous phase) was typically 20 ml. Emulsions with an alkoxide concentration less than 1 vol% were prepared by diluting a 1-vol% emulsion; otherwise, the emulsions were prepared by directly adding alkoxide to propylene carbonate. Water was added either immediately after the emulsion had formed or 20-25 min after emulsion formation. Powders were then washed as described above. Powder morphology was determined by scanning electron microscopy (SEM), by transmission electron microscopy (TEM), and by measuring particle-size distributions with a centrifugal particle-size analyzer.

Temperature Effects

Thirty milliliters of a 0.5 vol% $\text{Ti}(\text{O}-n\text{-Bu})_4$ -in-propylene carbonate emulsion was prepared, then divided into three 10-ml samples. One sample was left at room temperature ($T = 25^\circ\text{C}$), another was placed in a hot-water bath ($T = 65^\circ\text{C}$), and the third was placed in boiling water ($T = 100^\circ\text{C}$). The samples were equilibrated to the bath temperature for 10 min, then quickly poured into a centrifuge tube. Water was immediately added to each

emulsion to hydrolyze the alkoxide. The emulsions at 25°C and 65°C remained turbid; the emulsion at 100°C cleared, indicating that the alkoxide was completely miscible with the propylene carbonate at that temperature. However, in the process of pouring the 100°C sample into the centrifuge tube, the solution became slightly turbid, apparently indicating the formation of some droplets as it cooled. Powder morphology was determined by centrifugal particle-size analysis, SEM, and TEM.

Droplet- and Particle-Size Measurements

All glassware was flame-dried immediately before being placed in the glove box, and propylene carbonate was doubly distilled and stored over molecular sieves. Before use, the propylene carbonate was filtered through a 10- μm glass-frit filter. Emulsions (20 ml each) containing 2 vol% $\text{Ti}(\text{O}-2\text{-EtHex})_4$ in propylene carbonate were prepared by sonication. Samples for droplet-size measurement were prepared by diluting approximately 10 drops of emulsion in 2 ml propylene carbonate, then placing the mixture in a sample cell. To better seal the cells, the sample-cell lids were either wrapped with parafilm or dipped in hot wax. All sample preparation to this point (including the ultrasonication) was done in a N_2 -atmosphere glove box.

The samples were removed from the glove box, and droplet sizes measured by centrifugal particle-size analysis (Horiba CAPA 500, Irvine, CA). Emulsion droplet-size distributions were typically measured between 0.3 and 5.3 μm at 3000 rpm (measuring time ~30 min). While the droplet size was being measured, the remaining emulsion was hydrolyzed. The powders were washed and their particle sizes also measured by centrifugal particle-size analysis. Typically, particle-size distributions were

measured between 0.3 and 4.3 μm at 2000 rpm (measuring time ~ 15 min).

Particle-size distributions and average diameters of powders prepared under standard conditions (10-20 vol% alkoxide, $T = 25^\circ\text{C}$) were also measured to gauge the width and shape of the particle-size distribution.

Electron Microscopy

Transmission electron microscopy (TEM) samples were prepared using powders washed six times in isopropanol (dispersed in isopropanol, centrifuged, isopropanol decanted) as described above. Approximately 0.4 g of washed powder was dispersed in 3 ml isopropanol using an ultrasonic bath. Two-hundred-mesh, carbon-coated copper grids (Ladd Research Ind., Inc., Burlington, VT) were dipped into the dispersion and then dried on slightly warmed, clean microscope slides. TEM samples were examined at 100 kV using a Phillips EM300 (Phillips Co., Munich, West Germany) instrument.

Scanning electron microscopy (SEM) samples were deposited on an SEM aluminum stub using two methods. In many cases, powder was dispersed in isopropanol and then a few drops of the dispersion were placed on a warm sample stub. The isopropanol evaporated, leaving a sample with a smooth surface. In some cases, double-sided sticky tape was placed on the stub to hold a thin layer of dry powder.

Samples were coated with a thin layer of gold (~ 100 Å) using a gold sputterer (Desk II, Denton Vacuum, Inc., Cherry Hill, NJ), then examined using a scanning electron microscope (Model S-530, Hitachi Ltd., Tokyo, Japan).

Powder Surface Area Measurement

Powder surface area as a function of calcination temperature was

measured for alumina, zirconia, and titania samples. Powders were washed with tetrahydrofuran by Soxhlet extraction for 30 h. Samples were then heated in air at 10°C/min to 250, 600, and 1000°C and held for 2 h. Uncalcined samples were outgassed at 100°C under flowing nitrogen. All other samples were outgassed at 200°C (2 h, flowing nitrogen). Surface area was measured by the nitrogen adsorption method of Brunauer-Emmett-Teller ("BET", Quantachrome, Syosset, NY). Single-point measurements were made with a 30% N₂/70% He gas mixture. Sample weights varied from about 0.03 g for high-surface-area powders to about 0.1 g for low-surface-area samples. Reported surface areas were the average of five measurements.

Density Measurement

Each density measurement required a sample of at least 2-3 g depending on the density. Powder for each density measurement was prepared by hydrolyzing two 100-ml emulsions, each containing 20 vol% alkoxide phase (undiluted Ti(O-*n*-Bu)₄; Al(O-*sec*-Bu)₃ and Zr(O-*n*-Pr)₄ diluted with 20 vol% hexane). Powders from the two emulsions were combined and washed by Soxhlet extraction (30 h, THF). Density measurements were made with a helium gas stereopycnometer (Quantachrome, Syosset, NY). Densities reported were the average of three measurements that agreed to within 1%. Powder density was measured for uncalcined samples and samples calcined at 250, 600, and 1000°C (heating rate 10°C/min, held at temperature 2 h).

X-Ray Diffraction

Powder crystal structure as a function of calcination temperature was determined by X-ray diffraction using a rotating Cu (K_α = 1.54 Å) anode (Rigaku RU300, Danvers, MA). Samples were heated at 10°C/min to 250,

600, 1000, and 1200°C for either 2 h or 15 h. Each X-ray sample was prepared by spreading a collodion powder solution on a microscope slide.

Sample Composition

Bulk alkoxide and powder compositions were measured using inductively coupled plasma emission spectroscopy (ICP). Alkoxide samples were prepared for ICP analysis by dissolving ~0.2 ml alkoxide in either a nitric acid or sulfuric acid solution. Powder samples were dissolved in nitric acid. ICP analyses were conducted by Galbraith Laboratories (Knoxville, TN).

Particle composition and homogeneity were measured for powders prepared from Al-Ti and Al-Zr alkoxide mixtures using energy-dispersive X-ray analysis (EDS) combined with scanning transmission electron microscopy (STEM). The measured area was approximately 400 x 500 Å, compared to particle diameters ranging from ~1000 to 6000 Å (a scanning mode across a small area of the sample instead of a steady beam was used because the steady beam tended to burn a hole in the sample). Various points were measured for each particle.

RESULTS AND DISCUSSION

System Choice

Criteria for selecting the emulsion system

The first step in forming alkoxide droplets was to choose an appropriate emulsion system. This entailed choosing compatible alkoxide/continuous phase pairs and an appropriate surfactant. Compatible alkoxide/continuous phase pairs had to meet the following criteria: To form an emulsion, the alkoxide and continuous phase obviously had to be immiscible. It was also necessary for the alkoxide to have a low solubility in the continuous phase to minimize the amount of alkoxide

dissolved in the continuous phase and thus minimize alkoxide reaction outside the droplet. Lastly, it was necessary for the alkoxide to be inert with respect to the continuous phase so that no reaction could occur until water was added to the emulsion and so that the only reaction was a hydrolysis reaction between water and the alkoxide.

An emulsion was also desired that was stable long enough for the reaction to occur. Surfactants are typically added to improve an emulsion's stability. Ideally, the surfactant would stabilize the emulsion and also be inert toward the alkoxide. The following sections discuss how these criteria were met and how varying processing parameters within these guidelines affected powder morphology.

Alkoxide/continuous phase immiscibility and reactivity

Hildebrand parameters (δ) were used as guides to selecting potential alkoxide-immiscible solvents. Hildebrand parameters characterize solvents according to their self-attraction and can be thought of, in a very broad sense, as a measure of the solvents' polarity. Alkoxides can generally be viewed as nonpolar, and were therefore assumed to have low Hildebrand parameters. Because immiscibility is predicted for liquids differing substantially in Hildebrand parameters, potentially immiscible liquids were selected as those with very large Hildebrand parameters (polar liquids). Based on preliminary work that showed $\text{Ti}(\text{O}-n\text{-Bu})_4$ to be miscible in acetone ($\delta = 20.2 \text{ MPa}^{1/2}$) but immiscible in acetonitrile ($\delta = 24.3 \text{ MPa}^{1/2}$), $22 \text{ MPa}^{1/2}$ was chosen as a lower cutoff, and solvents with Hildebrand parameters greater than $22 \text{ MPa}^{1/2}$ were selected. From this list, solvents with obviously reactive groups (e.g., OH groups in ethylene glycol) and solvents that are either very toxic or very expensive were eliminated.

Table 1 lists the solvents that were then tested for alkoxide immiscibility.

All the solvents listed except for the alcohols were immiscible with $\text{Ti}(\text{O-}n\text{-Bu})_4$ and $\text{Al}(\text{O-}sec\text{-Bu})_3$. Any sign of reaction between the continuous phase and the alkoxide (Table 1) was noted. $\text{Ti}(\text{O-}n\text{-Bu})_4$ and nitromethane may have reacted, because the mixture became increasingly yellow over time, though the liquids remained immiscible. Pyrrolidone and formamide appeared to react with the $\text{Al}(\text{O-}sec\text{-Bu})_3$: the $\text{Al}(\text{O-}sec\text{-Bu})_3$ was initially immiscible with the pyrrolidone, but after a few minutes a clear solution formed; the $\text{Al}(\text{O-}sec\text{-Bu})_3$ also appeared to react with the formamide to form a clear gel. By visual inspection, $\text{Ti}(\text{O-}n\text{-Bu})_4$ did not appear to react with pyrrolidone or formamide. Neither $\text{Ti}(\text{O-}n\text{-Bu})_4$ nor $\text{Al}(\text{O-}sec\text{-Bu})_3$ appeared to react with acetonitrile or the carbonates.

Table 1. Solvents immiscible in alkoxides and their solubility parameters.

Solvent	Solubility parameter/ hydrogen bonding capacity	Alkoxide interaction	
		$\text{Ti}(\text{O-}n\text{-Bu})_4$	$\text{Al}(\text{O-}sec\text{-Bu})_3$
Acetonitrile	24.3/poor	immiscible	immiscible
Butylene carbonate	24.7/moderate	immiscible	immiscible
Ethyl alcohol	26.0/strong	miscible	miscible
Isopropyl alcohol	23.5/strong	miscible	miscible
Nitromethane	26.0/poor	immiscible/ reacts	immiscible
Propylene carbonate	27.2/moderate	immiscible	immiscible
Ethylene carbonate	30.0/moderate	immiscible	immiscible
Pyrrolidinone	30.1/strong	immiscible	reacts
Formamide	39.3/strong	immiscible	reacts

Emulsions were then prepared and reacted using any one of the selected solvents as a continuous phase. Emulsions formed with $\text{Ti}(\text{O-n-Bu})_4$ were milky-white; emulsions formed with $\text{Al}(\text{O-sec-Bu})_3$ were less turbid and had a gray-white color. After water was added, powder began to agglomerate and settle within seconds, indicating that the powder formed rapidly. SEM inspection showed that TiO_2 powders formed in nitromethane, acetonitrile, and butylene carbonate contained a mixture of fine ($\sim 0.1 \mu\text{m}$) and larger spherical particles ($0.2\text{-}10.0 \mu\text{m}$) as shown, for example, in Figure 1: powders formed in propylene carbonate, ethylene carbonate, and formamide had relatively few fine particles and consisted mostly of spherical particles with a diameter between 0.2 and $2.0 \mu\text{m}$ as shown, for example, in Figure 2.

Aluminum oxyhydroxide powders formed in nitromethane and acetonitrile contained a mixture of fine ($\sim 0.1 \mu\text{m}$) particles and larger spherical particles ($\sim 0.5\text{-}10 \mu\text{m}$) (Fig. 3a), while powders formed in propylene carbonate and ethylene carbonate appeared to have a more uniform distribution of primarily spherical particles with a diameter of ~ 0.2 to $2 \mu\text{m}$, as shown in Fig. 3b.

Based on these immiscibility and reactivity results, propylene carbonate and acetonitrile were investigated more fully as solvents for the continuous phase. Propylene carbonate was preferred to ethylene carbonate because the latter has a melting point above room temperature (36.2°C , per Lee, 1976). Butylene carbonate is much more expensive than propylene carbonate and also has a melting point close to room temperature ($21.2\text{-}21.5^\circ\text{C}$, per Lee, 1976).

Having established that inert, immiscible alkoxide/continuous phase pairs could be selected, the effect of the second criterion (alkoxide

solubility in the continuous phase) on powder morphology will now be described.

Alkoxide solubility in acetonitrile and propylene carbonate

When two liquids are immiscible, they separate to form two phases. Although complete immiscibility is often assumed (i.e., each phase contains a pure liquid), there is actually some mutual solubility of the two liquids. For example, with alkoxide and propylene carbonate emulsions, the two phases are an alkoxide-rich phase containing some dissolved propylene carbonate and a propylene carbonate-rich phase containing some dissolved alkoxide. To minimize reaction outside the droplet, the alkoxide must approach complete immiscibility in the continuous phase, i.e., the alkoxide must have a very low solubility in the continuous phase. Alkoxide solubility in propylene carbonate and in acetonitrile was measured by EDTA titration or ICP for a series of titanium alkoxides, $\text{Al}(\text{O-sec-Bu})_3$, and $\text{Zr}(\text{O-n-Pr})_4$.

The sample preparation procedure followed for measuring alkoxide solubility in the continuous phase paralleled the procedure followed in preparing an emulsion for a reaction. Because the two phases were equilibrated for a relatively short time (<1 h), the measured solubility could be less than the equilibrium alkoxide solubility.

The measured alkoxide solubilities, listed in Table 2, range from $<5.0 \times 10^{-5}$ to 4.7×10^{-2} volume fraction. To put these solubilities in perspective, for an emulsion containing 10 vol% alkoxide, an alkoxide solubility of 1×10^{-3} volume fraction would be equivalent to 1 vol% of the alkoxide phase being dissolved in the continuous phase. Alkoxide solubilities were consistently higher in acetonitrile than in propylene carbonate. It was found with the titanium alkoxide series that alkoxide

Table 2. Solubility of various alkoxides in acetonitrile and propylene carbonate.

Alkoxide	Acetonitrile*	Propylene carbonate*
Ti(OEt) ₄	12.6	3.9
Ti(O- <u>n</u> -Pr) ₄	miscible	47.2
Ti(O- <u>n</u> -Bu) ₄	0.6	0.3
Ti(O- <u>sec</u> -Bu) ₄	---	1.3
Ti(O-2-EtHex) ₄	0.2	<0.05
Al(O- <u>sec</u> -Bu) ₃	2.2	1.4
Al(O- <u>sec</u> -Bu) ₃ / hexane	---	0.9
Zr(O- <u>n</u> -Pr) ₄ / <u>n</u> -propanol	---	1.7
Zr(O- <u>n</u> -Pr) ₄ / hexane	---	1.3

* 1×10^{-3} volume fraction

solubility in acetonitrile or propylene carbonate showed a general decrease with increasing alkyl chainlength. For Al(O-sec-Bu)₃, the addition of hexane to the alkoxide decreased the solubility of the Al(O-sec-Bu)₃ in propylene carbonate. Removing the n-propanol and diluting with hexane reduced the solubility of Zr(OPr)₄ in propylene carbonate.

Emulsions were prepared using each of the alkoxides listed in Table 2, respectively, and either propylene carbonate or acetonitrile. Powder morphology was then examined as a function of alkoxide solubility in the continuous phase. SEM inspection showed that for alkoxides with relatively high solubilities, the resulting powders contained both very fine,

irregularly shaped particles (<0.01 - $0.15 \mu\text{m}$) and larger, spherical particles (0.2 - $10.0 \mu\text{m}$), as shown in Figure 4. When alkoxides with comparatively low solubilities were used, the number of fine particles decreased (SEM observation) so that with low-solubility alkoxide systems, few fine particles were observed and powders contained mostly 0.1 - $1\text{-}\mu\text{m}$ diameter, discrete spherical particles (Fig. 5). Consistent with the alkoxide solubilities' being lower in propylene carbonate than in acetonitrile, powders formed from the same alkoxide had a more uniform distribution when propylene carbonate was used as the continuous phase instead of acetonitrile.

Powders formed from $\text{Al}(\text{O-}\underline{\text{sec}}\text{-Bu})_3$ diluted with hexane had a more uniform distribution than powders formed from undiluted $\text{Al}(\text{O-}\underline{\text{sec}}\text{-Bu})_3$, as shown in Figure 6. This was partly due to the reduced solubility of $\text{Al}(\text{O-}\underline{\text{sec}}\text{-Bu})_3$ in propylene carbonate when hexane was added, and was also probably a result of the lowered alkoxide viscosity when hexane was added, which facilitated emulsification. Similarly, powders prepared with $\text{Zr}(\text{O-}\underline{\text{n}}\text{-Pr})_4$ diluted with 20 vol% hexane had a more uniform distribution than powders prepared with $\text{Zr}(\text{OPr})_4$ in $\underline{\text{n}}$ -propanol (Fig. 7).

Hydrolysis of alkoxide in the alkoxide-saturated continuous phase resulted in powders with a very fine particle size, and so it was hypothesized that 1) the fine particles resulted from the hydrolysis of alkoxide dissolved in the continuous phase, and 2) the spherical, 0.1 - $1\text{-}\mu\text{m}$ diameter particles resulted from the hydrolysis of alkoxide droplets. Thus, when higher-solubility alkoxides were used, more fine particles were observed, and when lower-solubility alkoxides were used, the number of fine particles decreased.

Using the alkoxide/continuous phase criteria of immiscibility and low alkoxide solubility in the continuous phase, either $\text{Ti}(\text{O}-n\text{-Bu})_4$ or $\text{Ti}(\text{O}-2\text{-EtHex})_4$ was used as a titanium source, $\text{Al}(\text{O}-\text{sec-Bu})_3$ diluted in hexane was used as an aluminum source, and $\text{Zr}(\text{O}-n\text{-Pr})_4$ diluted in hexane was used as a zirconium source. Based on SEM observations and alkoxide solubility measurements, propylene carbonate was preferred to acetonitrile as a continuous phase. Having established the alkoxide/continuous phase pairs finally selected, the effects of surfactant on emulsion stability and powder morphology are now discussed.

Surfactant choice

Emulsions are typically stabilized by adding surfactant. Surfactant addition can lead to smaller, more stable droplets because the surfactant, by lowering the interfacial tension, lowers the energy required to break the liquid into droplets; also, by acting as a barrier to coagulation/coalescence, the surfactant slows the coagulation/coalescence of droplets.

A variety of nonionic surfactants, including Span, Tween, and Brij surfactants, were investigated. Span surfactants are a class of sorbitan fatty acid esters; Tween surfactants are polyoxyethylene sorbitan fatty acid esters; and Brij surfactants are polyoxyethylene fatty ethers. Structures for these surfactants are shown in Figure 8. All of these surfactants contain hydroxyl groups (it was difficult to find commercial surfactants that did not contain reactive groups), but because the Brij surfactants have the fewest hydroxyl groups per molecule, they were preferentially used.

Emulsions of $\text{Ti}(\text{O}-n\text{-Bu})_4$ in either acetonitrile or propylene carbonate were prepared with surfactant concentrations ranging from 0 to 1.0 vol%. With acetonitrile, as the surfactant concentration increased, the emulsion

stability increased and the resulting powders decreased in size, e.g., from ~5-20 μm with no surfactant to ~0.2-5 μm with 1 vol% Brij 97.

Concurrent with this decrease in particle size, an increase in the number of fine particles was observed. These effects are shown in Figure 9.

In contrast, when propylene carbonate was used as the continuous phase, the addition of surfactant had little effect on the emulsion stability or the resulting particle size, and there was no significant increase in the number of fine particles with increasing surfactant concentration (Fig. 10). Comparison of a series of $\text{Ti}(\text{O}-n\text{-Bu})_4$ -in-propylene carbonate emulsions prepared with surfactant (1 vol% Brij 35) to those prepared with no surfactant showed the resulting average particle sizes (measured by centrifugal particle-size analysis) to be similar: $0.85 \pm 0.7 \mu\text{m}$ and $0.95 \pm 0.7 \mu\text{m}$ for powders prepared without and with surfactant, respectively.

Because the emulsion droplets were hydrolyzed immediately after formation, emulsion stability was required for less than 30 s. The difference in particle size between powders formed in acetonitrile and those formed in propylene carbonate when the emulsions were prepared without surfactant was attributed to a difference in stability of the emulsion droplets.

This stability difference was due, at least partially, to the higher viscosity of propylene carbonate (2.5 cp, per Lee, 1976) compared to the viscosity of acetonitrile (0.36 cp, per Coulter Product Reference Manual, 1982). Because collision frequency is indirectly proportional to the continuous phase viscosity (Hiemenz, 1977), emulsion stability increases with an increase in the viscosity of the continuous phase. The emulsion creaming rate is also indirectly proportional to the continuous phase

viscosity (Carroll, 1976). Creaming leads to an alkoxide-droplet-rich layer, which can contribute to droplet growth because of the increase in the droplet collision rate with increasing droplet concentration. The higher viscosity of propylene carbonate, therefore, decreased droplet coagulation by reducing the coagulation rate and the creaming rate.

It was hypothesized that the fine particles that appeared with increasing surfactant concentration in the acetonitrile system resulted either from the solubilization of the alkoxide within micelles or from the alkoxide's reaction with the surfactant, leading to acetonitrile-soluble alkoxide-surfactant molecules. In either case, the perceived solubility of $\text{Ti}(\text{O}-n\text{-Bu})_4$ in the continuous phase would increase as the surfactant concentration is increased.

Titanium solubility as a function of surfactant (Brij®35) concentration in both acetonitrile and propylene carbonate was measured to see if the formation of fine particles could be related to alkoxide solubility. These results, shown in Figure 11, indicate that in the acetonitrile system, as the surfactant concentration was increased from 0 to 1 vol%, the alkoxide solubility increased over 5 times, while in the propylene carbonate system, solubility increased only slightly. These results follow the trend observed in the pure solvent case: as the solubility increased, the number of fine particles also increased.

One explanation for the increased number of fine particles as the surfactant concentration was increased in powders formed in acetonitrile but not in propylene carbonate is that micelles form in acetonitrile but not in propylene carbonate. Possible micelle formation and its influence on the powder was of interest because the presence of micelles is one way in which emulsions could differ from aerosols and complicate the powder-

formation process. Micelles are surfactant aggregates that form above a solvent-specific surfactant concentration known as the critical micelle concentration (CMC). The micelle interior (in this case, a nonpolar, hydrocarbon-rich region) solubilizes material that is insoluble in the continuous phase. Micelle-solubilized alkoxide could react to yield the fine particles observed at higher surfactant concentrations. Particle formation has been shown to occur in various micelle (or microemulsion) systems (e.g., Lufimpadio, Nagy, and Derouane, 1984; Kandori, Kon-ho, and Kitahara, 1988).

The literature contains little information on micelle formation in polar, nonaqueous solvents. Micellization of nonionic surfactants has not been reported in acetonitrile or propylene carbonate, though it has been observed in a variety of polar solvents (Ray, 1971; Magrid, 1978). Ray (1971) found, in a study of micelle formation of polyoxyethylene (9) nonylphenol in a series of polar, nonaqueous solvents, that the CMC was dramatically higher than in water; typically, the CMC was several orders of magnitude higher in the nonaqueous solvents, and tended to increase with decreasing Hildebrand parameter. For example, in formamide, the CMC was 0.9 vol%. Ray only found evidence for micelle formation in solvents with two or more hydrogen-bonding centers. Others, in studies of ionic surfactants, found evidence of micelle formation in solvents with only one hydrogen-bonding center (Singh, Singh, and Tewari, 1976; Singh et al., 1980), and micellization of anionic surfactant in acetonitrile has also been reported (Fendler and Fendler, 1975).

To determine if micellization occurred in the acetonitrile in the present study, the surface tension of acetonitrile was measured as a function of surfactant concentration, using a surface tensiometer. At

surfactant concentrations less than the CMC, the surfactant, if surface active, should reduce the surface tension. Above the CMC, the surfactant associates to form micelles and does not act to reduce the surface tension. If micelles form, a sharp break in the slope of a plot of surface tension against surfactant concentration should occur at the CMC.

Our results showed that over the range of 0-1 vol% Brij®35, surface tension was independent of the surfactant concentration. Surface tension changes produced by adding surfactant to organic solvents are often small compared to surface tension changes produced by adding surfactants to water (Kertes and Gutman, 1976) because of the lower surface tension of nonaqueous solvents. Ray (1971) found that, in non-micelle-forming solvents, the surface tension of the solvent-surfactant mixture was that expected for a mixture of two liquids (i.e., the surfactant and the solvent). It is possible that acetonitrile and Brij®35 have similar surface tensions, and the addition of a small amount of surfactant does not change the surface tension noticeably. Based on surface tension measurements, no evidence of micelle formation in acetonitrile was observed. This would agree with Ray's (1971) conclusions that nonionic surfactants do not form micelles in solvents with fewer than two hydrogen-bonding centers.

Another explanation for the increase in the number of fine particles with surfactant concentration in powders formed in acetonitrile is that the alkoxide reacted with the surfactant to form an alkoxysurfactant product that was soluble in acetonitrile. It was calculated for a solution with 1 vol% Brij®35, assuming one OH group per surfactant molecule, that if each OH group reacted with an alkoxide molecule to form an acetonitrile-soluble product, the perceived titanium alkoxide solubility in acetonitrile would

increase to -9.6×10^{-3} volume fraction. The measured titanium alkoxide solubility with 1 vol% Brij®35 was 3.5×10^{-3} volume fraction, a value that is in reasonable agreement with the former, as it is possible that not every surfactant molecule would react. There are several explanations for the observation that the effect of surfactant addition was not as dramatic in propylene carbonate as in acetonitrile: it is possible that the alkoxysurfactant product was less soluble in propylene carbonate than in acetonitrile, or that propylene carbonate was a poorer solvent for the alkoxysurfactant reaction.

Because the addition of surfactant had little effect on the particle-size distribution of powders formed in propylene carbonate, a surfactant was not used with propylene carbonate. Addition of a surfactant added another nonvolatile carbon source that had to be removed after powder formation. For example, a typical surfactant concentration of 1 vol% in the emulsion corresponded, in an emulsion containing 10 vol% $\text{Ti}(\text{O}-n\text{-Bu})_4$, to approximately 40 wt% of the powder.

Based on the results described in this section, the emulsion system selected for further study was defined as one consisting of propylene carbonate as the continuous phase, $\text{Ti}(\text{O}-n\text{-Bu})_4$ or $\text{Ti}(\text{O}-2\text{-EtHex})_4$ as titanium sources, $\text{Al}(\text{O}-s\text{-oc-Bu})_3$ (20 vol% hexane) as an aluminum source, and $\text{Zr}(\text{O}-n\text{-Pr})_4$ (20 vol% hexane) as a zirconium source. No surfactant was used.

Powder Formation Mechanism

Investigative approach

The work described so far has been based on the assumption that droplets hydrolyze and retain their shape and composition, so that the

particle size is thus determined by the droplet. This assumption seemed valid based on work with alkoxide aerosols done by Visca and Matijevic (1979), Ingebrethsen and Matijevic (1980), Ingebrethsen, Matijevic, and Partch (1983), and Ishizawa et al. (1986), which showed that individual aerosol droplets hydrolyze or pyrolyze to form particles with a size and composition determined by the droplet. As with aerosols, liquid alkoxide droplets were reacted; the gaseous continuous phase of an aerosol, however, was replaced by a liquid. The present section discusses whether this assumption -- that individual droplets react to form particles -- proved valid for this new system.

Because the reaction occurs rapidly and in a turbid system, the progress of hydrolysis was difficult to monitor, specifically the location of water, alkoxide, and hydrolyzed alkoxide. Most methods for extrapolating information on the reaction mechanism involved either varying the processing parameters and noting whether changes in the powder morphology were consistent with our hypothesis, or comparing the initial emulsion system with the hydrolysis product and inferring how the alkoxide droplets transformed to solid particles. In this section, the results of these two approaches are described.

Variation of dispersed-phase concentration

Emulsions were prepared with $\text{Ti}(\text{O-}n\text{-Bu})_4$, $\text{Ti}(\text{O-2-EtHex})_4$, and $\text{Al}(\text{O-sec-Bu})_3$ (20 vol% hexane) over a range of alkoxide concentrations (0.1-20 vol%) to investigate the effect of alkoxide concentration on powder morphology, particularly on the particle-size distribution. If droplets react to form particles, the powder morphology would be expected to be relatively independent of the alkoxide-phase concentration, except for alkoxide concentrations at which the relative amount of dissolved alkoxide

becomes high (i.e., for low alkoxide concentrations) or for alkoxide concentrations at which the droplet concentration is high enough that collisions occur frequently and emulsion stability is decreased.

For $\text{Ti}(\text{O-}n\text{-Bu})_4$ and $\text{Al}(\text{O-}sec\text{-Bu})_3$, it was found that emulsions could be prepared with a dispersed-phase concentration ranging from ~1-20 vol% without significant changes in the particle-size distribution. At concentrations less than ~1 vol%, the percentage of fine particles in emulsions equilibrated ~20 min before hydrolysis became significant, as reflected in particle-size distributions (measured by centrifugal particle-size analysis) and TEM and SEM micrographs. At dispersed-phase concentrations greater than 20 vol%, emulsions separated rapidly after formation.

In Table 2, solubilities of $\text{Ti}(\text{O-}n\text{-Bu})_4$ and $\text{Al}(\text{O-}sec\text{-Bu})_3$ in propylene carbonate were reported. Based on these values, it was expected that for emulsions formed from $\text{Ti}(\text{O-}n\text{-Bu})_4$ and $\text{Al}(\text{O-}sec\text{-Bu})_3$, a significant amount of alkoxide would be dissolved from the droplet into the continuous phase at alkoxide concentrations less than ~1 vol%. As shown earlier in this report, this dissolved alkoxide hydrolyzed to form what were described as fine particles, i.e., irregularly shaped particles or flocs of particles with a primary particle size less than ~0.2 μm . Aluminum hydrous oxide powders prepared from $\text{Al}(\text{O-}sec\text{-Bu})_3$ had more fine particles than had titanium hydrous oxide powders at the same dispersed-phase concentration (as observed by SEM and TEM), as would be expected from the higher solubility of $\text{Al}(\text{O-}sec\text{-Bu})_3$ in propylene carbonate.

It was observed that emulsion stability increased with a decrease in alkoxide concentration. For example, emulsions formed with 1 vol% $\text{Ti}(\text{O-}n\text{-Bu})_4$ were stable for at least 20 min; emulsions formed with 20 vol%

$\text{Ti}(\text{O-}n\text{-Bu})_4$ showed signs of separation after only several minutes. Because of the limited emulsion stability at higher dispersed-phase concentration, 20 vol% was chosen as an upper limit for the alkoxide concentration in the emulsion.

Alkoxide concentration effects on particle size-distributions are shown in the particle-size distributions as a function of $\text{Ti}(\text{O-}n\text{-Bu})_4$ concentration for samples prepared from emulsions equilibrated for 20-25 min before hydrolysis (Fig. 12). At low $\text{Ti}(\text{O-}n\text{-Bu})_4$ concentrations (Fig. 12a), there were many fine particles (particle diameter $<0.2 \mu\text{m}$). At 1 vol% $\text{Ti}(\text{O-}n\text{-Bu})_4$, there were significantly fewer fine particles, and the particle-size distributions for powders prepared from 1 and 10 vol% $\text{Ti}(\text{O-}n\text{-Bu})_4$ were similar.

This effect of alkoxide concentration can be seen in micrographs of powders prepared from $\text{Ti}(\text{O-}n\text{-Bu})_4$ and $\text{Al}(\text{O-}sec\text{-Bu})_3$ (Figs. 13 and 14). At low alkoxide concentrations, TEM and SEM micrographs showed that the powders contained a mixture of fine, irregularly shaped or agglomerated particles and larger, spherical particles. Often, at magnifications used for SEM, these fine particles appeared as an almost smooth coating over the larger particles. At moderate alkoxide concentrations, the relative number of fine particles was reduced, and the overwhelming majority of particles were spherical, submicrometer- to micrometer-diameter particles. Figure 15 shows fine particles formed from $\text{Al}(\text{O-}sec\text{-Bu})_3$ and $\text{Ti}(\text{O-}n\text{-Bu})_4$ at high magnifications; note the irregular particle shape and agglomerated particles.

The results for $\text{Ti}(\text{O-}n\text{-Bu})_4$ and $\text{Al}(\text{O-}sec\text{-Bu})_3$ contrasted with those for powders prepared from $\text{Ti}(\text{O-}2\text{-EtHex})_4$ in the propylene carbonate emulsions. For $\text{Ti}(\text{O-}2\text{-EtHex})_4$, powders could be prepared from emulsions

containing as little as 0.2 vol% $\text{Ti}(\text{O}-2\text{-EtHex})_4$ with no dramatic changes in the relative number of fine particles. This low concentration of fine particles was consistent with the low $\text{Ti}(\text{O}-2\text{-EtHex})_4$ solubility in propylene carbonate ($<5 \times 10^{-5}$ volume fraction). Again, the upper limit for alkoxide concentration, 20 vol%, was set by the emulsion stability.

When the powders described above were prepared from dilute emulsions (<5 vol%), the emulsions were reacted ~20 min after sonication. When very dilute emulsions (<1 vol%) were reacted immediately after formation, very few fine particles were observed (Fig. 16). This lack of fine particles indicates that the dissolution of the alkoxide into the continuous phase takes time. This observation was supported by droplet-size measurements (centrifugal particle-size analyzer) made a few minutes after emulsion formation and 30 min after formation. These measurements showed that, for dilute $\text{Ti}(\text{O}-n\text{-Bu})_4$ -in-propylene carbonate emulsions, the average droplet size decreased with time as the droplets dissolved into the continuous phase until the equilibrium alkoxide concentration in propylene carbonate was reached.

Based on these results, three alkoxide-concentration regions were defined for $\text{Ti}(\text{O}-n\text{-Bu})_4$ and $\text{Al}(\text{O}-\text{sec-Bu})_3$ in propylene carbonate: low alkoxide concentrations ($\sim <1$ vol%) that, because of the finite solubility of the alkoxide in the propylene carbonate, caused many fine particles to form due to hydrolysis of the alkoxide in solution; moderate alkoxide concentrations ($\sim 1\text{-}20$ vol%) that caused the majority of particles to form due to hydrolysis of the alkoxide droplets; and high enough alkoxide concentrations ($\sim >20$ vol%) that the emulsion stability was reduced.

Temperature effects

Powder morphology was also examined as a function of reaction temperature for $\text{Ti}(\text{O}-n\text{-Bu})_4$ -in-propylene carbonate emulsions. At alkoxide concentrations greater than approximately 1 vol%, changes in reaction temperature (from -15°C to 100°C) did not strongly affect the powder morphology, presumably because the change in alkoxide solubility in propylene carbonate was small compared to the total alkoxide concentration.

At very dilute alkoxide concentrations (e.g., 0.2 vol% $\text{Ti}(\text{O}-n\text{-Bu})_4$), the powders that formed at a reaction temperature of 100°C provided an interesting contrast to powders that formed at room temperature. As the dilute emulsion was heated to 100°C , the turbid emulsion cleared, indicating that the alkoxide had become completely miscible with the propylene carbonate. Powders were formed from solution ($T = 100^\circ\text{C}$) and from an emulsion ($T = 25^\circ\text{C}$) at the same alkoxide concentration to compare the morphology of powders prepared from solution with that of powders prepared from droplet hydrolysis. Figure 17 shows that powders formed at 100°C from $\text{Ti}(\text{O}-n\text{-Bu})_4$ in solution had morphologies very different from those of powders formed at room temperature, a condition under which the alkoxide was immiscible and alkoxide droplets were hydrolyzed. This same effect can be seen in a comparison of the particle-size distributions of powders formed at 25°C with the distributions of powders formed at 100°C (Fig. 18). Powders formed at 100°C have a much smaller average particle size than powders formed from the reaction of alkoxide droplets at 25°C . Again, it was concluded that when the alkoxide is emulsified as droplets, the droplets act as microreactors and determine the shape and size of the particles.

Droplet-size and particle-size distributions

Part of the hypothesis is that the droplet acts as a microreactor and determines the particle size. To strengthen this hypothesis, the average droplet size and droplet-size distribution and the corresponding particle size and size distributions were measured for a series of emulsions. If each droplet reacts to form a particle, it should be possible to predict the particle-size distribution from the droplet-size distribution. If the particle-size distribution calculated from the droplet-size distribution agrees with the measured particle-size distribution, the hypothesis that each droplet reacts to form a particle would be strengthened. Droplet- and particle-size distributions were measured by centrifugal particle-size analysis. Because this technique requires very dilute samples (~0.1-0.2 vol%), droplet-size distributions were measured using $\text{Ti}(\text{O}-2\text{-EtHex})_4$ -in-propylene carbonate emulsions. It was previously shown that even at this dilution, most of the $\text{Ti}(\text{O}-2\text{-EtHex})_4$ remains in the droplet.

Droplet-size measurements were very sensitive to moisture, because at these low alkoxide concentrations, very little water is needed to hydrolyze the alkoxide (e.g., if the alkoxide concentration were 0.1%, the water concentration necessary to completely hydrolyze the alkoxide would be 0.006%.) To obtain reproducible results, it was necessary to flame-dry all glassware immediately before taking it into the glove box, perform all sample preparation in the glove box, and carefully distill the solvent before use.

It was calculated that droplet diameters would decrease by 40% when reacted to form powder particles (based on a $\text{Ti}(\text{O}-2\text{-EtHex})_4$ density of 0.93 g/cm³ and a measured uncalcined TiO_2 density of 2.2 g/cm³). The average particle diameter calculated from the average droplet diameter was then

compared to the corresponding measured average particle diameter. Measurement of a series of six samples showed that the ratio of the predicted average particle diameter to the actual average particle diameter was 0.91 ± 0.1 . Ideally, of course, a ratio of 1.0 would be expected, but 0.91 was within the accuracy of the size measurement.

The particle-size distribution shape and range calculated from the droplet-size distribution was also compared with the corresponding actual particle-size distribution. The distributions tended to show a comparable range of diameters and had roughly the same shape. Figure 19 shows a typical comparison between the predicted particle-size distribution and the actual particle-size distribution. In this case, for example, the predicted average particle diameter was $0.95 \pm 0.05 \mu\text{m}$; the average measured particle diameter was $0.91 \pm 0.05 \mu\text{m}$.

In some cases, the particle diameters and distributions predicted from droplet distributions were slightly skewed toward smaller sizes. This could be an effect of the droplets' dissolving (in the diluted sample) while the droplet diameters were being measured, or of miscible $\text{Ti}(\text{O}-2\text{-EtHex})_4$'s reacting with trace amounts of water. However, overall, the predicted particle-size distributions (based on droplet size) were found to be in good agreement with the actual particle-size distributions, giving further support to the hypothesis that individual droplets react to form powder particles.

Proposed droplet hydrolysis mechanism

Particles were assumed to form by hydrolysis at the droplet/continuous phase interface. As previously discussed, intermediate hydrolysis products tend to be viscous polymers. The partially hydrolyzed alkoxide could continue to diffuse within the droplet and condense with other alkoxide

molecules before the droplet solidifies. The alcohol products are soluble in the continuous phase and could be dissolved out of the droplet/particle into the continuous phase.

Several rate-limiting steps can be assumed for the transformation of alkoxide droplets to solid particles, including diffusion of water to the alkoxide/propylene carbonate interface, the chemical reaction at the interface, and diffusion of water through a solid shell around the partially reacted particle. Because a large excess of water was used, the rate-limiting steps were assumed to be either the chemical reaction time or diffusion of water through the solid shell.

The assumption that a solid shell forms around the reacting droplet assumes that the conversion of the alkoxide to a solid occurs faster than diffusion of partially hydrolyzed alkoxide within the droplet/particle, so that a solid shell develops around an unreacted alkoxide core. Assuming a diffusivity of $1 \times 10^{-5} \text{ cm}^2/\text{s}$ and a reaction time of 1 ms, the diffusivity distance is calculated to be about 1 μm . However, as the alkoxide reacts, it becomes much more viscous (Bradley, Mehrotra, and Gaur, 1978), and the size of the diffusing species increases so that the diffusivity rate could rapidly decrease by several orders of magnitude. One micrometer would be an upper limit to the possible diffusion distance. It appears likely, based on this approximate calculation, that reaction shells could form, particularly in larger droplets.

The chemical reaction time and the diffusion time of water through a porous shell were then compared for different droplet diameters. Although reaction rates have not been measured for fast-reacting alkoxides, Matijevic (1984) estimates that aerosol alkoxide droplets hydrolyze to form particles in milliseconds. Three reaction times were assumed for a 1- μm

droplet: 0.5, 1.0, and 5.0 ms. These were used to calculate a reaction rate constant, k_s , using the following relation for reaction time at the surface of a shrinking spherical particle:

$$\tau = \rho_{\text{drop}}(R - r_p)/(2k_s C_w) \quad (1)$$

where ρ_{drop} is the molar density of the droplet, C_w is the water molar concentration, R is the initial alkoxide-droplet size, and r_p is the final particle size. Using these rate constants, reaction times as a function of droplet diameter were then calculated.

The time required for a water molecule to diffuse through an oxyhydroxide layer was calculated from the relation:

$$\tau = \rho_{\text{drop}} R^2 [1 - 3(r_p/R)^2 + 2(r_p/R)^3] / (12DC_w) \quad (2)$$

The diffusivity, D , was assumed to be that of water in propylene carbonate through a porous layer, and was calculated from the relation (Smith, 1981):

$$D = \epsilon_\mu^2 [kT/6\pi\eta\alpha] \quad (3)$$

where ϵ_μ is the void fraction, which was assumed to be 0.4, based on measured densities of the powders.

Figure 20 shows the ratio of the diffusion time to the chemical reaction time as a function of droplet radius for the three reaction times. For the fastest assumed reaction time (0.5 ms), the conversion rate is controlled by the chemical reaction rate for radii less than 3.8 μm , and by diffusion for larger radii. (It should be noted, however, that when the diffusion and reaction times differ within an order of magnitude of each other, neither step is considered to be rate-controlling, and the reaction

control is assumed to be mixed.) When slower reaction rates were assumed, the radius at which diffusion became rate-limiting increased.

Physically, particle shells or dimpled particles might be expected when diffusion is rate-limiting because the alkoxide centers do not react. Although no particle shells were observed, dimpled particles were found in powders formed from $\text{Ti}(\text{O-}n\text{-Bu})_4$, especially for larger particles, as shown in Figure 21, indicating that for these particles, the reaction rate might be diffusion-controlled.

Powder Characteristics

Powder morphology

It was found that spherical particles with diameters ranging from 0.2 μm to several micrometers could be formed by hydrolyzing emulsions of $\text{Ti}(\text{O-}n\text{-Bu})_4$, $\text{Ti}(\text{O-2-EtHex})_4$, $\text{Al}(\text{O-}sec\text{-Bu})_3$, $\text{Zr}(\text{O-}n\text{-Pr})_4$, or mixtures of these alkoxides in propylene carbonate. Titanium hydrous oxide powders tended to have slightly higher average particle sizes than did aluminum or zirconium hydrous oxide powders, and contained more particles with diameters greater than 1 μm . For some TiO_2 powders, it was observed that some of the particles were dimpled (e.g., Fig. 21). Dimpled particles probably form because not all the alkoxide reacts and the particle collapses into the unreacted alkoxide. Aluminum and zirconium hydrous oxide powders did not contain dimpled particles. TEM observation of aluminum hydrous oxide particles showed that each particle appeared to consist of many smaller particles. No particle substructure was observed for TiO_2 or ZrO_2 particles (Fig. 22).

Weight loss

Weight loss as a function of temperature (TGA) was measured for the

single-oxide powders. Weight loss was attributed to many factors, including residual solvent or surfactant (when used), unreacted alkoxide groups, condensation of hydroxyl groups in the hydrous oxides, and physisorbed and chemisorbed water.

Weight losses for zirconium and titanium hydrous oxide powders were typically ~28-30 wt%, while weight losses for aluminum hydrous oxide powders were around 45 wt%. TGA traces for each powder were quite distinctive; representative traces are shown in Figures 23, 24, and 25.

It was hypothesized that, although the powders were washed extensively in a volatile, easily removed solvent, remaining propylene carbonate would coat the powder or be incorporated into the particles. Just as the alkoxide has a limited solubility in propylene carbonate, propylene carbonate also has a limited solubility in the alkoxide droplets and could be trapped in the particles. Propylene carbonate in its pure state volatilizes completely by 160°C. TGA traces of unwashed TiO_2 powders (containing large amounts of residual propylene carbonate) showed that weight loss below 200°C was dramatically greater than that of washed TiO_2 powders, which seemed to indicate that the majority of the propylene carbonate coating particles burned off below 200°C. However, the weight loss above 200°C was still slightly higher than that for washed powders, possibly indicating that the propylene carbonate burnoff was incomplete, leading to carbon char, which burned off at higher temperatures.

The amount of oxide in the product depends, among other things, on the specific alkoxide, the water-to-alkoxide ratio, and -- for aluminum alkoxides -- the hydrolysis temperature and aging conditions (Yoldas, 1982b). A water-to-alkoxide ratio of ~20 was used in the present study, but that did not necessarily compare directly with Yoldas's (1982b) results, because

the number of water molecules each alkoxide molecule in an alkoxide droplet "sees" probably differs from that in a dilute alkoxide-alcohol solution. Because the hydrolysis product composition for zirconium alkoxides was independent of water concentration, zirconium hydrous oxide provided a good baseline for determining the percentage of weight loss due to burnout of propylene carbonate, adsorbed water, and residual alkoxide groups.

The zirconium hydrolysis product obtained in the present study was assumed to contain 80 wt% ZrO_2 (Yoldas, 1982b and 1986a). Because weight losses were typically around 30 wt%, it was estimated that the additional 10% weight loss was due to burnout of solvent, water, and alkoxide groups. Carbon analysis showed that the ZrO_2 powders (before calcination) had a carbon content of 5-6 wt%. Carbon burnout would account for much of the additional weight loss for powders prepared by the emulsion method compared to the weight loss reported for powders prepared by Yoldas (1982b).

Hydrolysis of $Al(O\text{-}\underline{\text{sec}}\text{-Bu})_3$ below 80°C initially results in an amorphous aluminum monohydroxide, $AlOOH$, which can convert to the trihydroxide if aged in water (Yoldas, 1973). Based on weight loss measurements which corresponded more closely to the trihydroxide (35 wt% weight loss) than to the monohydroxide (15 wt% weight loss) and on density measurements, it was assumed that the hydrolysis product in the present study was a mixture of the monohydroxide and the trihydroxide and that it contained a greater amount of trihydroxide. Carbon analysis of the hydrolysis product (aluminum hydrous oxide) showed that uncalcined powders contained only 1-2 wt% carbon, so it was assumed that the greater weight loss for the aluminum hydrous oxide powders compared with the titanium and zirconium oxyhydroxide powders was due to water weight loss as the hydroxides condensed to the oxide.

Weight losses for the titanium oxyhydroxide powders in the current study were roughly 30 wt%. According to Yoldas (1986b), if hydrolysis occurs in solution, the oxide content should be approximately 90 wt%, for a water-to-Ti(OBu)₄ ratio of 20. Barringer (1983) and Jean and Ring (1986) found that for TiO₂ powders precipitated from ethanolic Ti(OEt)₄ solutions (water-to-Ti(OEt)₄ molar ratio = 4.6), weight loss was approximately 20 wt%. Barringer (1983) also found that the uncalcined powders contained little carbon (0.18 wt%). Carbon analysis of powders formed by the reaction of emulsion droplets in the current study showed that the uncalcined samples contained approximately 7 wt% carbon. The additional weight loss in powders formed from emulsions was probably due to residual propylene carbonate and to residual butoxy groups, as Ishino and Minami (1953) showed that butoxy groups are more difficult to completely hydrolyze than ethoxy groups.

Crystallinity

All powders as-formed were shown to be amorphous by X-ray diffraction (detection limit, ~1%), but upon calcination to 600°C, X-ray diffraction measurements showed that all powders had crystallized to some degree. Particles retained a spherical shape through the calcination process, and, for loose powders held for short times (2 h) at 1000°C, little neck growth was observed by SEM, although the powders had a coarser texture.

Titanium hydrous oxide powders as-formed were amorphous. After calcining at 600°C (2 h), the powders transformed to anatase; after heating to 1000°C (2 h), the powders transformed completely to rutile. X-ray diffraction patterns are shown in Figure 26. This is consistent with the findings of Yoldas (1986b) and Visca and Matijevic (1979), who have synthesized powders and gels from titanium alkoxides and shown that,

initially, the powders are amorphous, but on calcining they crystallize first to anatase and then to rutile.

Aluminum hydrous oxide powders calcined at 250°C transformed to crystalline boehmite, AlOOH . After the powders had been calcined at 600°C, their X-ray spectra showed very broad peaks that appeared to correspond to either $\gamma\text{-Al}_2\text{O}_3$ or $\theta\text{-Al}_2\text{O}_3$. The peak assignments for the two phases are very similar and because of the peak broadening, it was difficult to distinguish between the two phases. Dynys, Ljungberg, and Halloran (1984) and Morgan et al. (1986) have identified the crystal phase (in powders and gels prepared from $\text{Al}(\text{O-sec-Bu})_3$ hydrolysis) as $\gamma\text{-Al}_2\text{O}_3$. After heating to 1000°C, the crystal phase was identified as $\theta\text{-Al}_2\text{O}_3$. Because the region between 600°C and 1000°C was not investigated, it is not known if the powder transformed directly from the γ to the θ phase or if it passed through an intermediate δ phase. The δ phase, however, has not been reported to form from poorly crystallized boehmite (Dynys, Ljungberg, and Halloran, 1984) and so it was not expected to form in this case. After the powder was heated to 1300°C, the diffraction peaks were sharp and corresponded to $\alpha\text{-Al}_2\text{O}_3$. X-ray diffraction patterns for the Al_2O_3 are shown in Figure 27.

The X-ray peaks for the γ and θ phases were very broad. From Scherrer X-ray line broadening (Cullity, 1956), the average crystallite size for the γ phase was calculated to be 85 ± 10 Å; for the θ phase, the average crystallite size was calculated to be 110 ± 10 Å. These crystallite sizes are comparable to the primary particle size calculated from the BET surface areas: from the surface area, an average primary particle size of 65 ± 8 Å was calculated for powders calcined at 600°C; the calculated value was 120 ± 10 Å after powders had been calcined at 1000°C.

Zirconia powders were amorphous both as prepared and after they had been heated to 250°C. When calcined at 600°C, the powders crystallized to form predominately the metastable tetragonal phase with some monoclinic phase. After being heated to 1000°C, the samples were primarily monoclinic, with some metastable tetragonal phase. X-ray diffraction patterns for ZrO_2 are shown in Figure 28. The monoclinic phase is the stable phase below 1150°C (Subbarao, 1981), but a metastable tetragonal phase is known to occur in certain synthesis procedures, including alkoxide hydrolysis and decomposition. Mazdiasni, Lynch, and Smith (1966) and Yoldas (1986a) also reported the formation of a low-temperature amorphous/metastable cubic phase in the uncalcined powders. With X-ray diffraction, no evidence of formation of this cubic phase was observed.

It was found that all powders as prepared were amorphous. After heating to 600°C, the powders were crystalline. The crystallization sequences agreed with others reported in the literature for alkoxide-derived powders.

Density and surface area measurements

Powder densities and surface area were measured as functions of calcination temperature for the aluminum, titanium, and zirconium hydrous oxide powders. The results are shown in Figures 29 and 30. Titanium hydrous oxide powders had a density of $2.1 \pm 0.1 \text{ g/cm}^3$ as prepared and a specific surface area of $320 \pm 25 \text{ m}^2/\text{g}$. After the powders were heated to 600°C, their density increased to $3.8 \pm 0.1 \text{ g/cm}^3$ and the surface area decreased to $4\text{-}5 \text{ m}^2/\text{g}$, indicating that the particles were almost fully dense (density of anatase = 3.84 g/cm^3 , per Weast, 1983). Similarly, after the powders were heated to 1000°C, their density increased to $4.1 \pm 0.2 \text{ g/cm}^3$ (theoretical density of rutile = 4.26 g/cm^3 , per Weast, 1983) and the

surface area decreased to $1-2 \text{ m}^2/\text{g}$. These values correspond to fully dense particles with little to no accessible porosity.

Density measurements for the as-prepared aluminum hydrous oxide powders showed an average density of $2.4 \pm 0.2 \text{ g/cm}^3$. This corresponded well with the reported density for Al(OH)_3 , 2.42 g/cm^3 (Weast, 1983); weight loss measurements were also consistent with Al(OH)_3 formation. The powders again densified as they were heated, but even after heating to 1000°C for 2 h (X-ray diffraction showed the powders had crystallized to the θ phase, with a theoretical density of 3.56 (Gitzen, 1970)), the powder density was only 92% of theoretical. This incomplete densification was reflected in the high surface areas: although the surface area decreased from $380 \pm 20 \text{ m}^2/\text{g}$ (as prepared), it was still $150 \text{ m}^2/\text{g}$ after the powders had been heated to 1000°C . This corresponded to a primary particle size of $110 \pm 10 \text{ \AA}$ and indicated that the particles were still porous. High surface areas even after calcining are characteristic of alumina powders prepared from gelatinous boehmite (Harris and Sing, 1958; Russell and Cochran, 1950). For example, Russell and Cochran (1950) found that after heating to 1200°C , alumina prepared from boehmite (initial surface area, $340 \text{ m}^2/\text{g}$) still had a surface area of $70 \text{ m}^2/\text{g}$.

Zirconium hydrous oxide powders followed the titanium trend. Initially amorphous, they also had a high surface area and relatively low density. As the powders were heated, the particles densified with a corresponding decrease in surface area. After calcining at 600°C , the powders had a density of 5.26 g/cm^3 with a surface area of $30 \text{ m}^2/\text{g}$, and still appeared to have some porosity. After calcining at 1000°C , the powders appeared fully dense, with a density of 5.89 g/cm^3 (density of monoclinic $\text{ZrO}_2 = 5.85$, per Weast, 1983) and a surface area of $5-6 \text{ m}^2/\text{g}$.

Composite powders

As stated earlier, one objective of reacting emulsion droplets is to prepare homogeneous mixed-oxide particles with a controlled morphology. The previous section showed that the results support the hypothesis that droplets act as "microreactors". If droplets do act as microreactors, and if we start with droplets having a mixed composition, the resulting individual particles should also have a mixed composition.

Alkoxides were mixed to form clear solutions with the alkoxides homogeneously distributed throughout the solutions. Mixtures of $\text{Al}(\text{O-sec-Bu})_3$ with $\text{Ti}(\text{O-n-Bu})_4$ and of $\text{Al}(\text{O-sec-Bu})_3$ with $\text{Zr}(\text{O-n-Pr})_4$ had much higher viscosities than had the original single alkoxides. Since aluminum alkoxides are known to form bimetallic complexes (Bradley, Mehrotra, and Gaur, 1978), it is believed that the increase in viscosity was due to the formation or partial formation of double alkoxides. In the $\text{Y}(\text{O-i-Pr})_3/\text{Zr}(\text{O-n-Pr})_4$ case, the single alkoxides were refluxed using a procedure similar to one described by Ishizawa et al. (1986), who conjectured that the reflux product contained an Y-Zr double alkoxide.

The resulting powders were inspected by TEM and SEM, which showed that the particles appeared similar to those formed from single alkoxides, as shown in Figures 31 to 33. The particles were spherical, and the Al-Ti oxide and Al-Zr oxide particles had approximately the same size range. The Y-Zr oxide powders tended to be smaller, with a significant number of spherical particles in the 0.1- μm range. TEM inspection of small Y-Zr particles showed the particles to be unevenly dense (Fig. 33).

The bulk composition of the powder was compared to that of the alkoxide mixture to ensure that the composition of the powder could be determined from the composition of the alkoxide mixture. The cation

composition of mixed oxide powders was measured (by ICP) and compared to the alkoxide mixture's composition. Results for various compositions are shown in Table 3, which shows that the powder compositions compared closely (within 2 wt%) with their corresponding alkoxide compositions. This was expected, since the powder yields from single alkoxides were high (>95%) and almost all the alkoxide converts to the solid oxyhydroxide form.

Table 3. Mixed-oxide cation compositions.

Alkoxide solution composition		Measured alkoxide solution composition*		Measured powder composition*	
<u>%Al</u>	<u>%Ti</u>	<u>%Al</u>	<u>%Ti</u>	<u>%Al</u>	<u>%Ti</u>
20.0	80.0	--	--	20.4	79.6
43.1	56.8	--	--	42.2	57.8
69.1	30.9	69.9	30.0	69.7	30.3
<u>%Al</u>	<u>%Zr</u>	<u>%Al</u>	<u>%Zr</u>	<u>%Al</u>	<u>%Zr</u>
13.9	86.1	15.4	84.5	13.7	86.3
32.7	67.7	--	--	32.2	67.7
58.9	41.1	61.1	38.8	59.5	40.5
<u>%Y</u>	<u>%Zr</u>	<u>%Y</u>	<u>%Zr</u>	<u>%Y</u>	<u>%Zr</u>
18.2	81.7	30.0	70.0	20.0	80.0

* ICP analysis, Galbraith Laboratories, Knoxville, TN

The cation distribution in the particles was also of interest. Did the powders contain, for example, some Al_2O_3 -rich and some TiO_2 -rich particles, or did each particle have a homogeneously mixed cation

composition? Cation distributions across individual particles were measured using EDS combined with STEM. Various points were measured for each particle, and differences between the particle edges and particle interiors particularly noted. Composition was also measured as a function of particle diameter.

For Al-Ti particles, very little difference in composition between the edges and interiors was observed. This result contrasts with that obtained by Ingebrethsen, Matijevic, and Partch (1983), who measured the surface properties of alkoxide-derived Al-Ti oxide powders by electron spectroscopy for chemical analysis (ESCA). They found that mixed Al-Ti powders showed a surface enrichment of titanium. For the present work, the composition of the outer shell (not the surface) was measured, but there was no indication that the surface composition differed from the interior composition. With Al-Zr powders, EDS indicated that the particle edges had a slightly lower (1-2%) aluminum concentration than had the particle interiors.

Composition of Al-Zr and Al-Ti oxide particles as a function of particle diameter showed the aluminum concentration to be lowest for small particles ($\sim <0.1 \mu\text{m}$), as shown in Figure 34; it should be noted that these particles constitute a small fraction of the total number of particles and the compositional deviations are small. At moderate diameters (0.2-0.6 μm), the aluminum concentration appeared to reach a constant value. Composition of larger particles could not be measured because of thickness absorption effects.

One explanation for the lower aluminum concentration in the Al-Ti particles is that $\text{Al}(\text{O-sec-Bu})_3$ has a higher solubility in propylene carbonate than has $\text{Ti}(\text{O-n-Bu})_4$. As droplet diameters decrease, the solubility of the droplet material increases due to the higher chemical

potential of small droplets compared with larger droplets. Table 4 shows the change in solubility for $\text{Al}(\text{O-sec-Bu})_3$ with droplet diameter for two typical water/oil interfacial tensions (the interfacial tension for alkoxide and propylene carbonate was not known).

Table 4. Change in $\text{Al}(\text{O-sec-Bu})_3$ solubility with droplet size.

$\gamma = 20 \text{ ergs/cm}^2$		$\gamma = 40 \text{ ergs/cm}^2$	
Droplet diameter (μm)	C_r/C_∞	Droplet diameter (μm)	C_r/C_∞
0.4	1.02	0.4	1.04
0.2	1.04	0.2	1.08
0.1	1.08	0.2	1.17

$\text{Zr}(\text{O-n-Pr})_4$, however, has a higher solubility in propylene carbonate than does $\text{Al}(\text{O-sec-Bu})_3$. In this case, it is possible that the aluminum dissolved out of the particles after they were formed, as evidenced by the slightly lower aluminum concentration in the particle edges than in the particle centers.

It was found that the composition of the powder could be controlled through the composition of the starting alkoxide solution. In addition, individual particles were shown to have a homogeneous, mixed-cation composition.

CONCLUSIONS

To form emulsions containing alkoxide droplets, it was necessary to find immiscible alkoxide/continuous phase pairs for which the continuous phase was also unreactive with the alkoxide. Several pairs of liquids were found that met these criteria, and from these, propylene carbonate and

acetonitrile were chosen for further study. Emulsions could be formed with these liquids and titanium, aluminum, and zirconium alkoxides. These emulsions were easily diluted in the polar, nonaqueous liquid, implying that the emulsions contained alkoxide droplets and that the polar liquid formed the continuous phase.

Surfactant concentration in propylene carbonate had little effect on emulsion stability or on the resulting particle-size distributions (surfactant concentration, 0-1 vol%) and was consequently rarely used. In acetonitrile, an increase in surfactant (0-1 vol%) decreased the particle size and concurrently led to an increase in the number of fine particles.

Powder morphology was found to be dependent on the alkoxide solubility in the continuous phase. Powders formed from alkoxides with low solubilities in the continuous phase ($\sim 1 \times 10^{-3}$ volume fraction) contained spherical particles with diameters between 0.2 and 2 μm . Powders formed from alkoxides with high solubilities in the continuous phase contained a mixture of spherical, micrometer-diameter particles and many fine, agglomerated or irregularly shaped particles. These fine particles appeared to result from the hydrolysis of alkoxide dissolved in the continuous phase. Alkoxide solubilities were uniformly lower in propylene carbonate than in acetonitrile, and correspondingly, powders prepared in propylene carbonate had fewer fine particles than had powders prepared in acetonitrile.

Evidence was found to support the hypothesis that each droplet reacts to form a particle, thus determining the particle shape, size, and composition. Average particle diameters compared well with diameters predicted from the emulsion droplet diameters, and predicted particle-size distributions based on the droplet-size distributions had approximately the

same size and range as the actual corresponding particle-size distributions. The morphology of powder formed in a miscible system (low alkoxide concentration and high temperature) was also found to differ greatly from that of powder formed in a similar system in which immiscible droplets were reacted (low alkoxide concentration and low temperature). In all cases, reaction of the droplets resulted in 0.1-micrometer- to micrometer-size spherical particles; reaction of alkoxide remaining in solution resulted in fine, irregularly shaped particles.

Particle-size distributions were relatively independent of alkoxide (droplet) concentration over an alkoxide range of ~1 to 20 vol%. At higher alkoxide concentrations, stable emulsions were difficult to prepare. At lower alkoxide concentrations, the number of particles formed from miscible alkoxide often became comparable to the number of particles formed from immiscible alkoxide.

It was also demonstrated that this technique could be used to prepare mixed oxide powders having an overall cation composition determined by the initial alkoxide cation composition. Individual particles were also shown to have a uniform, mixed composition.

Uncalcined powders were amorphous, with high surface areas and low densities. After calcination, powders became crystalline and surface area decreased, with a corresponding increase in density. Particles retained their spherical shape after heating (1000°C).

Based on these conclusions, emulsion processing with alkoxides is a powder-preparation technique that has potential for preparing a variety of oxide compositions, including complex oxide mixtures. It is a simple technique that appears to have the potential to be easily scaled up. From an economic standpoint, because propylene carbonate is a fairly inexpensive

(and recoverable) solvent, the materials' cost would be dominated by the cost of the alkoxide. Alkoxides are expensive starting materials, so powders prepared by this method would best be suited for high-value-added applications in which the benefits of good chemical homogeneity and moderate control over particle size would outweigh the increased cost of the powder.

REFERENCES

- E.A. Barringer, "The Synthesis, Interfacial Electrochemistry, Ordering and Sintering of Monodisperse Titanium Oxide Powders"; PhD Thesis. Dept. Mat. Sci. Eng., MIT, Cambridge, MA, Sept. 1983.
- A.F.M. Barton, CRC Handbook of Solubility Parameters and other Cohesions Parameters. CRC Press, Boca Raton, FL, 1983.
- H.K. Bowen, "Basic Research Needs on High Temperature Ceramics for Energy Applications," Mat. Sci. and Eng., 44, 1-56 (1980).
- D.C. Bradley, R.C. Mehrotra, and D.P. Gaur, Metal Alkoxides. Academic Press, New York, 1978.
- J. Carroll, "The Stability of Emulsions and Mechanisms of Emulsion Breakdown"; pp. 1-68 in Surface and Colloid Science, Vol. 9. Edited by E. Matijevic. John Wiley & Sons, New York, 1976.
- Coulter Model N4 Product Reference Manual, Technical Communications, Coulter Electronics, Hialeah, FL (1982).
- B.D. Cullity, Elements of X-ray Diffraction. Addison-Wesley Publishing Co. Inc., Reading, MA, 1956.
- F.W. Dynys, M. Ljungberg, and J.W. Halloran, "Microstructural Transformations in Alumina Gels"; pp. 321-26 in Materials Research Society Symposium Proceedings, Vol. 32, Better Ceramics Through Chemistry. Edited by C.J. Brinker, D.E. Clark, and D.R. Ulrich. Elsevier Science Publishing Co., New York, 1984.
- J.H. Fendler and E.H. Fendler, Catalysis in Micellar and Macromolecular Systems; p. 324. Academic Press, New York, 1975.
- W.H. Gitzen, Alumina as a Ceramic Material. The American Ceramic Society, Inc., Columbus, OH, 1970.
- M.R. Harris and K.S.W. Sing, "Surface Properties of Precipitated Alumina. III. Samples Prepared from Aluminum Isopropoxides," J. Appl. Chem., 8, 386-89 (1958).

D.C. Hiemenz, Principles of Colloid and Surface Chemistry. Marcel Dekker Inc., New York, 1977.

B.J. Ingebrethsen and E. Matijevic, "Preparation of Uniform Colloidal Dispersions by Chemical Reactions in Aerosols. II. Spherical Particles of Aluminium Hydrous Oxide," J. Coll. & Interface Sci., 11, 271-80 (1980).

B.J. Ingebrethsen, E. Matijevic, and R.I. Partch, "Preparation of Uniform Colloidal Dispersions by Chemical Reactions in Aerosols. III. Mixed Titania/Alumina Colloidal Spheres," J. Coll. & Interface Sci., 65 [1] 228-39 (1983).

T. Ishino and S. Minami, "Hydrolysis of Butyl Titanate," Tech. Rep. Osaka Univ., 3, 357-66 (1953).

H. Ishizawa, O. Sakurai, N. Mizutani, and M. Kato, "Homogeneous Y_2O_3 -Stabilized ZrO_2 Powder by Spray Pyrolysis Method," Am. Ceram. Soc. Bul., 65 [10] 1399-1404 (1986).

J.H. Jean and T.A. Ring, "Processing Monosized TiO_2 Powders Generated with HPC Dispersant," Am. Ceram. Soc. Bul., 65 [12] 1574-77 (1986).

K. Kandori, K. Kon-ho, and A. Kitahara, "Preparation of $BaCo_3$ Particles in Ionic W/O Microemulsions," J. Disp. Sci. Tech., 9 [1] 61-73 (1988).

A.S. Kertes and H. Gurtman, "Surfactants in Organic Solvents: The Physical Chemistry of Aggregation and Micellization"; pp. 193-296 in Surface and Colloid Science, Vol. 8. Edited by E. Matijevic. John Wiley and Sons, New York, 1976.

W.H. Lee, "Cyclic Carbonates"; pp. 167-245 in The Chemistry of Non-Aqueous Solvents, Vol. IV. Edited by J.J. Lagowski. Academic Press, New York, 1976.

N. Lufimpadio, J.B. Nagy, and E.G. Derouane, "Preparation of Colloidal Iron Boride Particles in the CTAB-n-Hexanol-Water Reversed Micellar System"; pp. 1483-97 in Surfactants in Solution, Vol. 3. Edited by K.L. Mittal and B. Lindman. Plenum Press, New York, 1984.

L. Magid, "Solvent Effects on Amphiphilic Aggregation"; pp. 439-41 in Solution Chemistry of Surfactants. Edited by K.L. Mittal. Plenum Press, New York, 1979.

E. Matijevic, "Monodisperse Colloidal Metal Oxides, Sulfides, and Phosphates: New Materials for Research and Applications"; pp. 334-52 in Ultrastructure Processing of Ceramics, Glasses and Composites. Edited by L.L. Hench and D.R. Ulrich. John Wiley & Sons, New York, 1984.

K.S. Mazdiasni, C.T. Lynch, and J.S. Smith, "Metastable Transitions of Zirconium Oxides Obtained from Decomposition of Alkoxides," J. Am. Ceram. Soc., 49 [5] 286-87 (1966).

P.E.D. Morgan, H.A. Bump, E.A. Pugar, and J.J. Ratto, "Oxy-alkoxy Polymer Network"; pp. 327-34 in Science of Ceramic Chemical Processing. Edited by L.L. Hench and D.R. Ulrich. John Wiley & Sons, New York, 1986.

J. Periard, G. Reiss, and M.J. Neyer-Gamez, "Etude de Copolymers Sequences de Faible Mass Moleculaire Utilises comme Agents Emulsifiants du Type Huile-dans-Huile-Associations en Milieu Solvent Selectif," Europ. Polym. J., 9, 687-96 (1973).

R. Pribil, Applied Complexometry. Pergamon Press, Elmsfield, NY, 1982.

A. Ray, "Solvophobic Interactions and Micelle Formation in Structure Forming Nonaqueous Solvents," Nature, 231, 313-15 (1971).

A.S. Russell and C.N. Cochran, "Surface Areas of Heated Alumina Hydrates," Ind. Eng. Chem., 42 [7] 1336-40 (1950).

H.N. Singh, S.M. Saleem, R.P. Singh, and K.S. Birdi, "Micelle Formation of Ionic Surfactants in Polar Nonaqueous Solvents," J. Phys. Chem., 84, 2191-94 (1980).

H.N. Singh, S. Singh, and K.C. Tewari, "Surface Active Anions in Polar Solvents: 1. Conductometric Studies on Solutions of Sodium Decyl and Dodecyl Sulphate in Water, N,N-Dimethylformamide and Dimethyl Sulfoxide," Am. Oil. Chem. Soc. J., 52, 436-38 (1976).

J.M. Smith, Chemical Engineering Kinetics, Third Edition. McGraw-Hill Book Co., New York, 1981.

E.C. Subbarao, "Zirconia -- an Overview"; pp. 1-13 in Advances in Ceramics. Science and Technology of Zirconia, Vol. 3. Edited by A.H. Heuer and L.W. Hobbs. The American Ceramic Society Inc., Columbus, OH (1981).

M. Visca and E. Matijevic, "Preparation of Uniform Colloidal Dispersions by Chemical Reactions in Aerosols. I. Spherical Particles of Titanium Dioxide," J. Coll. & Interface Sci., 68 [2] 308-19 (1979).

R.C. Weast, Ed., CRC Handbook of Chemistry and Physics, 64th Edition. CRC Press Inc., Boca Raton, FL, 1983.

T.S. West, Complexometry with EDTS and Related Reagents. BDH Chemicals Ltd., Poole, U.K. (1969).

B.E. Yoldas, "Hydrolysis of Aluminum Alkoxides and Bayerite Conversions," J. Appl. Chem. Biotech., 23 [11] 803-09 (1973).

B.E. Yoldas, "Preparation of Glasses and Ceramics from Metal-Organic Compounds," J. Mat. Sci., 12, 1203-08 (1977).

B.E. Yoldas, "Introduction and Effect of Structural Variations in Inorganic Polymers and Glass Networks," J. Non-Cryst. Sol., 51, 105-21 (1982a).

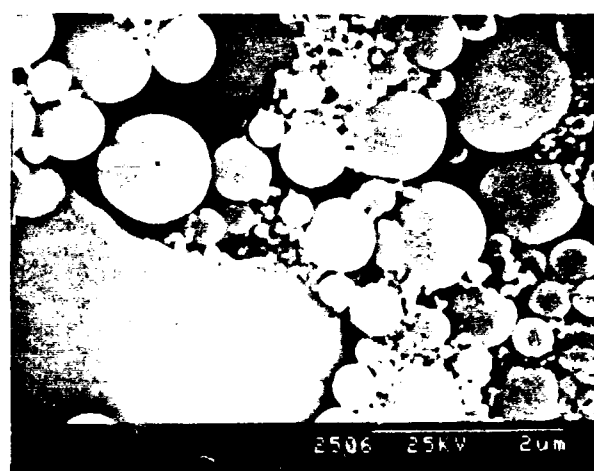
B.E. Yoldas, "Effect of Variations in Polymerized Oxides on Sintering and Crystalline Transformations," J. Am. Ceram. Soc., 65 [8] 387-93 (1982b).

B.E. Yoldas, "Zirconium Oxides Formed by Hydrolytic Condensation of Alkoxides and Parameters that Affect Their Morphology," J. Mat. Sci., 21, 1080-86 (1986a).

B.E. Yoldas, "Hydrolysis of Titanium Alkoxides and Effects of Hydrolytic Polycondensation Parameters," J. Mat. Sci., 21, 1087-92 (1986b).

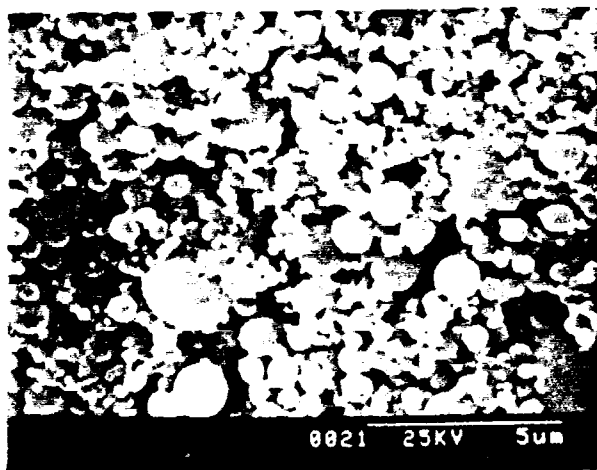


(a)

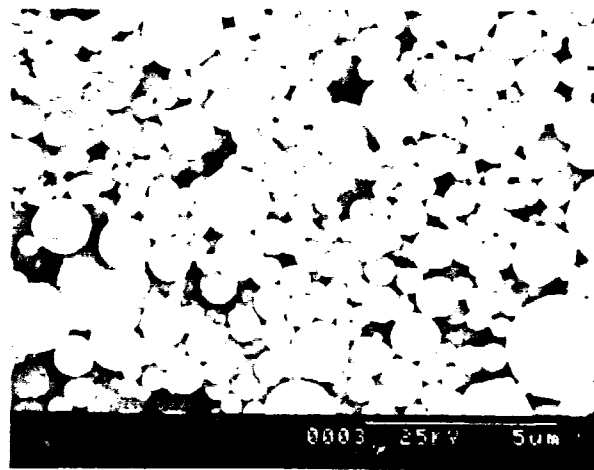


(b)

Figure 1. SEM micrographs of powders formed from (a) a $\text{Ti}(\text{O-n-Bu})_4$ -in-acetonitrile emulsion and (b) a $\text{Ti}(\text{O-n-Bu})_4$ -in-butylene carbonate emulsion.



(a)



(b)

Figure 2. SEM micrographs of powders formed from (a) a $\text{Ti}(\text{O-n-Bu})_4$ -in-propylene carbonate emulsion and (b) a $\text{Ti}(\text{O-n-Bu})_4$ -in-formamide emulsion.

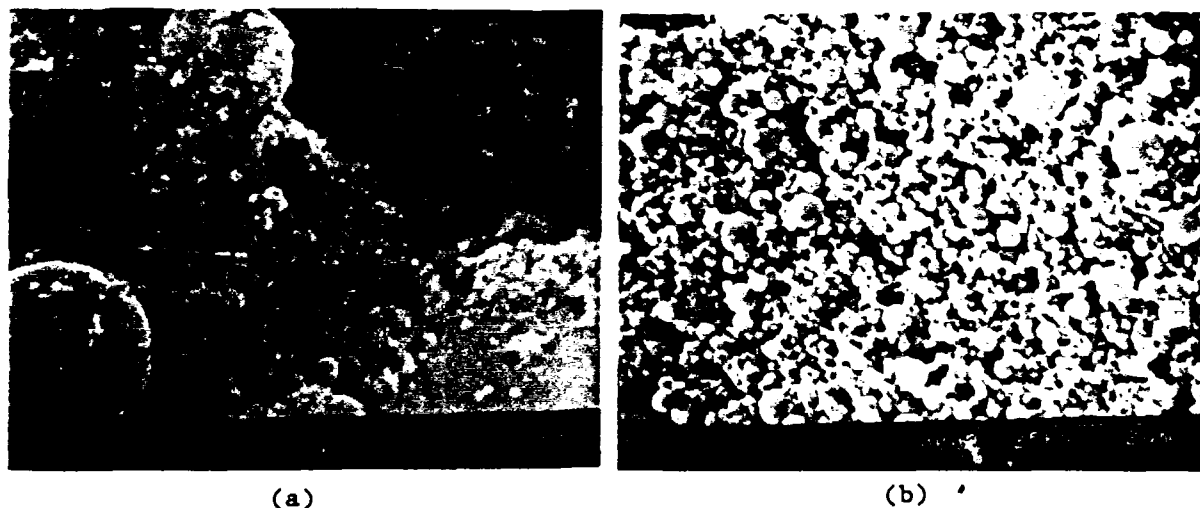


Figure 3. SEM micrographs of powders formed from (a) an Al(O-sec-Bu)₃-in-acetonitrile emulsion and (b) an Al(O-sec-Bu)₃-in-propylene carbonate emulsion.

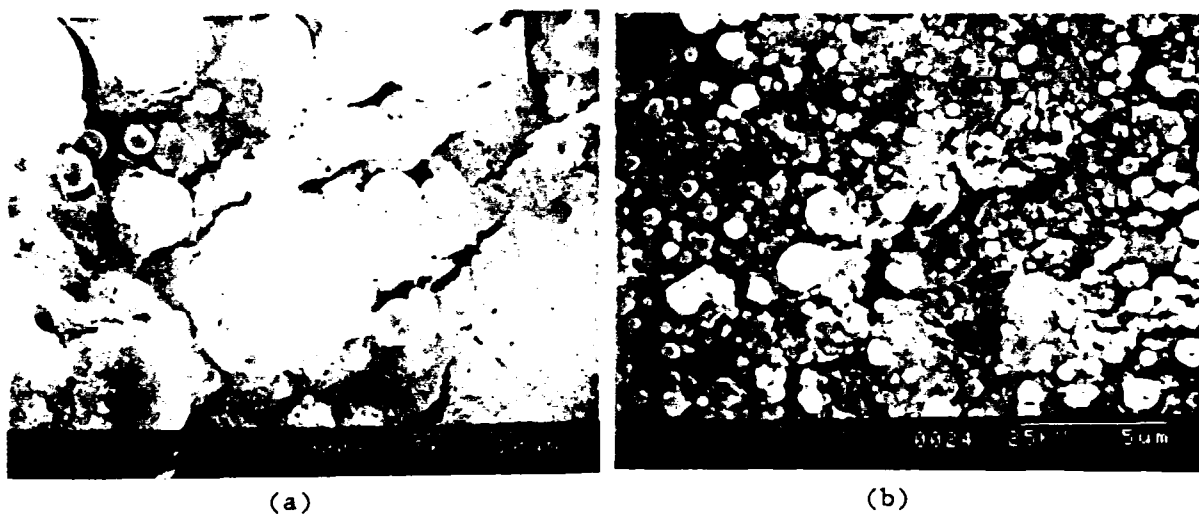
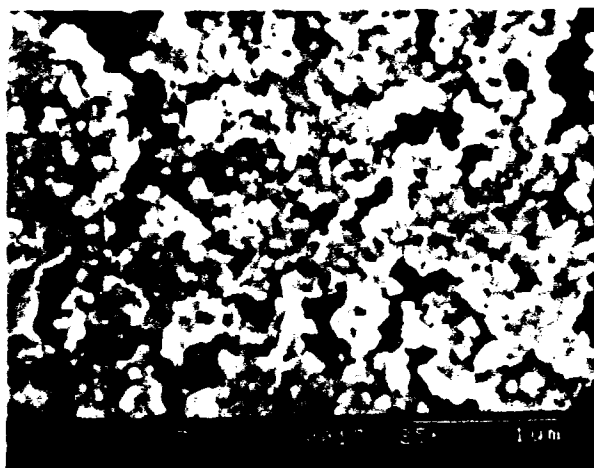


Figure 4. SEM micrographs of powders formed from (a) Ti(O-sec-Bu)₄-in-acetonitrile and (b) Ti(O-sec-Bu)₄-in-propylene carbonate.



(c)

Figure 4. SEM micrograph of powder formed from a $\text{Ti}(\text{OEt})_4$ -in-propylene carbonate emulsion.

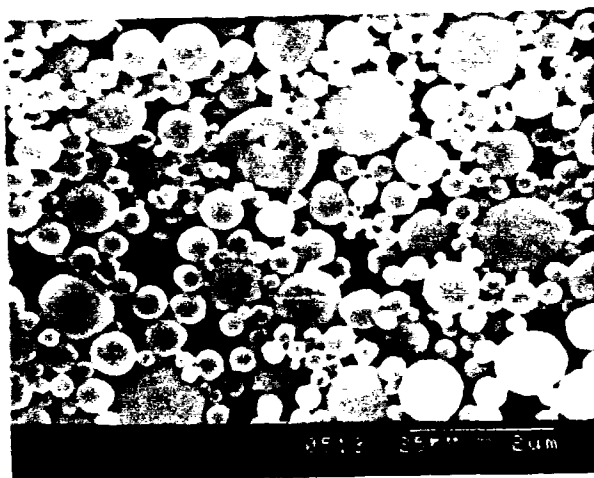


Figure 5. SEM micrograph of powder formed from an emulsion of $\text{Ti}(\text{O-n-Bu})_4$ in propylene carbonate.

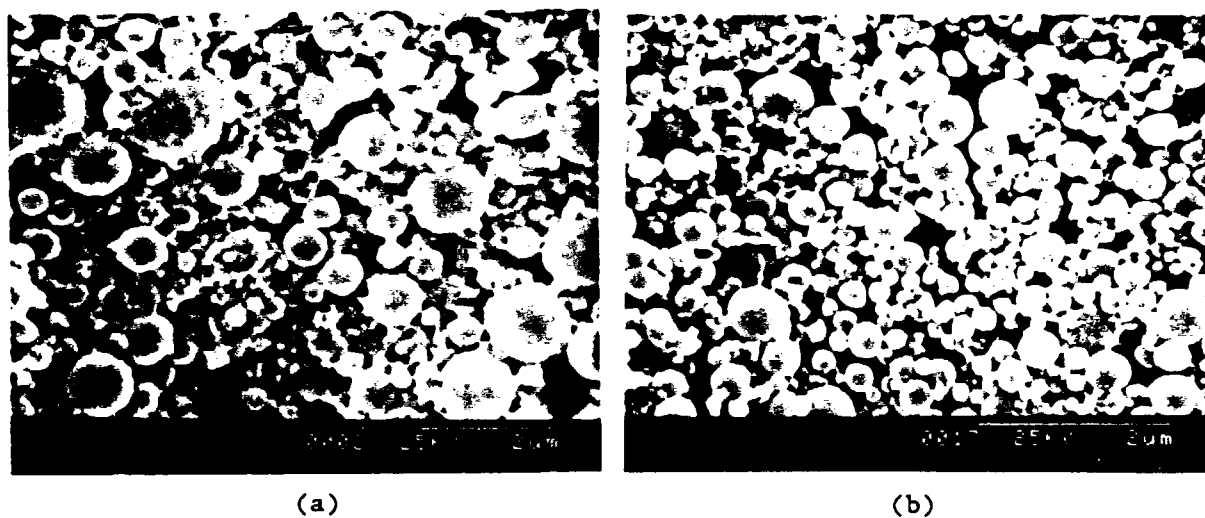


Figure 6. SEM micrographs of powders formed from (a) undiluted $\text{Al}(\text{O-sec-Bu})_3$ and (b) $\text{Al}(\text{O-sec-Bu})_3$ diluted with 20 vol% hexane in propylene carbonate.

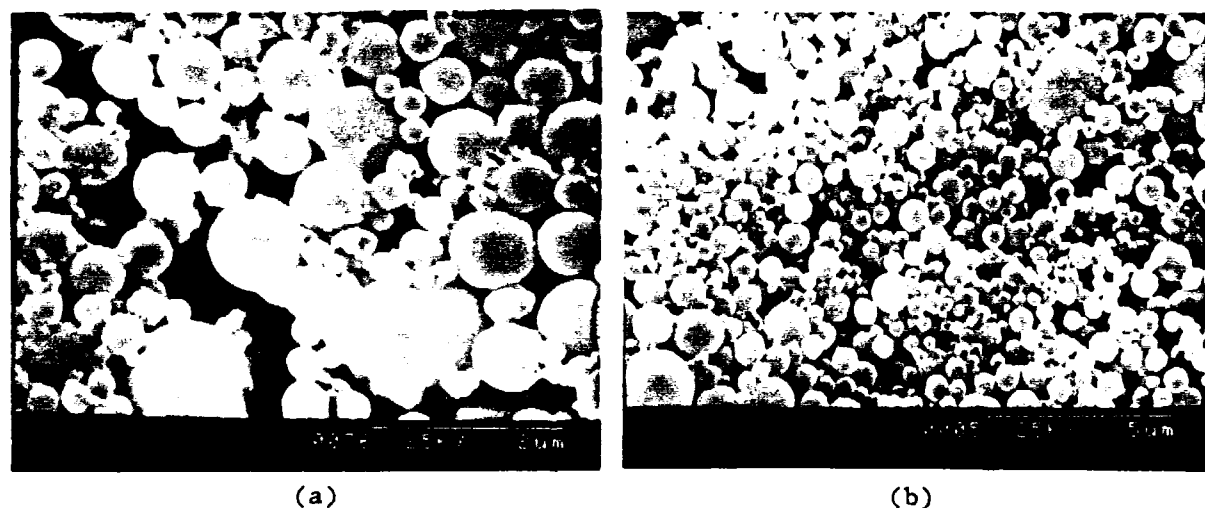
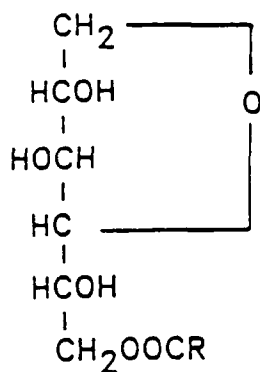
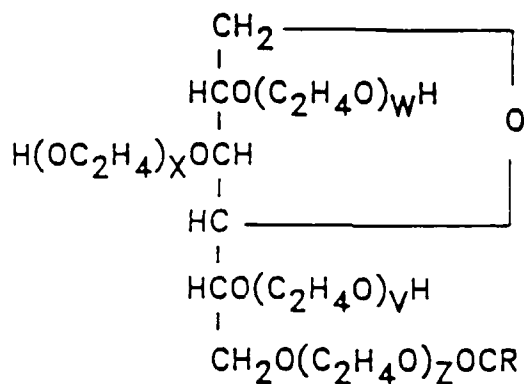


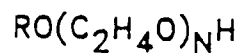
Figure 7. SEM micrographs of powders formed from (a) $\text{Zr}(\text{O-n-Pr})_4$ (with *n*-propanol) and (b) $\text{Zr}(\text{O-n-Pr})_4$ (with hexane) in propylene carbonate.



1,4 sorbitan monoester



polyoxyethylene sorbitan monoester



polyoxyethylene

fatty ether

Figure 8. Chemical structures of Span (top), Tween (middle), and Brij (bottom) surfactants.

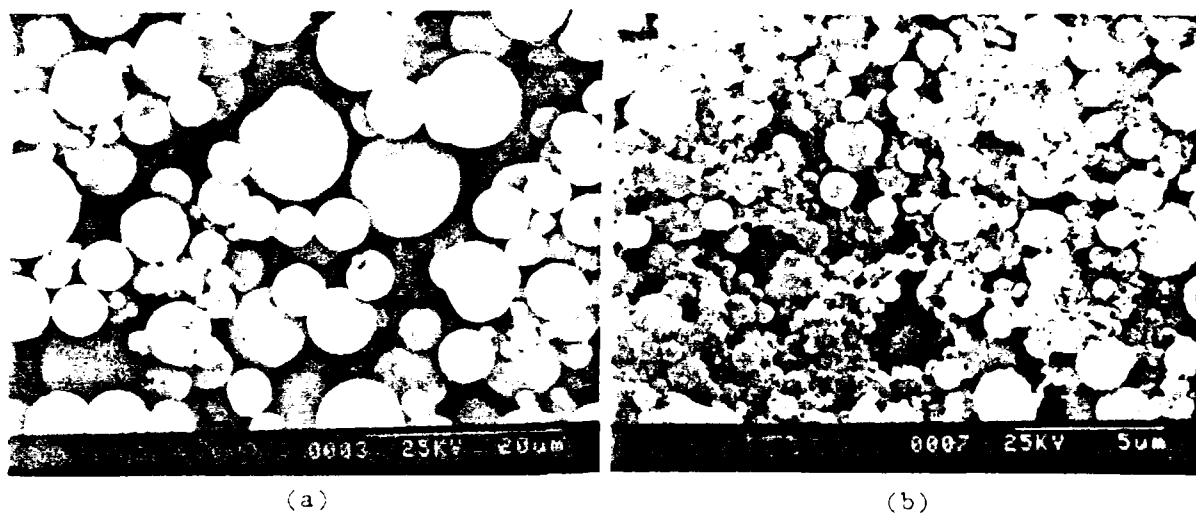


Figure 9. SEM micrographs of powders formed from a $Ti(O-n-Bu)_4$ -in- n -hexane emulsion with (a) no surfactant and (b) 1 vol.-% Brif 35.

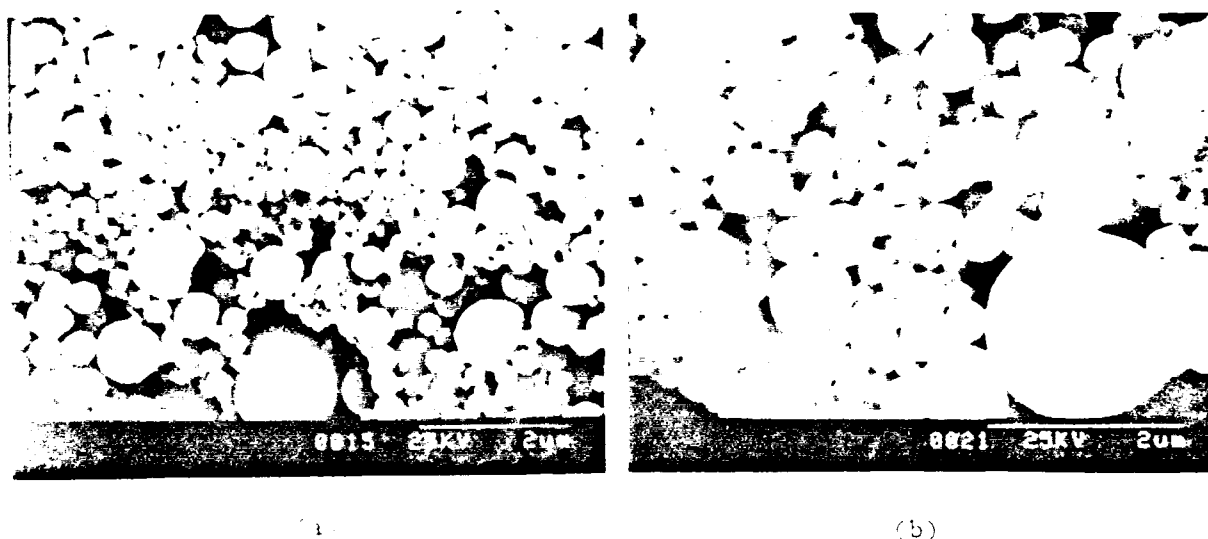


Figure 10. SEM micrographs of powders prepared from a $Ti(O-n-Bu)_4$ -in- n -hexane emulsion with (a) no surfactant and (b) 1 vol.-% Brif 35.

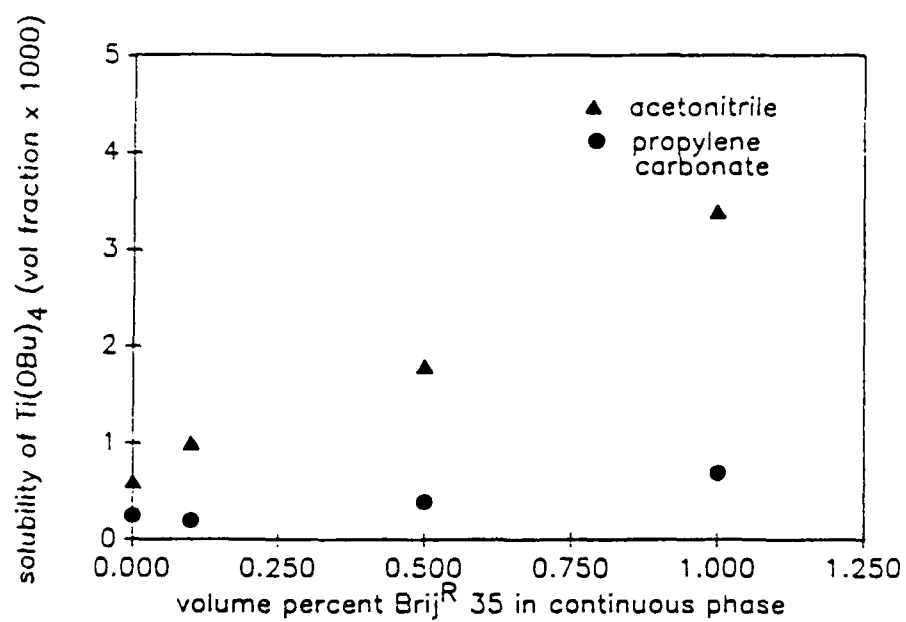


Figure 11. Solubility of $\text{Ti}(\text{O-n-Bu})_4$ in acetonitrile and propylene carbonate as a function of Brij[®]35 concentration.

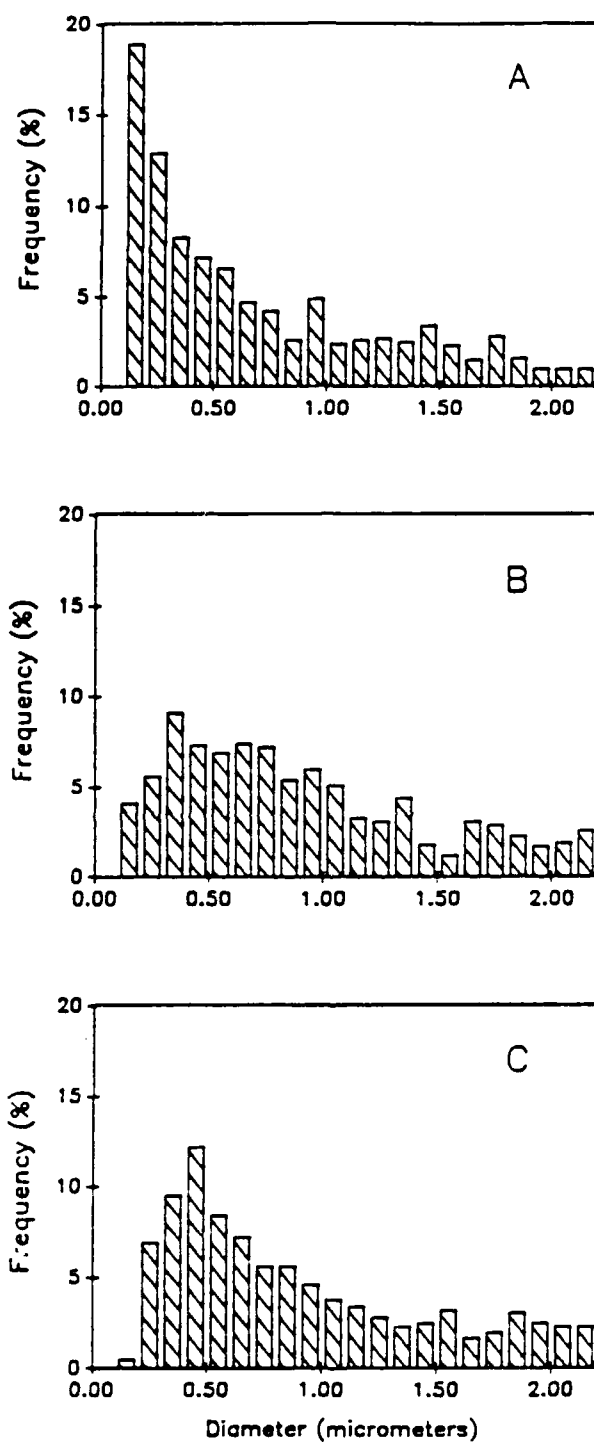


Figure 12. Particle-size distribution for powders prepared from a (a) 0.2 vol%, (b) 1.0 vol%, and (c) 10 vol% $\text{Ti}(\text{O-n-Bu})_4$ -in-propylene carbonate emulsion.

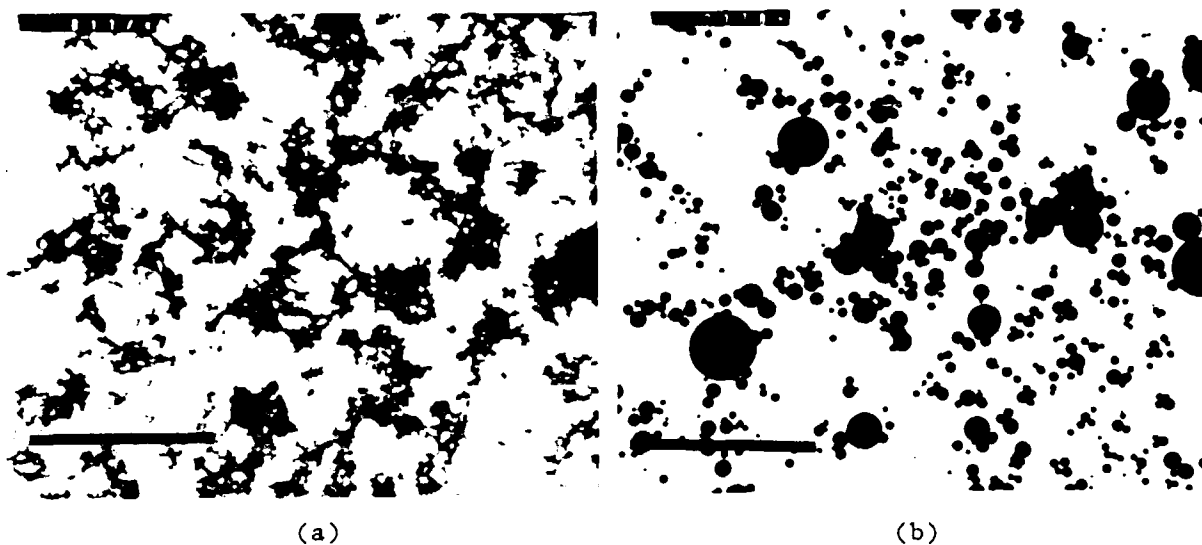


Figure 13. TEM micrographs of powders formed from (a) a 0.5 vol% and (b) a 20 vol% $\text{Ti}(\text{O-n-Bu})_4$ -in-propylene carbonate emulsion (each bar = 5.0 μm).

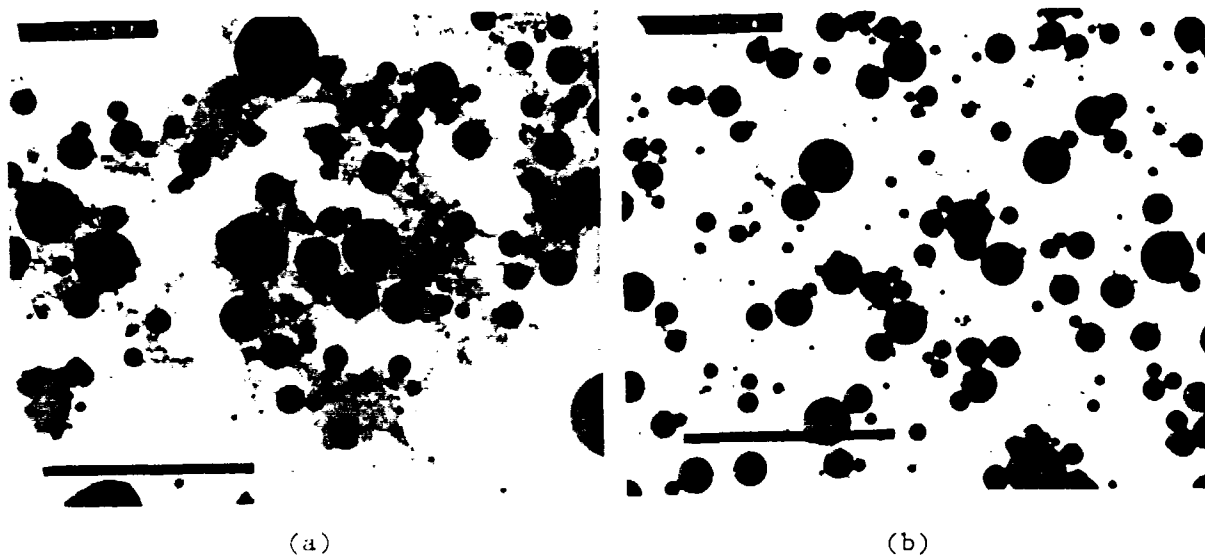


Figure 14. TEM micrographs of powders prepared from (a) a 0.5% vol% and (b) a 20 vol% $\text{Al}(\text{O-sec-Bu})_3$ (with 20 vol% hexane)-in-propylene carbonate emulsion (each bar = 5.0 μm).

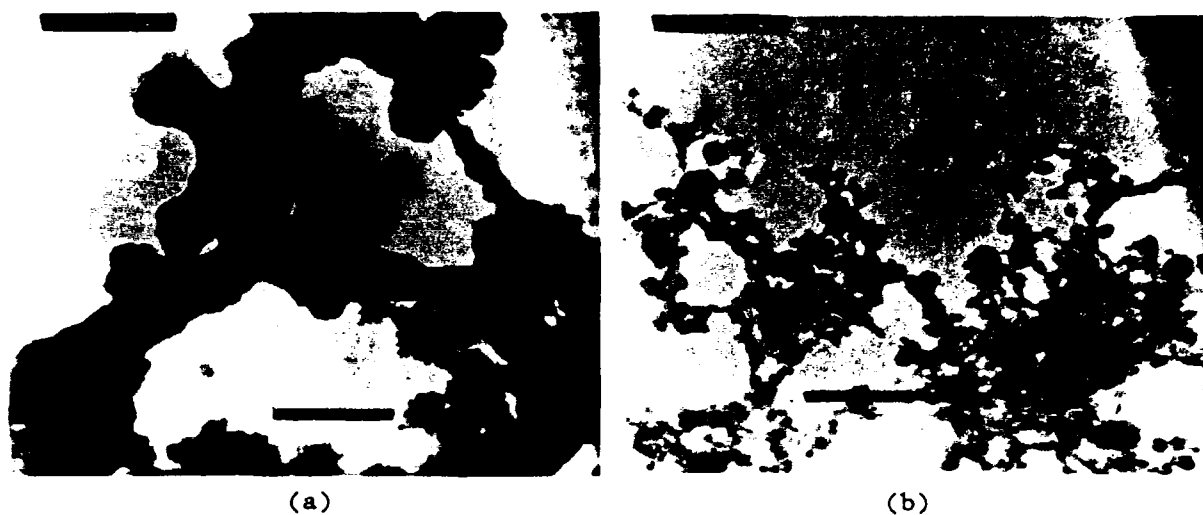


Figure 15. TEM micrographs of "fine" particles formed from the hydrolysis of (a) $\text{Ti}(\text{O-}n\text{-Bu})_4$ and (b) $\text{Al}(\text{O-}sec\text{-Bu})_3$ (each bar = 2 μm).

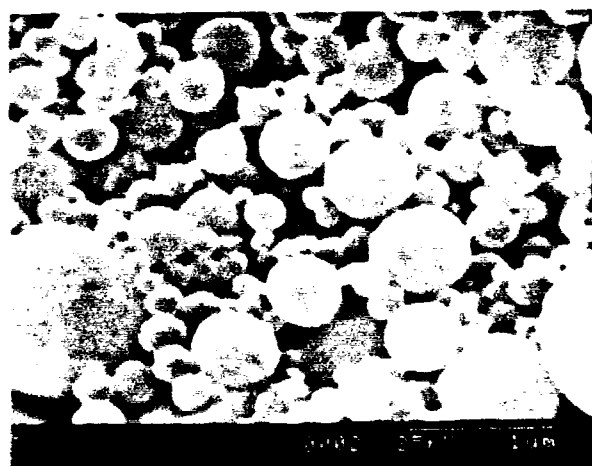


Figure 16. SEM micrograph of powder prepared from a 0.2 vol% $\text{Ti}(\text{O-}n\text{-Bu})_4$ in-propylene carbonate emulsion (water added immediately after formation).

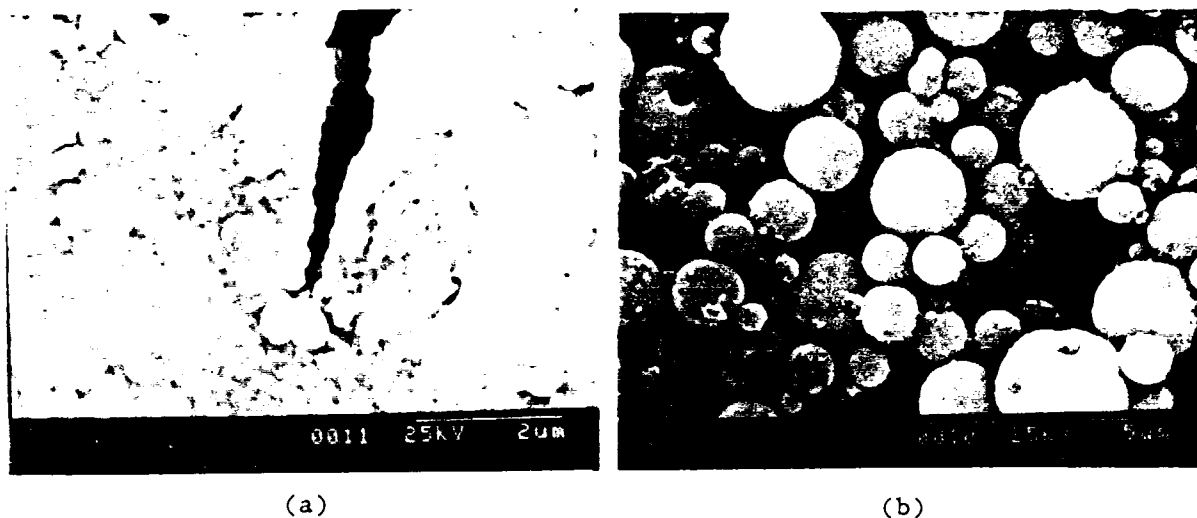


Figure 17. SEM micrographs of powders prepared from (a) an alkoxide solution ($T = 100^{\circ}\text{C}$) and (b) reaction of emulsion droplets ($T = 25^{\circ}\text{C}$).

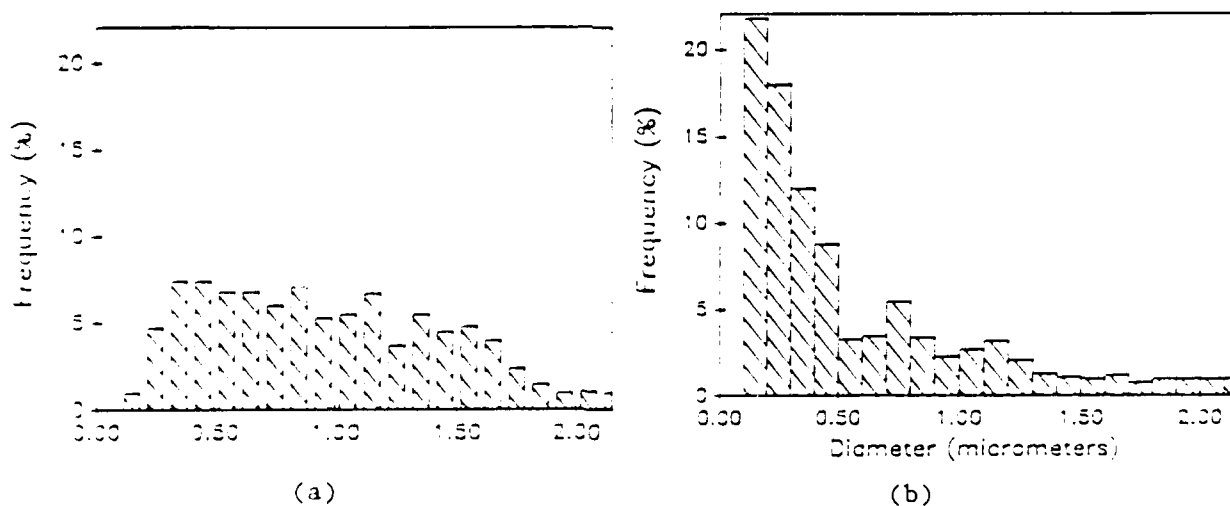


Figure 18. Particle-size distributions of powder prepared from (a) reaction of $\text{Ti}(\text{O-n-Bu})_3$ droplets ($T = 25^{\circ}\text{C}$) and (b) $\text{Ti}(\text{O-n-Bu})_3$ droplets in solution ($T = 100^{\circ}\text{C}$).

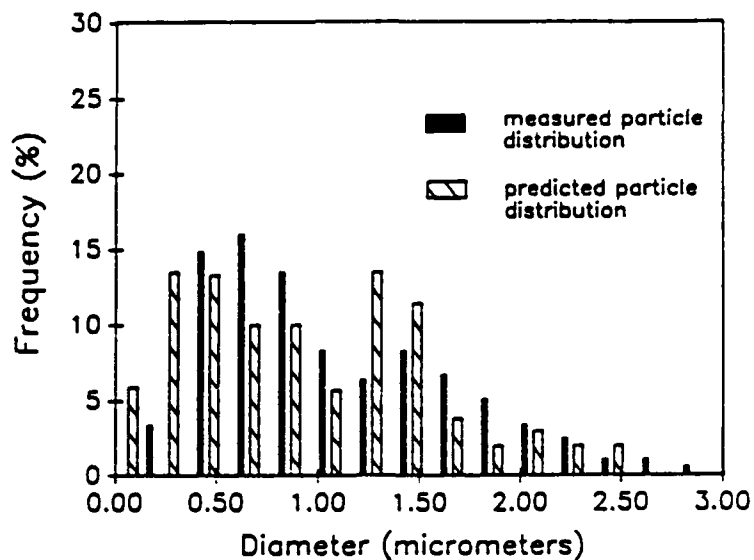


Figure 19. Comparison of the measured particle-size distribution with the corresponding particle-size distribution as calculated from the droplet-size distribution.

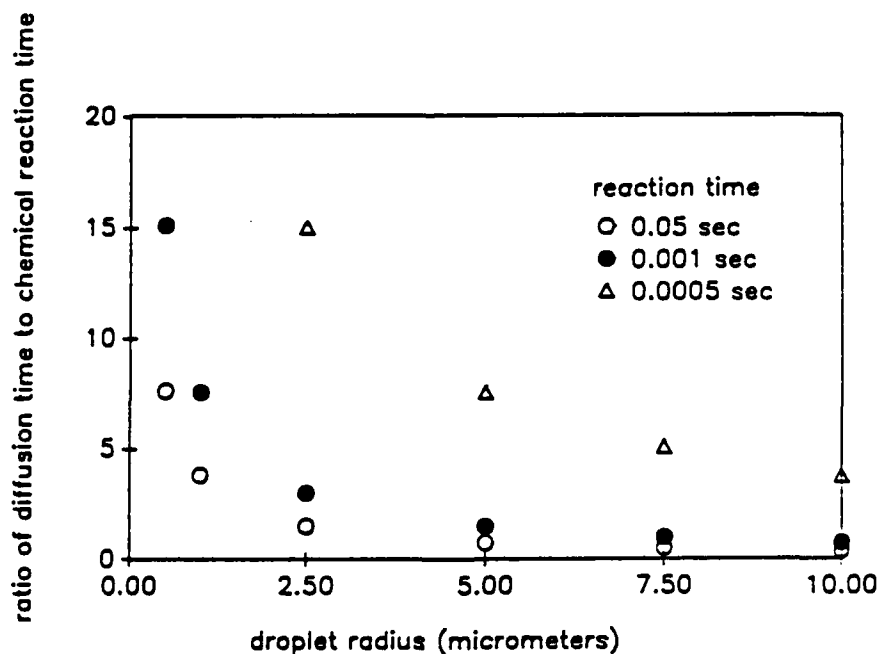


Figure 20. Comparison of reaction times for chemical reaction and diffusion-controlled droplet-to-particle conversion.

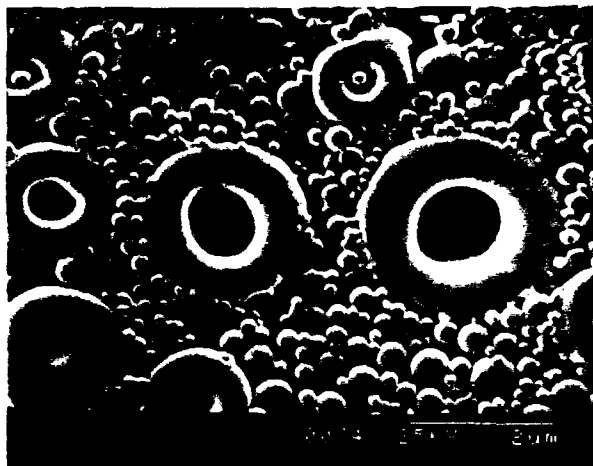


Figure 21. SEM micrograph of dimpled particles in powder formed from a $\text{Ti}(\text{O}-n\text{-Bu})_4$ -in-propylene carbonate emulsion.

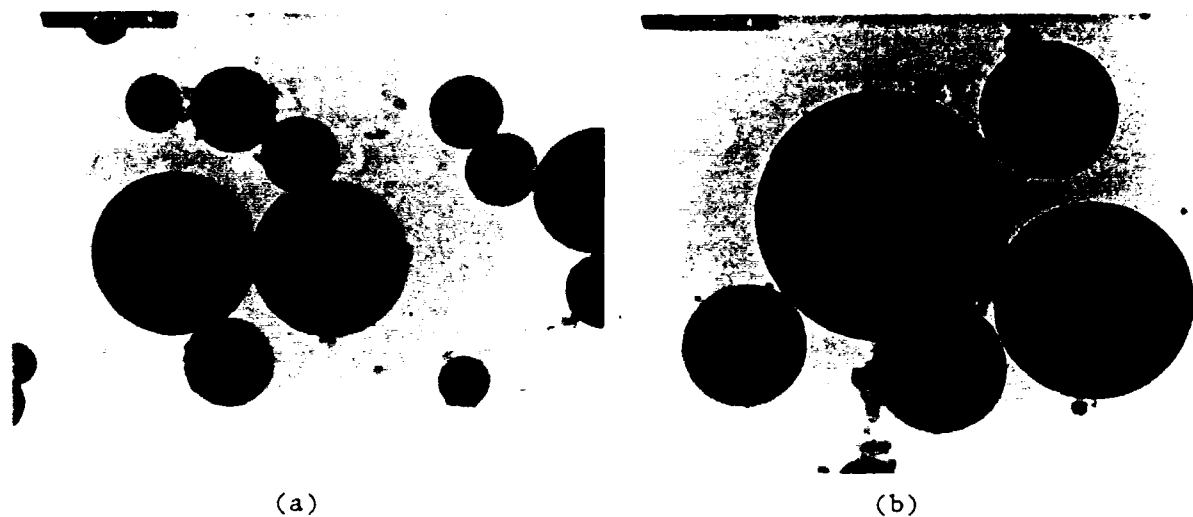


Figure 22. Comparison of particle structures of (a) titanium hydroxide powder and (b) aluminum hydroxide powder.

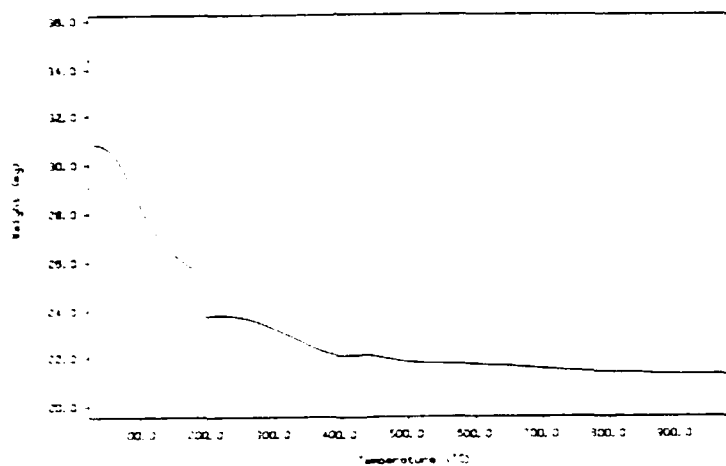


Figure 23. Thermogravimetric analysis of titanium hydroxide powder.

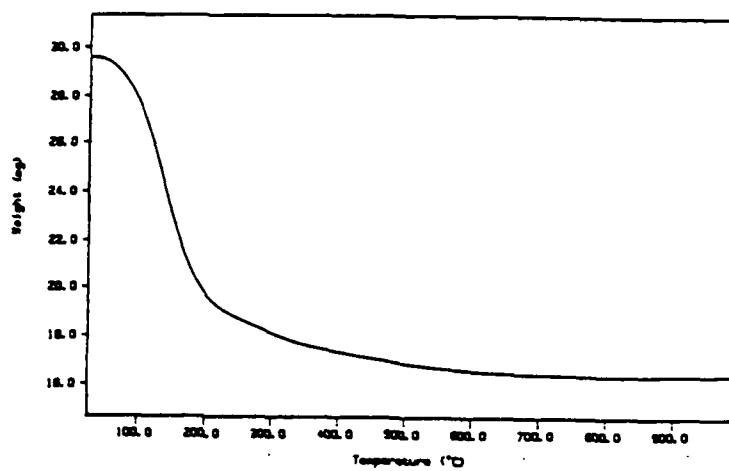


Figure 24. Thermogravimetric analysis of aluminum hydrous oxide powder.

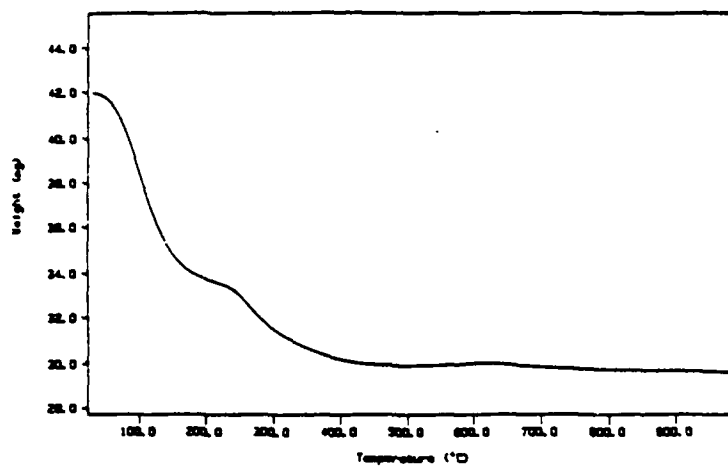


Figure 25. Thermogravimetric analysis of zirconium hydrous oxide powder.

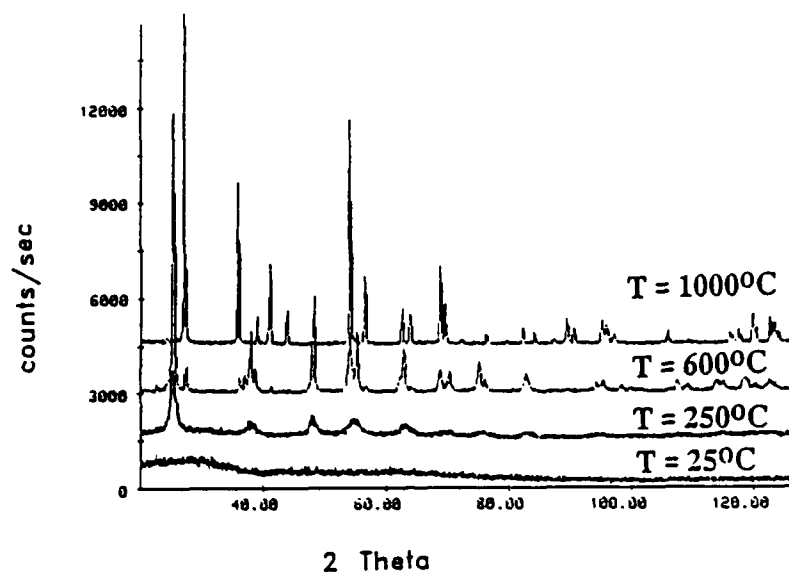


Figure 26. X-ray diffraction patterns for TiO_2 powders as a function of calcination temperature.

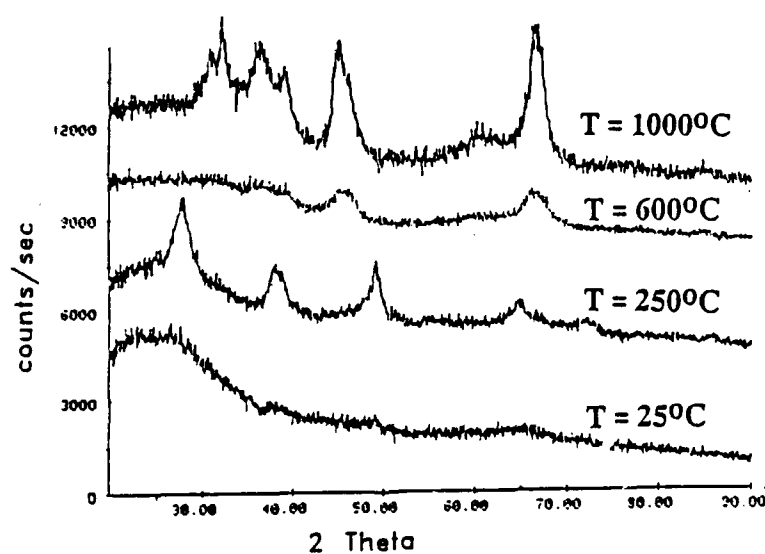


Figure 27. X-ray diffraction patterns for Al_2O_3 powder as a function of calcination temperature.

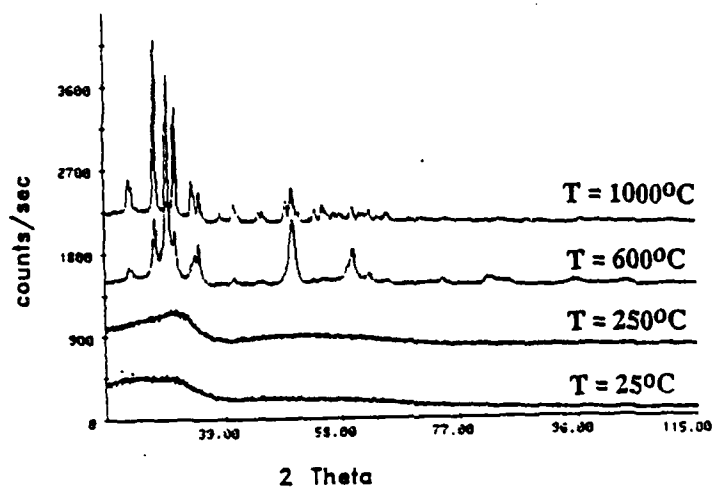


Figure 28. X-ray diffraction patterns for ZrO_2 powder as a function of calcination temperature.

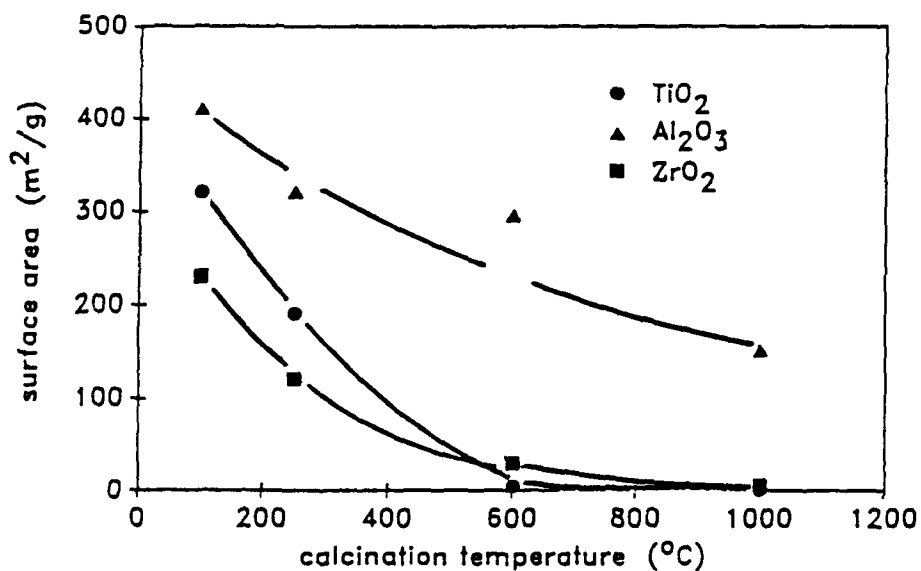


Figure 29. Surface area as a function of calcination temperature for TiO_2 , Al_2O_3 , and ZrO_2 powders.

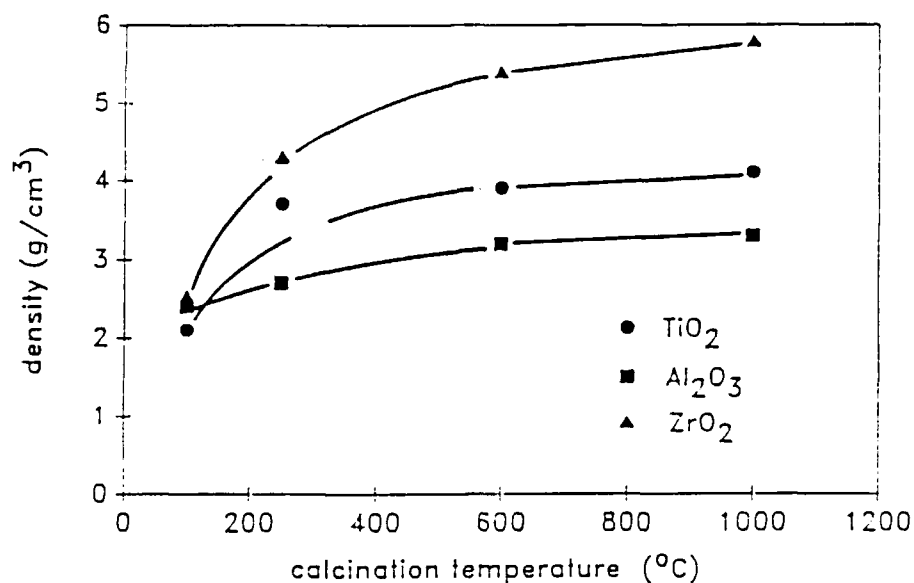
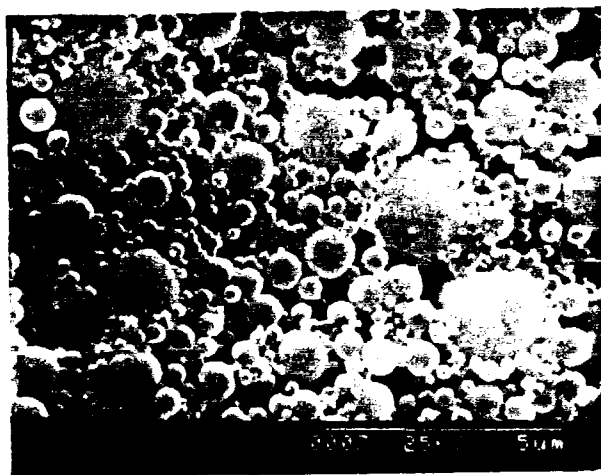
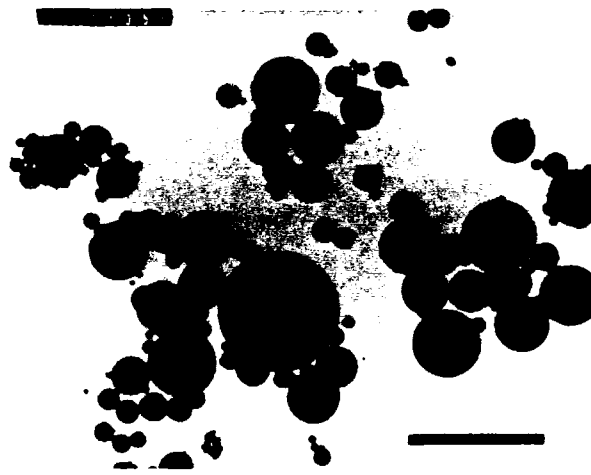


Figure 30. Density as a function of calcination temperature for TiO_2 , Al_2O_3 , and ZrO_2 powders.

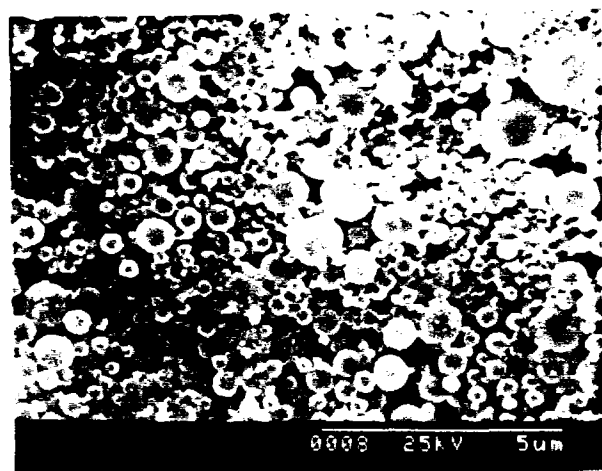


(a)

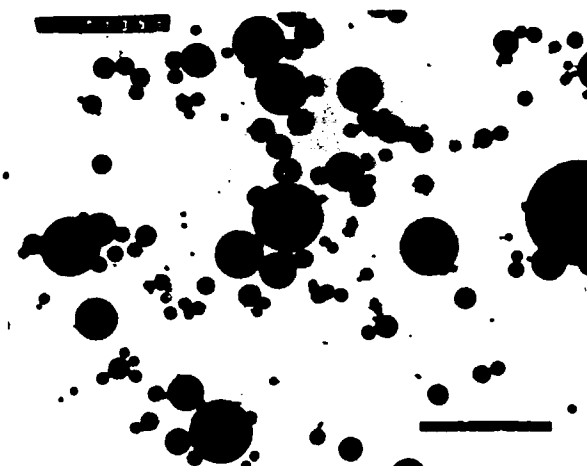


(b)

Figure 31. (a) SEM and (b) TEM micrographs of powder prepared from a 1:1 volume ratio mixture of $\text{Ti}(\text{O}-n\text{-Bu})_4$ and $\text{Al}(\text{O}-\text{sec-Bu})_3$ (bar in TEM = $2.0 \mu\text{m}$).

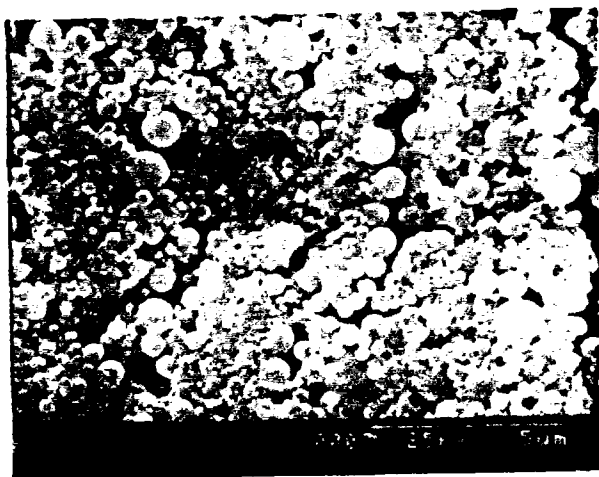


(a)

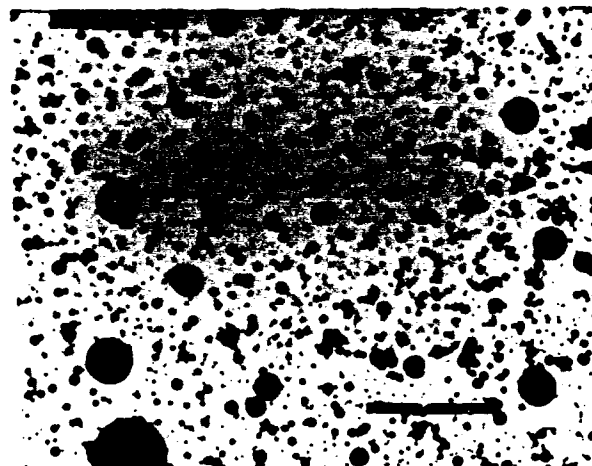


(b)

Figure 32. (a) SEM and (b) TEM micrographs of powder prepared from a 1:1 volume ratio mixture of $\text{Al}(\text{O-sec-Bu})$ and $\text{Zr}(\text{O-n-Pr})_4$ (bar in TEM = 2 μm).



(a)



(b)

Figure 33. (a) SEM and (b) TEM micrographs of powder prepared from a $\text{Y}(\text{O-i-Pr})_3$ and $\text{Zr}(\text{O-n-Pr})_4$ mixture (bar in TEM = 2 μm).

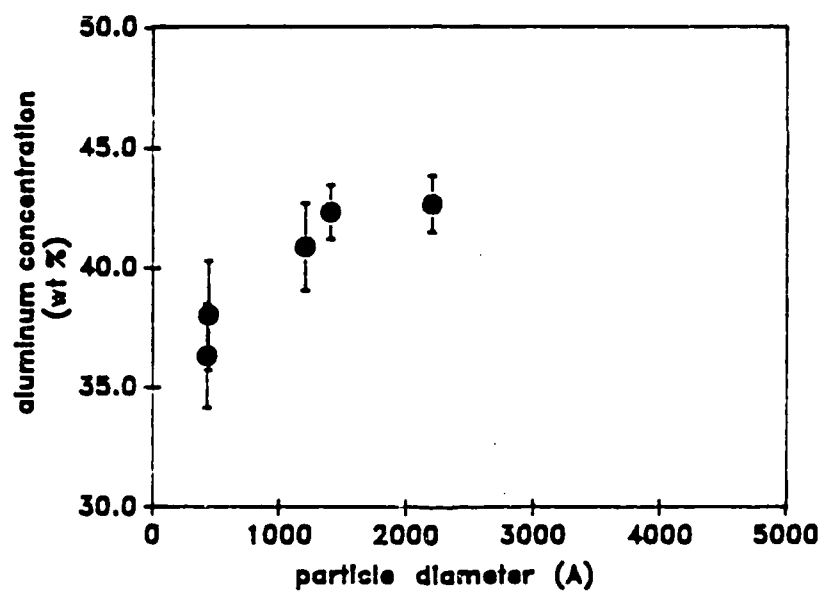
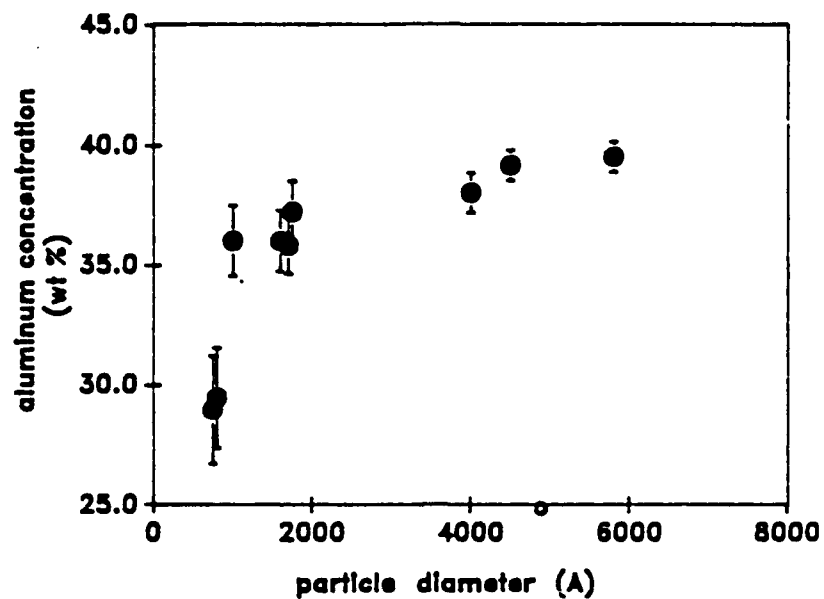


Figure 34. Aluminum content in Al-Ti and Al-Zr oxide particles as a function of particle size.

PREPARATION OF BaTiO_3 AND SrTiO_3 USING A WATER-IN-OIL EMULSION TECHNIQUE

Christophe Zing

ABSTRACT

A water-in-oil emulsion technique was investigated for preparing SrTiO_3 and BaTiO_3 . In previous research, precursors for multicomponent oxides were dissolved in the dispersed phase of the emulsion. In this effort, only the alkaline earth precursor was dissolved in the dispersed phase, and after emulsification, a titanium alkoxide was added to the continuous phase. The titanium alkoxide reacted with the emulsion droplets to form the titanates.

INTRODUCTION

It has been demonstrated that submicrometer and monosized titania powders sinter better than powders derived from classical solid-state reactions (Barringer and Bowen, 1982). This enhanced sinterability provides better control over the ceramic microstructure (e.g., density, uniformity, and grain size). Sintering can also be performed at lower temperatures, allowing metallic alloys with less precious metal to be used for cofiring. Moreover, in the case of titanates, strict control over stoichiometry (ratio of titanium to alkaline earth) is important not only for controlling sinterability, but also for improving dielectric properties.

Novel synthetic techniques such as synthesis through emulsions can provide control over both morphology and stoichiometry (Hardy et al., 1988); Akinc and Richardson, 1986). For example, hydrolysis of alkoxides can generate oxides of very high purity, and emulsion techniques can be used to control morphology. These two techniques can be combined to produce submicrometer, monosized, unagglomerated oxide powders of high chemical purity and homogeneity. In such a method, emulsification of the reactive

medium generates spherical "micro-reactors," each of which leads, ideally, to a single particle upon hydrolysis.

In this work, an aqueous solution of the inorganic precursor was emulsified and reacted with a titanium alkoxide dissolved in the continuous phase. This approach was studied to determine the versatility of emulsion techniques.

EXPERIMENTAL PROCEDURE

Both barium and strontium titanates were prepared by the procedure described in Figure 1, using the reagent quantities given in Table 1. The aqueous solutions were prepared with de-ionized, outgassed water and

Table 1. Reagent concentrations used to synthesize BaTiO₃ and SrTiO₃ by the water-in-oil emulsion technique.

Sample #	Reagents	Quantity (mol/L)
1	Ba(OH) ₂ ·8H ₂ O/Ti(O- <i>i</i> -Pr)	1.80 x 10 ⁻²
2	BaCl ₂ /Ti(O- <i>i</i> -Pr) ₄	1.77 x 10 ⁻²
3	Ba(NO ₃) ₂ /Ti(O- <i>i</i> -Pr) ₄	2.50 x 10 ⁻²
4	SrCl ₂ ·6H ₂ O/Ti(O- <i>n</i> -Pr) ₄	1.51 x 10 ⁻¹
5	SrCl ₂ ·6H ₂ O/Ti(O- <i>i</i> -Pr) ₄	1.51 x 10 ⁻¹
6	SrCl ₂ ·6H ₂ O/Ti(O- <i>n</i> -Bu) ₄	1.51 x 10 ⁻¹
7	SrCl ₂ ·6H ₂ O/Ti(O-2-EtHex) ₄	1.51 x 10 ⁻¹

Ba(OH)₂·8H₂O, BaCl₂, Ba(NO₃)₂, or SrCl₂·6H₂O, then emulsified in a mixture of heptane and a non-ionic surfactant, Span®80 (ICI Americas, Inc., Wilmington, DE). The composition of the emulsion was 10 vol% aqueous solution/90 vol% heptane/1.5 wt% surfactant. Emulsification was performed with an Ultra-Turrax homogenizer (Janke and Kunkel GMBH and Co.) or by sonication (Model W-220, Heat Systems-Ultrasonics, Farmingdale, NY). The resulting emulsions were then reacted under a CO₂-free (N₂) atmosphere with

stoichiometric amounts of as-received titanium alkoxides: (Ti(O-i-Pr)₄, Ti(O-n-Pr)₄, Ti(O-n-Bu)₄, and Ti(O-2-EtHex)₄), all obtained from Alfa Products (Danvers, MA). After the reaction, ammonia gas was bubbled through the reaction medium to form ammonium chloride or nitrate and the alkaline earth hydroxide. After the solutions had been refluxed to dehydrate the powders by azeotrope distillation (79°C), the powders were collected by centrifugation, washed with isopropanol, and dried under vacuum at 60°C. An additional washing with isopropanol was performed with a Soxhlet extractor. The powders were then calcined at 950°C for 10 h.

RESULTS AND DISCUSSION

Figure 2 shows the morphologies of barium titanate powders obtained (Samples #1, 2, and 3) after washing. The three powders are characterized by a high degree of agglomeration, and particles are not spherical, as would have been expected if the particles had formed in the emulsion droplets. The particle-size distributions, as determined by centrifugal particle-size analysis (Horiba CAPA 500, Irvine, CA) and assuming a density of 6.02 g/cm³, revealed that the powders had a wide particle-size distribution and an average size of 0.65 μm (Fig. 3). Upon calcination, the powders coarsened: the average particle sizes (based on cross-sectional area) before calcination were 0.65, 0.45, and 0.55 μm for barium hydroxide, barium chloride, and barium nitrate-derived powders, respectively; after calcination, the values were 0.67, 1.30, and 0.80 μm, respectively (X-ray diffraction indicated that all powders crystallized in the tetragonal form of barium titanate).

Since spherical barium titanate particles could not be obtained, the influence of such parameters as alkaline-earth ion concentration, aqueous

phase pH, and the composition of titanium alkoxide reacting with the emulsion was investigated for the strontium titanate powder preparation. In this case, no additional washing with a Soxhlet extractor was performed, since the alkaline earth hydroxides are soluble and can be removed during washing.

In reactions of titanium alkoxides with emulsions of SrCl₂, gels formed for Emulsions #4, 5, 6, and 7 as the titanium alkoxide solutions were added. This behavior is similar to that observed when water dissolved in alcohol is slowly added to alcoholic solutions of titanium alkoxides to form highly cross-linked gels. Figure 4 shows a scanning electron micrograph (SEM) of the product obtained using Ti(O-n-Bu)₄ before bubbling ammonia gas through the emulsion. Energy dispersive analysis by X-ray (EDAX) semi-quantitative analysis was performed at different locations on the sample. The rounded particles near the middle of the micrograph in Figure 4 were found to be ten times richer in strontium and chlorine than the gel-looking material at the left side of the micrograph, which essentially contained titanium with minor quantities of strontium and chlorine.

The average particle size of calcined powders was also found to be smaller when higher-molecular-weight alkoxides were used (Figs. 5a and b): average particle sizes were 0.80, 0.70, 0.53, and 0.51 μm for, respectively, the Ti(O-n-Pr)₄, Ti(O-i-Pr)₄, Ti(O-n-Bu)₄, and Ti(O-2-EtHex)₄-derived strontium titanate powders. This result has been observed by Yoldas (1986) in alkoxide-derived TiO₂ powders obtained by calcining the hydrolytic polycondensates. Yoldas explained this observation by assuming that the slower hydrolysis and diffusion for the bulkier alkoxides result

in lower-molecular-weight polymeric condensates, and therefore smaller particles.

Upon calcination, the powders crystallized in the cubic structure; X-ray diffraction showed SrTiO₃ to be the major phase, with only TiO₂ as a minor phase, indicating an excess of titanium in the products.

Lastly, the particle-size distributions of the strontium titanate powders were studied as a function of strontium ion concentration in the dispersed phase, the emulsions being reacted with the corresponding stoichiometric amounts of Ti(O-*i*-Pr)₄; the aqueous phase content in the emulsions was kept at 10 vol%. In Figure 6, the average particle size after calcination was plotted against the molar concentration of strontium in the aqueous phase (molar concentrations in the total emulsions are one tenth of these values). Contrary to what would be expected if the amount of water were controlling particle size, the mean particle size decreased as the Sr:water ratio increased. Again, this result was obtained by Yoldas (1982, 1986). It is a general trend in the hydrolysis and polymerization of alkoxides: the higher the water:alkoxide ratio, the higher the oxide content of the hydrolytic polycondensates, and thus the greater the particle radius.

These facts lead us to conclude that the droplet-size distribution of water-in-oil emulsions does not control powder morphology. In this case, the droplets serve as reservoirs of both water for hydrolysis and of alkaline-earth ions, and particle size is controlled by the kinetics of hydrolysis and diffusion of the titanium species in the dispersing phase.

SUMMARY

The preparation of barium and strontium titanate powders through a

combination of alkoxide hydrolysis and an emulsion technique has been investigated. This method did not yield unagglomerated BaTiO₃ powders after calcination; fine, unagglomerated, submicrometer SrTiO₃ powders, however, were obtained.

The study of parameters such as the reactivity of the titanium alkoxide precursors and the water:alkoxide ratio has led us to believe that the hydrolysis and condensation reactions of the alkoxides were occurring in the dispersing phase, and, accordingly, the morphology of the as-prepared powders could not be controlled by the size of the aqueous droplets.

As the mechanism for (Sr,Ba)-Ti-oxo-hydroxide formation in this dispersed system seems very similar to that in non-dispersed systems, the potential offered by the former medium to slow hydrolysis and alkoxide condensation or to react with species that do not dissolve in the same solvent has yet to be addressed in ceramic powder synthesis.

REFERENCES

- M. Akinc and K. Richardson, "Preparation of Ceramic Powders from Emulsions"; pp. 99-109 in Materials Research Society Symposia Proceedings, Vol. 73: Better Ceramics Through Chemistry II. Edited by C.J. Brinker, D.E. Clark, and D.R. Ulrich. Materials Research Society, Pittsburgh, 1986.
- E.A. Barringer and H.K. Bowen, "Formation, Packing, and Sintering of Monodisperse TiO₂ Powders," J. Amer. Ceram. Soc., 65, C199-C201 (1982).
- A.R. Hardy, G. Gowda, T.J. McMahon, R.E. Riman, W.E. Rhine, and H.K. Bowen, "Preparation of Oxide Powders," pp. 407-28 in Ultrastructure Processing of Advanced Ceramics. Edited by J.D. Mackenzie and D.R. Ulrich. John Wiley & Sons, Inc., New York, 1988.
- B.E. Yoldas, "Effect of Variations in Polymerized Oxides on Sintering and Crystalline Transformations," J. Amer. Ceram. Soc., 65 [8] 387-393 (1982).
- B.E. Yoldas, "Hydrolysis of Titanium Alkoxides and Effects of Hydrolytic Polycondensation Parameters," J. Mater. Sci., 21, 1087-92 (1986).

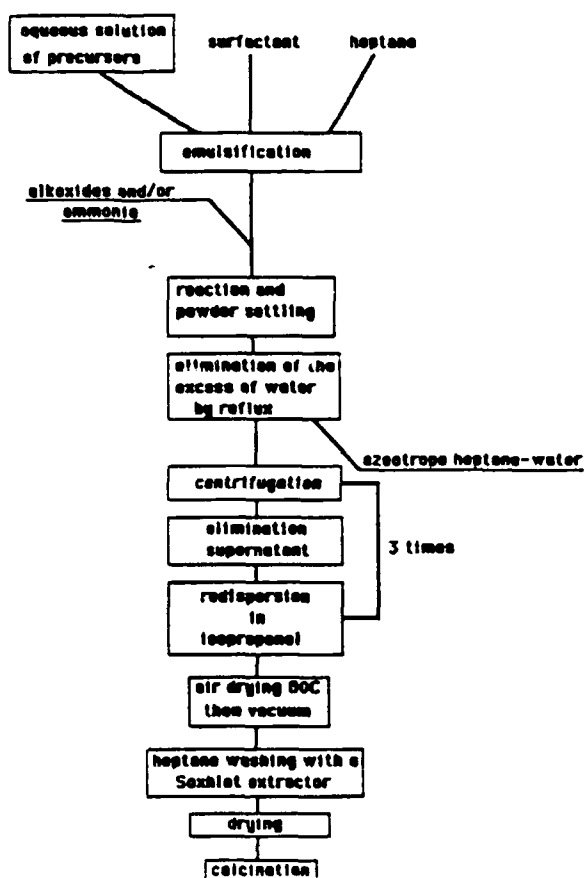
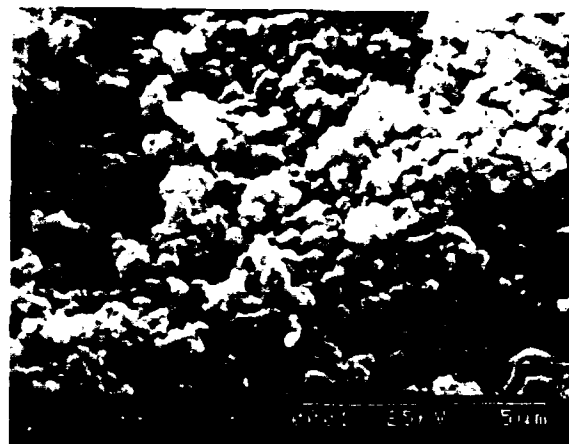
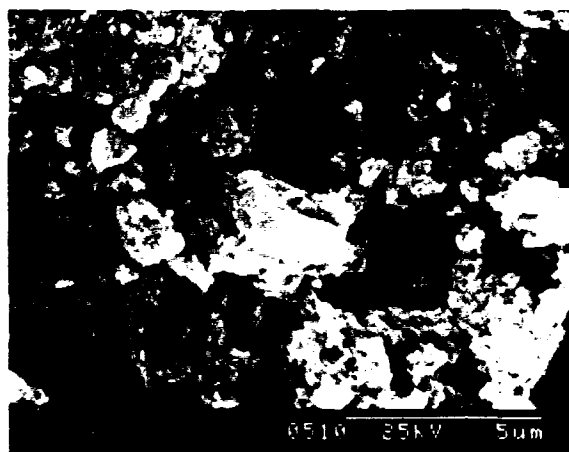


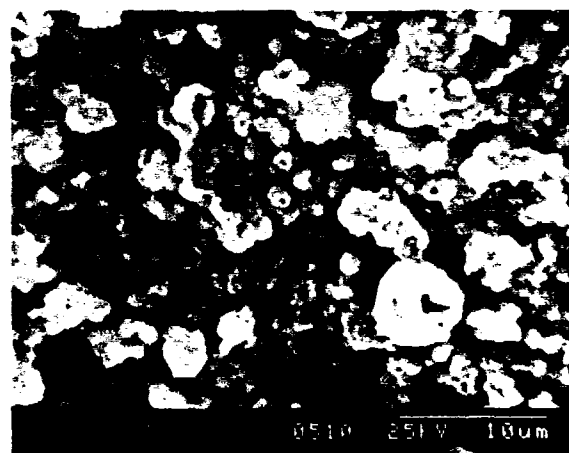
Figure 1. Flow diagram of powder preparation method.



(a)



(b)



(c)

Figure 2. SEMs of barium titanate powder obtained from a) Sample 1, b) Sample 2, and c) Sample 3.

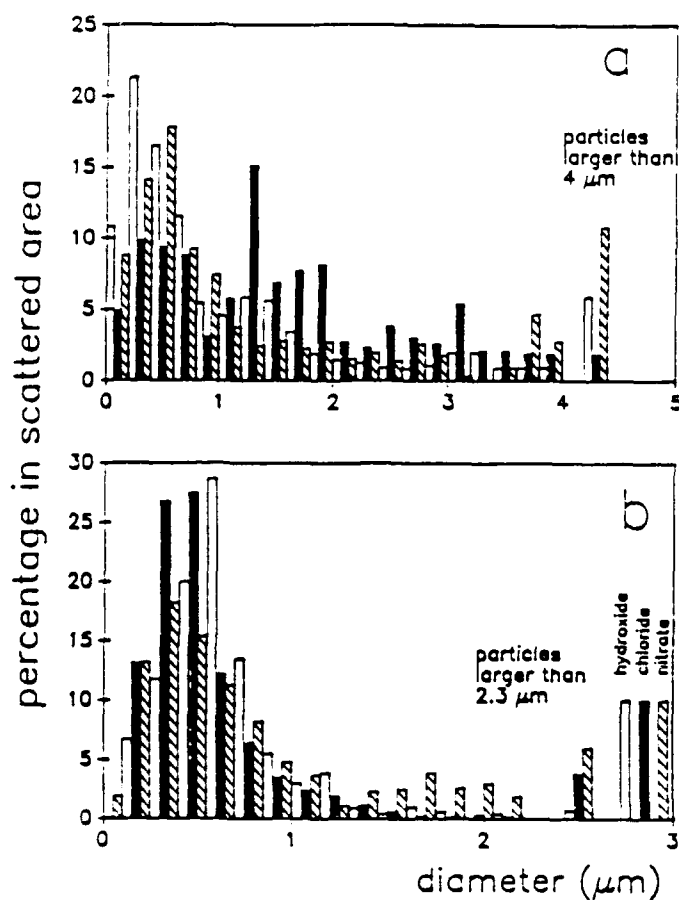


Figure 3. Particle-size distribution of synthesized barium titanate powders, as determined by centrifugal particle-size analysis.



Figure 4. SEM of strontium titanate product obtained without ammonia addition.

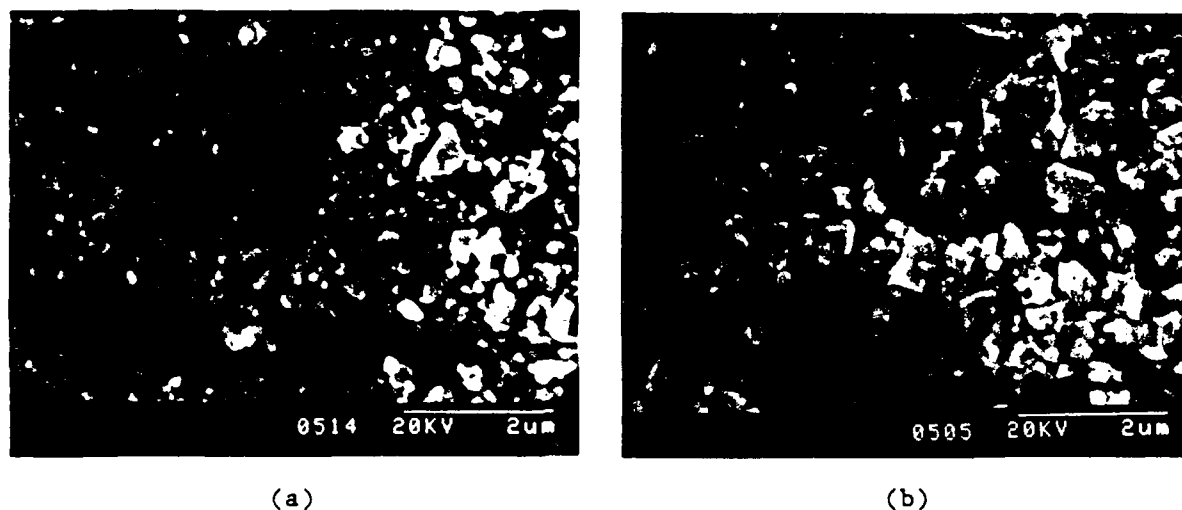


Figure 5. SEMs of strontium titanate powder obtained from a) $\text{Ti}(\text{O-n-Pr})_4$ and b) $\text{Ti}(\text{O-2-EtHex})_4$.

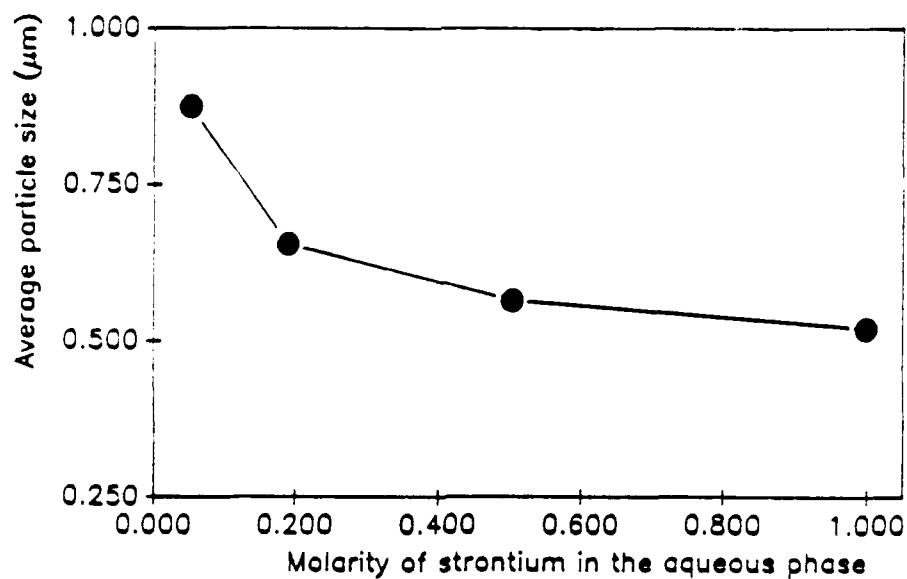


Figure 6. Plot of average strontium titanate particle size after calcination versus strontium ion concentration in the aqueous phase.

SYNTHESIS OF AlN POWDER FROM DIMETHYLAMINOALANE

Mari-Ann Einarsrud

ABSTRACT

Two precursors for aluminum nitride have been synthesized from dimethylaminoalane and ammonia in hydrocarbon solutions, using different reaction routes in order to try to control the powder morphology. Both precursors gave very fine, agglomerated, high-purity AlN powders after heat-treatment. A crystalline powder having a large surface area was formed at 1000°C. At 1500°C the surface area decreased to ~10% of the value at 1000°C and coarsening was observed. At 1600°C the surface area decreased further and densification occurred. A sample formed by colloidal pressing densified to 95% of theoretical density at 1750°C.

INTRODUCTION

Aluminum nitride (AlN) has potential application as an electronic substrate material for high-power, high-density electronic circuits because of its high theoretical thermal conductivity (330 W/mK) (Slack, 1973). The thermal conductivity decreases, however, if oxide impurities are present in the ceramics (Slack, 1973), so a ceramic powder of high purity is desired. The commercial procedures for preparing AlN powder involve the carbothermal reduction of alumina in the presence of nitrogen (Ste d'Electrochimie, 1957) or the reaction of aluminum with either ammonia or nitrogen (Samsonov and Dubovik, 1962; Yamashita *et al.*, 1986). The powders produced by these methods often contain high concentrations of oxygen and other impurities and are grey in color.

Several other chemical synthesis routes have been investigated in the literature to produce high-purity AlN powder. For example, AlN can be prepared by reacting ammonia with either $AlCl_3$ (Lewis, 1970) or $(NH_3)_6AlF_6$ (Huseby, 1983), though these reactions require high temperatures and yield highly corrosive byproducts.

Several other researchers have alternatively proposed an organoaluminum compound as a good starting material for synthesizing AlN powder. Interante *et al.* (1986) reacted triethylaluminum with ammonia to form a precursor of high-purity AlN powder. Thermal decomposition of this precursor can lead to carbon contamination of the final product. Bolt and Tebbe (1987) also used triethylaluminum as a starting material to synthesize a thermoplastic precursor of AlN. This precursor could be drawn into fibers that densified between

1600°C and 1800°C without the use of sintering additives.

Wiberg and May (1955) reported that AlH_3 reacts with ammonia in THF solution to form various compounds in which amino or imido groups replace one or more hydrogens in AlH_3 . These compounds were shown to release NH_3 or H_2 upon heating and approach the stoichiometry of AlN. However, these researchers did not describe the conditions required to form AlN. Maya (1986) investigated these reactions, reacting $AlH_3 \cdot Et_2O$ with NH_3 to form a product with the empirical formula $[Al(NH_2)NH]_n$, and converting this intermediate product into AlN. Ochi, Rhine, and Bowen (1988) studied the reaction between AlH_3 and NH_3 in a tetrahydrofuran (THF) solution. When excess NH_3 was used, a white, high-purity AlN powder was obtained; when a stoichiometric amount of NH_3 was used, however, the synthesized AlN contained a carbon residue, probably due to THF decomposition during heat-treatment through association with the precursor.

Preparation of AlN powder by a vapor-phase reaction of the $Al(i-Bu)_3-NH_3$ system has also been investigated, using a 'flow' method (Tsuchida *et al.*, 1987); particle size varied with the reaction temperature used. The as-synthesized powder, however, contained 18.8 wt% oxygen, an amount that could be decreased to 4.5 wt% by heat-treatment in a H_2-NH_3 gas mixture at 1400°C for 2 h.

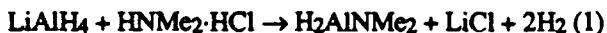
Sekercioglu (1986) has submitted a patent application for a process by which AlN can be produced by reacting aluminum sulfide with either ammonia or nitrogen and hydrogen at a temperature above 1100°C. The powder product may contain 4.5 - 11.2 wt% oxygen, but Sekercioglu's analyses suggest that most of this oxygen resides on the powder surface.

In the present study, H_2AlNMe_2 was investigated as a starting material for synthesizing a precursor for AlN powder. The compound H_2AlNMe_2 is soluble in hydrocarbons, which should facilitate solvent removal. Two synthesis routes were tried, in efforts to control the morphology of the powder produced.

EXPERIMENTAL

Due to the reactivity of aluminum hydride compounds with oxygen and/or moisture, handling of the chemicals and all the experimental work were performed in an inert atmosphere or under vacuum.

Dimethylamine hydrochloride, HNMe_2HCl (Aldrich Chemical Company, Milwaukee, WI, 98%; dried under vacuum at room temperature for 24 h), was reacted with excess LiAlH_4 (Alfa Products, Danvers, MA; 1.5-M solution in THF, used as received) in 150 ml of THF according to the following equation:



Due to vigorous gas evolution, the solid dimethylamine hydrochloride had to be added slowly to the THF solution. The resulting solution was filtered and the solvent removed under vacuum. The H_2AlNMe_2 sublimed easily at 50–60°C (–70°C at the cold spot); the product was sublimed twice to give a total yield of 77%.

The reaction scheme below was used to synthesize AlN powder. This paper discusses AlN powder production following the two synthesis routes shown in Table 1.



AlN via Precursor I

H_2AlNMe_2 (3.6 g) was dissolved in toluene and reacted with excess NH_3 at –70°C. At this temperature, ammonia condensed into the reaction flask. Upon heating, gas evolved, beginning at –60°C, and a voluminous white precipitate formed. The solvent was removed under vacuum at room temperature. The precipitate (Precursor I) was placed in an alumina or molybdenum boat and heat-treated for 2 h under nitrogen at a rate of 10K/min to various selected temperatures to form AlN. This same synthesis was also performed in a hexane solution instead of toluene, but the change in solvent did not affect the morphology of the powder produced.

AlN via Precursor II

In the second synthesis, H_2AlNMe_2 (3.6 g) was dissolved in 150 ml hexane, and this solution was reacted with a slight excess of ammonia at room temperature. The reaction took place at the interface between the solution and the gas phase as ammonia flowed over the solution. A white layer formed on the solution surface and the powder gradually sank to the bottom of the flask; gas evolved from the product at the bottom of the reaction flask. The solvent was removed under vacuum and a white precipitate obtained. The precipitate (Precursor II) was pyrolyzed under ammonia at temperatures up to 200°C, then heat-treated under nitrogen to 1000°C.

Powder Characterization

Fourier transform infrared (FTIR) spectra were recorded using a closed diffuse-reflectance cell with KBr windows (IR44, IBM Instruments, Danbury, CT). Surface areas of the powders obtained by both synthesis routes were measured by the one-point BET method using N_2 gas (Quantachrome, Syosset, NY). X-ray dif-

fraction (XRD) patterns were measured using Cu K α radiation (RU300, Rotaflex, Rigaku/USA, Inc., Danvers, MA). The powder morphologies were studied by scanning electron microscopy (SEM) (S-530, Hitachi Scientific Instruments, Rockville, MD) and the particle-size distribution was measured using a centrifugal particle-size distribution analyzer (CAPA-500, Horiba Instruments, Irvine, CA). Chemical analyses were performed by commercial laboratories (Galbraith Laboratories, Inc., Knoxville, TN, and IRT Corporation, San Diego, CA).

Sintering

Colloidal pressing produced green compacts with higher green densities than were obtained by dry pressing. The AlN powder was dispersed in a hexane solution using 4 wt% OLOA™1200 (Chevron Chemical Company, San Francisco, CA) as the dispersant. The resulting AlN compact was pressed at 10 000 psi and sintered under 1 atm nitrogen in a molybdenum crucible at 1700–1800°C. Final density was measured using Archimedes' method.

RESULTS AND DISCUSSION

Precursor Characterization

The FTIR spectra obtained for Precursors I and II after pyrolysis under ammonia are shown in Figure 1. The broad band at $\sim 750\text{ cm}^{-1}$ is due to Al–N stretching vibrations; the broad bands in the region 3000–3300 cm^{-1} are due to N–H stretching vibrations; the band at $\sim 1800\text{ cm}^{-1}$ is due to Al–H stretching vibrations; and the rather sharp bands in the region 1500–1600 cm^{-1} are N–H bending modes. For Precursors I and II after pyrolysis under ammonia, no absorption is apparent in the Al–H stretching region (1700–1800 cm^{-1}) and only weak features can be detected in the C–H stretching region (2850–3050 cm^{-1}). From these observations, we conclude that both hydrogens and almost all of the NMe₂ groups on the aluminum atom of the starting compound must have been replaced by ammonia, and that both precursors were probably an imide-amide, $[\text{AlNH}(\text{NH}_2)]_n$. Maya (1986) also observed absorption bands at the frequencies 3200, 1505, 900, and 680 cm^{-1} for a precursor with empirical formula $\text{Al}(\text{NH})(\text{NH}_2)]_n$.

Also included in Figure 1 is an FTIR spectrum of Precursor II before pyrolysis under ammonia. The spectrum shows a broad band at $\sim 3200\text{ cm}^{-1}$ due to N–H stretching vibrations, bands at $\sim 2900\text{ cm}^{-1}$ due to C–H stretching vibrations, a band at $\sim 1800\text{ cm}^{-1}$ due to Al–H stretching vibrations, and the broad feature below 1000 cm^{-1} due to Al–N stretching vibrations. The bands between 1200 and 1600 cm^{-1} are probably C–H and N–H bending modes. This spectrum suggests that the precursor is $\text{H}(\text{NH}_2)\text{AlNMe}_2$.

Characterization of AlN Powders

The AlN powders derived from heat-treatment of the two precursors were white or slightly grey. Chemical analysis of AlN obtained from Precursor I calcined at 1200°C showed it to contain 33.10% nitrogen and 65.24% aluminum (theoretical: 34.17% N, 65.83% Al), which gives an Al/N ratio of 1.02. The sample contained 0.547 ± 0.022 wt% oxygen (neutron activation analysis); the oxygen source was presumably the atmosphere during heat-treatment of the precursor.

Figure 2 shows the development of X-ray diffraction patterns of the AlN powder derived from Precursor I after heat-treatment at 1000, 1200, and 1500°C. At 1000°C the AlN peaks are broad, but at higher temperatures the intensity increases and the peaks sharpen. At the lowest temperatures, the (101) peak at $2\theta = 37.3^\circ$ has a lower intensity than the (002) peak at 35.4° , but at 1500°C this ratio changes and is in agreement with literature data (American Society for Testing and Materials). The FTIR spectrum of a sample calcined at 1000°C showed a weak N-H stretching band at 3200 cm^{-1} , indicating a small amount of hydrogen still present in the AlN produced at this temperature. No N-H stretching band was observed for powders heat-treated at higher temperatures. Hydrogen in the AlN lattice might cause the change in the observed intensity ratio in the XRD pattern. Figure 3 shows the XRD pattern of AlN powder produced from Precursor II; the same pattern was observed for AlN produced from Precursor I at the same temperature.

The surface areas of powders obtained from Precursor I when calcined at different temperatures are given in Figure 4. At 1000°C, the surface area was rather high ($118\text{ m}^2/\text{g}$), indicating high reactivity of the powder; the surface area decreased to $1.3\text{ m}^2/\text{g}$ at 1600°C. The surface area of an AlN powder obtained from Precursor II, when calcined at 1000°C, was measured to be $109\text{ m}^2/\text{g}$, slightly lower than that of the powder obtained from Precursor I.

Heat-treating Precursor II at 1200°C in a nitrogen atmosphere without pyrolysis under ammonia yielded a black product. The XRD pattern confirmed that the product was AlN and that the black color was probably due to carbon residue from the pyrolysis. Chemical analysis showed 9.95% carbon in the AlN produced and an Al/N ratio of 0.99. The relatively large amount of carbon after heat-treatment shows that pyrolysis under ammonia at low temperatures is necessary. The action of carbon as a scavenger of oxygen in conventional AlN powder processing is suggested by its inclusion in sintering additives (Huseby and Bobik, 1986). By partial pyrolysis of Precursor II under ammonia followed by heat-treatment under nitrogen, an AlN powder with a

desired percentage of carbon could perhaps be synthesized.

Figures 5a-b show scanning electron micrographs (SEMs) of the AlN powders obtained from Precursors I and II, respectively, after calcination to 1000°C. The powders produced at 1000°C consisted of very fine, agglomerated particles. From the SEMs, the particle size can be estimated to be less than $0.1\text{ }\mu\text{m}$. The particle-size distribution (as measured by the centrifugal method) of dispersed (4 wt% OLOA™1200/hexane) AlN powder synthesized from Precursor I is shown in Figure 6. The results show an average agglomerate size of $\sim 0.40\text{ }\mu\text{m}$.

Sintering behavior

Heat-treatment to 1500°C of the powder produced from Precursor I coarsened the particles. At this temperature, the surface area was about 10% of its value after calcination at 1000°C. At 1600°C, the surface area had decreased to $1.3\text{ m}^2/\text{g}$ and sintering was observed. In some samples, only partial sintering was observed: some sections were almost 100% dense, others were more porous. This variability in sintering may be due to differences in impurities and oxygen content, a suggestion offered by other authors (Bolt and Tebbe, 1987).

Dry-pressing the powder (10 000 psi) gave a very low green density and a final density only 67% of theoretical. Colloidal pressing produced a higher-density green compact that sintered to an average of 95% of theoretical without the use of sintering aids.

Scanning electron microscopy of the section of this sample that was topmost during sintering showed it to be almost 100% dense (Fig. 7a). The average grain size was $1.5\text{ }\mu\text{m}$, with only a few pores apparent in the microstructure. This part of the sample, $\sim 100\%$ of the theoretical density, was slightly grey in color. The bottom section of the sample during sintering was porous (Fig. 7b). The difference in density might be an artifact of the colloidal pressing, producing different green densities in the two sections of the sample.

CONCLUSIONS

- Two precursors for AlN have been synthesized from H_2AlNMe_2 and NH_3 in a hydrocarbon solution.
- Upon pyrolysis under NH_3 and/or N_2 , high-purity AlN powder has been formed.
- The powder has a high surface area at low calcination temperatures (1000°C) and consists of very fine ($0.1\text{-}\mu\text{m}$) particles.
- From 1000°C to 1500°C, the surface area decreases almost linearly with the temperature,

and at 1500°C particle coarsening occurs.

- At 1600°C, the surface area decreases to 1.3 m²/g and sintering occurs. Partial sintering has been observed in which some sections of samples were almost 100% dense while other sections were more porous.
- A sample formed by colloidal pressing sintered to an average density of 95% of theoretical without the use of sintering aids.

REFERENCES

American Society for Testing and Materials, "X-Ray Powder Data File," Philadelphia, PA.

J.D. Bolt and F.N. Tebbe, Proceedings of the American Ceramics Society Electronics Division Meeting, Denver, CO, 1987.

I.C. Huseby, *J. Am. Ceram. Soc.*, **66**, 217-20 (1983).

I.C. Huseby and C.F. Bobik, U.S. Patent 4,578,232 (1986).

L.V. Interante, L.E. Carpenter, C. Whitmarsh, and W. Lee, *Mat. Res. Soc. Symp. Proc.*, **73**, 359-66 (1986).

D.W. Lewis, *J. Electrochem. Soc. Electrochem. Technol.*, **117**, 978-82 (1970).

L. Maya, *Adv. Ceram. Mater.*, **1**, 150-53 (1986).

A. Ochi, W.E. Rhine, and H.K. Bowen, Proceedings of the Materials Research Society Spring Meeting, Reno, NV, 1988.

G.N. Samsonov and T.V. Dubovik, *Tsvet. Metal.*, **35**, 56 (1962).

I. Sekercioglu, *Pat. Appl.* WO86/06360 (1986).

G.A. Slack, "Nonmetallic Crystals with High Thermal Conductivity," *J. Phys. Chem. Solids*, **34** [2] 321-35 (1963).

Ste d'Electrochimie: French Patent 1,149,539 (1957).

K. Tsuchida, Y. Takeshita, A. Yamane, and A. Kato, *Yogyo-Kyokai-Shi*, **95**, 54-57 (1987).

E. Wiberg and A. May, *Z. Naturforsch.*, **10B**, 229-32 (1955).

H. Yamashita, Y. Imai, R. Oguma, and T. Hayashi, *Pat. Appl.* 86/205606, Jpn. Kokai Tokkyo Koho JP61/205606 (1986).

Table 1. Reaction conditions for the synthesis of AlN precursors.

	Temperature (°C)	Solvent	Amount NH ₃	Atm. for pyrolysis
Precursor I	-70°C	toluene	excess	N ₂
Precursor II	25°C	hexane	slight excess	NH ₃ /N ₂

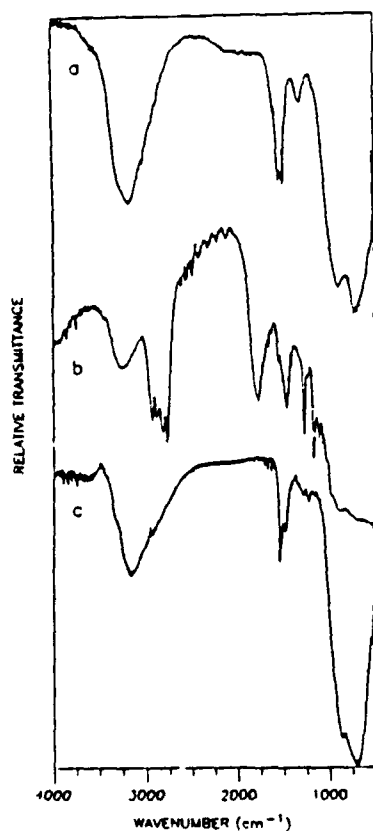


Figure 1. FTIR diffuse reflectance spectra of the intermediate compounds (AlN precursors): a) Precursor I, b) Precursor II before pyrolysis under ammonia, and c) Precursor II after pyrolysis under ammonia.

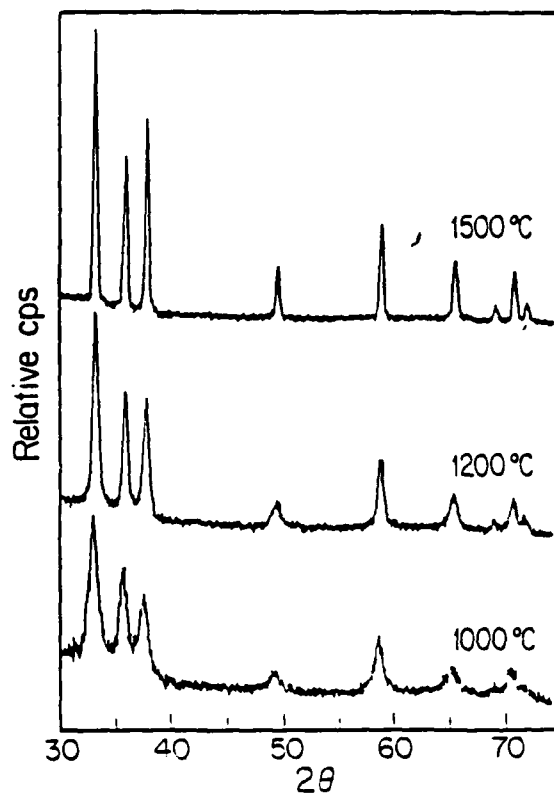


Figure 2. XRD patterns of AlN powder prepared from Precursor I and heat-treated at a) 1000°C, b) 1200°C, and c) 1500°C.

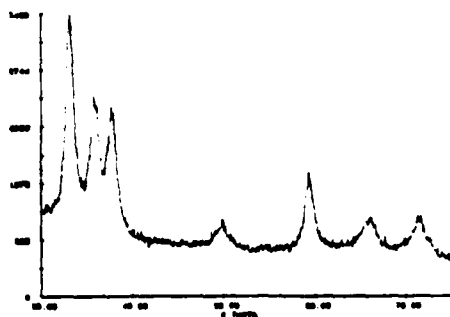


Figure 3. XRD pattern of AlN powder prepared from Precursor II after pyrolysis under ammonia to 200°C and subsequent heat treatment under nitrogen to 1000°C.

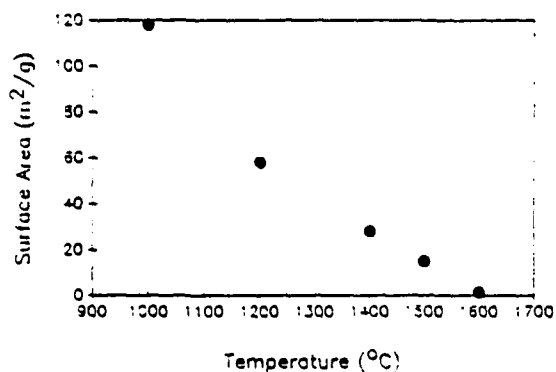


Figure 4. Surface areas of AlN powders prepared from Precursor I.

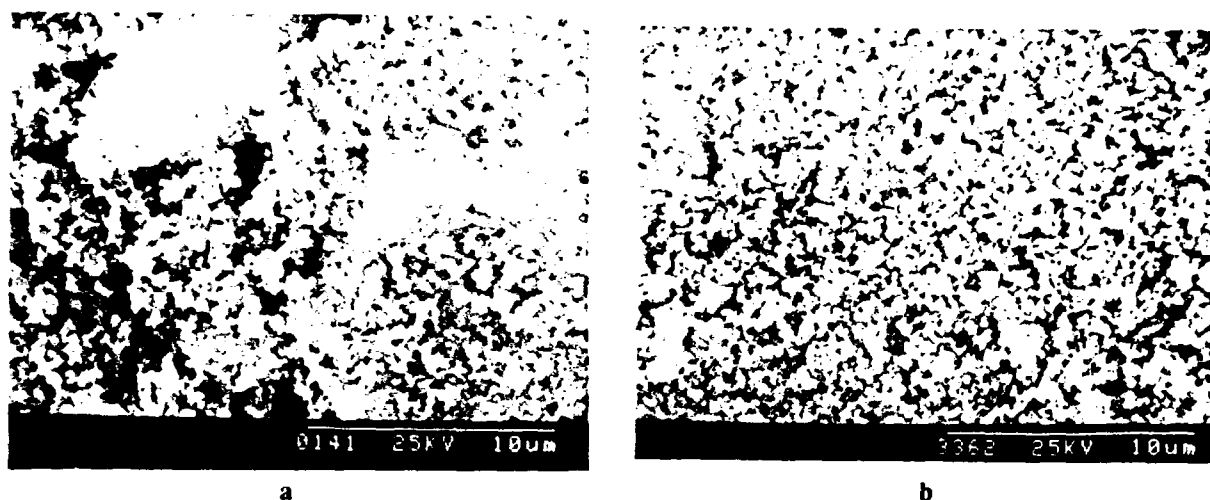


Figure 5. Scanning electron micrographs of AlN powder produced at 1000°C from a) Precursor I and b) Precursor II.

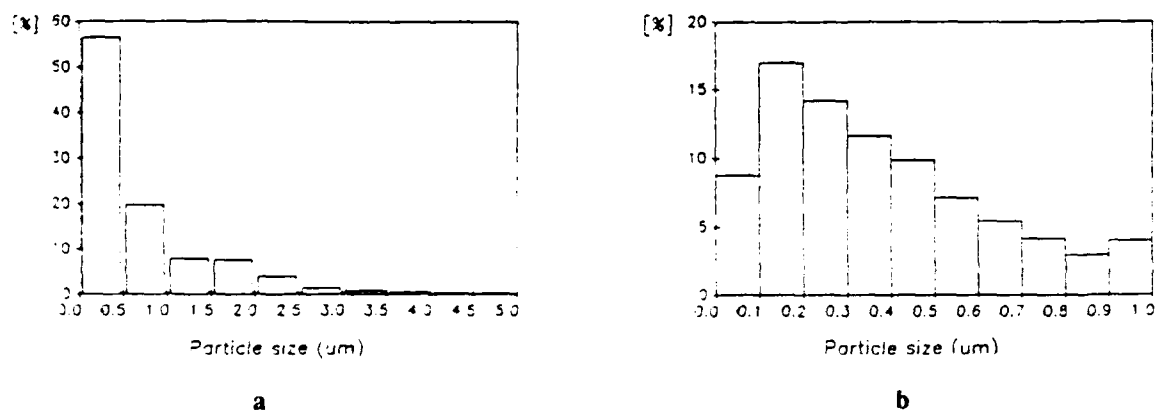


Figure 6. Particle-size distribution of AlN powder synthesized from Precursor I dispersed in 4 wt% OLOA™ 1200/hexane, to a) 1.0 μm and b) 5.0 μm.

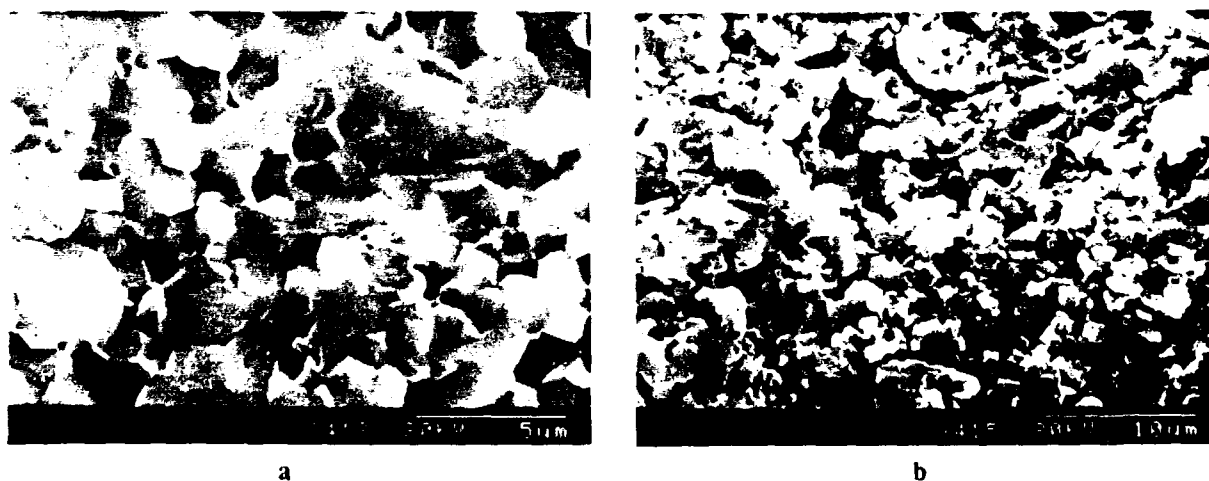


Figure 7. Scanning electron micrographs of the fracture surfaces of an AlN compact prepared by colloidal pressing and sintered at 1750°C: a) topmost section and b) bottom-most section during sintering.

FLOCCULATION OF POLYMER-CONTAINING POWDER DISPERSIONS BY THE ADDITION OF NONSOLVENTS

William C. Moffatt

ABSTRACT

A ceramics processing technique based on precipitating polymer-powder flocs from polymer-powder-solvent dispersions by adding a nonsolvent for the polymer was developed. The floc-formation mechanism and floc-character dependence on processing variables were investigated.

Precipitating alumina-polyvinyl alcohol flocs from polyvinyl alcohol solutions containing alumina powder by adding acetone requires polymer adsorption onto the powder surface. Precipitation occurs by the synergistic interaction of polyvinyl alcohol with acetone, and is fully reversible by acetone removal. Floc texture is unrelated to absolute loading levels of polymer and powder, but related to their ratio.

INTRODUCTION

A novel technique for producing highly homogeneous ceramic composites has been developed.^{1,2} It involves dispersing two or more ceramic powders in a dilute polymer solution and precipitating powder-polymer flocs from this dispersion by adding a second solvent (fully miscible with the first) in which the polymer is insoluble. The flocs are processed using wet forming techniques to yield high-density, homogeneous green bodies that can be fired to dense ceramic bodies with excellent properties.

This technique appears to have general applicability, although experimental details have been investigated for only one system so far. Dispersions consisting of both alumina and zirconia powders in dilute solutions of polyvinyl alcohol in water were precipitated by adding acetone. This system was chosen for two reasons: First, alumina-zirconia composites are commercially important for such valuable properties as high fracture toughness, low wear rate, and strength at relatively high temperatures. Second, the solvents and polymer used are safe and inexpensive. A nonaqueous analogue of this technique was also developed.

This paper offers a mechanistic explanation of this technique, developed during the course of an experimental study of the interactions of the reagents in the dispersions. Numerous physical-chemical interactions may be important -- for example, the pairwise interactions between ZrO_2 , Al_2O_3 , polyvinyl alcohol, water, and acetone.

LITERATURE REVIEW

Polymer-Solvent-Nonsolvent Phase Equilibria

A schematic ternary phase diagram for a polymer-solvent-nonsolvent system is shown in Figure 1. Such phase diagrams typically have a single-phase region and a two-phase region separated by a "binodal curve". The two-phase region is spanned by "tie-lines" -- lines connecting the dilute and concentrated phases in thermodynamic equilibrium with each other. The critical point of the binodal curve is the point at which the length of the tie-line in the two-phase region becomes zero. If the binodal curve is crossed from the single-phase side at the critical point, the homogeneous polymer solution separates into two phases of incrementally different polymer concentration. If the binodal curve is crossed elsewhere, the polymer concentration difference between the two phases will be macroscopic.^{3,4}

The ternary solvent-nonsolvent-polymer system should not be viewed as a binary mixture of a single (two-component) solvent and a polymer. If the system phase-separates, the solvent mixture will generally differ in the two phases.³

Phase Separation of Polyvinyl Alcohol

Polyvinyl alcohol solutions can be phase-separated by a couple of methods, one of which involves changing the solution temperature⁵: For

example, hot concentrated solutions of polyvinyl alcohol in a solvent or solvent mixture can phase-separate upon cooling (this phenomenon serves as the basis for one technique for spinning polyvinyl alcohol fibers⁹).

Polyvinyl alcohol solutions can also be phase-separated by adding acetone^{6,7} or congo red.⁸ Polyvinyl alcohol has been purified by repeatedly putting it into solution and precipitating with acetone.⁷

Adsorption of Polyvinyl Alcohol

A number of authors¹⁰⁻¹⁹ have investigated the adsorption of polyvinyl alcohol onto oxide ceramics. There is wide agreement that the pH of the polymer solution significantly affects the adsorption behavior, with maximum adsorption often occurring at the point of zero charge on the oxide.¹⁰⁻¹⁵ Adsorption of polyvinyl alcohol onto oxide surfaces is thought to involve not only hydrogen bonding,^{10,11,14-16} but also donor-acceptor bonding, with surface-layer electron-acceptor levels in metal oxides taking on electrons.^{15,16} Hydrogen bonding dominates for high-isoelectric-point oxides; donor-acceptor bonding dominates for low-isoelectric-point oxides.¹⁶

Polyvinyl alcohol is thought not to attach directly to oxide particle surfaces, but rather to form a bond through "bridge" water.^{11,16} Water layer thickness increases with increasing isoelectric point of the oxide powder¹¹; highly hydrophilic powder surfaces may be inaccessible to macromolecules.¹⁶ Polyvinyl alcohol adsorption causes a large drop in electrophoretic mobility as adsorption increases because of Stern layer displacement.¹⁹ The electrokinetic potential is found to increase with adsorption for small polymer concentrations, due to the potential established across the adsorbed layer by the oriented adsorption of polar

groups, before dropping at higher concentrations as the Stern plane is displaced.¹⁶ High adsorption of polyvinyl alcohol onto hydrated aluminum oxide is attributed to the low free energy of adsorption.¹⁹

Phase Separation of Particle-Containing Polymer Solutions

Although studies of polymer adsorption onto powder particles^{20,21}, and of phase-separation of polymers from sterically stabilized dispersions²¹ have been reported, very little has been written about the phase separation of polymers from electrostatically stabilized dispersions. This subject is, however, central to the work reported here.

When silica and polyvinyl alcohol are present in a certain fixed ratio in aqueous dispersion at low pH, phase separation can take place, giving a viscous phase enriched in polyvinyl alcohol and silica, and a supernatant deficient in both.²² According to Iler,²² the SiO_2 -rich phase contains silica particles coated with a monomolecular layer of polyvinyl alcohol; the hydrophilic silanol sites are saturated by hydrogen bonding to hydroxyl groups of the polyvinyl alcohol, exposing the hydrocarbon backbone of the polyvinyl alcohol to the solvent. The resulting hydrophobic particle coating causes phase separation.

ADSORPTION ISOTHERM

Experimental Procedure

The adsorption isotherm of polyvinyl alcohol onto Sumitomo AKP-HP alumina (Sumitomo Chemical America, 345 Park Ave., 14th Floor, New York, NY 10154) was measured in the following way. A 0.667 wt% stock solution of polyvinyl alcohol in water was heated to 80°C and held for 0.5 h. It was then cooled to room temperature and used within 24 h, since the properties of polyvinyl alcohol solutions change over time.²³⁻²⁵ Solutions containing

0, 12.5, 25, 50, 100, or 200 mg polyvinyl alcohol per liter of deionized water were made by diluting the stock solution. To 250 ml of each polymer solution was added 1.165 g of alumina powder (surface area, 6.25 m^2) and 5 drops (0.2 ml) of concentrated nitric acid to bring the pH down to 2-3.

The resulting slurries were ultrasonically agitated (Model W-220F Sonicator Cell Disruptor with a 0.5-inch-diameter titanium tip, Heat Systems Ultrasonics, Inc., 1938 New Highway, Farmingdale, NY 11735) in 250-ml polypropylene bottles at a power level of 50 W for 2 min. Following ultrasonic agitation, the plastic bottles were sealed. The bottles were tumbled for >48 h to equilibrate the polymer solutions with the powder surfaces. Approximately 40 ml of the sample slurries were centrifuged and their supernatants poured off. Forty milliliters of acidified water was then added to each sample to replace the supernatant, and the centrifuge cakes were ultrasonically dispersed. This "washing" process was performed twice before final centrifugation. Separate experiments confirmed that two washings were sufficient to remove essentially all polymer from solution. After the final washing, the supernatant in each sample was poured off and the centrifuge cake dried at $60\text{-}80^\circ\text{C}$ in laboratory air.

The weight loss of each sample was characterized using a thermogravimetric analyzer (Perkin-Elmer TGA 7 Thermogravimetric Analyzer, Perkin-Elmer Corp., Main Ave., Norwalk, CT 06856). Water-washed, oven-dried alumina was also characterized in this way, to allow subtraction of weight loss unrelated to polymer burnout.

Results and Discussion

The calculated adsorption densities, based on the corrected weight losses and the BET surface area of the alumina powder, are shown in Figure 2. The error bars in Figure 2 represent the maximum range of values

expected for a minimum sample weight of 50 mg and a maximum sample-to-sample random error in weight loss of 10 μg . The latter value is based on the variation in results obtained from thermogravimetric analysis runs made with an empty sample pan.

The area of an adsorbed vinyl alcohol segment is assumed to be 0.285 nm^2 (after Tadros²⁶). Then the measured extent of polyvinyl alcohol adsorption from a solution with a concentration of 200 mg/L, namely 0.215 mg/m^2 , leads to a calculated alumina surface coverage of 0.838 monolayer. This calculated surface coverage agrees with the results of an earlier study, which indicated that polyvinyl alcohol covers alumina to the extent of one monolayer.²⁷

EFFECT OF SOLUTION CHEMISTRY ON APPARENT PARTICLE SIZE

Procedure

To quantitatively determine the effect of polyvinyl alcohol, acetone, and polyvinyl alcohol plus acetone on aqueous dispersions of the three ceramic powders used to produce alumina-zirconia-yttria composite ceramics using this nonsolvent flocculation technique (Sumitomo AKP-HP alumina, Toyo Soda TZ-O zirconia, and Toyo Soda TZ-3Y zirconia-yttria (Toyo Soda USA, 1700 Water Place, Atlanta, GA 30339)), photon correlation particle-size studies were conducted.

Dispersions for these studies were made using two different solvent conditions: 1) 200 ml deionized water, 20 g ceramic powder, and 4 drops (0.15 ml) of concentrated nitric acid, or 2) 100 ml deionized water, 100 ml 0.667 wt% polyvinyl alcohol solution, 20 g ceramic powder, and 4 drops (0.15 ml) of concentrated nitric acid (in both cases, the final slurry pH was 2-3). All dispersions were ultrasonically agitated at a power level of

100 W for 3 min in 250-ml polypropylene bottles. Two dispersions were made for each powder/solvent condition. One sample of each was set aside for 0.5 h after ultrasonic agitation; the other was diluted with 250 ml of filtered reagent-grade acetone (10-20- μ m glass frit), ultrasonically agitated at a power level of 100 W for 3 min in a 250-ml polypropylene bottle, and set aside for 0.5 h.

Results and Discussion

The particle-size distributions of the dispersions were then characterized using cumulant analysis on a photon correlation spectrometer (Coulter N4 Sub-Micron Particle Analyzer, Coulter Electronics, Inc., 600 20th St., Hialeah, FL 33010). Results are given in Table I (ceramic powder-water-acetone-polyvinyl alcohol mixes were not analyzed, as obvious

Table I. Photon Correlation Mean Particle Sizes for Ceramic Powders in Different Polymer-Solvent Environments.

Powder	Apparent Particle Size in:			
	Water	PVA Solution	Water + Acetone	PVA Solution + Acetone
	(nm)	(nm)	(nm)	
Sumitomo AKP-HP alumina	501	509	A	B
Toyo Soda TZ-O zirconia	283	253	415	B
Toyo Soda TZ-3Y zirconia-yttria	289	332	391	B

A: Measured particle size drifted slowly upward.

B: Particles were too large and settled too rapidly to be measured using the photon correlator.

phase separation and settling precluded the possibility of obtaining useful information).

Dispersions of the ceramic powders in polyvinyl alcohol solutions or in water/acetone mixes flocculated very slowly, if at all. Dispersions containing both polyvinyl alcohol and acetone flocculated and settled very rapidly. This rapid flocculation is certainly the result of synergistic interaction between the acetone and the polyvinyl alcohol, with some fraction of the polyvinyl alcohol attached to the powder particle surfaces.

FLOC TEXTURE STUDIES

Experimental Procedure

Polyvinyl alcohol solutions having the concentrations specified in Table II were prepared. Four hundred milliliters of each solution was acidified to pH 2-3 using eight drops (0.3 ml) of concentrated nitric acid. Varying amounts of powder, as given in Table II, were added, and the slurries were ultrasonically agitated at a power level of 100 W for 8 min

Table II. Qualitative Texture Data on Polymer-Powder Flocs.

Powder Content (g)	Polymer Solution Concentration (mg/l)		
	3333	1054	333
4	A	B	C
12.65	B	C	D
40	C	D	E

A: rubbery, dry product

B: rubbery product, with more retained liquid than A

C: cottage cheese-like product, with lots of retained liquid

D: somewhat fluid, yoghurt-like product

E: very fluid product

in a one-liter polypropylene bottle. The slurries were then flocculated with 500 ml of acetone, shaken vigorously for 10 s, and set aside for 15 min before being filtered through a 325-mesh screen. The samples were allowed to drain for 5 min before their textures were qualitatively characterized by visual inspection (Table II).

Results and Discussion

The results in Table II clearly show that the floc texture depends importantly on the ratio of powder to polymer in the slurries, being independent of the absolute loading levels of these materials, which is consistent with our expectations. The systems with a lot of polymer and little powder were rubbery, reflecting a continuous polymer phase extending through the flocculated sample. The systems with a lot of powder and little polymer were very fluid, reflecting local binding of powder particles and the absence of a continuous polymer phase.

The Ceramics Processing Research Laboratory has investigated the effect of pH on the polyvinyl alcohol content and texture of flocs resulting from the precipitation of dispersions containing either alumina or silica in polyvinyl alcohol solution by adding acetone.²⁸ Powders were dispersed in polyvinyl alcohol solutions having the same powder loading levels and differing only in pH. The texture of the flocs changed as the pH changed: when flocs had a high polymer content they were firm; when they had a low polymer content they were quite fluid.²⁹ Under pH conditions in which the polymer content of the powder flocs was low, large polymer flocs with a low powder content also formed. It seems clear to the present author that polymer adsorption plays a large role in the operation of this ceramic processing technique.

To show that the nonsolvent flocculation technique is applicable to nonaqueous systems, 400 ml of a 0.5 wt% solution of 93,300 MW poly(methyl methacrylate) (PMMA) in toluene was prepared. Thirty-two grams of Sumitomo AKP-HP alumina powder and 8 g of Toyo Soda TZ-O zirconia powder were added and ultrasonically agitated at high power (100 W, 20 kHz) for 8 min. The dispersion was allowed to equilibrate for 24 h. PMMA did not prove to be a particularly good steric stabilizer for alumina and zirconia in toluene; a dispersion marginally adequate for the purposes of this study was produced. Six hundred milliliters of hexane was added to flocculate the dispersion, and the resulting two-phase mixture was filtered through a 325-mesh screen. The flocs produced this way could be pressed into green bodies more readily than could those produced in an aqueous environment.

Poly(methyl methacrylate) adsorbs from benzene solutions to alumino-silicate surfaces³⁰; since the solubility parameters for n-heptane, benzene, and toluene are similar, adsorption of poly(methyl methacrylate) to alumina particle surfaces in toluene is also expected.

If a polar solvent is added to a dispersion of ceramic powder particles in a dilute polymer solution with a nonpolar solvent, the amount of adsorbed polymer can decrease and become negative.³⁰ Flocculation is a fast process; polymer desorption is slow. Rapidly adding a second solvent that adsorbs onto ceramic powder particle surfaces to a solvent-polymer-ceramic powder dispersion may cause powder-polymer flocs to precipitate before the polymer has time to desorb from the particle surfaces.

REVERSIBILITY OF PRECIPITATION

An alumina-20 wt% zirconia dispersion in 400 ml of a 0.333 wt% polyvinyl alcohol-0.167 wt% polyethylene glycol solution was pH-adjusted

with six drops (0.2 ml) of concentrated nitric acid (polyethylene glycol is a plasticizer for polyvinyl alcohol). The slurry was ultrasonically agitated at a power level of 100 W for 3 min in a one-liter polypropylene bottle. The particle size was then characterized using a photon correlation spectrometer. Next, the dispersion was flocculated with 500 ml of acetone and the resulting dispersion was filtered through a 325-mesh sieve. Two grams of the wet flocs collected on the sieve were removed and placed in a one-liter polypropylene bottle containing 400 ml of deionized water pH-adjusted with 6 drops (0.23 ml) of concentrated nitric acid. The slurry was then ultrasonically agitated at a power level of 100 W for 6 min. The particle size was then characterized using a photon correlation spectrometer. The difference in average particle size between the original dispersion and the dispersion formed from the ultrasonically agitated flocs was well within the experimental error of the technique, indicating that the flocculation process is completely reversible.

GENERAL DISCUSSION

The results of the experiments above correspond to the following physical picture, illustrated in Figure 3. When ceramic powder particles are dispersed in a dilute polymer solution, some portion of the polymer molecules adsorbs to the particle surfaces, leaving, in general, "loops" and "tails" dangling into the solution.³¹ The remaining polymer is present as dispersed molecules. When a nonsolvent for the polymer is added in large quantity, the energy of the polymer-polymer contacts becomes less than that of the polymer-solvent contacts. Pinning points form among the dispersed polymer molecules, as well as between the dispersed polymer molecules and molecules adsorbed on powder particle surfaces. If the

polymer and powder concentrations are appropriate, ceramic powder particles are immobilized in a gelatinous polymer matrix in this way.

CONCLUSIONS

Polyvinyl alcohol adsorbs onto alumina particle surfaces. The precipitation of alumina-polyvinyl alcohol flocs from polyvinyl alcohol solutions containing alumina powder by adding acetone requires polymer adsorption onto powder particle surfaces. Precipitation is brought about by the synergistic interaction of the polyvinyl alcohol with the acetone, and is fully reversible by improving the solvent quality (removing acetone). Floc texture is unrelated to the absolute loading levels of polymer and powder, but related to their ratio. The polymer-powder precipitation process is quite general, operating in both aqueous and nonaqueous systems, and including a variety of polymers and solvents.

REFERENCES

1. W.C. Moffatt and H.K. Bowen, "Composite Ceramic Production by Precipitation of Polymer Solutions Containing Ceramic Powder," J. Mat. Sci. Lett., 6 [4] 383-85 (1987).
2. W.C. Moffatt, P. White and H.K. Bowen, "Production of Alumina-Zirconia Composite Ceramics by Nonsolvent Flocculation of Polymer-Containing Powder Dispersions"; pp. 645-53 in Ceramic Transactions: Ceramic Powder Science II, the Proceedings of the First International Conference on Ceramic Powder Processing Science (Orlando, FL, November 1-4, 1987).
3. P.J. Flory, Principles of Polymer Chemistry; pp. 541-94. Cornell University Press, Ithaca, NY, 1953.
4. H. Tompa, Polymer Solutions. Academic Press, New York, 1956.
5. M. Komatsu, T. Inoue, and K. Miyasaka, "Light Scattering Studies on the Sol-Gel Transition in Aqueous Solutions of Polyvinyl Alcohol," J. Polymer Sci. B, 24 [2] 303-11 (1986).
6. J.G. Pritchard, Polyvinyl Alcohol. MacDonald, London, 1975.
7. T. Kawai, "Freezing Point Depression of Polymer Solutions and Gels," J. Polymer Sci., 32, 425-44 (1958).

8. H. Beltman and J. Lyklema, "Rheological Monitoring of the Formation of Polyvinyl Alcohol-Congo Red Gels"; pp. 92-100 in Faraday Discussions of the Chemical Society No. 57: Gels and Gelling Processes. The Chemical Society, London, 1975.
9. M.M. Zwick, J.A. Duizer, and C. van Bochove, "Phase Separation Spinning of Polyvinyl Alcohol Fibers"; pp. 188-207 in Properties and Applications of Polyvinyl Alcohol. Edited by W.R.A.D. Moore and C.A. Finch. Society of Chemical Industry, London, 1968.
10. Th.F. Tadros, "Adsorption of Polyvinyl Alcohol on Silica at Various pH Values and Its Effect on the Flocculation of the Dispersion," J. Colloid Interface Sci., 64 [1] 36-47 (1978).
11. B.E. Platonov, A.G. Bratunets, F.D. Ovcharenko, and T.A. Polishchuk, "NMR Study of Adsorption of Polyvinyl Alcohol on the Surface of Aluminum Oxide," Kolloidn. Zh., 44 [2] 360-62 (1982).
12. B.E. Platonov, A.A. Baran, and T.A. Polishchuk, "Adsorption of Polyvinyl Alcohol and Its Effect on the Electrosurface Characteristics of Some Oxides," Acta Phys. Chem., 25 [3-4] 201-08 (1979).
13. S. Chibowski and J. Szczypa, "Studies on the Mechanism of Polyvinyl Alcohol Adsorption on Titanium Dioxide Surface," Pol. J. Chem., 58 [10-12] 1155-60 (1984).
14. B.E. Platonov, T.A. Polishchuk, and V.M. Kalyuzhnyi, "Studies in the Adsorption of Polyvinyl Alcohol on the Surface of Metal Oxides by Multiple Attenuated Total Internal Reflection (MATIR)," Dopov. Akad. Nauk Ukr. RSR. Ser. B: Geol. Khim. Biol. Nauki, 11, 41-44 (1981).
15. B.E. Platonov, "Adsorption of Polyvinyl Alcohol from Aqueous Solutions on the Surface of Inorganic Oxides," Adsorbts. Adsorbenty, 9, 71-76 (1981).
16. B.E. Platonov and T.A. Polishchuk, "Zinc Oxide-Aqueous Polyvinyl Alcohol Solution Interface," Kolloidn. Zh., 41 [6] 1141-45 (1979).
17. A.P. Il'in, Yu.G. Shirokov, and V.A. Smirnov, "Adsorption of Carboxymethylcellulose and Polyvinyl Alcohol on Metal Oxides," Izv. Vyssh. Uchebn. Zaved. Khim. Khim. Tekhnol., 25 [4] 452-55 (1982).
18. G. Christakos, U. Hofmann, B. Weick, and G. Joppien, "Steric Stabilization and Flocculation of Aqueous Titania and Silica Suspensions by Adsorbed Polymer Layers," Ber. Bunsen-Ges. Phys. Chem., 88 [11] 1067-70 (1984).
19. B.V. Kavanagh, A.M. Posner, and J.P. Quirk, "Effect of Polymer Adsorption on the Properties of the Electric Double Layer"; pp. 242-49 in Faraday Discussions of the Chemical Society No. 59: Physical Adsorption in Condensed Phases. The Chemical Society, London, 1975.

20. Th.F. Tadros, The Effect of Polymers on Dispersion Properties; pp. 1-80, 207-20. Academic Press, London, 1981.
21. D.H. Napper, Polymeric Stabilization of Colloid Dispersions; pp. 197-213, 332-72. Academic Press, New York, 1983.
22. R.K. Iler, "Coacervates of Polyvinyl Alcohol and Colloidal Silica," J. Colloid Interface Sci., 51 [3] 388-93 (1975).
23. E. Gruber, B. Soehendra, and J. Schurz, "Ordering in Solutions of Polyvinyl Alcohol in Water as Detected by Light Scattering," J. Polymer Sci., Symposium No. 44, 105-17 (1974).
24. N.K. Kolnibolotchuk, V.J. Klenin, and S.Ya. Frenkel, "Formation of Supermolecular Order in Aqueous Solutions of Polyvinyl Alcohol," J. Polymer Sci., Symposium No. 44, 119-29 (1974).
25. V.J. Klenin, O.V. Klenina, B.I. Shvartsburd, and S.Ya. Frenkel, "Thermodynamic Nature of Supermolecular Order in the Aqueous Solutions of Polyvinyl Alcohol," J. Polymer Sci., Symposium No. 44, 131-40 (1974).
26. Th.F. Tadros, "The Adsorption of Cetyltrimethylammonium Bromide and Dodecylbenzene Sulfonate with Polyvinyl Alcohol. Adsorption of the Polymer-Surfactant Complexes on Silica," J. Colloid Interface Sci., 46 [3] 528-40 (1974).
27. E.A. Derkach and T.V. Gutsol, "Effect of Molecular Weight of Polyvinyl Alcohol on Adsorption from Solutions"; pp. 55-60 in Fiz. Khim. Polim. Kompozitsii. Edited by Yu.S. Lipatov. Naukova Dumka, Kiev, 1974.
28. J.R. Kelly, "Effect of pH on the Precipitation of Dilute PVA Solutions Containing Ceramic Powders," CPRL Report #R11, MIT, pp. 114-18 (1987).
29. J.R. Kelly, unpublished observations (1987).
30. V.M. Patel, K.C. Patel, and R.D. Patel, "Adsorption of Poly(methyl Methacrylate) from Binary Solvent Systems," Angew. Makromol. Chem., 62 [1] 177-85 (1977).
31. G.J. Fleer and J. Lyklema, "Adsorption of Polymers"; pp. 153-220 in Adsorption from Solution at the Liquid/Solid Interface, Chapt. 4. Edited by G.D. Parfitt and C.H. Rochester. Academic Press, New York, 1983.

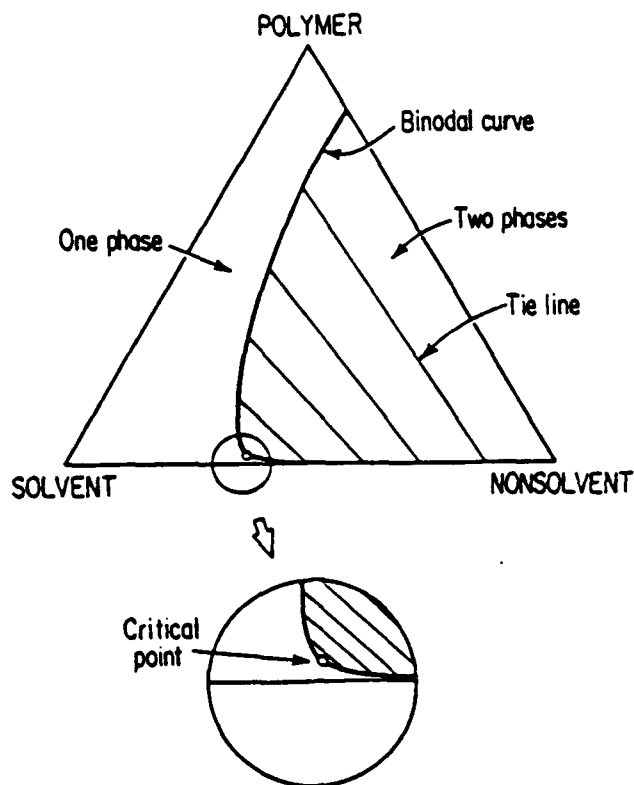


Figure 1. Polymer-solvent-nonsolvent ternary phase diagram.

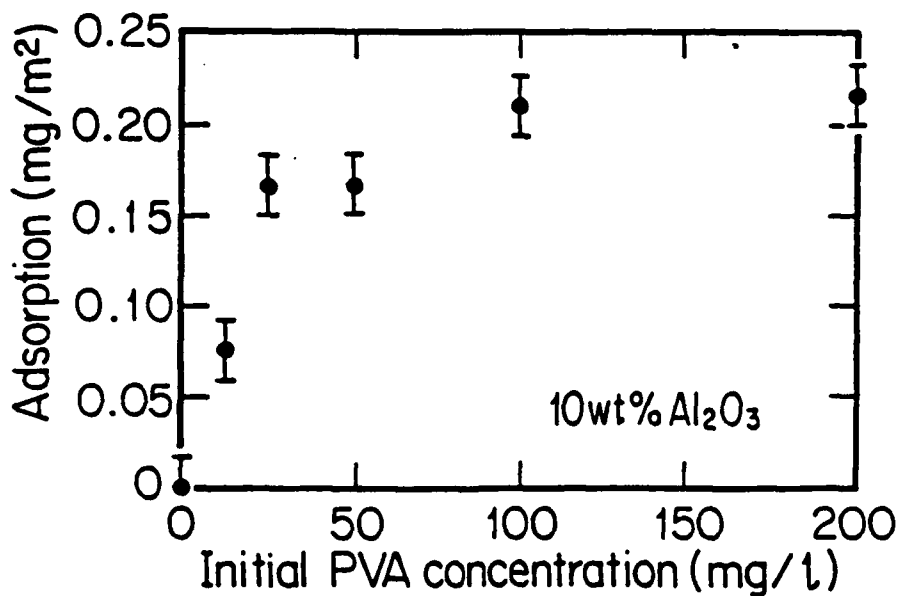
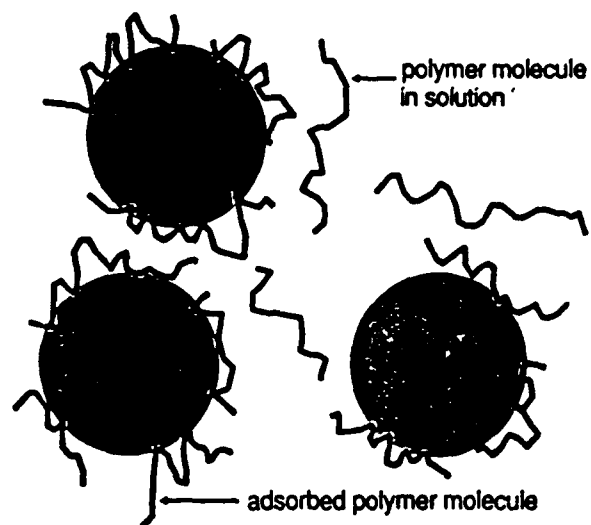
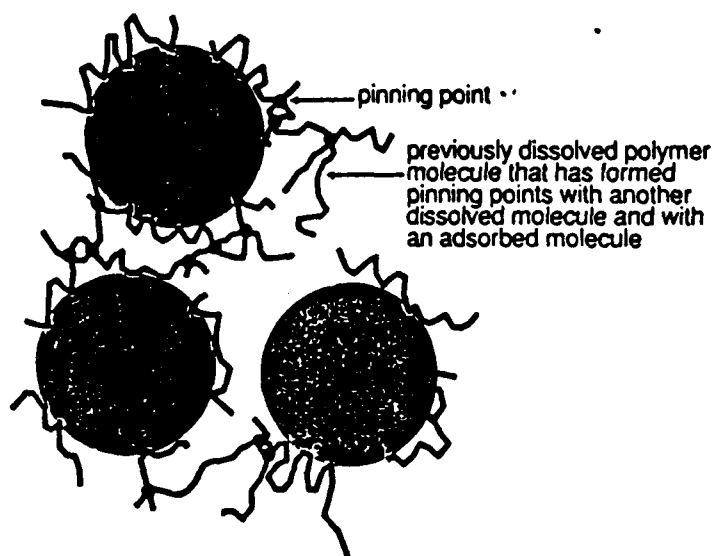


Figure 2. Adsorption of polyvinyl alcohol on alumina as a function of initial concentration of polymer in aqueous solution.



(a)



(b)

Figure 3. Schematic of nonsolvent flocculation process a) before nonsolvent addition and b) after nonsolvent addition.

THERMAL PROCESSING AND PROPERTIES OF HIGHLY HOMOGENEOUS ALUMINA-ZIRCONIA COMPOSITE CERAMICS

William C. Moffatt

ABSTRACT

Alumina-zirconia composites were made using a novel processing technique involving nonsolvent precipitation of a dilute polymer solution containing dispersed ceramic powder particles.

Seven identical alumina-nominally 15 wt% zirconia composite green bodies were fired at different temperatures. An optimal firing temperature of 1500°C was found, above and below which sample fracture strengths, densities, and tetragonal zirconia contents were lower. Fracture strengths correlated well with porosity.

An alumina-14.06 wt% (zirconia-1.35 mol% yttria) composite had excellent resistance to abnormal grain growth upon high-temperature annealing. The tetragonal zirconia content increased with increasing annealing time; this was attributed to the equilibration of zirconia particles with widely varying yttria concentrations.

1. INTRODUCTION

Many studies of the processing of composite materials have had the goal of uniformly distributing second-phase particles in a matrix material. This is because uniform particle distribution is thought to lead to better properties and higher reliability than would be achieved with less uniform distribution.

Various paths have been taken to produce composite ceramics in the past. Techniques used in the alumina-zirconia system, in particular, have included the milling of powders in air, water, or other liquids [1-7], oxidation or decomposition of soluble, often organic, ceramic precursors [1,8-11], heterocoagulation of sols [12], and the high-shear mixing of flocced sols [13]. Some powders have been consolidated wet, using slip casting [13,14] or centrifugal casting [12]; others have been consolidated dry [1,3-8,11], often by hot pressing [1,6-8]. Consolidation techniques have

generally not been well integrated with powder production or mixing techniques.

A rapid, flexible technique for producing uniform composite ceramics has been developed at the Ceramics Processing Research Laboratory, based on nonsolvent precipitation of dilute polymer solutions containing co-dispersions of ceramic powders. Preliminary results for the alumina-zirconia system are given in Reference 15. The effects of varying the zirconia content and zirconia phase chemistry of alumina-zirconia composites produced in this way on the composites' mechanical properties are described in Reference 16.

This paper describes the effects of variations in the thermal processing of alumina-zirconia composites produced using this nonsolvent precipitation technique on their microstructures, phase structures, and mechanical properties. The paper is divided into two parts, the first of which details the effects of variations in firing temperature on the properties of a series of identical green bodies. The second part details the effects of high-temperature anneals of varying duration on the properties of a fired body.

2. EXPERIMENTAL

2.1. Specimen Production and Characterization

Alumina-zirconia composite ceramics were made in the following way. A 0.333 wt% water solution of polyvinyl alcohol (MW=14,000, Aldrich Chemical Co., Milwaukee, WI) was filtered through a 10-20- μm glass frit. Four hundred milliliters of the filtered solution was poured into a one-liter polypropylene bottle under a laminar-flow hood. Forty grams of an appropriate mixture of alumina (Sumitomo AKP-HP, Sumitomo Chemical America, New York, NY), zirconia (Toyo Soda TZ-O, Toyo Soda USA, Atlanta, GA), and

zirconia-yttria (Toyo Soda TZ-3Y) powders was then added. The bottle's contents were adjusted to pH 2-3 with 0.3 ml of concentrated nitric acid, and ultrasonically agitated (Model W-220F Sonicator Cell Disruptor, Heat Systems Ultrasonics, Inc., Farmingdale, NY) at high power (100 W) for 8 min. This agitation significantly warmed the slurry. The bottle containing the slurry was resealed, and the contents were allowed to gravitationally settle for 24 h.

The middle 300 ml of the supernatant was removed using a cannulation procedure at a rate of about 5 ml/s. Filtered air (0.1- μm filter) was used as the cover gas during cannulation. The cannulated supernatant was homogenized before further use. It was then flocculated with 375 ml of filtered reagent-grade acetone. The flocculated slurry was allowed to stand for 15 min, and was then poured onto a 100-mesh stainless steel screen.

The retained flocs were scooped into a colloid press (Fig. 1), where they were consolidated at a pressure of 35 MPa over a period of 15-30 min. The sample was held in the press for 30 min after the press came to equilibrium, then was ejected from the press, dried at 60-80°C in laboratory air, and cold isostatically pressed at 280 MPa. The green density was typically 57-58% of theoretical, and the volume of the green body was typically 15% of the volume of the flocs from which it was pressed. Binder burnout and bisque firing were accomplished by ramping the specimen at 2°C/min from room temperature to 600°C and at 5°C/min from 600°C to 1200°C. A flow chart of this processing route is given in Fig. 2.

Some fired samples were machined into 2 mm x 1.5 mm x 25 mm bend specimens, which were mechanically tested using a four-point jig having an

inner span of 10 mm and an outer span of 20 mm. The crosshead displacement rate was 0.025 cm/min (stress rate -50 MPa/s). Weibull plots and probability of failure-fracture strength plots were constructed from the fracture data. Fracture toughnesses of the specimens were determined for polished surfaces using the microindentation technique described by Evans and Charles [17]. Surface-grinding alumina-zirconia composite ceramics can result in residual compressive surface stresses as high as 1 GPa [18], which can interfere with fracture toughness determinations [19-21]. The normal grinding and polishing stresses in this study were kept to <50 kPa to minimize surface damage, and an indentation load of 10 kg was applied to ensure fully developed cracks. Indentations were made using a Vickers diamond pyramid indenter attached to an Instron machine, with an indenter displacement rate of 0.005 cm/min and a hold time after loading of 1 min; the load typically relaxed less than 10% during the hold period. Five indents were made on each sample. The tetragonal zirconia fractions were determined from x-ray diffraction analysis, which involved the relative monoclinic and tetragonal phase integrated x-ray peak areas [22] as determined from samples with polished surfaces. Chemical analyses of the specimens were obtained using a Hitachi S-530 Scanning Electron Microscope (Hitachi Scientific Instruments, Nissei Sangyo America, Rockville, MD) fitted with an EG&G ORTEC Model 7938-4ST Si(Li) X-Ray Detector, and EG&G ORTEC System 5000 spectral analysis software (EG&G Ortec, Inc., Oak Ridge, TN).

2.2. Effect of Thermal History on Properties

Seven billets containing 14.98 wt% zirconia were produced using the procedure described above. These were fired in vacuum for 2 h at 1300, 1350, 1400, 1450, 1500, 1550, and 1600°C, respectively. Ten bend bars were

W. Moffatt AFOSR/1988 $\text{Al}_2\text{O}_3\text{-ZrO}_2$: THERMAL PROCESSING, PROPERTIES
machined from each of the fired specimens. The fracture strengths,
indentation fracture toughnesses, and tetragonal zirconia fractions were
determined as described above.

Weibull plots of the specimens tested are shown in Fig. 3a for the
fired billets; probability of failure/fracture strength plots for the same
billets are shown in Fig. 3b. Fig. 4 shows the average fracture
strengths and Weibull moduli for the samples tested. The fracture
strengths are quite high for alumina-zirconia composites produced without
hot-pressing. The maximum in Fig. 4 may be interpreted as follows: below
 1500°C the specimens are probably not fully densified; above 1500°C rapid
grain growth may stop sintering short of theoretical density.

The fracture strengths, Weibull moduli, fracture toughnesses, and
tetragonal zirconia fractions of these specimens are reported in Table I.

Table I. Properties of $\text{Al}_2\text{O}_3\text{-14.98 wt\% ZrO}_2$ Composites Fired at Various
Temperatures.

Firing Temperature ($^\circ\text{C}$)	Fracture Strength (MPa)	Weibull Modulus	Fracture Toughness ($\text{MPa}\cdot\text{m}^{1/2}$)	Tetragonal Zirconia Fraction
1300	508(10)*	9.1	----	0.21 ± 0.02
1350	734(10)	9.0	$5.02 \pm 0.09(5)^{**}$	0.38 ± 0.04
1400	860(10)	8.2	$4.98 \pm 0.13(5)$	0.49 ± 0.05
1450	943(10)	7.7	$5.13 \pm 0.20(5)$	0.46 ± 0.05
1500	1048(10)	15.8	$4.69 \pm 0.16(5)$	0.58 ± 0.06
1550	939(10)	8.1	$5.19 \pm 0.25(5)$	0.58 ± 0.06
1600	838(10)	8.5	$4.92 \pm 0.15(5)$	0.49 ± 0.05

*Numbers in parentheses indicate the number of bend bars tested.

**Numbers in parentheses indicate the number of indents made.

No fracture toughness determination could be made for the sample fired at 1300°C because the cracks at the corners of the microindentations were too diffuse to be easily measured in this low-density material. The tetragonal zirconia fraction was found to increase with sample density. Tetragonal zirconia particles close to or in contact with pores in the sample will be less constrained than particles surrounded by a dense alumina matrix and will thus transform more readily upon cooling or machining. At high temperatures, zirconia phase coarsening may lead to increased monoclinic zirconia content.

Figs. 5a-g show scanning electron fractographs of samples sintered at selected temperatures ranging from 1300°C to 1600°C . A scanning electron micrograph of a polished section of the material in Fig. 5e is shown in Fig. 6. It is clear from these figures that fine zirconia particles are located at grain corners, and that the distribution of these particles is very homogeneous. The effect of variations in fired sample density on the fracture strengths of the materials in this series is shown in Fig. 7. Samples fired both above and below the optimal firing temperature are seen to have the same dependence of fracture strength on fired density. The sharp rise in strength at high fired densities is consistent with the reported exponential dependence of the fracture strength of alumina on porosity [23]. A semilogarithmic plot of fracture strength versus porosity is shown in Fig. 8. The least squares data fit to the points given has a slope of -3.56, well within the range of values reported in the literature for pure alumina [24-26]. The strengths seen here are, however, substantially higher than those found in the studies on alumina. This may be due to the small grain size of the alumina-zirconia

W. Moffatt AFOSR/1988 $\text{Al}_2\text{O}_3\text{-ZrO}_2$: THERMAL PROCESSING, PROPERTIES
composites. It seems that the dependence of fracture strength on porosity
arises from largely material-independent geometrical considerations.

2.3. Effect of High-Temperature Annealing on Properties

An alumina-14.06 wt% (zirconia-1.35 mol% yttria) sample was made using the defect-resistant processing technique. The green body was broken into five pieces, which were then prefired as described above and fired for 2 h at 1500°C under vacuum. The pieces were subsequently annealed at 1600°C for 0, 1, 3, 9, and 27 h, respectively. The fracture toughnesses and tetragonal zirconia fractions, determined as described above, are reported in Table II. Scanning electron micrographs of polished sections of these specimens are shown in Figs. 9a-e. The microstructures were highly resistant to exaggerated grain growth and grain boundary breakaway from second-phase particles upon high-temperature annealing.

Table II. Properties of Al_2O_3 -14.06 wt% (ZrO_2 -1.35 mol% yttria)
Composites Annealed at Elevated Temperature.

Hours at 1600°C	Fracture Toughness ($\text{MPa}\cdot\text{m}^{1/2}$)	Tetragonal Zirconia Fraction
0	$4.98 \pm 0.20(5)^*$	-----
1	$4.98 \pm 0.09(5)$	0.35 ± 0.04
3	$5.05 \pm 0.16(5)$	0.39 ± 0.04
9	$5.04 \pm 0.08(5)$	0.57 ± 0.06
27	$5.55 \pm 0.25(5)$	0.85 ± 0.09

* Numbers in parentheses indicate the number of indents made.

The intermediate yttria content of this alumina-zirconia-yttria composite ceramic was achieved using a mixture of two zirconia powders: one

with no yttria, the other with a high yttria content. As a result of this processing approach, the yttria content of the individual zirconia particles could be expected to vary between the two extremes of 0.0 mol% yttria and 3.0 mol% yttria. Only the high-yttria zirconia particles are expected to retain the tetragonal structure upon cooling from the sintering temperature to room temperature. High-temperature annealing would cause the yttria in high-yttria/zirconia particles to diffuse to low-yttria/zirconia particles. In addition, grain growth in the alumina matrix would bring about zirconia particle impingement and coalescence. An increase in the volume fraction of zirconia particles containing enough yttria to resist transformation to the monoclinic structure upon cooling to room temperature is thus expected. This is consistent with the tetragonal zirconia fractions found experimentally after high-temperature anneals of various lengths.

3. CONCLUSIONS

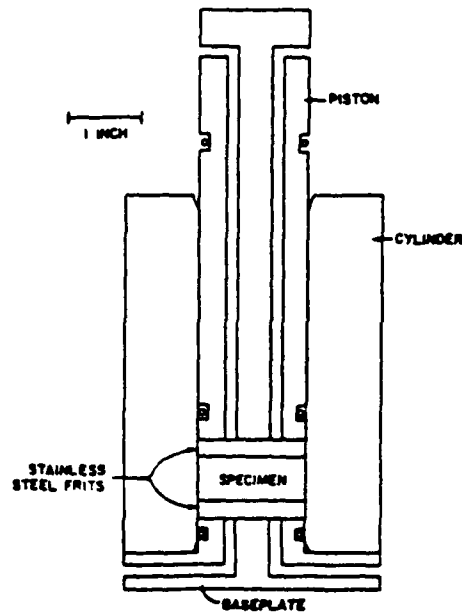
When alumina-15 wt% zirconia composites processed as described above were fired at different temperatures, an optimal firing temperature of 1500°C was found. Fracture strengths, densities, and tetragonal zirconia contents were lower both above and below this temperature. Fracture strengths correlated well with porosity.

An alumina-14.06 wt% (zirconia-1.35 mol% yttria) composite processed as described above had excellent resistance to abnormal grain growth upon high-temperature annealing. The tetragonal zirconia content increased with increasing annealing time; this was attributed to the equilibration of zirconia particles with widely varying yttria concentrations.

REFERENCES

1. A.H. HEUER, N. CLAUSSEN, W.M. KRIVEN, and M. RÜHLE, "Stability of Tetragonal ZrO₂ Particles in Ceramic Matrices," J. Am. Ceram. Soc., 65 [12] 642-50 (1982).
2. N. CLAUSSEN, "Fracture Toughness of Al₂O₃ with an Unstabilized ZrO₂ Dispersed Phase," J. Am. Ceram. Soc., 59 [1-2] 49-51 (1976).
3. N. CLAUSSEN, R.L. COX, and J.S. WALLACE, "Slow Growth of Microcracks: Evidence for One Type of ZrO₂ Toughening," J. Am. Ceram. Soc., 65 [11] C190-C191 (1982).
4. E.P. BUTLER and A.H. HEUER, "X-Ray Microanalysis of ZrO₂ Particles in ZrO₂-Toughened Al₂O₃," J. Am. Ceram. Soc., 65 [12] C206-C207 (1982).
5. D.R. CLARKE and F. ADAR, "Measurement of the Crystallographically Transformed Zone Produced by Fracture in Ceramics Containing Tetragonal Zirconia," J. Am. Ceram. Soc., 65 [6] 284-88 (1982).
6. M.V. SWAIN and N. CLAUSSEN, "Comparison of K_{IC} Values for Al₂O₃-ZrO₂ Composites Obtained from Notched-Beam and Indentation Strength Techniques," J. Am. Ceram. Soc., 66 [2] C27-C29 (1983).
7. H. RUF and A.G. EVANS, "Toughening by Monoclinic Zirconia," J. Am. Ceram. Soc., 66 [5] 328-32 (1983).
8. P.F. BECHER, "Transient Thermal Stress Behavior in ZrO₂-Toughened Al₂O₃," J. Am. Ceram. Soc., 64 [1] 37-39 (1981).
9. M. KAGAWA, M. KIKUCHI, Y. SYONO, and T. NAGAE, "Stability of Ultrafine Tetragonal ZrO₂ Co-Precipitated with Al₂O₃ by the Spray-ICP Technique," J. Am. Ceram. Soc., 66 [11] 751-54 (1983).
10. D.W. SPROSON and G.L. MESSING, "Preparation of Alumina-Zirconia Powders by Evaporative Decomposition of Solutions," J. Am. Ceram. Soc., 67 [5] C92-C93 (1984).
11. B. FEGLEY, JR., P. WHITE, and H.K. BOWEN, "Preparation of Zirconia-Alumina Powders by Zirconium Alkoxide Hydrolysis," J. Am. Ceram. Soc., 68 [2] C60-C62 (1985).
12. F.F. LANGE and M.M. HIRLINGER, "Hindrance of Grain Growth in Al₂O₃ by ZrO₂ Inclusions," J. Am. Ceram. Soc., 67 [3] 164-68 (1984).
13. E. CARLSTROM and F.F. LANGE, "Mixing of Flocced Suspensions," J. Am. Ceram. Soc., 67 [8] C169-C170 (1984).
14. I.A. AKSAY, F.F. LANGE, and B.I. DAVIS, "Uniformity of Al₂O₃-ZrO₂ Composites by Colloidal Filtration," J. Am. Ceram. Soc., 66 [10] C190-C192 (1983).

15. W.C. MOFFATT and H.K. BOWEN, "Composite Ceramic Production by Precipitation of Polymer Solutions Containing Ceramic Powder," J. Mat. Sci. Lett., 6 [4] 383 (1987).
16. W.C. MOFFATT, P. WHITE, and H.K. BOWEN, "Production of Alumina-Zirconia Composite Ceramics by Nonsolvent Flocculation of Polymer-Containing Powder Dispersions"; pp. 645-53 in Ceramic Transactions: Ceramic Powder Science II, the Proceedings of the 1st International Conference on Ceramic Powder Processing Science (Orlando, Florida, November 1-4, 1987). Edited by G.L. Messing, E.R. Fuller, and H. Hausner. The American Ceramic Society, Westerville, OH (1988).
17. A.G. EVANS and E.A. CHARLES, "Fracture Toughness Determinations by Indentation," J. Am. Ceram. Soc., 59 [7-8] 371-72 (1976).
18. D.J. GREEN, F.F. LANGE, and M.R. JAMES, "Factors Influencing Residual Surface Stresses Due to a Stress-Induced Transformation," J. Am. Ceram. Soc., 66 [9] 623-29 (1983).
19. Y. IKUMA and A.V. VIRKAR, "Crack-Size Dependence of Fracture Toughness in Transformation-Toughened Ceramics," J. Mat. Sci., 19 [7] 2233-38 (1984).
20. D.J. GREEN, "Comments on 'Crack Size Dependence of Fracture Toughness in Transformation Toughened Ceramics'," J. Mat. Sci., 20 [11] 4239-41 (1985).
21. Y. IKUMA and A.V. VIRKAR, "Reply to 'Comments on 'Crack Size Dependence of Fracture Toughness in Transformation Toughened Ceramics'''," J. Mat. Sci., 20 [11] 4241-44 (1985).
22. H. TORAYA, M. YOSHIMA, and S. SOMIYA, "Calibration Curve for Quantitative Analysis of the Monoclinic-Tetragonal ZrO_2 System by X-Ray Diffraction," J. Am. Ceram. Soc., 67 [6] C119-C121 (1984).
23. E. DÖRRE and H. HÜBNER, Alumina. Springer-Verlag, New York, 1984.
24. R.L. COBLE and W.D. KINGERY, "Effect of Porosity on Physical Properties of Sintered Alumina," J. Am. Ceram. Soc., 39 [11] 377-85 (1956).
25. A.G. EVANS and G. TAPPIN, "Effects of Microstructure on the Stress to Propagate Inherent Flaws," Proc. Brit. Ceram. Soc., 20, 275-79 (1972).
26. B.R. STEELE, F. RIGBY, and M.C. HESKETH, "Investigations on the Modulus of Rupture of Sintered Alumina Bodies," Proc. Brit. Ceram. Soc., 6, 83-94 (1966).



BRASS COLLOID PRESS

Figure 1. Fritted press.

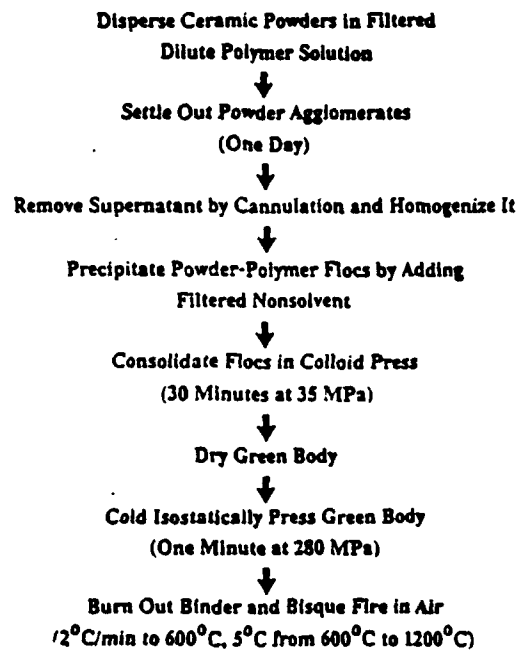
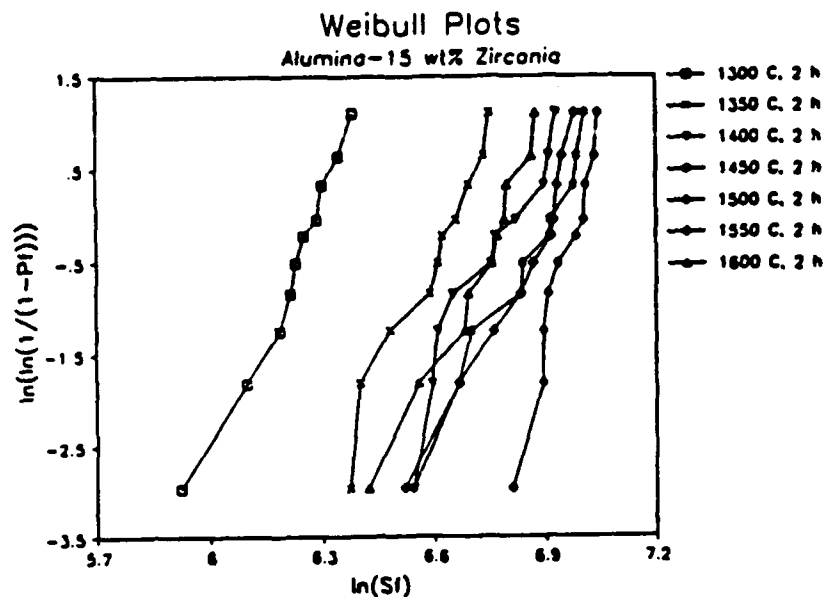
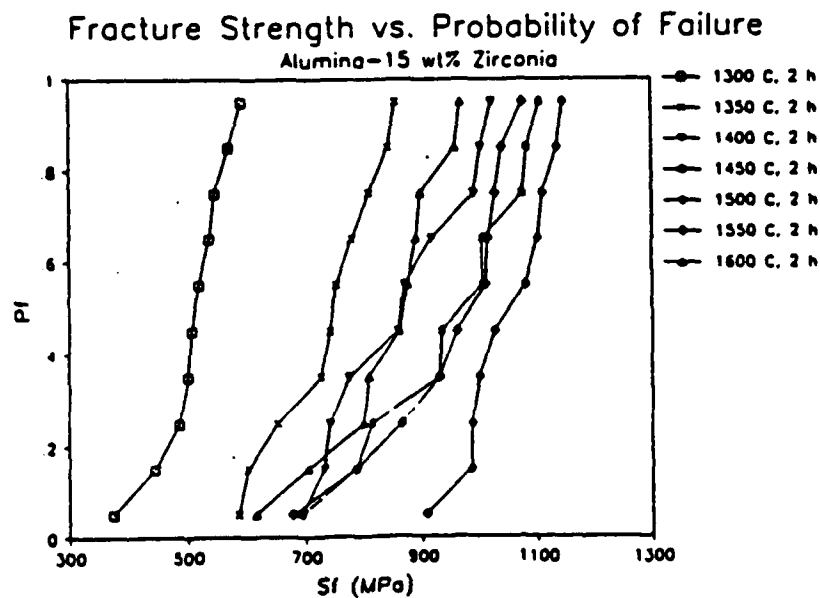


Figure 2. Flow chart of defect-resistant processing technique.



(a)



(b)

Figure 3. Alumina-nominally 15.0 wt% zirconia composites fired at various temperatures: a) Weibull plots and b) probability of failure/fracture strength plots.

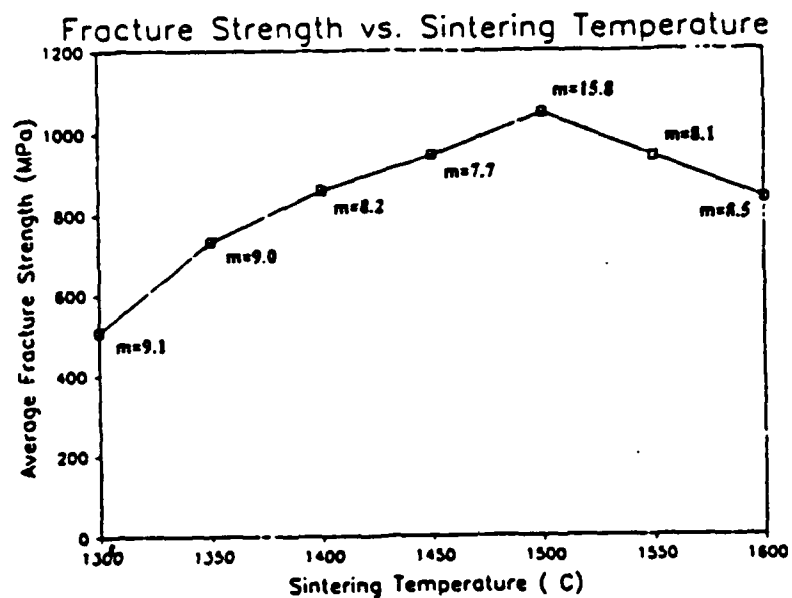
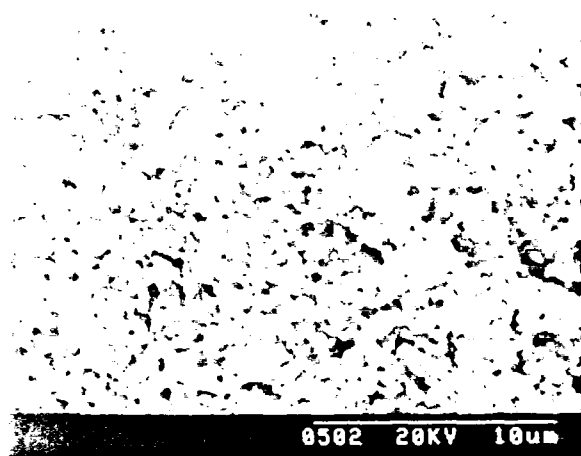


Figure 4. Average fracture strength vs sintering temperature for alumina-nominally 15.0 wt% zirconia samples (m = Weibull modulus).



(a)



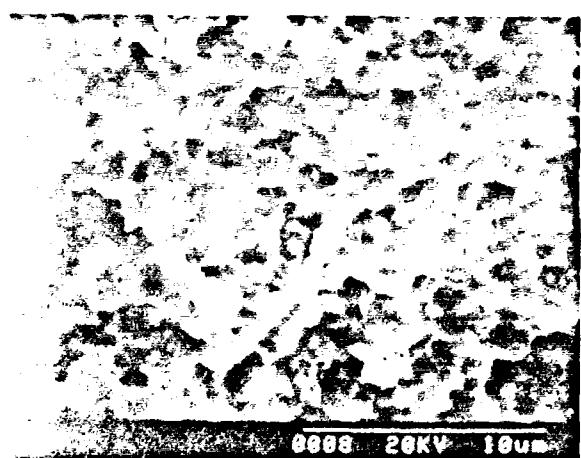
(b)



(c)



(d)

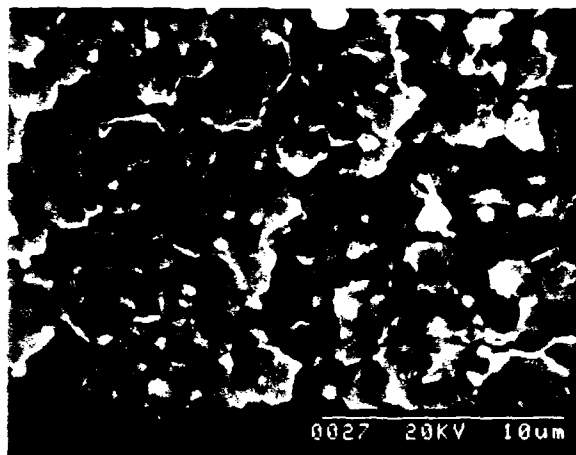


(e)



(f)

Figure 5. Scanning electron micrographs of the surface of $\text{Al}_2\text{O}_3\text{-ZrO}_2$ after thermal processing at 1500°C for 10 hours. The images show the granular morphology of the material.



(g)

Figure 5 (cont'd). Scanning electron fractograph of an alumina-nominally 15.0 wt% zirconia sample fired in vacuum at g) 1600°C.

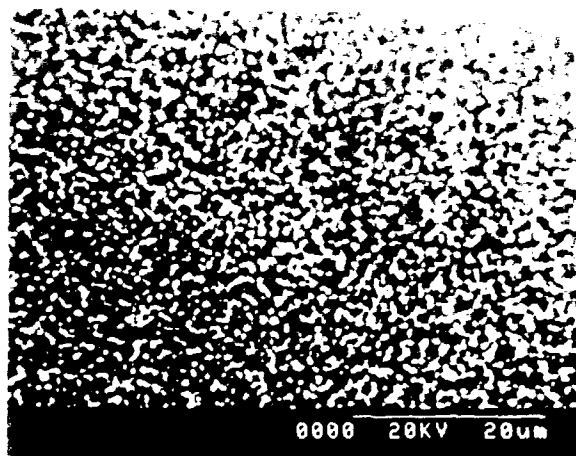


Figure 6. Scanning electron micrograph of a polished section of an alumina-nominally 15.0 wt% zirconia sample fired at 1500°C in vacuum.

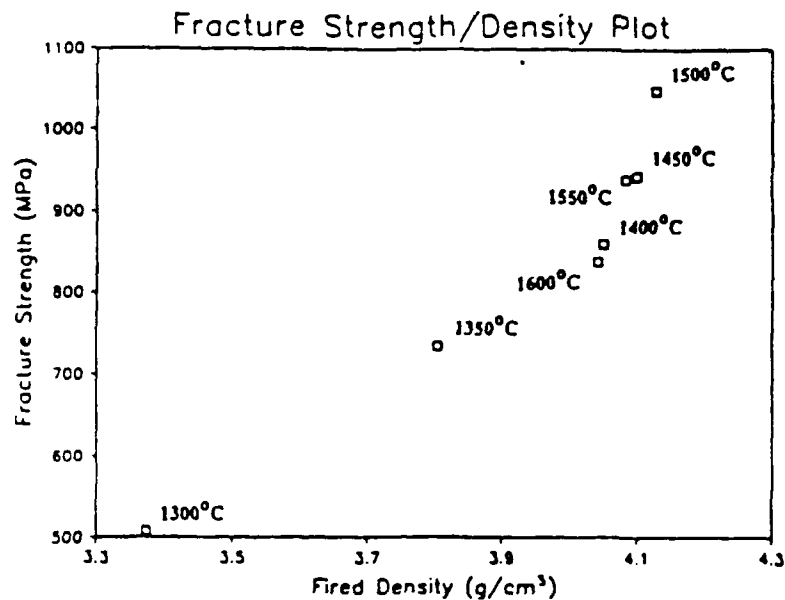


Figure 7. Dependence of fracture strength on density for alumina-nominally 15.0 wt% zirconia composites.

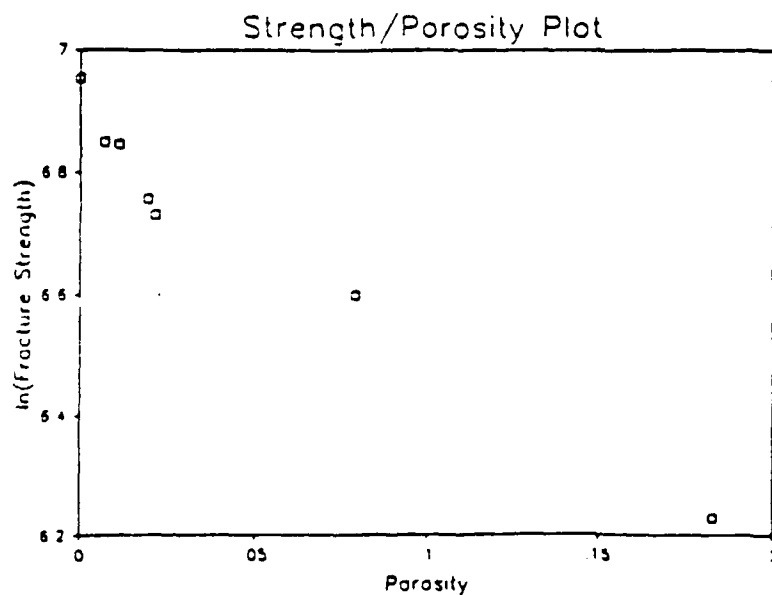


Figure 8. Dependence of fracture strength on porosity for alumina-nominally 15.0 wt% zirconia composites.

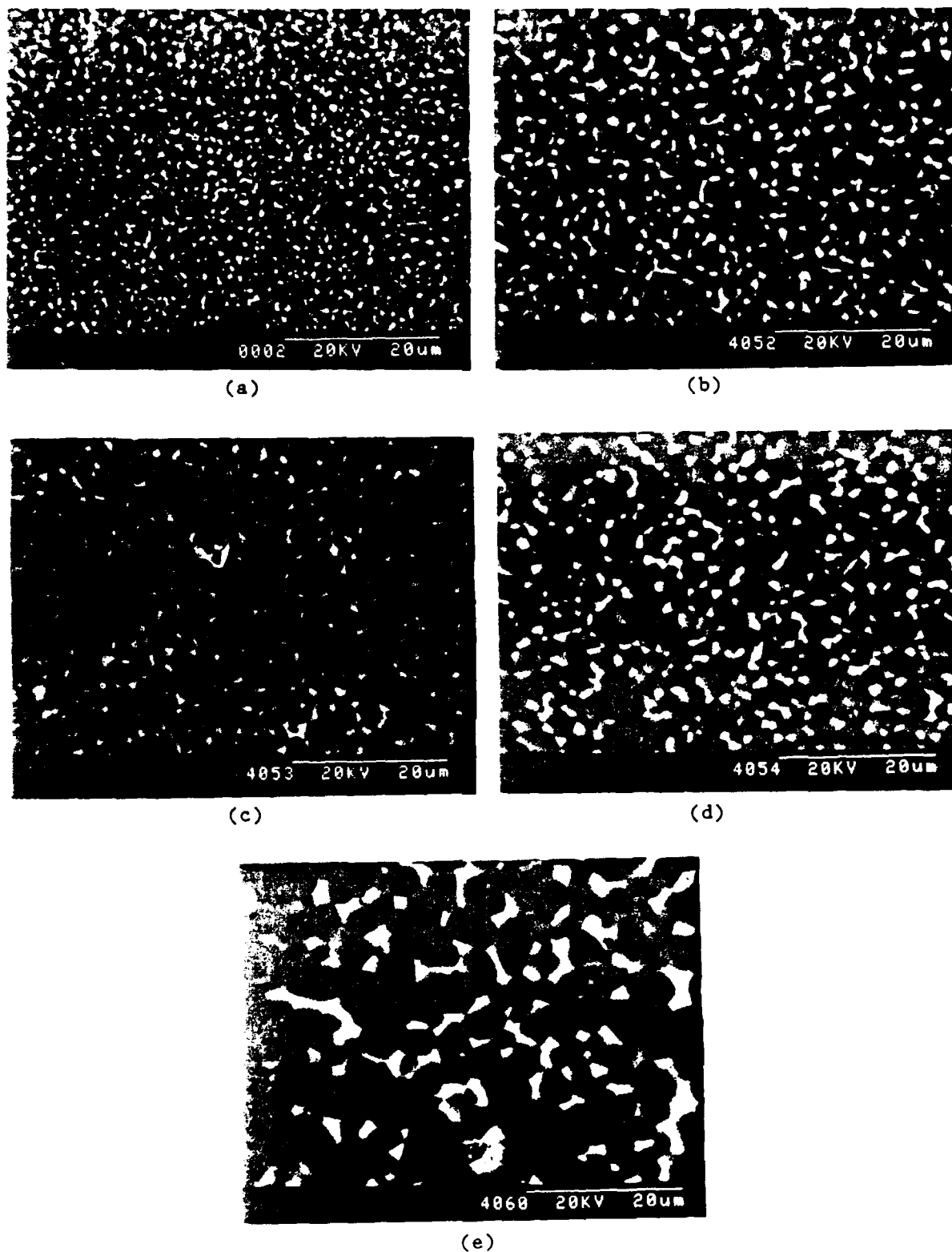


Figure 9. Scanning electron micrographs of a polished surface of an alumina-14.06 wt% zirconia-1.35 mol% yttria sample fired at 1500°C (a) and annealed at 1600°C for b) 1 h, c) 3 h, d) 9 h, or e) 27 h.

PROCESSING AND MICROSTRUCTURAL CONTROL OF Al_2O_3 - Al_2TiO_5 - TiO_2 COMPOSITES
FORMED BY CYCLIC ANNEALING

Sumio Kamiya

ABSTRACT

Flocculation and cyclic annealing were studied as possible means for processing and controlling the microstructure of Al_2O_3 - TiO_2 composites. Homogeneous green bodies were obtained by colloid-pressing flocs composed of polyvinyl alcohol (PVA) and ceramic powders. Sintered materials, which contained Al_2O_3 and Al_2TiO_5 , cracked due to the large thermal anisotropy of Al_2TiO_5 , but the cracks were completely eliminated by annealing. The densities of the materials decreased during annealing due to the volume shrinkage resulting from Al_2TiO_5 decomposition; a reheating treatment was necessary to increase the densities of the annealed materials. A combination of cyclic annealing and the reheating treatment gave various interesting microstructures of Al_2O_3 composites interspersed with Al_2TiO_5 and TiO_2 , suggesting that this process could create composites with unique mechanical properties.

INTRODUCTION

Although aluminum titanate (Al_2TiO_5) can be produced with a low thermal expansion coefficient, its practical application to structural materials remains uncertain because of its low mechanical strength. The low thermal expansion coefficient and low strength both result from grain-boundary microcracking due to the large thermal anisotropy of Al_2TiO_5 crystals (1).

Another characteristic of this material, generally considered a problem, is its decomposition to Al_2O_3 and TiO_2 (rutile) below -1200°C (2). In the present study, this characteristic is effectively used in the microstructural control of Al_2O_3 - TiO_2 composites: If a material containing Al_2O_3 and Al_2TiO_5 is annealed below the Al_2TiO_5 decomposition temperature range, TiO_2 and Al_2O_3 can form within the initial Al_2TiO_5 grains or at the grain boundaries. During subsequent annealing above the Al_2TiO_5 formation temperature range, the TiO_2 reacts with adjacent Al_2O_3 grains to form Al_2TiO_5 once more. This alternating Al_2TiO_5 decomposition/formation

S. Kamiya AFOSR/1988 CYCLICALLY ANNEALED COMPOSITES: PROCESSING/CONTROL
reaction sequence through cyclic annealing has potential as a method for
microstructural control that may lead to unique mechanical properties in
 Al_2O_3 - TiO_2 composites.

A powder preparation method involving flocculation was applied in this
study to the Al_2O_3 - TiO_2 system. The method is similar to one used for the
 Al_2O_3 - ZrO_2 system, in which Al_2O_3 and ZrO_2 were dispersed in an aqueous
polyvinyl alcohol (PVA) solution, then flocculated with acetone to obtain
homogeneous powder mixtures (3).

A previous paper described the microstructural refinement obtained in
the Al_2O_3 - Al_2TiO_5 - TiO_2 system using flocculation and cyclic annealing as
somewhat discouraging, but the irregularly shaped, intertwined grains
formed during the annealing (4). This paper describes the further
application of the flocculation technique to Al_2O_3 - TiO_2 compact preparation
and reports further results of cyclic annealing studies on Al_2O_3 - TiO_2
composites.

EXPERIMENTAL PROCEDURE

Degussa TiO_2 (Degussa Corp. P-25 anatase, Teterboro, NJ) mixed with
either Sumitomo Al_2O_3 (Sumitomo AKP-HP, Sumitomo Chemical America, New
York, NY) or the 0.2-0.3- μm cut of classified Reynolds Al_2O_3 (RC-172DBM
without MgO, Reynolds Metals Co., Bauxite, AR) was used as the starting
powder. Twenty-five grams of powder containing 5.0, 10.0, 15.0, or 20.7
wt% TiO_2 was dispersed in 250 ml of an aqueous polyvinyl alcohol (mol. wt.
14,000, Aldrich Chemical Co., Inc., Milwaukee, WI) solution (0.2-1.0
wt%; vacuum-filtered through a 10-20- μm glass frit before using) containing
enough concentrated HNO_3 to adjust the pH to 2.0-3.0. Each mixture was
ultrasonically agitated at a power of 20 KHz, 100 W for 5-30 min; the
suspension was then flocculated with 313 ml of reagent-grade acetone. In

some cases, the particle dispersion was allowed to settle for 24 h to eliminate possible agglomerates, inclusions, dust, etc.; the upper stable suspension (180 ml) was then removed by cannulation using a pipet, homogenized for 1 h in a ball mill without any milling media, and flocculated with 225 ml of reagent-grade acetone. The liquid was vacuum-filtered through analytical paper, and the retained flocs were colloid-pressed into pellets ~38 mm in diameter; the applied pressure and holding time were 35 MPa and 30 min, respectively.

The pellets were dried at room temperature for 6 h and at 60°C for 12 h in air, after which they were heated at a rate of 1°C/min to 600°C and held at temperature for 1 h to burn out the PVA. The samples were then isopressed at 280 MPa for 1 min and sintered or annealed in air. Following heat treatment, the specimens were wet-ground into powder using reagent-grade ethanol and an agate mortar, and the phases identified by X-ray diffraction. The percent of Al_2TiO_5 decomposition that had taken place in each sample was determined using the ratio:

$$\text{rutile}(110)/[\text{rutile}(110) + \text{Al}_2\text{TiO}_5(110)]$$

The X-ray peak intensity ratio for each diffraction pattern, as represented by peak height, was taken to be the average of five patterns obtained at a slow scanning speed of 0.5° (i.e., 2θ)/min.

The quantitative X-ray phase analyses (5) of the powdered, heat-treated specimens used powdered single-crystal silicon as an internal standard material. The calibration curve for phase analysis was determined by measuring the peak-intensity ratios of $\text{rutile}(110)/\text{silicon}(111)$ and $\alpha\text{-Al}_2\text{O}_3(104)/\text{silicon}(111)$ for mixtures of rutile, $\alpha\text{-Al}_2\text{O}_3$, and 30 wt% silicon powder. Approximately 50 mg of these powder mixtures was obtained

by mixing the rutile, $\alpha\text{-Al}_2\text{O}_3$, and silicon powder for 30 min using reagent-grade ethanol and an agate mortar. The X-ray peak intensity ratio for each diffraction pattern was measured by averaging five patterns with a slow scanning speed of 0.5° (i.e., 2θ)/min. The TiO_2 and Al_2O_3 contents for each heat-treated material can be expressed by the following equations, obtained by the least-squares method, based on the calibration curves shown in Figure 1:

$$\text{TiO}_2(\text{wt}\%) = 42.8 \cdot I(\text{TiO}_2)/I(\text{Si})$$

$$\text{Al}_2\text{O}_3(\text{wt}\%) = 120.9 \cdot I(\text{Al}_2\text{O}_3)/I(\text{Si})$$

where I is the X-ray peak intensity, represented by peak height. The phase compositions of the annealed materials were determined by first measuring the peak-intensity ratios for a mixture of 30 wt% silicon powder and the powdered, annealed specimen, then using the above equations.

The bulk density of each annealed pellet was measured by Archimedes' method, using reagent-grade n -butanol as the solvent. The specimens used for microstructural observation were cut from the heat-treated materials using a diamond saw; the surface parallel to the direction of colloid-pressing was polished with a diamond disk (15- μm roughness) and finished with increasingly fine diamond pastes of 9-, 6-, 3-, 1-, and 0.25- μm granularity. After cleaning by ultrasonication, SEM observations were made of the finished surface, followed by chemical etching at 170°C for 30 min with concentrated H_3PO_4 .

RESULTS AND DISCUSSION

Powder Preparation Using a Flocculation Technique

A suitable concentration of aqueous PVA solution for the $\text{Al}_2\text{O}_3\text{-ZrO}_2$

system was determined to be between 0.3 and 0.5 wt% when Sumitomo AKP-HP Al_2O_3 (surface area, $5.3 \text{ m}^2/\text{g}$) and Toyo Soda ZrO_2 (surface area, 12-15 m^2/g) powders were used (3). The TiO_2 powder employed in this study had a fine particle size ($0.03 \mu\text{m}$) and high surface area ($50 \pm 15 \text{ m}^2/\text{g}$); a relatively large quantity of PVA would therefore be necessary to form the large, soft flocs best suited for colloid-pressing. On the other hand, a small amount of PVA would be most favorable in terms of binder-burnout considerations. For the Al_2O_3 - TiO_2 system, therefore, flocs were formed at PVA concentrations ranging from 0.2 to 1.0 wt%. The flocs were normally powder-like at PVA concentrations of less than 0.4 wt%, but became rubbery as the PVA concentration increased. The flocs were small and powder-like, and colloid pressing consequently rather difficult at a PVA concentration of 0.2 wt%. The adsorption of PVA onto powder surfaces, therefore, critically affects the floc characteristics.

The relative densities of materials sintered at 1500°C for 0.5 and 2.0 h using Sumitomo Al_2O_3 (starting composition, 20.7 wt% TiO_2 - 79.3 wt% Al_2O_3) are shown in Figure 2 for selected PVA concentrations. The relative densities obtained were 94-96% of theoretical, independent of the PVA concentration between 0.2 and 1.0 wt%. Figure 3 shows SEMs taken of the (unetched) polished surfaces of samples made with Sumitomo Al_2O_3 and either 0.2 or 1.0 wt% PVA, sintered at 1500°C for 0.5 h. The pore sizes and pore distributions observable by SEM are the same for both PVA concentrations. Higher PVA concentrations could therefore still be used for this Al_2O_3 - TiO_2 powder system. As is apparent in Figure 3, the sintered materials usually contained cracks a few hundred micrometers long. A starting powder composition of 20.7 wt% TiO_2 corresponded to a final sample composition of 47.2 wt% Al_2TiO_5 - 52.8 wt% Al_2O_3 in material

sintered above the Al_2TiO_5 formation temperature range; the large amount of Al_2TiO_5 is probably responsible for the many small cracks formed during cooling, since Al_2TiO_5 exhibits strong thermal anisotropy. These cracks, however, were completely eliminated by annealing.

Figure 4 plots relative density versus sonication time for both Sumitomo and classified Reynolds Al_2O_3 compacts (starting powder composition of each, 20.7 wt% TiO_2) prepared using a 1.0 wt% PVA solution and sintered at 1500°C for 0.5-2.0 h. No significant change in relative density resulted from changing the sonication time for either type of Al_2O_3 ; suspension homogeneity was therefore attained even after the shorter sonication times used under the conditions employed in this study.

Noteworthy, however, is the fact that the relative density attained for the classified Reynolds Al_2O_3 was 97-98% of theoretical, compared to the 93-94% of theoretical density attained with the Sumitomo alumina under the same processing conditions. Figure 5 compares SEMs taken of the polished surfaces of sintered materials made with Sumitomo Al_2O_3 and those made with classified Reynolds Al_2O_3 . The pore sizes as observed in the SEMs decreased for sintered samples containing classified Reynolds Al_2O_3 as the samples' relative densities increased. This suggests that Reynolds Al_2O_3 , which was classified for this study into a 0.2-0.3- μm particle-size range, yielded sintered materials with higher densities than were obtained with the Sumitomo AKP-HP Al_2O_3 due to both the classified powder's narrower particle-size distribution and its smaller particles.

Based on the above results, the following experiments were performed using the materials and powder preparation conditions shown in Table 1.

Table 1. Materials and conditions used in this study to prepare Al_2O_3 - TiO_2 powder using the flocculation technique.

Al_2O_3	0.2-0.3- μm classified Reynolds alumina (RC-172DBM)
TiO_2	0.03- μm Degussa titania (P-25)
Starting composition	5.0, 10.0, 15.0, and 20.7 wt% TiO_2
Ratio of powder weight to PVA solution volume	1:10 (g:ml)
PVA concentration	1.0 wt%
Volume ratio of PVA solution to acetone	1 : 1.25
pH	2.0-3.0
Sonication time	20 min (20 KHz, 100 W)

Decomposition Behavior of Al_2TiO_5

The decomposition behavior of Al_2TiO_5 in the sintered materials containing Al_2O_3 and Al_2TiO_5 was studied between the annealing temperatures of 800°C and 1250°C (Fig. 6). Samples with the starting composition of 20.7 wt% TiO_2 were sintered at 1500°C for 2 h, then annealed for 6 h at various temperatures without being cooled to room temperature. The fastest decomposition occurred at 1050°C, the slowest above ~1200°C and below ~900°C, as shown by Figure 6. The results shown in this figure are consistent with recent results obtained for the decomposition behavior of Al_2TiO_5 solid solutions (6). A consideration of aluminum titanate's thermodynamic stability alone is not enough to understand this material's decomposition behavior, because its decomposition seems also to be associated with some strain energy (7) due to the strong thermal anisotropy of the Al_2TiO_5 crystal. One possible additional explanation is that the 1050°C temperature favors release of this strain, resulting in rapid

decomposition during annealing. Consequently, the decomposition behavior could be explained by a low driving force near the decomposition temperature and slow kinetics at the low temperatures.

Based on the above results, a second experiment was conducted with an annealing temperature of 1050°C. The decomposition behavior of Al_2TiO_5 versus annealing time is shown in Figure 7. Two different sets of sintering conditions were employed: 1350°C/0.16 h and 1500°C/2 h. The former sintering conditions led to faster Al_2TiO_5 decomposition than did the latter, possibly due to residual TiO_2 before Al_2TiO_5 decomposition, especially in the early stages of decomposition. However, Al_2TiO_5 was difficult to completely decompose in an annealing time of less than 12 h. These results form the basis for our speculation that some microstructural control of the Al_2O_3 - TiO_2 system can be achieved using cyclic annealing.

Microstructural Control by Cyclic Annealing

Ten sintering/annealing schedules were used for powders containing 20.7 wt% TiO_2 . The first sets of sintering conditions and annealing conditions used were 1500°C/2 h and either 1050°C/6 h or 1050°C/3 h, respectively. The second set of sintering conditions employed was 1350°C/0.16 h, since a small amount of TiO_2 was expected to promote Al_2TiO_5 decomposition at this temperature. The heating and cooling rates were both 10°C/min in all cases. The results are shown in Table 2. The relative densities obtained in the annealed materials decreased from 95.6% to 93.3% of theoretical as the number of annealing cycles increased (Conditions B, C, and D); note that the relative density after sintering at 1500°C for 2 h was 97.9% of theoretical.

Table 2. Densities and phase compositions of samples sintered and/or annealed under the designated conditions (continued next page).

Condition	A	B	C	D	E
Temp/time (°C/h)	1500/2	1500/2 1050/6	1500/2 1050/6 1350/0.16 1050/3	1500/2 1050/6 1350/0.16 1050/3 1350/0.16 1050/3 1350/0.16 1050/3	1500/2 1050/6 1280/12
# Annealing cycles	0	1	2	4	1
# Reheats	0	0	0	0	1
Density (g/ml)	3.776	3.798	3.747	3.681	3.842
Al ₂ O ₃ (wt%)	54.8 ± 2.7	70.6 ± 1.9	64.0 ± 2.0	67.0 ± 1.8	69.4 ± 0.4
TiO ₂ (wt%)	0	12.9 ± 0.8	9.8 ± 0.5	10.0 ± 0.4	10.3 ± 0.5
Al ₂ TiO ₅ (wt%)	45.2	16.5	26.2	23.0	20.3
Relative density (%TD)	97.9 ± 1.6	95.6 ± 1.8	95.1 ± 1.9	93.3 ± 1.7	97.1 ± 0.4

Table 2 (cont'd). Densities and phase compositions of annealed materials.

Condition	F	G	H	I	J
Temp/time (°C/h)	1350/0.16 1050/6 1280/12	1350/0.16 1050/3 1350/0.16 1050/6 1280/12	1350/0.16 1050/6 (above sequence 3 times) 1350/0.16 1050/12 1280/12	1350/0.16 1050/3 1280/6 1350/0.16 1050/6 1280/12	1350/0.16 1050/3 1280/6 (above sequence 3 times) 1350/0.16 1050/6 1280/12
# Annealing cycles	1	2	4	2	4
# Reheats	1	1	1	2	4
Density (g/ml)	3.887	3.870	3.812	3.884	3.846
Al ₂ O ₃ (wt%)	65.4 ± 1.6	74.6 ± 3.4	68.6 ± 3.8	68.2 ± 1.6	66.1 ± 1.3
TiO ₂ (wt%)	12.2 ± 0.7	13.4 ± 0.4	12.5 ± 0.5	12.6 ± 0.5	11.6 ± 0.9
Al ₂ TiO ₅ (wt%)	22.4	12.0	18.9	19.2	22.3
Relative density (%TD)	98.3 ± 1.6	97.0 ± 3.3	96.1 ± 3.7	97.9 ± 1.6	97.3 ± 1.3

The microstructures of these materials are shown in Figure 8. Rectangular grains appeared during annealing, but the bulk materials coarsened and the pores grew after annealing. These microstructural changes resulted from density changes during Al₂TiO₅ decomposition. The theoretical densities of α -Al₂O₃, TiO₂ (rutile), and Al₂TiO₅ are 3.987, 4.250, and 3.702 g/ml, respectively. The sintered materials had a composition of 52.8 wt% Al₂O₃ - 47.2 wt% Al₂TiO₅, so their calculated theoretical density should be 3.853 g/ml. If the Al₂TiO₅ had completely decomposed, the sample composition would have changed to 79.3 wt% Al₂O₃ and 20.7 wt% TiO₂, with a resultant theoretical density increase to

4.042 g/ml. This means that the solids would have undergone a 4.7% volume decrease due to Al_2TiO_5 decomposition, a volume shrinkage reasonable for the coarsening actually observed in the material after annealing.

It was determined that after each annealing cycle, a reheating treatment was necessary, the conditions of which would allow a higher density but still limit Al_2TiO_5 reformation. Figures 9 and 10 show X-ray diffraction patterns of specimens with a starting composition of 20.7 wt% TiO_2 , heated for 3-24 h at 1250°C or 1280°C. At 1250°C, a trace of Al_2TiO_5 was observed after heat treatment for 3 h; the peak height of Al_2TiO_5 increased slightly with heating time. However, Al_2TiO_5 formation was very slow: only a small amount of Al_2TiO_5 was detected even after heating for 24 h. The formation reaction rate was slightly higher at 1280°C than at 1250°C (Fig. 10). These results indicate that Al_2TiO_5 formation takes place even below 1250°C, though the reaction rate is slow.

Figure 11 shows a series of changes in the X-ray diffraction patterns for Al_2TiO_5 formation (1350°C/0.16 h), Al_2TiO_5 decomposition (1050°C/6 h), and four reheating treatments. A small amount of TiO_2 (rutile) was observed in the specimen heated at 1350°C for 0.16 h, due to incomplete Al_2TiO_5 formation (Fig. 11f). Most of the Al_2TiO_5 decomposed to Al_2O_3 and TiO_2 when annealed at 1050°C for 6 h (Fig. 11e). A slight increase in Al_2TiO_5 content was also observed after reheating for 12 h at 1250°C or 1280°C (Figs. 11b and c), but no significant change is apparent in the X-ray diffraction patterns of specimens reheated at 1220°C (Fig. 11d) and in the patterns of specimens that were not reheated (Fig. 11e). This indicates that Al_2TiO_5 reformation occurred above 1250°C for the heating time employed in this study. However, complete Al_2TiO_5 reformation took place only after reheating at 1300°C for 12 h, suggesting that a rapid

formation reaction occurs between 1290°C and 1300°C (Fig. 11a). Therefore, a reheating treatment of 1280°C for 6 or 12 h can be employed after each annealing cycle to increase the density of annealed materials, because the Al_2TiO_5 formation reaction is still slow at 1280°C.

The relative density of samples increased from 95.6% to 97.1% of theoretical when such a treatment was incorporated (compare Conditions B and E in Table 2). A density of 98.3% was obtained by reheating, even when the first sintering conditions were 1350°C/0.16 h, as in Condition F. Therefore, the samples were sintered at 1350°C for 0.16 h before cyclic annealing for Conditions F through J. The annealed materials contained more Al_2TiO_5 than TiO_2 (see Conditions E, F, H, I, and J; ~19-22 wt% Al_2TiO_5 , ~10-13 wt% TiO_2). The higher Al_2TiO_5 compositions are due to Al_2TiO_5 reformation during the reheating treatment at 1280°C. The relative densities obtained were all more than 96%, but decreased from 98.3 to 96.1% of theoretical as the number of annealing cycles increased (compare Conditions F, G, and H). When samples were reheated after each annealing cycle, the density increased from 96.1 to 97.3% of theoretical (compare Conditions H and J). Even so, the density obtained using Condition J was lower than that obtained using Condition I. Relative densities obtained for the annealed materials are summarized in Figure 12.

Figure 13 shows typical microstructures of samples annealed under Conditions E, F, I, and J. These materials show denser microstructures than do those prepared without the reheating treatment. The grains obtained under Condition E are smaller than those obtained under Condition F. The grain size also increased slightly when the number of reheating cycles was increased, as under Conditions I and J, indicating that the grain size of annealed materials depends on both the first sintering

condition and the number of reheating treatments. The conditions of 1350°C/0.16 h are favorable because the grains produced are still small. Conditions I and J, which incorporate 2 cycles/ 2 reheating treatments and 4 cycles/ 4 reheating treatments, respectively, not only produced irregular grains, but also caused white or grey grains (possibly TiO_2 or Al_2TiO_5) to intertwine with the Al_2O_3 grains. These microstructural changes could be due to the cyclic decomposition and formation reaction of Al_2TiO_5 .

Effects of Settling and Starting Composition on Annealed Materials' Properties

The mechanical strength of a ceramic material is determined by its surface defects and internal defects, which are associated primarily with processing. In this study, a settling step was incorporated into the processing procedure to eliminate possible agglomerates, inclusions, dust, etc. The powder preparation method used was that described above, except that the suspension was allowed to settle for 24 h after sonication. Table 3 summarizes the properties of materials formed through processes that incorporated both a settling step and an annealing step (Conditions E, F, I, and J), performed on powder with a starting composition of 20.7 wt% TiO_2 . Figure 14 shows relative densities for the annealed materials formed with and without the settling step; there was no significant difference between the relative densities of materials produced with and without the settling step. The highest densities were around 97 and 98% of theoretical; densities greater than 99% of theoretical were difficult to obtain. The highest relative density was obtained using annealing condition F (1 cycle/ 1 reheating treatment, 1350°C/0.16 h sintering conditions). The density then gradually decreased as the number of annealing cycles increased, as shown by a comparison of Conditions I and J.

Table 3. Densities and phase compositions of annealed materials formed through processes incorporating a settling step.

Condition	E	F	I	J
Temp/time (°C/h)	1500/2 1050/6 1280/12	1350/0.16 1050/6 1280/12	1350/0.16 1050/3 1280/6 1350/0.16 1050/6 1280/12	1350/0.16 1050/3 1280/6 (above sequence 3 times) 1350/0.16 1050/6 1280/12
# Annealing cycles	1	1	2	4
# Reheats	1	1	2	4
Density (g/ml)	3.899	3.923	3.898	3.867
Al ₂ O ₃ (wt%)	78.5 ± 2.1	73.9 ± 2.2	77.8 ± 2.7	77.5 ± 3.2
TiO ₂ (wt%)	10.5 ± 0.6	11.7 ± 0.4	12.2 ± 0.3	11.9 ± 0.4
Al ₂ TiO ₅ (wt%)	11.0	14.4	10.0	10.6
Relative density (%TD)	97.9 ± 2	98.6 ± 2.2	97.7 ± 2.8	97.0 ± 3.3

The phase compositions, as determined by quantitative X-ray analysis, for the annealed materials with and without the settling step are shown in Figure 15. The figure shows an increase in Al₂O₃ and a decrease in Al₂TiO₅ content attributable to settling, with no change in the TiO₂ (rutile) content. This suggests that some change in composition could occur during settling.

Figure 16 shows bulk and relative densities versus starting powder compositions for materials annealed under Condition I (2 cycles/ 2 reheating treatments, sintering conditions of 1350°C/0.16 h). Four powder compositions -- 5.0, 10.0, 15.0, and 20.7 wt% TiO₂ -- were employed for

this experiment. Table 4 shows the properties of the annealed materials. The relative densities for starting TiO_2 compositions of 5 and 10 wt% reached 99.6% of theoretical, a high level. The relative densities decreased from 99.1 to 97.7% of theoretical, however, as the starting TiO_2 composition increased from 15 to 20.7 wt%.

Table 4. Densities and phase compositions of annealed materials with the designated starting powder compositions, annealed using Condition F.

	Starting composition (wt% TiO_2)			
	5.0	10.0	15.0	20.7
Density (g/ml)	3.945	3.950	3.941	3.898
Al_2O_3 (wt%)	85.7 ± 3.7	82.0 ± 1.5	78.9 ± 4.4	77.8 ± 2.7
TiO_2 (wt%)	2.6 ± 0.3	5.4 ± 0.3	8.9 ± 0.5	12.2 ± 0.3
Al_2TiO_5 (wt%)	11.7	12.6	12.2	10.0
Relative density (%TD)	99.6 ± 3.8	99.6 ± 1.5	99.1 ± 4.4	97.7 ± 2.8

Figure 17 shows phase compositions versus starting powder compositions. The final TiO_2 content increased from 2.6 to 12.2 wt% as the starting TiO_2 composition increased from 5.0 to 20.7 wt%. The Al_2TiO_5 content, however, did not significantly change with the starting powder composition.

Tables 5 and 6 show the amount of titanium converted to titanium oxide for each annealing condition, as calculated from the phase compositions of each material. The results indicate that for all but the starting compositions of 5.0 and 10.0 wt% TiO_2 , a small weight percent of titania powder was presumably lost during settling; note, however, that in Table 5

Table 5. Change in powder composition due to settling (calculations based on phase composition, as determined by X-ray quantitative analysis).

TITANIUM CONTENT (WT%), SHOWING CONVERSION TO TiO ₂						
	E (1)	F (1)	Annealing Condition (Number of cycles)		Average Content	Starting Content
			I (2)	J (4)		
Without settling	19.2	22.0	21.0	21.4	20.9	20.7
With settling	15.3	18.0	16.6	16.6	16.6	20.7

Table 6. Change in powder composition attributable to settling.

TITANIUM CONTENT (WT%), SHOWING CONVERSION TO TiO ₂				
Starting powder	5.0	10.0	15.0	20.7
With settling	7.7	10.9	14.3	16.6

the calculated amount of titanium oxide is higher than the starting composition for the 5.0 and 10.0 wt% TiO₂ compositions.

Figure 18 shows polished, etched SEMs of the materials annealed using Conditions E, F, I, and J and incorporating the settling step, for powders with the starting composition of 20.7 wt% TiO₂; note how similar these microstructures are to those obtained without the settling step (Fig. 13). The largest grain size was obtained from samples processed under Condition E, when the initial sintering conditions were 1500°C/2 h; the smallest grain size was obtained using Condition F (1 cycle/ 1 reheat, sintering conditions of 1350°C/0.16 h); an increase in grain size accompanied an increase in the number of cycles. The pore sizes observed in SEMs for

Conditions E and J are slightly larger than those observed in samples processed under Conditions F and I, but they are still less than $\sim 5 \mu\text{m}$, and are discrete and homogeneously distributed. The samples obtained using Conditions E and J also show irregularly shaped grains and a homogeneously distributed second phase surrounded by an Al_2O_3 matrix.

Microstructural changes in relation to starting powder composition are shown in Figure 19 for the materials annealed using Condition I (2 cycles/2 reheat treatments, sintering conditions of $1350^\circ\text{C}/0.16 \text{ h}$). The materials with starting compositions of 5.0 and 10.0 wt% TiO_2 were most dense; the pore sizes increased slightly with an increase in TiO_2 content, a result consistent with the relative densities obtained for these materials. Their microstructures are generally fine, and contain irregularly shaped grains that are homogeneously distributed. A small amount of TiO_2 (<1.0 wt%) is known to promote grain growth and densification of Al_2O_3 (8); however, no significant change in grain size accompanied an increase in the starting powder's TiO_2 composition from 5.0 to 20.7 wt%. Consequently, this unique process combining cyclic annealing with a reheat treatment yielded materials with an almost constant grain size and constant Al_2TiO_5 content over a wide range of starting powder compositions, from 5.0 to 20.7 wt% TiO_2 . The interesting microstructures obtained for Al_2O_3 composites interspersed with Al_2TiO_5 and TiO_2 could prove to have unique mechanical properties.

CONCLUSIONS

Flocculation and cyclic annealing were studied as possible means for processing and controlling the microstructure of Al_2O_3 - TiO_2 composites. The results obtained in this study are summarized below.

1. A flocculation technique can be applied to the Al_2O_3 - TiO_2 system to obtain homogeneous green bodies; the densities obtained for the sintered materials were independent of PVA concentrations between 0.2 and 1.0 wt%.
2. Classified Reynolds Al_2O_3 (a cut of 0.2-0.3- μm particles) yielded sintered Al_2O_3 - TiO_2 composites with higher densities than were obtained with Sumitomo Al_2O_3 , due to the Reynolds powder's narrower particle-size distribution and smaller particles.
3. The densities of the annealed materials decreased as the number of annealing cycles increased, due to the volume shrinkage associated with Al_2TiO_5 decomposition; a reheating treatment was therefore deemed necessary to increase the annealed materials' densities.
4. Combining cyclic annealing with a reheating treatment led to interesting microstructures in Al_2O_3 composites interspersed with Al_2TiO_5 and TiO_2 . The composites contained irregular, intertwined grains, suggesting that they would exhibit unique mechanical properties.

REFERENCES

1. W.R. Buessem, N.R. Thielke, and R.V. Sarakauskas, "Thermal Expansion Hysteresis of Al_2TiO_5 ," Ceramic Age, 60 [5] 38-40 (1952).
2. S.M. Lang, C.L. Filmore, and L.H. Maxwell, "The System Beryllia-Alumina-Titania: Phase Relations and General Physical Properties of Three-Component Porcelains," J. Res. Nat. Bur. Stds., 48, 298-312 (1952).
3. W.C. Moffatt and H.K. Bowen, "Composite Ceramics Production by Precipitation of Polymer Solutions Containing Ceramic Powder," J. Mat. Sci. Lett., 6, 383-85 (1987).

4. S. Kamiya and H.K. Bowen, "Microstructural Control of Al_2O_3 - TiO_2 Composites by Cyclic Annealing," pp. 978-88 in Ceramic Transactions: Ceramic Powder Science II, the Proceedings of the First International Conference on Ceramic Powder Processing Science (11/1-4/87, Orlando, FL). Edited by G.L. Messing, E.R. Fuller, Jr., and H. Hausner. The American Ceramic Society, Inc., Westerville, OH, 1988.
5. B.D. Cullity, Elements of X-Ray Diffraction. Addison-Wesley Publishing Co., Reading, MA, 1978.
6. M. Ishitsuka, T. Sato, T. Endo, and M. Shimada, "Synthesis and Thermal Stability of Aluminum Titanate Solid Solutions," J. Am. Ceram. Soc., 70 [2] 69-71 (1987).
7. B. Freudentberg and A. Mocellin, "Aluminum Titanate Formation by Solid-State Reaction of Coarse Al_2O_3 and TiO_2 Powders," J. Am. Ceram. Soc., 71 [1] 22-28 (1988).
8. C. Hwang, Z. Nakagawa, and K. Hamano, "Microstructures and Mechanical Properties of TiO_2 -Added Alumina Ceramics," J. Ceram. Soc. Japan, 94 [8] 761-66 (1986).

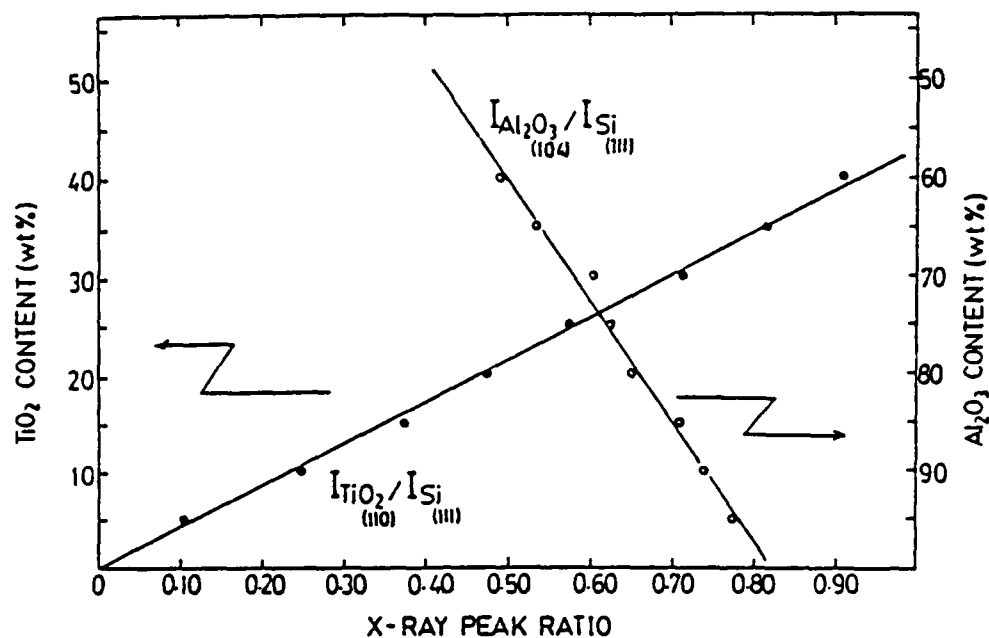


Figure 1. Calibration curves for TiO₂(rutile) and α Al₂O₃ content versus X-ray peak-intensity ratio, as determined by the internal standard method.

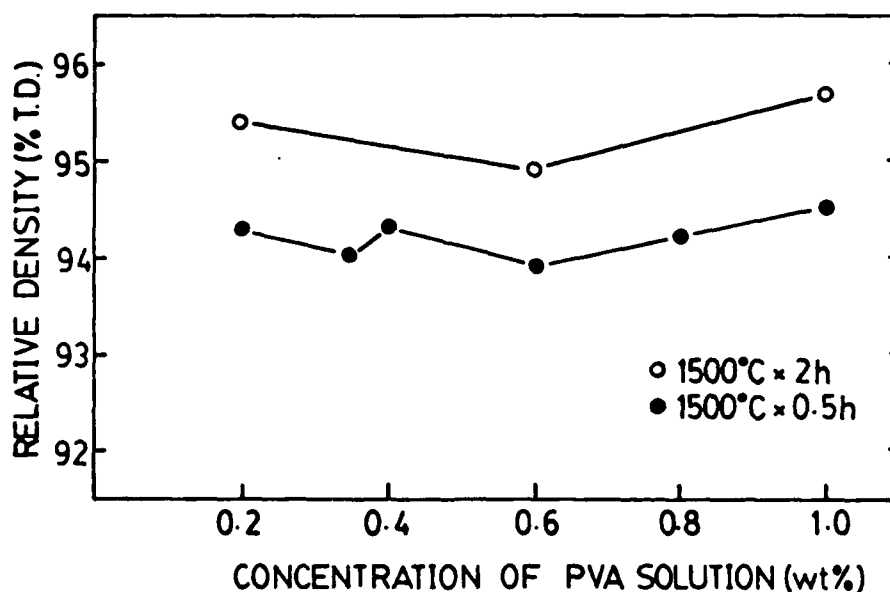


Figure 2. Relative density versus polyvinyl alcohol concentration for Al₂O₃-Al₂TiO₅ samples having a starting powder composition of 20.7 wt% TiO₂, containing Sumitomo Al₂O₃ and sintered at 1500°C for 0.5 or 2.0 h.

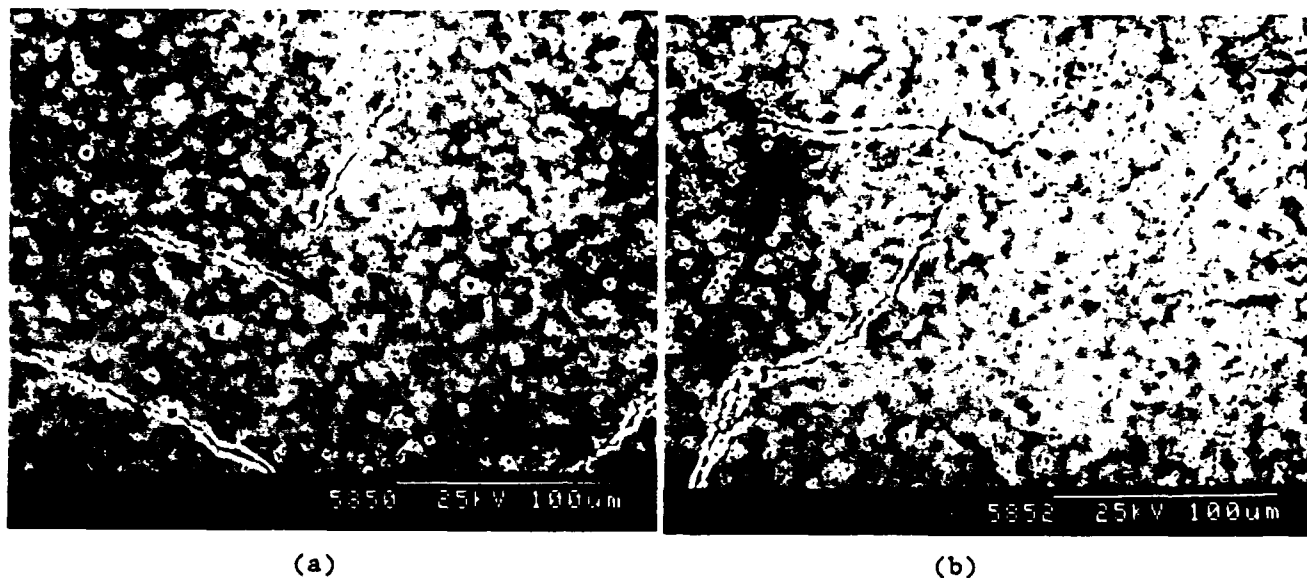


Figure 3. SEMs of polished surfaces of $\text{Al}_2\text{O}_3\text{-Al}_2\text{TiO}_5$ samples made with Sumitomo Al_2O_3 and a) 0.2 wt% or b) 1.0 wt% polyvinyl alcohol, fired at 1500°C for 0.5 h.

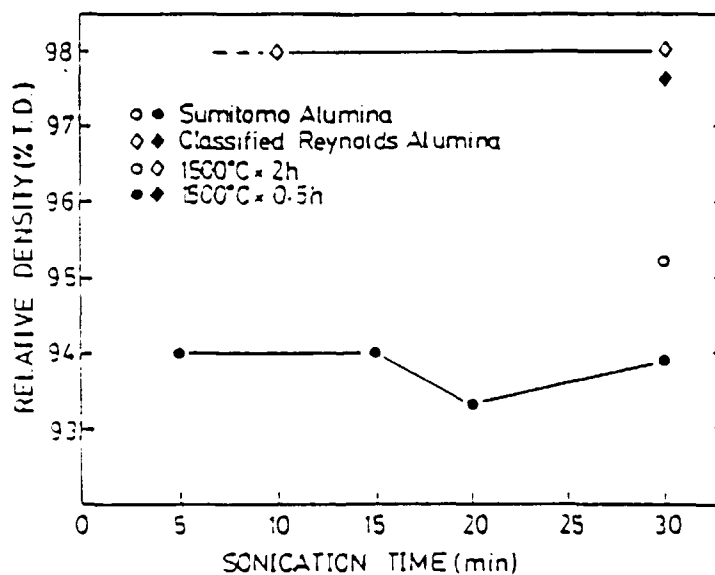


Figure 4. Relative density versus sonication time for $\text{Al}_2\text{O}_3\text{-Al}_2\text{TiO}_5$ samples having a starting powder composition of 20.7 wt% TiO_2 , using Sumitomo and classified Reynolds Al_2O_3 and sintering conditions of 1500°C for either 0.5 or 2.0 h.

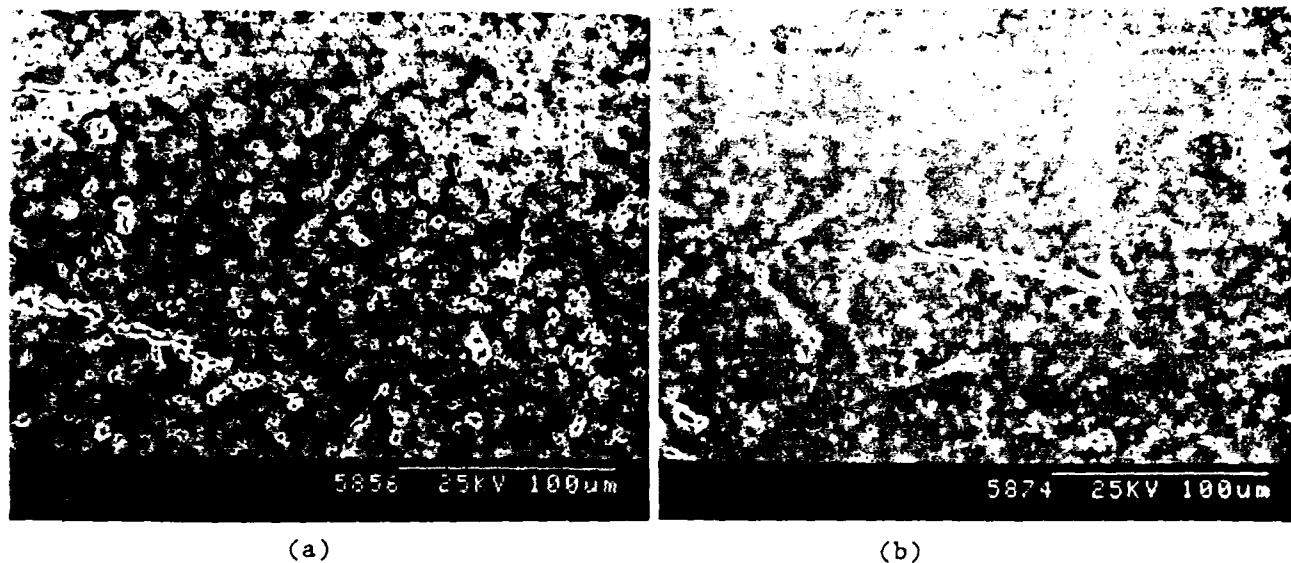


Figure 5. SEMs of polished surfaces of Al_2O_3 - Al_2TiO_5 samples made with a starting powder composition of 20.7 wt% TiO_2 , using a) Sumitomo and b) classified Reynolds Al_2O_3 .

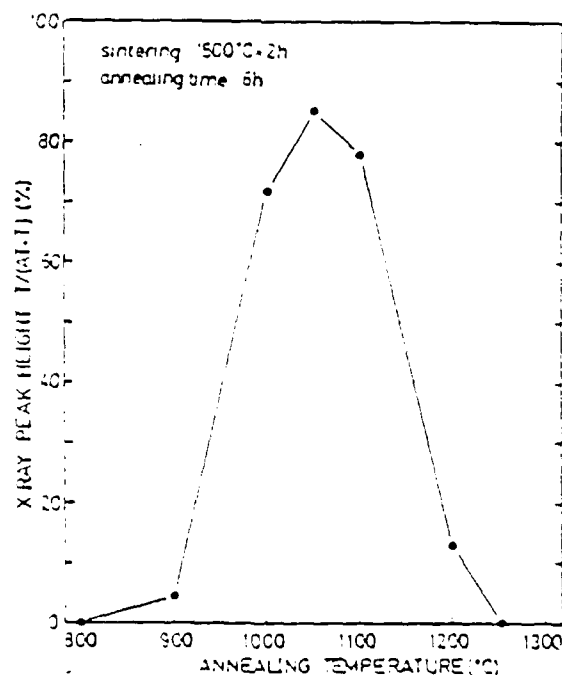


Figure 6. Decomposition ratio of Al_2TiO_5 in an Al_2O_3 - Al_2TiO_5 sample versus annealing temperature. Sintering temperature 1500°C, annealing time 6h.

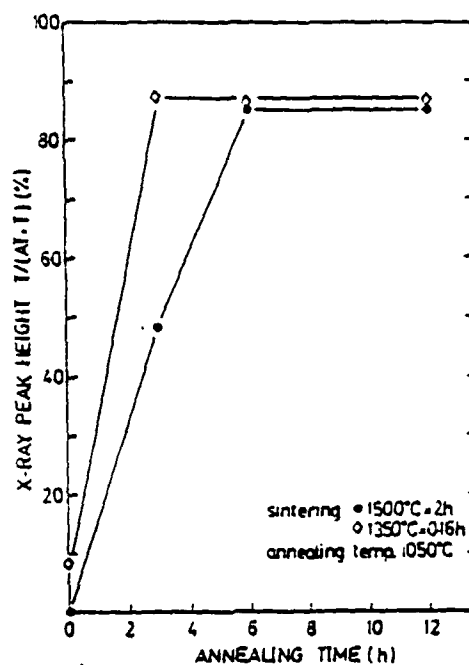


Figure 7. Decomposition ratio of Al_2TiO_5 in an Al_2O_3 - Al_2TiO_5 sample versus annealing time at 1050°C .

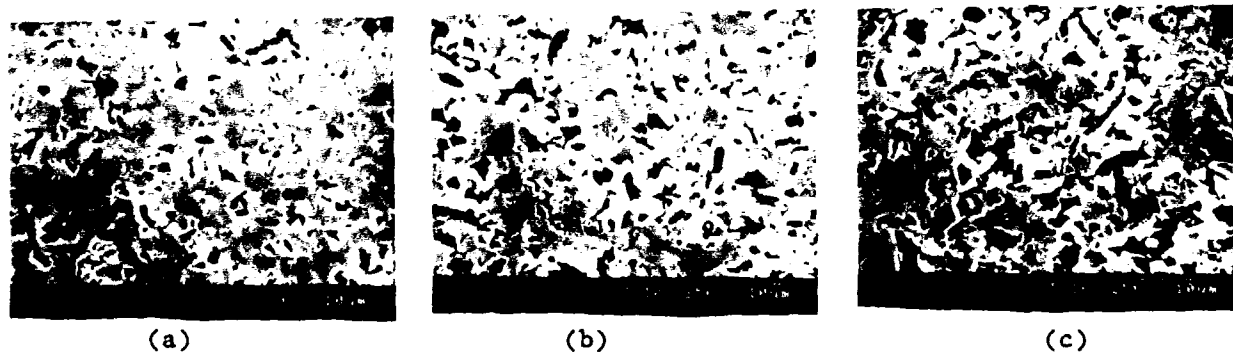


Figure 8. SEMs of the polished, etched surfaces of cyclically annealed materials obtained using a) Condition E, b) Condition C, and c) Condition D (see Table 2).

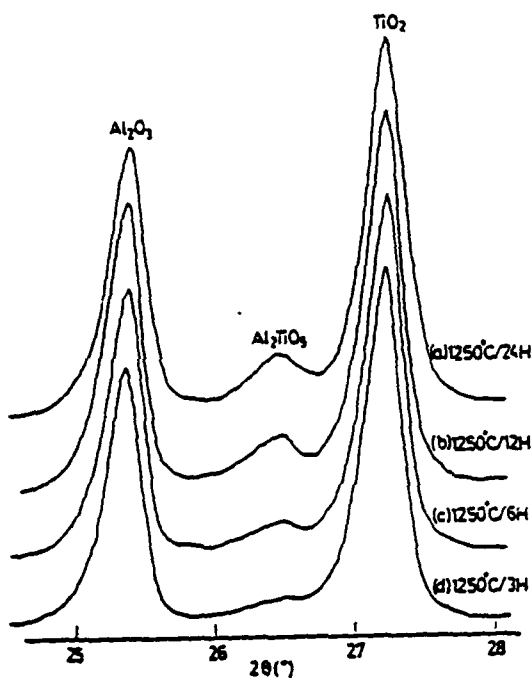


Figure 9. X-ray diffraction patterns of Al_2O_3 - TiO_2 specimens having a starting powder composition of 20.7 wt% TiO_2 , reheated at 1250°C for a) 24 h, b) 12 h, c) 6 h, and d) 3 h.

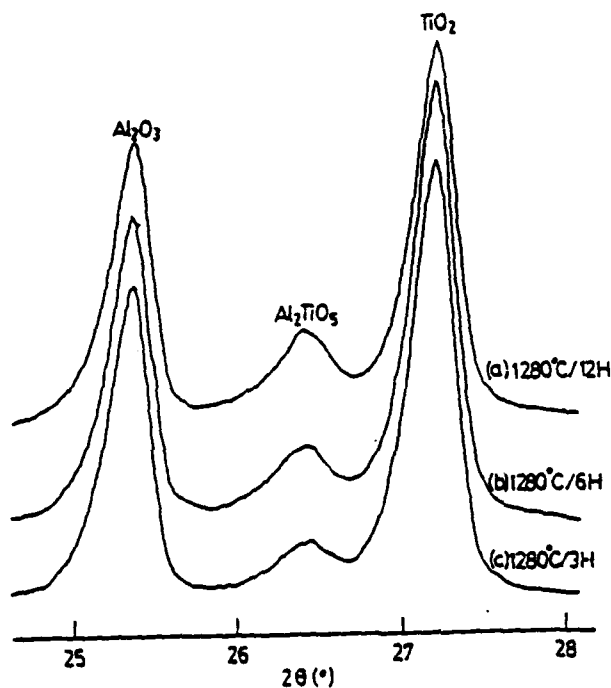


Figure 10. X-ray diffraction patterns of Al_2O_3 - TiO_2 specimens having a starting powder composition of 20.7 wt% TiO_2 , reheated at 1280°C for a) 12 h, b) 6 h, and c) 3 h.

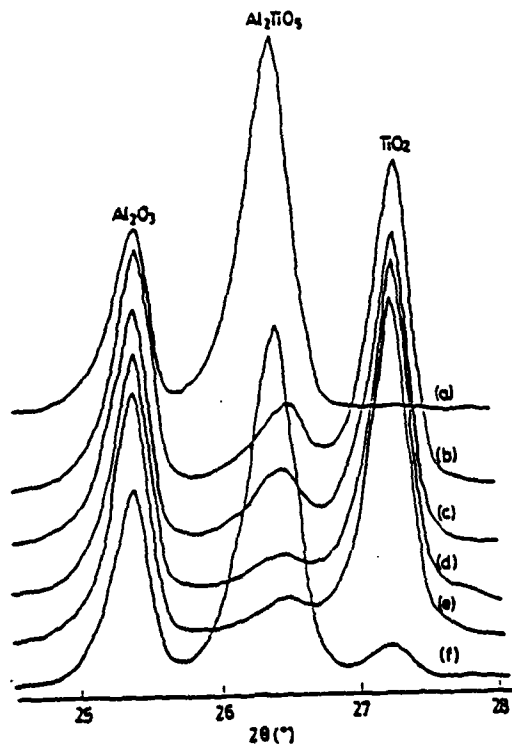


Figure 11. X-ray diffraction patterns of Al_2O_3 - TiO_2 specimens having a starting powder composition of 26.7 wt% TiO_2 , and sintered or annealed according to the following schedules: a) $1350^{\circ}C/0.16\text{ h} \rightarrow 1050^{\circ}C/6\text{ h} \rightarrow 1300^{\circ}C/12\text{ h}$, b) $1350^{\circ}C/0.16\text{ h} \rightarrow 1050^{\circ}C/6\text{ h} \rightarrow 1280^{\circ}C/12\text{ h}$, c) $1350^{\circ}C/0.16\text{ h} \rightarrow 1050^{\circ}C/6\text{ h} \rightarrow 1250^{\circ}C/12\text{ h}$, d) $1350^{\circ}C/0.16\text{ h} \rightarrow 1050^{\circ}C/6\text{ h} \rightarrow 1220^{\circ}C/12\text{ h}$, e) $1350^{\circ}C/0.16\text{ h} \rightarrow 1050^{\circ}C/6\text{ h}$, and f) $1350^{\circ}C/0.16\text{ h}$.

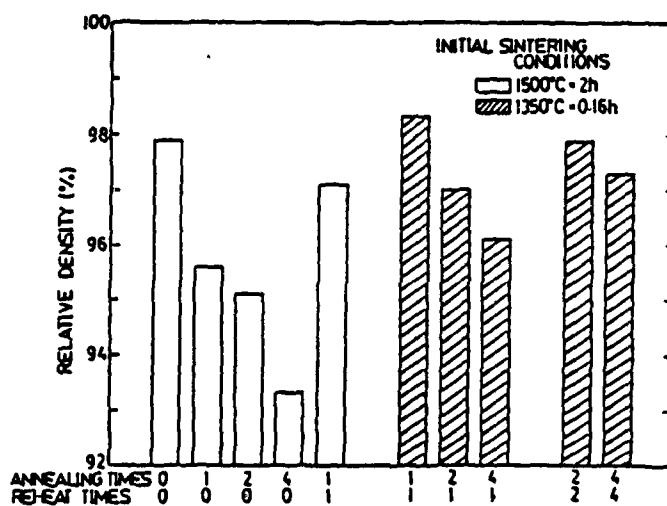
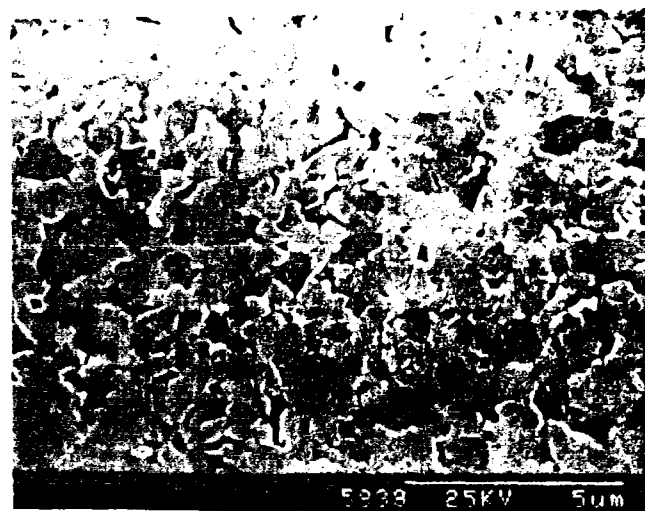


Figure 12. Relative densities of materials after various cyclic annealing schedules.



(a)



(b)



(c)



(d)

Figure 13. SEMs showing the typical microstructures obtained for materials produced using a. Condition E, b. Condition F, c. Condition I, and d. Condition J (see Table 2).

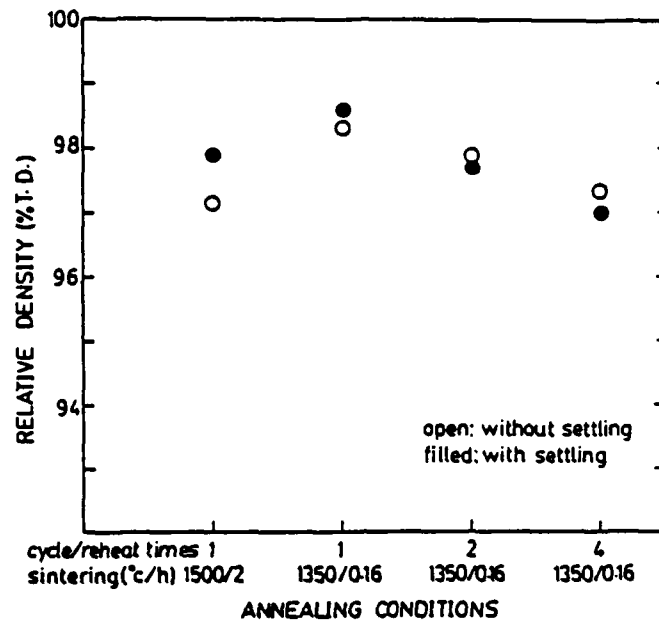


Figure 14. Relative densities of annealed materials that had a starting powder composition of 20.7 wt% TiO_2 , formed through processes with and without a settling step.

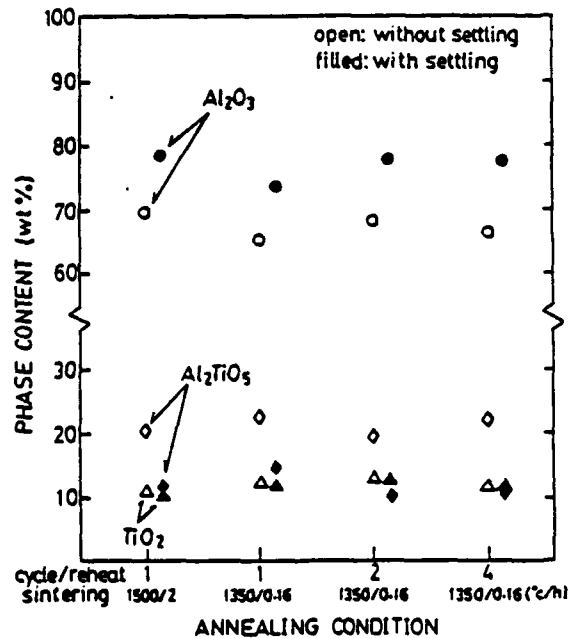


Figure 15. Phase compositions of annealed materials with a starting powder composition of 20.7 wt% TiO_2 , formed through processes with and without a settling step.

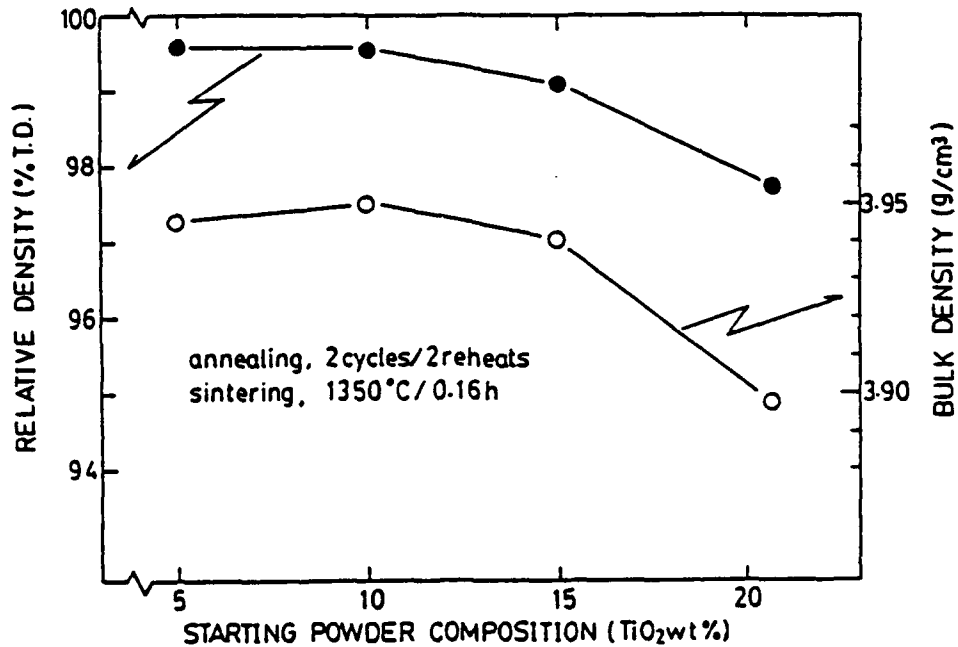


Figure 16. Bulk and relative densities versus starting powder composition for materials annealed using Condition I (see Table 2).

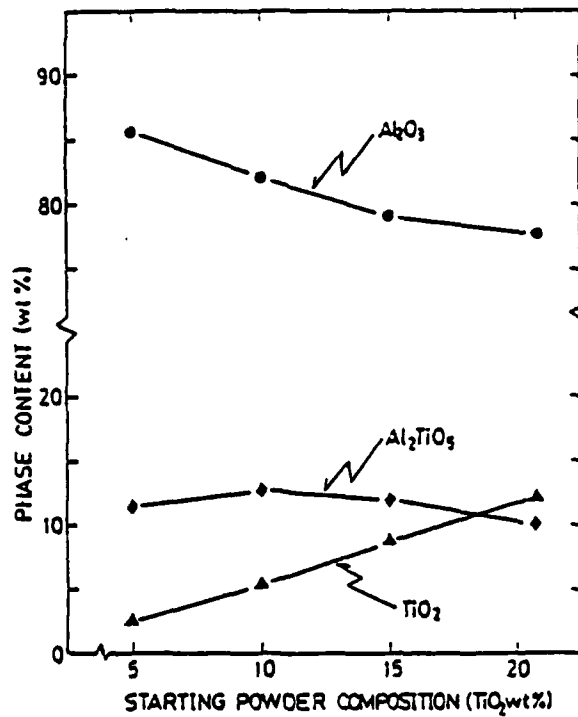


Figure 17. Phase content versus starting powder composition for materials annealed using Condition I (see Table 2).

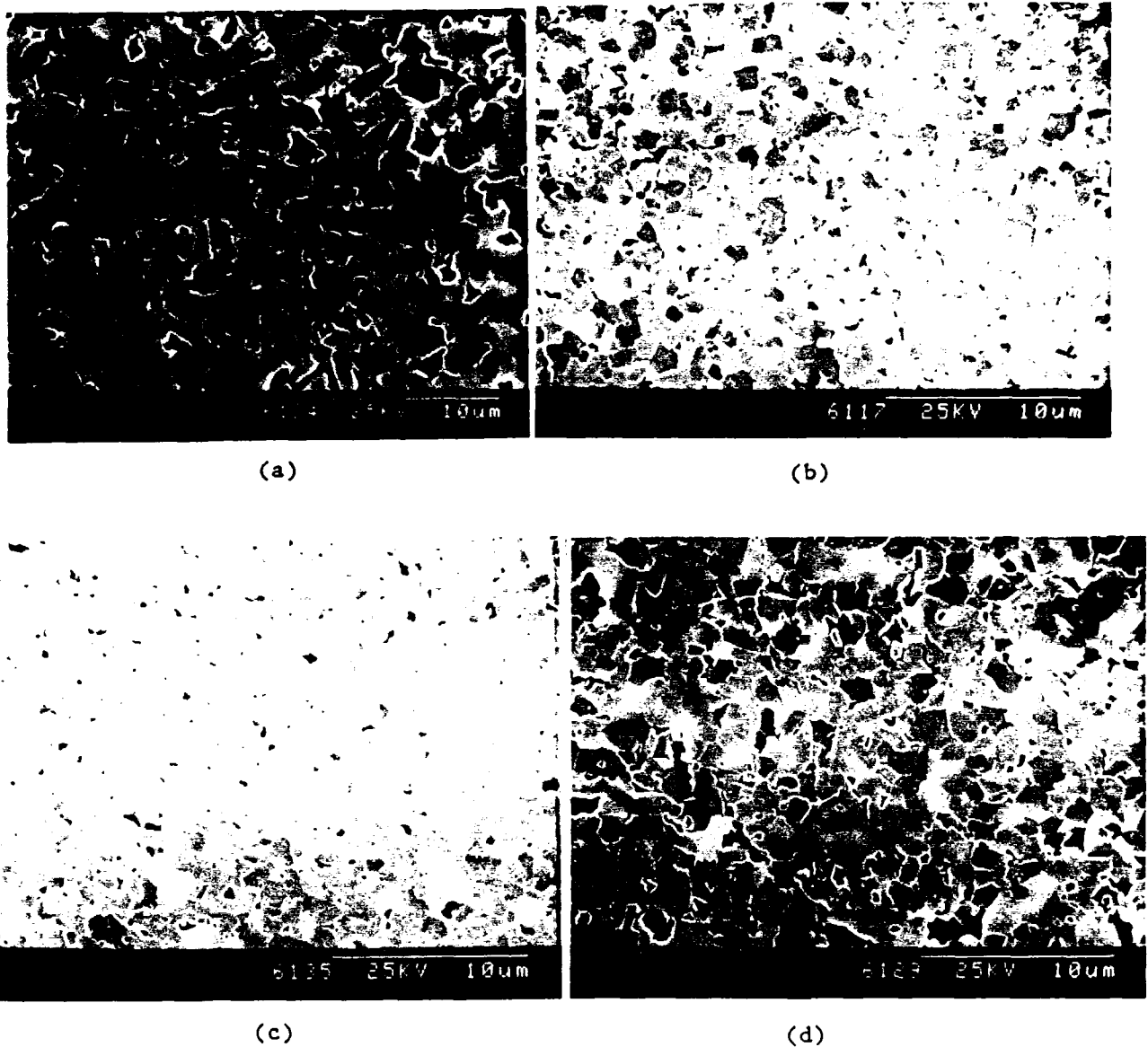


Figure 18. SEMs showing typical microstructures obtained for materials with a starting powder composition of 20.7 wt% TiO_2 , produced using a) Condition E, b) Condition F, c) Condition I, and d) Condition J (see Table 2).

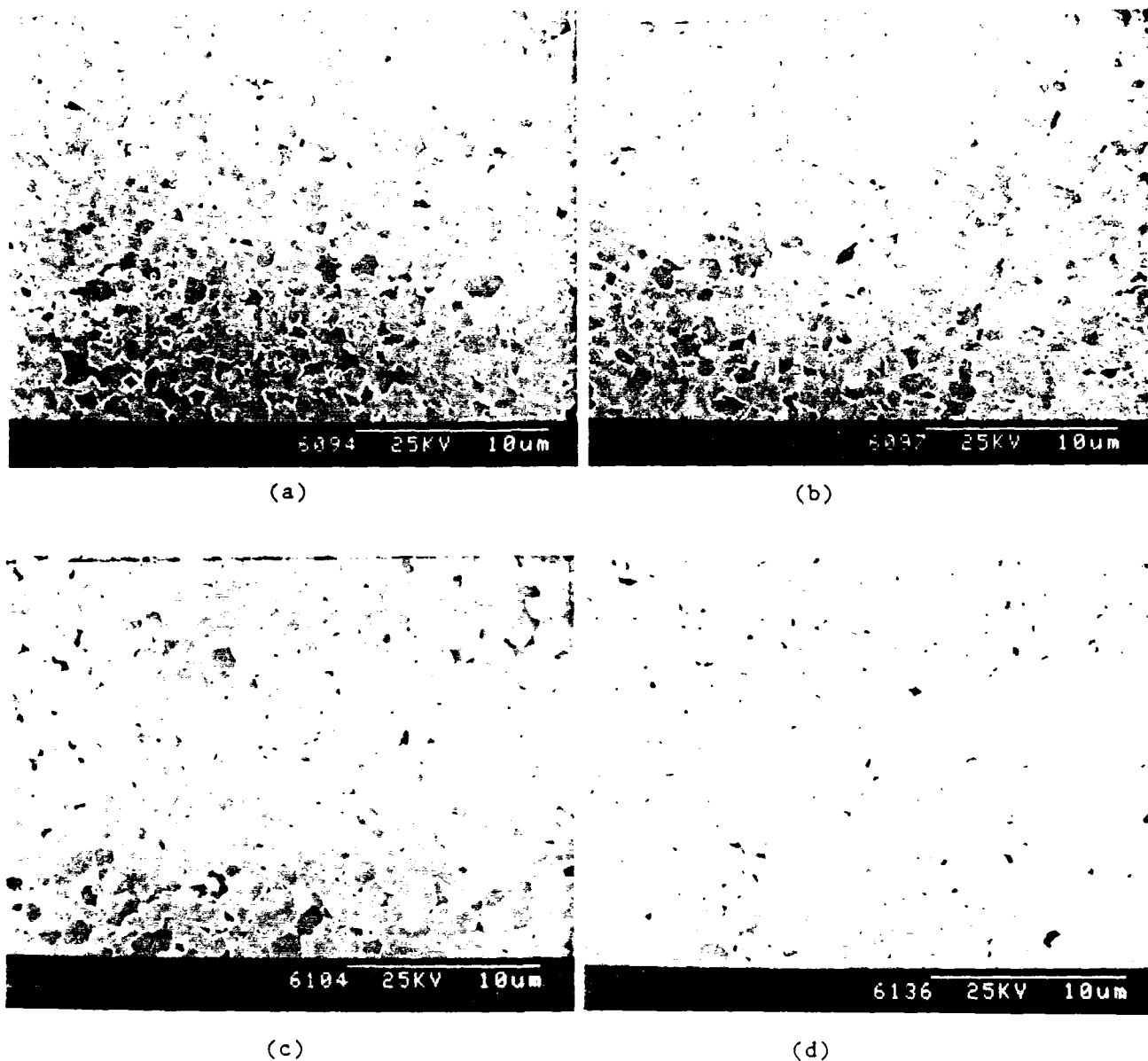


Figure 19. SEMs showing typical microstructures obtained for materials produced using Condition I (see Table 2), with a starting powder composition of a) 5.0, b) 10.0, c) 15.0, and d) 20.7 wt% TiO_2 .

MECHANICAL PROPERTIES OF CYCLICALLY ANNEALED Al_2O_3 - Al_2TiO_5 - TiO_2 COMPOSITES

Sumio Kamiya

ABSTRACT

Cyclically annealed Al_2O_3 - Al_2TiO_5 - TiO_2 composites synthesized from powder containing 5.0 wt% TiO_2 exhibited an average bend strength of 580 MPa and an average fracture toughness of 3.7 MPa $\sqrt{\text{m}}$. Increasing the starting TiO_2 composition to 20.7 wt% reduced the bend strength to 460 MPa and the fracture toughness to 3.1 MPa $\sqrt{\text{m}}$. Specimens denser than 99% of theoretical were strong and tough, but even low-density specimens with large grains showed high values, suggesting that Al_2TiO_5 grain size and the bonding strength between grains are important determiners of a composite's mechanical properties. Fractography revealed the composites' fracture origins to be micropores, very large grains, process-induced defects, and possibly surface flaws due to machining. The process-induced defects and exaggerated grains could be due, respectively, to the rather high PVA solution concentrations used and the initial sintering condition of 1500°C for 2 h.

INTRODUCTION

In previous papers, such interesting microstructural features as irregularly shaped grains, large grain-size distributions, and multiple grain sizes, phase compositions, and densities were reported for Al_2O_3 - Al_2TiO_5 - TiO_2 composites in which the Al_2TiO_5 and TiO_2 phases had been formed by cyclic annealing (1, 2). This paper evaluates the mechanical properties (i.e., bend strength, fracture toughness, Young's modulus, hardness) of Al_2O_3 - Al_2TiO_5 - TiO_2 composites obtained using various cyclic annealing conditions, to clarify the correlations between processing, microstructure, and mechanical properties.

Bend strengths for Al_2O_3 - TiO_2 composites have been reported by Hwang et al. (3), and Hori et al. (4) have reported fracture toughnesses for corundum-rutile composites. Nothing has been reported, however, for the mechanical properties of three-phase composites containing Al_2O_3 , Al_2TiO_5 , and TiO_2 . This paper reports the first such data, including the bend strengths and fracture toughnesses of these unique composites.

EXPERIMENTAL PROCEDURE

Twenty-five grams of a powder mixture containing Al_2O_3 (0.2-0.3- μm classified Reynolds RC-172DBM without MgO, Reynolds Metals Co., Bauxite, AR) and either 5.0, 10.0, 15.0, or 20.7 wt% TiO_2 (Degussa Corp. P-25 anatase, Teterboro, NJ) were dispersed in 250 ml of an aqueous polyvinyl alcohol (PVA) solution (1.0 wt%) that had been vacuum-filtered through a 10-20- μm glass frit. Concentrated HNO_3 was then added to adjust the pH to 2.0-3.0. The mixture was ultrasonically agitated for 20 min and allowed to settle for 24 h to eliminate possible agglomerates, inclusions, dust, etc. The upper stable suspension (180 ml) was removed by cannulation using a pipet, homogenized for 1 h in a ball mill containing no milling media, then flocculated with 225 ml of reagent-grade acetone. The flocs were colloid-pressed into pellets ~38 mm in diameter and ~7 mm thick; the applied pressure and holding time were 35 MPa and 30 min, respectively.

The pellets were dried in air, first at room temperature for 6 h, then at 60°C for 12 h; this was followed by a PVA burnout procedure of heating at a rate of 1°C/min to 600°C and holding at temperature for 1 h. The pellets were then isopressed at 280 MPa for 1 min and annealed under one of several sets of conditions (Fig. 1). The initial sintering condition was 1500°C for 2 h for Condition A, and 1350°C for 0.16 h for Conditions B, C, and D. The number of annealing cycles used for Conditions A, B, C, and D were 1, 1, 2, and 4, respectively.

The bulk density of each annealed pellet was measured by Archimedes' method using reagent-grade *n*-butanol. Quantitative X-ray phase analyses were done for powdered specimens of the annealed materials using a powdered single crystal of silicon as an internal standard material.

Each annealed pellet was machined for mechanical testing into 10

specimens, each measuring 2 x 1.5 x 25.0 mm. Approximately 0.2 mm was also removed from each corner of the specimens. The 4-point bend test was performed using a jig having an inner span of 10 mm, an outer span of 20 mm, and a crosshead speed of 0.25 mm/min (Model 1125 Electrochemical Testing System, Instron Corp., Canton, MA).

Fracture toughness, K_{IC} , of the annealed materials was measured by the indentation method using the following equation (5):

$$K_{IC} = \xi (E/H_V)^{1/2} (P \cdot C)^{-3/2} \quad (1)$$

where ξ is a constant (0.016), K_{IC} is the fracture toughness ($\text{MPa}\sqrt{\text{m}}$), H_V is the Vickers hardness measurement (GPa), E is Young's modulus (GPa), P is the indentation load (N), and C is the average crack length (μm).

Indentations were made using an indentation load of 49 N. A specimen 3 x 4 x 27 mm was cut from the annealed pellet to determine Young's modulus, which was measured from the elastic deflection for four-point bending (inner span, 10 mm; outer span, 25 mm) using the equation $E = \sigma/\epsilon$, in which σ is the four-point bend stress at a load of 245 N, and ϵ is the strain as monitored by strain gauges (Kyowa Electronic Instruments Co., Ltd., Type KFC-1-D9-11) attached to the specimen's lower surface.

Scanning electron micrographs (SEMs) were taken of the fracture surfaces after the bend test to determine fracture origins and the fracture mode.

RESULTS

Relation of Annealed Material Properties to Starting Powder Composition

Table 1 summarizes the densities, phase compositions, and mechanical properties of materials with starting powder compositions of 5.0, 10.0,

Table 1. Densities and phase compositions of annealed materials with the specified starting powder compositions, annealed under Condition C.

Properties of Annealed Materials	Starting Powder Composition (TiO ₂ wt%)			
	5.0	10.0	15.0	20.7
Bulk density (g/ml)	3.945	3.950	3.941	3.898
Relative density (% of theoretical)	99.6 ± 3.8	99.6 ± 1.5	99.1 ± 4.4	97.7 ± 2.8
Al ₂ O ₃ content (wt%)	85.7 ± 3.7	82.0 ± 1.5	78.9 ± 4.4	77.8 ± 2.7
TiO ₂ content (wt%)	2.6 ± 0.3	5.4 ± 0.3	8.9 ± 0.5	12.2 ± 0.3
Al ₂ TiO ₅ content (wt%)	11.7	12.6	12.2	10.0
Bend strength (MPa)	580 ± 100	550 ± 80	550 ± 80	460 ± 60
Weibull parameter	6.2	8.0	8.3	9.5
Fracture toughness (MPa√m)	3.7 ± 0.5	3.4 ± 0.1	3.2 ± 0.2	3.1 ± 0.2
Young's modulus (GPa)	360	360	350	320
Vickers hardness (GPa)	13.3	13.1	13.0	11.5

15.0, and 20.7 wt% TiO₂, annealed under Condition C (2 cycles/2 reheats, sintered at 1350°C for 0.16 h: Fig. 1). A Weibull plot of these materials' bend strengths is shown in Figure 2. The highest average bend strength, 580 MPa, was obtained for samples made with 5.0 wt% TiO₂, though the strengths of such samples ranged from 370 to 700 MPa. At 10.0 and 15.0 wt% TiO₂, the average strength was 550 MPa; this decreased to 460 MPa at 20.7 wt% TiO₂. The Weibull moduli ranged from 6.2 to 9.5 for these composites.

Fracture toughness and Vickers hardness showed a similar tendency with respect to the starting composition; K_{IC} and H_V both decreased, from 3.7 to 3.1 MPa \sqrt{m} , and from 13.3 to 11.5 GPa, respectively.

Figures 3-5 show SEMs of the fracture surfaces of annealed materials after the bend tests had been performed. Figure 3 shows the fracture surfaces of materials with a starting powder composition of 5.0 wt% TiO₂, which produced specimens with the highest average strength. The fracture origins of the high-strength (700 MPa) specimen in this group were difficult to determine, but obvious crack-like defects (8 x 35 μ m) in the mirror region were the fracture origins in the low-strength (460 MPa) specimen.

Figure 4 shows fracture surfaces of samples with a starting powder composition of 15.0 wt% TiO₂; the flaws were, once again, observable in the low-strength material (Figs. 4a and b).

Fracture surfaces at higher magnifications are shown in Figure 5 for the range of starting powder compositions from 5.0 to 20.7 wt% TiO₂. Because of the samples' fine-grained microstructures, the fracture modes were mostly intergranular. Grains were less than a few micrometers in diameter regardless of the starting powder composition.

Relation of Annealed Material Properties to Annealing Conditions

Table 2 summarizes the properties of materials annealed by the four cyclic annealing schedules (Fig. 1) for the starting powder composition of 20.7 wt% TiO₂. Figure 6 is a Weibull plot of bend strength versus failure probability for each annealed specimen. The specimens annealed with 4 cycles/4 reheating treatments (Condition D) had an average bend strength of 520 MPa, though the strengths ranged from >600 MPa to <400 MPa. A similar tendency was observed for specimens annealed using the 1 cycle/1 reheating

Table 2. Properties of annealed materials in this study.

Properties of Annealed Materials	Annealing Condition (A-D), Initial Sintering Conditions ($^{\circ}\text{C}/\text{h}$), and Number of Cycles (1-4)			
	(A)	(B)	(C)	(D)
	1500/2 1	1350/0.16 1	1350/0.16 2	1350/0.16 4
Bulk density (g/ml)	3.899	3.923	3.898	3.867
Relative density (% of theoretical)	97.9 ± 2.1	98.6 ± 2.2	97.7 ± 2.8	97.0 ± 3.3
Al_2O_3 content (wt%)	78.5 ± 2.1	73.9 ± 2.2	77.8 ± 2.7	77.5 ± 3.2
TiO_2 content (wt%)	10.5 ± 0.6	11.7 ± 0.4	12.2 ± 0.3	11.9 ± 0.4
Al_2TiO_5 content (wt%)	11.0	14.4	10.0	10.6
Bend strength (MPa)	530 ± 80	470 ± 60	460 ± 60	520 ± 110
Weibull parameter	7.3	9.6	9.5	5.3
Fracture toughness ($\text{MPa}\sqrt{\text{m}}$)	3.7 ± 0.2	3.6 ± 0.3	3.1 ± 0.2	3.5 ± 0.5
Young's modulus (GPa)	330	340	320	320
Vickers hardness (GPa)	10.1	13.1	11.5	9.9

treatment and an initial sintering condition of 1500°C for 2 h (Condition A). The specimens annealed with 1 cycle/1 reheating treatment (Condition B) and 2 cycles/2 reheating treatments (Condition C) had almost the same average bend strengths, which were lower than those for specimens annealed under Conditions A and D, even though the Weibull moduli for Conditions B and C were higher.

Fracture toughnesses obtained for the specimens annealed using Conditions A, B, and D were 3.7, 3.6, and $3.5 \text{ MPa}\sqrt{\text{m}}$, respectively; the

lowest value, $3.1 \text{ MPa}\sqrt{\text{m}}$, was obtained for a specimen annealed under Condition C. Vickers hardness values ranged from 9.9 to 13.1 GPa for these specimens.

Figures 7-11 are SEMs taken after the bend tests of the fracture surfaces of annealed pellets with starting powder compositions of 20.7 wt% TiO_2 . Figure 7 shows the fracture surfaces of specimens annealed under Condition A, which had the highest average strengths; the actual fracture origins for the specimen with the highest strength (660 MPa) was difficult to determine (Fig. 7a), but a $20\text{-}\mu\text{m}$ grain apparent in the tensile side region of a specimen with a strength of 420 MPa (Figs. 7a and b) was probably the fracture origin for this specimen.

Figure 8 shows the fracture surfaces of specimens annealed under Condition B. The mirror region is apparent in Figure 8 at the corners of the tensile sides, but no actual fracture origins were observed in this region even under higher magnification (Fig. 8b). Surface flaws due to machining were possibly the fracture origins for this specimen.

The fracture surfaces of specimens annealed under Condition C are shown in Figure 9; note the mirror regions at the tensile surface. The mirror region size for the high-strength specimen was smaller than that for the lower-strength specimen, as shown by Figures 9a and 9c. A crack-like defect was observed in the lower-strength specimen (Fig. 9d).

The fracture surfaces of specimens annealed under Condition D are shown in Figure 10; micropores less than $\sim 10 \mu\text{m}$ in diameter were observed for specimens with strengths of 620 MPa (Fig. 10b).

Figure 11 shows fracture surfaces at higher magnifications for specimens annealed under Conditions A-D. These SEMs indicate the primary fracture mode for each condition to be mostly intergranular, although a

partial transgranular mode is also apparent, along with a possible pull-out of such secondary phases as Al_2TiO_5 and TiO_2 . One interesting point to be drawn from Figure 11 is that the specimens with larger grains (Figs. 11a and d) had higher strengths than those with smaller grains (Figs. 11b and c).

DISCUSSION

Internal Cracks and Possible Ways to Improve Processing

Fracture toughness, K_{IC} , is expressed by the following equation (6):

$$K_{IC} = \sigma\sqrt{a\pi c} \quad (2)$$

where σ is the strength, "c" is the internal crack size, and "a" is a constant. The value for "a" was proposed to be 1.93 if the internal crack size is very small compared to the size of the specimen (7). Fractography revealed the fracture origins in lower-strength specimens to be exaggerated grains or crack-like defects; the actual fracture origins in high-strength specimens were rather difficult to identify. The internal crack sizes as calculated using the above equation and experimentally measured K_{IC} values were between 4.3 and 5.2 μm for strengths above 600 MPa. It is therefore reasonable to conclude that micropores of around 5 μm were the fracture origins for high-strength specimens. For low-strength specimens (~400 MPa), the typical internal cracks observed by fractography were 8 x 35 μm crack-like defects (Figs. 3c and d) and 20 x 35 μm large grains (Figs. 7a and b). The internal crack sizes, as calculated from the observed strengths and fracture toughnesses, were 10.6 and 12.9 μm for fracture origins of crack-like defects and exaggerated grains, respectively; these calculated crack sizes, however, are smaller than those observed. Strength

depends not only on crack size but also on the shape of the crack and its orientation with respect to the applied stress. For example, the defect shown in Figs. 3c and 3d is 35 μm long and has a sharp edge; the sharp edge, however, is parallel to the tensile stress applied. Therefore, this specimen showed a relatively high strength of 460 MPa even though the crack was large (the calculated stress would be 250 MPa for $c = 35 \mu\text{m}$ and $K_{IC} = 3.7 \text{ MPa}\sqrt{\text{m}}$).

A 1.0 wt% (PVA:solvent) aqueous PVA solution was employed in this study to produce flocs suitable for colloid pressing, because previous work (1) has shown no significant change in the relative densities of sintered materials for PVA concentrations between 0.2 and 1.0 wt%. Assuming that all of the PVA in solution precipitates after adding acetone, the compact contains 9.1 wt% PVA. Crack-like defects could be process-induced by high PVA concentrations, and such defects were difficult to eliminate completely even after isopressing. A lower PVA concentration appears necessary to eliminate these process-induced defects. If process-induced defects and large grains could be eliminated, the average bend strength would be ~600-700 MPa, which is relatively high.

An additional experiment was therefore performed to examine the effect of lower PVA concentrations on strength. Powder containing 20.7 wt% TiO_2 was prepared using a 0.4 wt% PVA solution (instead of 1.0 wt%), and the sample pellet was annealed under Condition D (4 cycles/4 reheating treatments). Unfortunately, the annealed pellet was machined into only five specimens -- not enough to evaluate the mechanical data. Bend strengths for the available samples are shown in Figure 12. The average bend strength increased slightly, from 520 to 540 MPa, and the standard deviation decreased from ± 110 MPa to ± 20 MPa when the PVA concentration was

reduced from 1.0 to 0.4 wt%. This result suggests that reducing the PVA concentration could potentially eliminate crack-like defects. The floc characteristics obtained, however, were rather poor for colloid-pressing when the PVA concentration was 0.4 wt%. Therefore, an alternative method for producing good flocs with a lower PVA concentration might be to use TiO_2 powder with a lower surface area.

Relation of Mechanical Properties to Starting Powder Composition

Bend strength and fracture toughness decreased as the starting powder's TiO_2 content increased from 5.0 to 20.7 wt%, but the average bend strengths were still high (>550 MPa) in the range from 5.0 to 15.0 wt% TiO_2 (Fig. 13). Materials containing between 5.0 and 15.0 wt% TiO_2 sintered to densities higher than 99% of theoretical and contained irregularly shaped grains less than a few micrometers in length (2). Such microstructures are probably responsible for these composites' high strength. However, the increase in TiO_2 content reduced the strength or toughness values obtained, because it lowered the samples' density due to an increase in their rutile phase content, which has poor mechanical properties relative to the Al_2O_3 matrix.

Alumina composites interspersed with Al_2TiO_5 are particularly interesting for both their mechanical strength and their thermal expansion behavior. The main problem is that an increase in Al_2TiO_5 leads to an improvement in thermal expansion behavior but a rapid reduction in strength. Interestingly, for the Al_2O_3 - Al_2TiO_5 - TiO_2 composites in this study, no significant change in Al_2TiO_5 content (~10-13 wt%) occurred over the relatively wide TiO_2 composition range (5.0-20.7 wt%) in the starting powder, due to the unique processing combinations of cyclic annealing and

reheat treatments. The various composites, which show better thermal expansion behavior than does pure Al_2O_3 , could therefore be prepared without a rapid reduction in strength accompanying the increased amount of TiO_2 in the starting powder composition.

Relation of Strength to Grain Size

As mentioned earlier, one interesting result of the fractography study was that rather large-grained composites with a starting composition of 20.7 wt% TiO_2 showed higher strengths than did those containing small grains when annealed by any of the four annealing schedules (Fig. 6). Moreover, they showed rather high average strengths of 520-530 MPa for densities 97-98% of theoretical (Figs. 6 and 13). One possible explanation is as follows. As the annealed materials were reheated at 1280°C for 12 h to increase their densities, some Al_2TiO_5 reformed (2), resulting in volume expansion, which in turn produced a compressive stress in the Al_2O_3 matrix. Strength data suggest that a critical grain size of Al_2TiO_5 is required to produce this compressive stress, which strengthens the grain boundaries. The bonding strength between grains, associated with the compressive stress, appears to be an important factor in determining the strengths of composites in this study. Further studies of strength versus Al_2TiO_5 grain size should be made to confirm the above hypothesis, under conditions that would prevent the effects of process-induced defects, exaggerated grains, and pores on composite strength.

Relation of Annealing Schedule to Strength

Of the four annealing schedules, Conditions A and D produced the highest average strengths. Both conditions, however, have disadvantages: for example, the initial sintering condition of 1500°C for 2 h (Condition

A) often led to exaggerated grain growth, creating fracture origins, and for all practical considerations, Condition D requires too much time (54 h) for its 4 cycles and 4 reheating treatments.

If, however, the initial sintering is conducted at a temperature below 1500°C (at 1400°C/2 h or 1350°C/2 h, perhaps) and the starting TiO_2 composition is less than 20.7 wt%, relatively high-strength composites could be obtained with shorter cycle times.

Literature Review of Al_2O_3 - TiO_2 Mechanical Properties and Comparison to This Study's Results

Bend strengths have been reported by Hwang et al. for compacts containing various amounts of Al_2O_3 and TiO_2 , sintered at 1500°C for 2 h (3). The Hwang materials, therefore, were two-phase composites containing both Al_2O_3 and Al_2TiO_5 . The samples' bend strengths were found to decrease from ~400 MPa to 250 MPa as the starting powder's TiO_2 composition increased from 1 wt% to 16 wt%. The composites formed in the present study were almost twice as strong as Hwang's for the same starting composition because of the unique process used here of flocculating Al_2O_3 with Al_2TiO_5 and TiO_2 .

Hori et al. (4) reported fracture toughness data for corundum-rutile composites. They used Al_2O_3 - TiO_2 powder synthesized by chemical vapor deposition and tried to sinter the powder below 1280°C, but achieved a relative density of only ~90% of theoretical even using very fine powder. When a specimen accidentally contaminated with sodium was sintered at 1250°C, however, the resulting material reached almost full density due to liquid-phase sintering, and elongated plate-shaped corundum grew after the samples had aged 10-30 h, increasing the samples' fracture toughness from 3 to 6 $\text{MPa}\sqrt{\text{m}}$. These results are interesting, but the high-temperature

capabilities of the Horl specimens are questionable because sodium is known to degrade the high-temperature properties of Al_2O_3 composites.

CONCLUSIONS

The results obtained in this study are summarized below.

1. Al_2O_3 composites interspersed with Al_2TiO_5 and TiO_2 , formed by cyclic annealing and a reheating treatment, produced the highest bend strengths and fracture toughnesses (580 MPa and $3.7 \text{ MPa}\sqrt{\text{m}}$, respectively, for samples with a starting powder composition of 5.0 wt% TiO_2 , decreasing to 460 MPa and $3.1 \text{ MPa}\sqrt{\text{m}}$, respectively, as the starting TiO_2 composition increased).
2. The strengths of even low-density (~97-98% of theoretical) specimens with large grains were high, suggesting that the Al_2TiO_5 grain size and the bonding strength between grains (associated with compressive stress) are important determiners of strength.
3. Typical fracture origins were micropores, process-induced defects, and very large grains; the process-induced defects and exaggerated grains could be due, respectively, to a high PVA concentration and an initial sintering condition of $1500^\circ\text{C}/2 \text{ h}$.
4. The fracture mode for all samples was almost intergranular, together with a partial transgranular mode and the possible pull-out of second phases.

REFERENCES

1. S. Kamiya and H.K. Bowen, "Microstructural Control of Al_2O_3 - TiO_2 Composites by Cyclic Annealing," pp. 978-88 in Ceramic Transactions: Ceramic Powder Science II, the Proceedings of the First International Conference on Ceramic Powder Processing Science (11/1-4/87, Orlando, FL). Edited by G.L. Messing, E.R. Fuller, Jr., and H. Hausner. The American Ceramic Society, Inc., Westerville, OH, 1988.
2. S. Kamiya and H.K. Bowen, "Processing and Microstructural Control of Al_2O_3 - TiO_2 Composites by Cyclic Annealing," submitted to J. Am. Ceram. Soc., 1989.
3. C. Hwang, Z. Nakagawa, and K. Hamano, "Microstructures and Mechanical Properties of TiO_2 -Added Alumina Ceramics," J. Ceram. Soc. Japan, 94 [8] 761-66 (1986).
4. S. Hori, H. Kaji, M. Yoshimura, and S. Somiya, "Deflection-Toughened Corundum-Rutile Composites," pp. 283-88 in Advanced Structural Ceramics. Materials Research Society Symposium Proceedings, Vol. 78 (1987).
5. G.R. Anstis, P. Chantikul, B.R. Lawn, and D.B. Marshall, "A Critical Evaluation of Indentation Techniques for Measuring Fracture Toughness: I, Direct Crack Measurements," J. Am. Ceram. Soc., 64 [9] 533-43 (1981).
6. A.S. Tetelman and A.J. McEvily, Jr., p. 46 in Fracture of Structural Materials. John Wiley and Sons, New York (1967).
7. W.F. Brown and J.E. Srawley, ASTM No. 410 (1967).

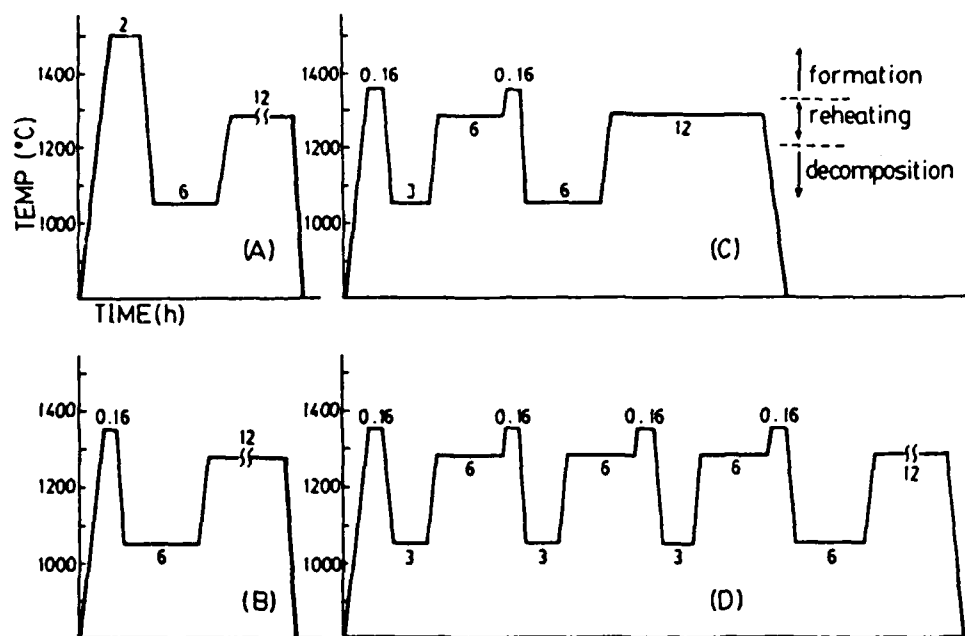


Figure 1. Typical cyclic-annealing conditions employed in this study (heating/cooling rate: 10°C/min).

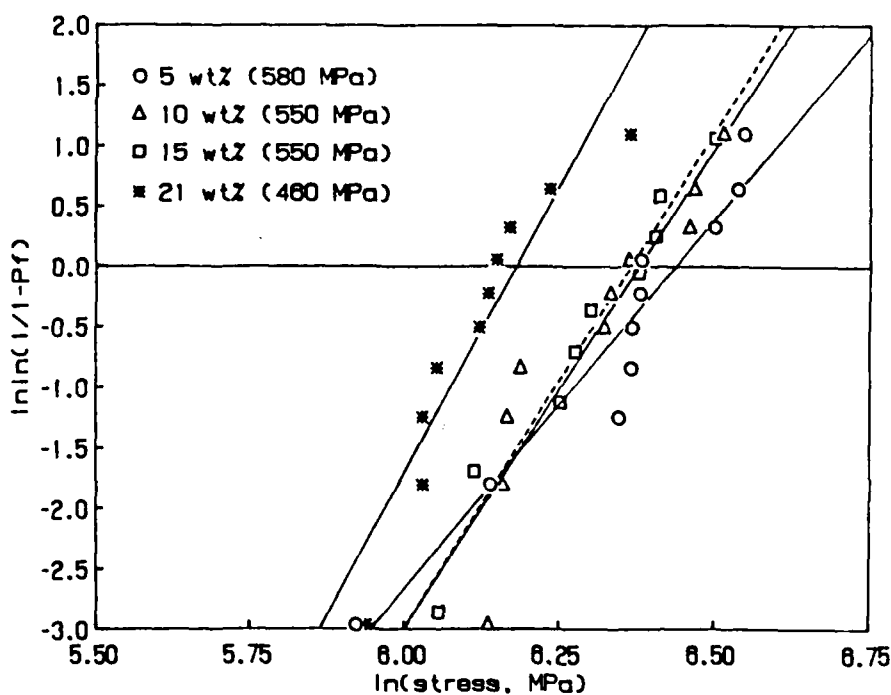


Figure 2. Weibull plot of bend strength versus failure probability for materials with the specified starting TiO_2 compositions, annealed using Condition C (see Fig. 1).

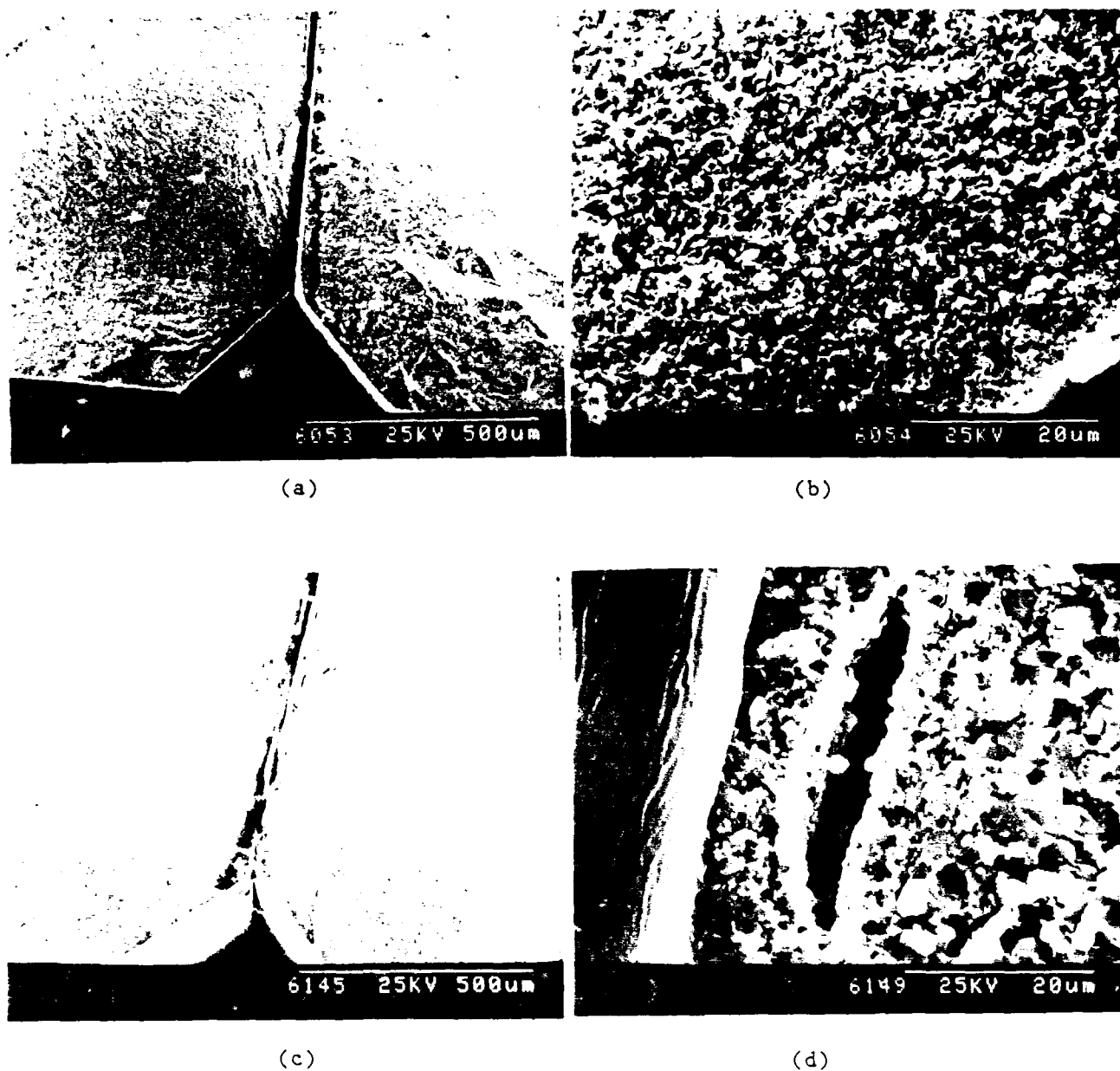


Figure 3. Pairs of SEMs showing low and high magnification, respectively, of fracture surfaces of composites made with a starting powder composition of 5.0 wt% TiO_2 , annealed using Condition C, and having bend strengths of 700 MPa (a and b) and 460 MPa (c and d).

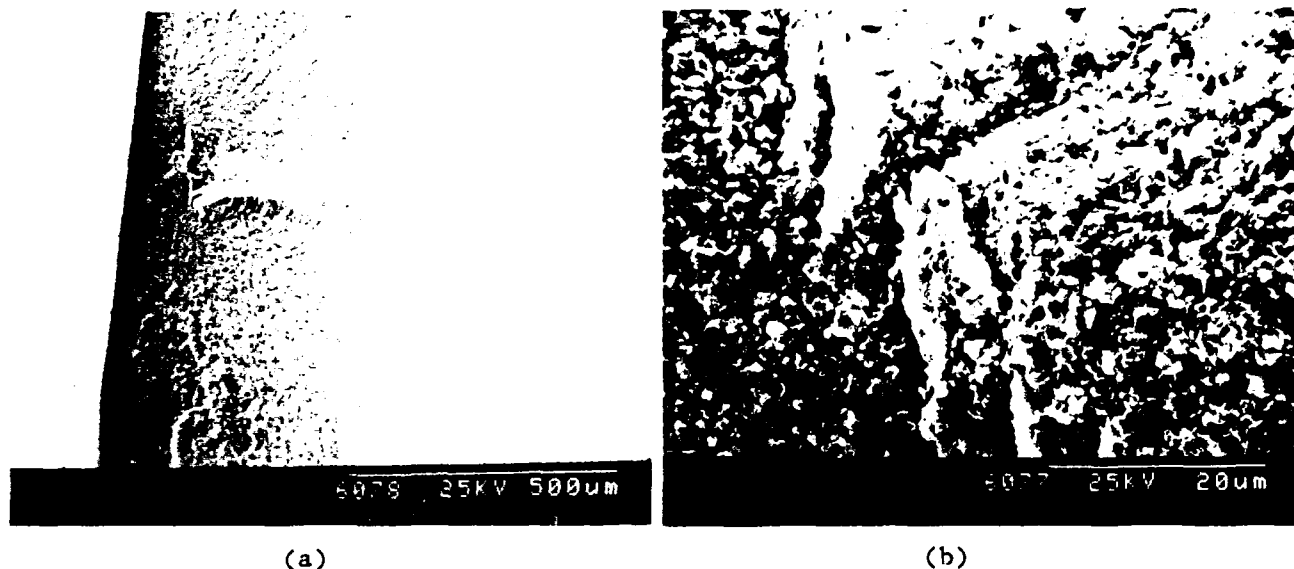


Figure 4. SEMs showing a) low and b) high magnification of fracture surfaces of composites made with a starting powder composition of 15.0 wt% TiO_2 , annealed using Condition C, and having a bend strength of 430 MPa.

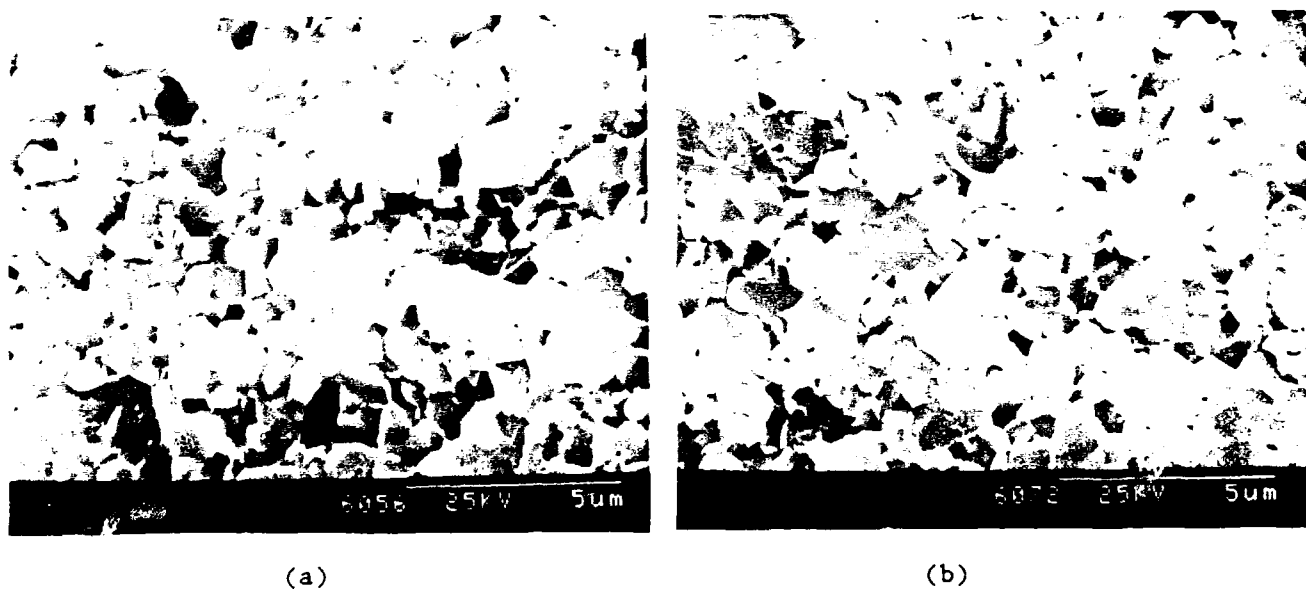


Figure 5. High-magnification SEMs of fracture surfaces of composites annealed using Condition C, made with the following starting TiO_2 compositions and having the specified bend strengths: a) 5.0 wt% TiO_2 -- 700 MPa, b) 10.0 wt% TiO_2 -- 670 MPa.

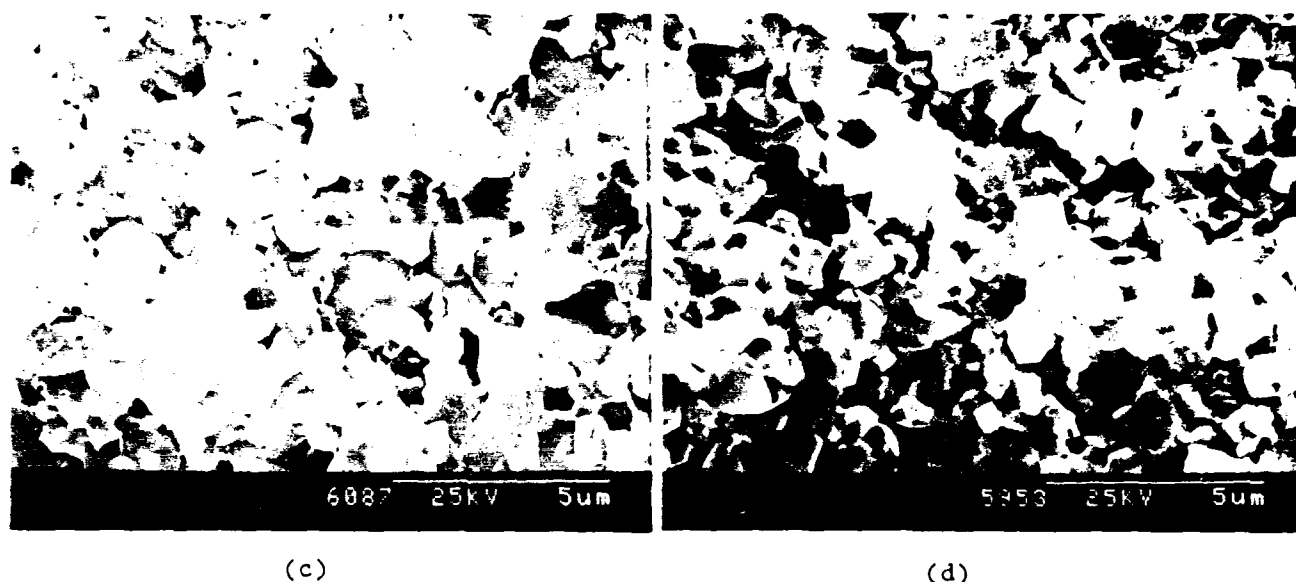


Figure 5 (cont'd). High-magnification SEMs of fracture surfaces of composites annealed using Condition C, made with the following starting TiO_2 compositions and having the specified bend strengths:
c) 15.0 wt% TiO_2 -- 670 MPa, and d) 20.7 wt% TiO_2 -- 580 MPa.

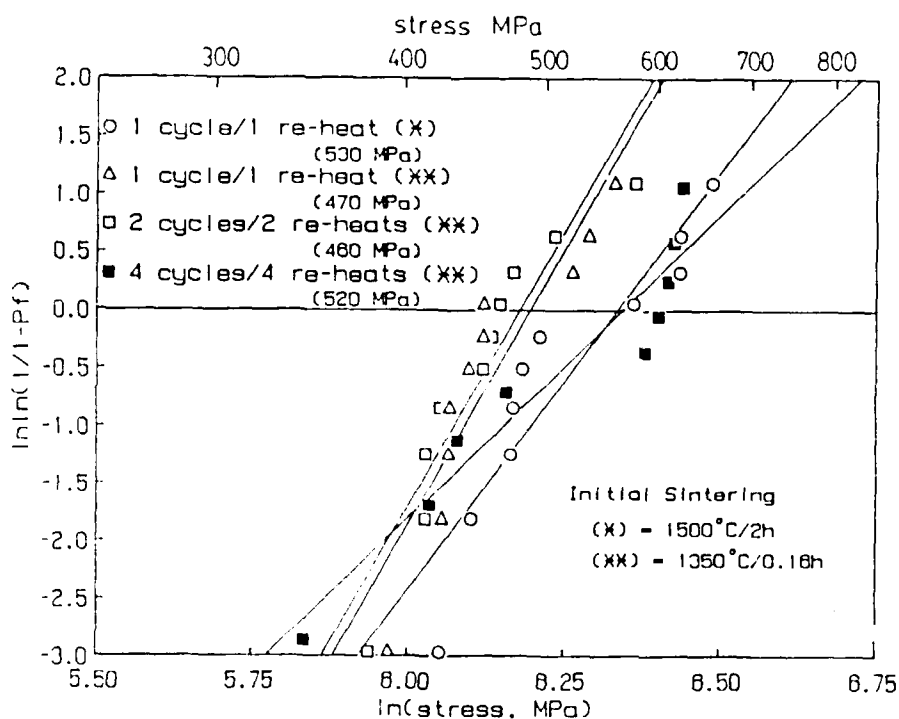


Figure 6. Weibull plot of bend strength versus failure probability for materials made from a starting powder composition of 20.7 wt% TiO_2 , annealed under the specified conditions. Average strength obtained is noted in parentheses below annealing description.

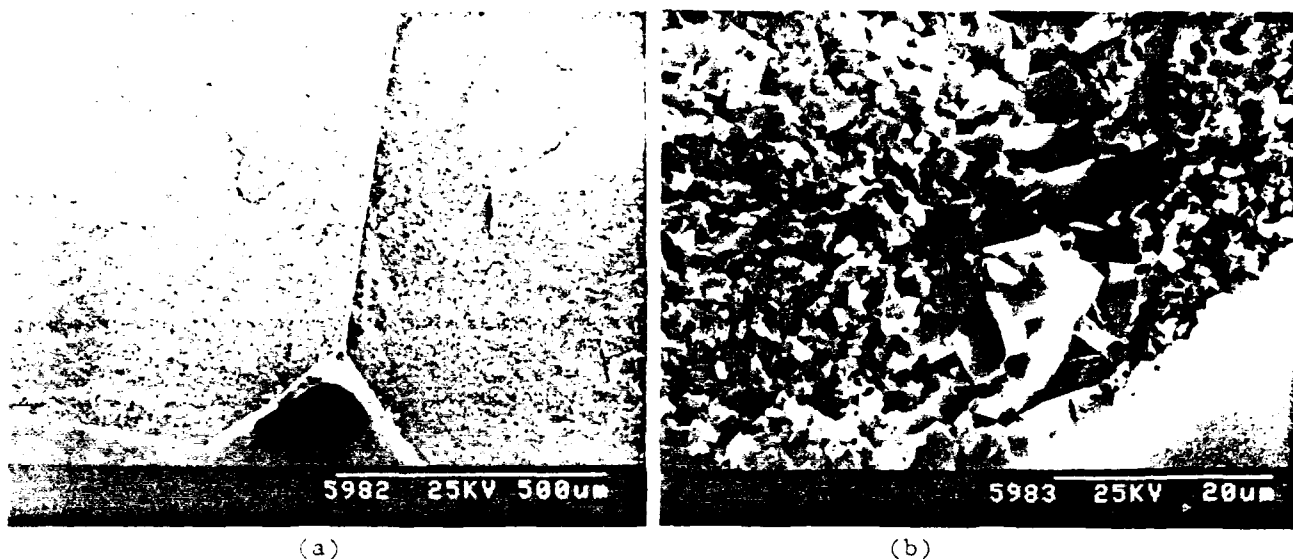


Figure 7 SEMs showing a low and b) high magnification of fracture surfaces of composites made from a starting powder composition of 20.7 wt% TiB₂, annealed using Condition A, and having a bend strength of 427 MPa.

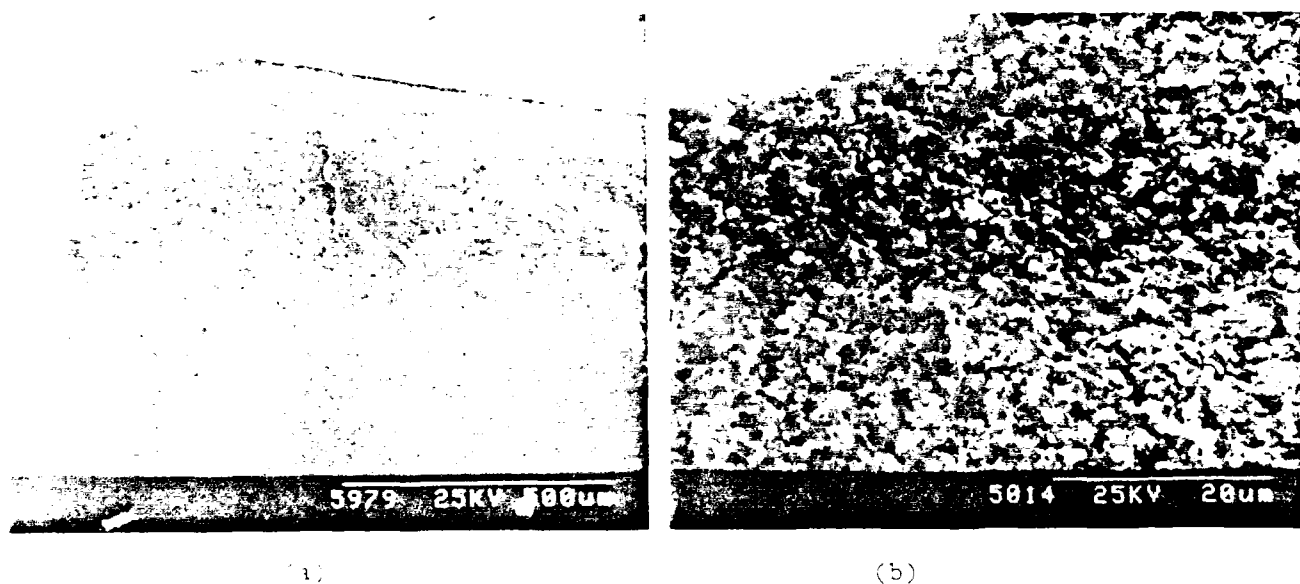
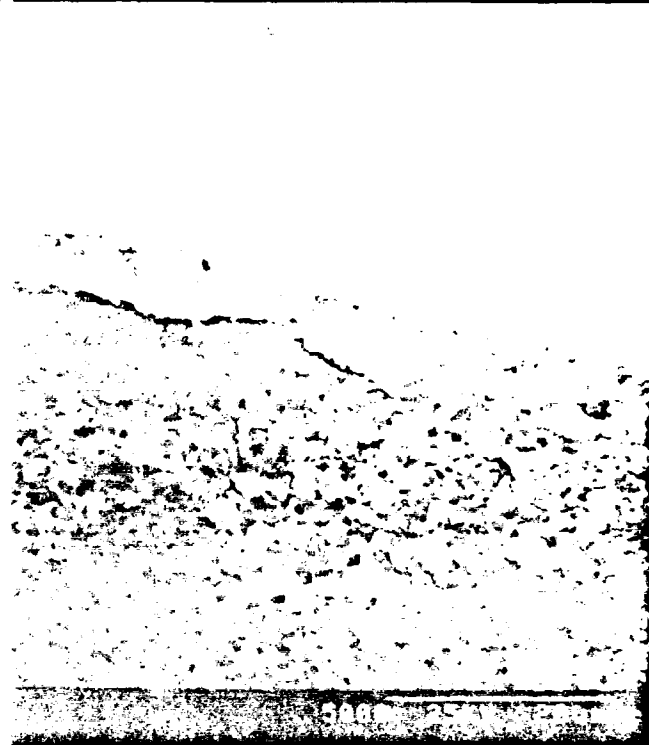


Figure 8 SEMs showing a low and b) high magnification of fracture surfaces of composites made from a starting powder composition of 20.7 wt% TiB₂, annealed using Condition C, and having a bend strength of 427 MPa.



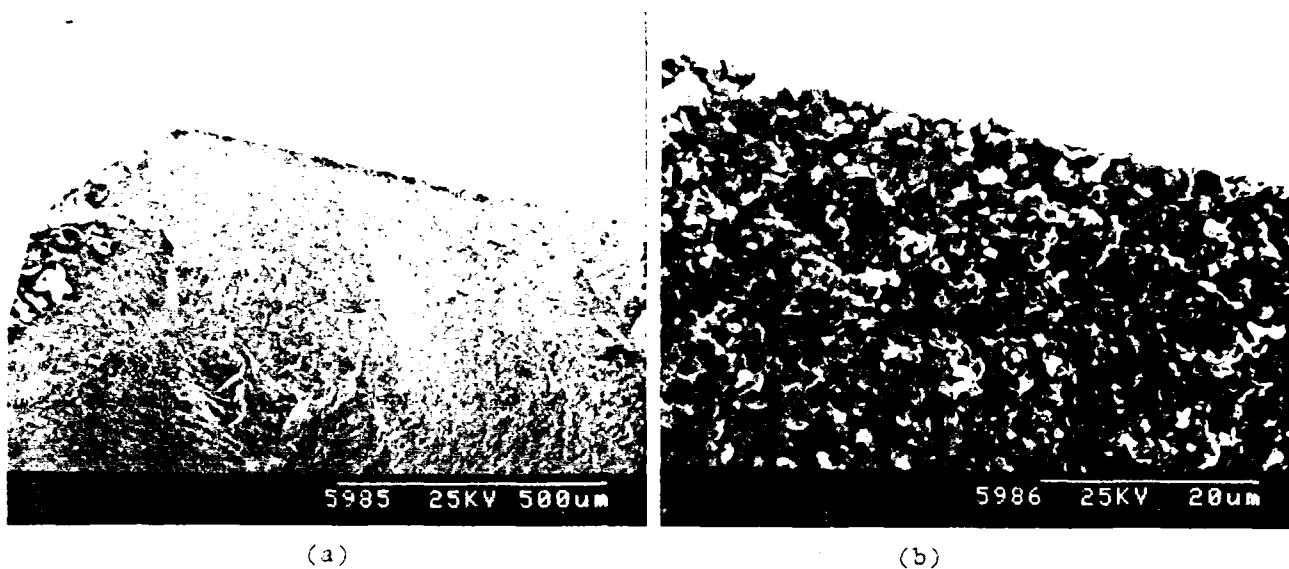


Figure 10. SEMs showing a) low and b) high magnification of fracture surfaces of composites made from a starting powder composition of 20.7 wt% TiO_2 , annealed using Condition D and having a bend strength of 620 MPa.

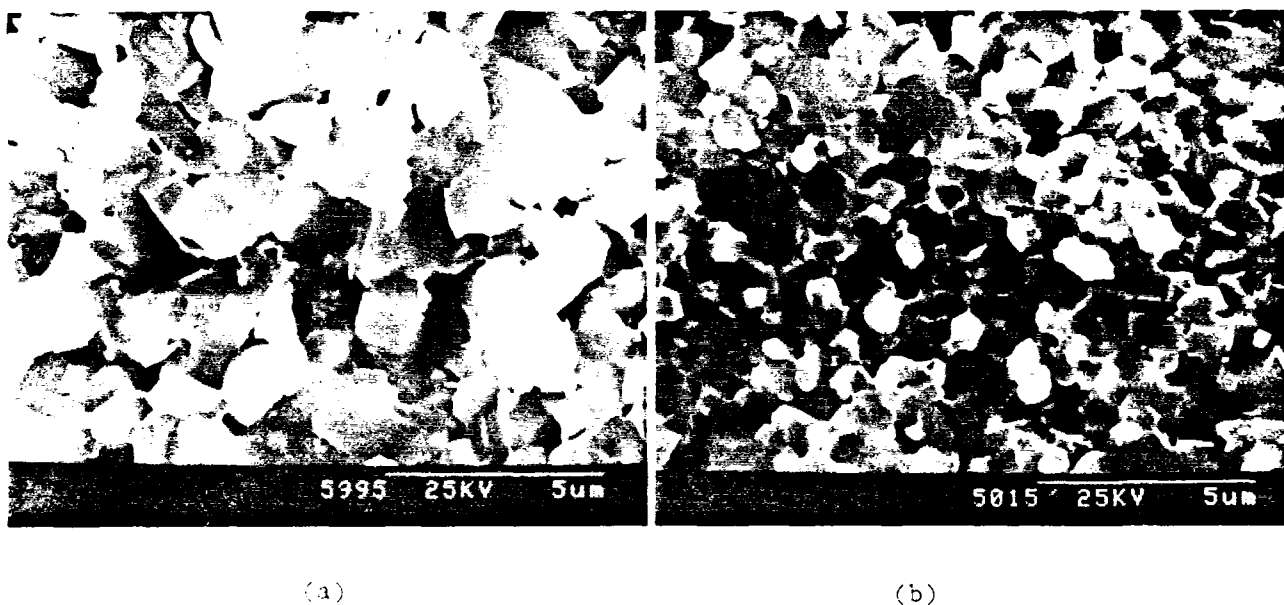


Figure 11. High-magnification SEMs of fracture surfaces of composites made from a starting powder composition of 20.7 wt% TiO_2 , annealed using the following conditions and having the specified bend strength: a) Condition A -- 660 MPa, b) Condition B -- 660 MPa.

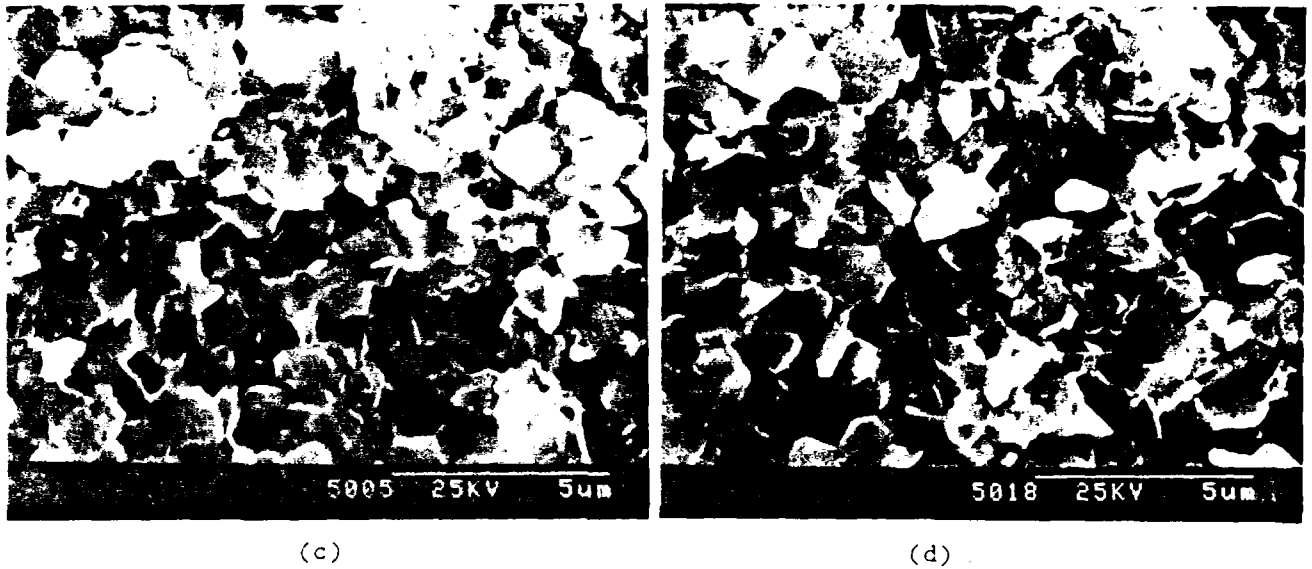


Figure 11 (cont'd). High-magnification SEMs of fracture surfaces of composites made from a starting powder composition of 20.7 wt% TiO_2 , annealed using the following conditions and having the specified bend strengths: c) Condition C -- 580 MPa, and d) Condition D -- 620 MPa.

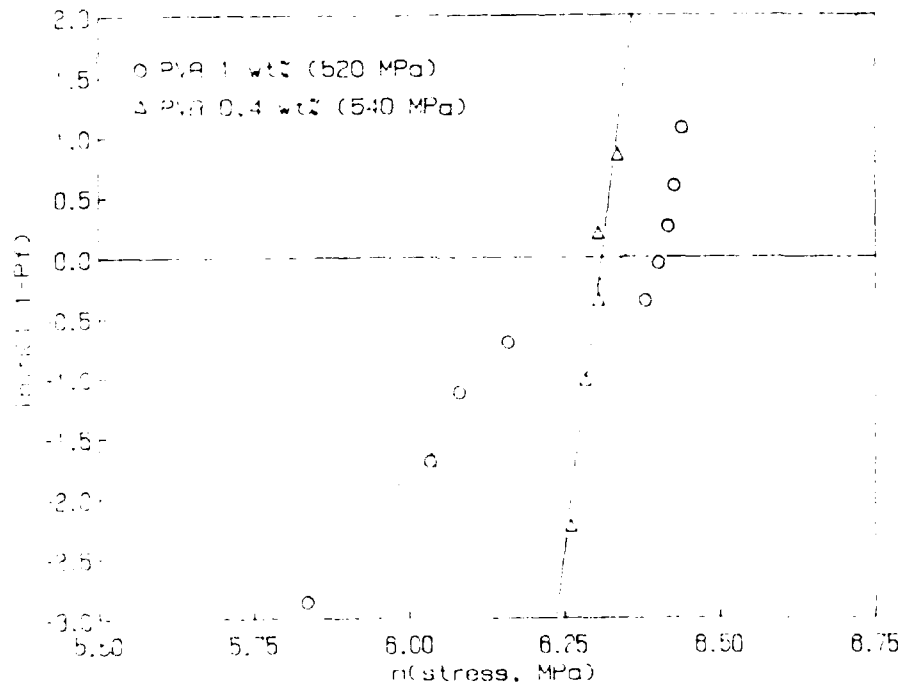


Figure 12. A log-log plot of failure probability versus log(stress, MPa) for composites made from a starting powder composition of 20.7 wt% TiO_2 , annealed using the following conditions and having the specified bend strengths: c) Condition C -- 580 MPa, and d) Condition D -- 620 MPa.

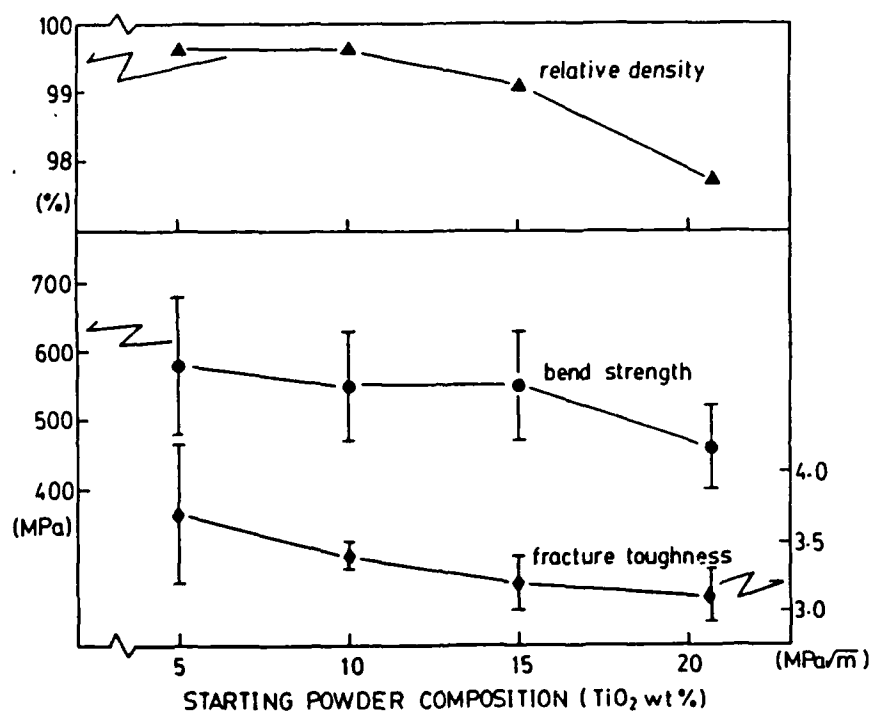


Figure 13. Mechanical properties and densities of samples studied versus their starting powder compositions.

DENSIFICATION OF Al_2O_3 -SiC POWDER COMPOSITES:
I. EFFECTS OF A POLYMER COATING ON SiC PARTICLES

Hyun M. Jang

ABSTRACT

One possible approach to improving the densification of powder composites containing a major crystalline phase which densifies (e.g., Al_2O_3) and a difficult-to-sinter phase (e.g., SiC) is to accommodate the matrix volume shrinkage with a "disappearing" polymer coating. A polymer coating prevents contact between the nonsinterable particles and the surrounding matrix. The coating can be burned off prior to sintering, allowing the matrix phase to "shrink-fit" around the nonsinterable particles during sintering. The effects of a polymer coating on the densification of a two-phase particle system were tested using SiC powder dispersed in an Al_2O_3 matrix. The composites processed with a polymer coating showed more densification during equivalent firing cycles than did those processed without a polymer coating. Densification during sintering was approximately proportional to the amount of polymer adsorbed on SiC, suggesting that the Al_2O_3 matrix did "shrink-fit" into the gaps between the SiC particles and the surrounding Al_2O_3 matrix. Differences in the pore-size distributions of polymer-coated green compacts and uncoated compacts indicated a perturbation of the green microstructure by the gaps. The estimated average thickness of the gap is approximately 20 nm, ~8% of the average radius of the SiC powder used in this study.

I. INTRODUCTION

Heterogeneities in a green compact typically densify at different rates than that at which the matrix phase densifies, and thereby influence sintering behavior in several ways. Recently, an increasing number of experimental and theoretical studies have been conducted on the sintering behavior of a heterogeneous powder packing system that has two or more regions with intrinsically different rates of sintering.¹⁻¹¹ These studies can be divided into the following three categories:

1. studies of the effects of processing-related defects (e.g., agglomerates, inner fine-grained zones, and voids) on sintering uniformity¹⁻²

2. studies of the sintering behavior of bimodal powder compacts containing a uniform dispersion of a hard, nonsinterable second-phase material³⁻⁸
3. studies of constrained sintering, such as the densification of particulate films on rigid substrates⁹⁻¹¹

In bimodal packing systems, a second phase of nonsinterable particles decreases the sintering rate considerably by introducing shear stress in the matrix and tensile hoop stress at the hard-particle/matrix interface. However, it appears that there has been no systematic investigation of an efficient pressureless densification route for composites containing dense second-phase particles that do not densify under the conditions at which the matrix sinters.

One possible approach to efficient pressureless densification for such a heterogeneous packing system involves coating the hard second-phase particles with a polymer, preventing contact between the nonsinterable particles and the surrounding matrix. The coating can be burned off prior to sintering, yielding a free volume for the matrix phase to "shrink-fit" around the nonsinterable particle during sintering. In previous work on the pressureless sintering of SiC whisker-reinforced alumina composites,¹² an attempt was made along this line (that is, an attempt was made to "shrink-fit" an alumina matrix around SiC whiskers during densification). However, it has not been demonstrated that a polymer coating that leaves a void space around the SiC when removed leads to more efficient densification than any other possible processing scheme. Furthermore, it is difficult to directly observe the effects of a polymer coating on the densification of an Al₂O₃-SiC whisker composite, due to the difference in shape and size between Al₂O₃ and SiC (Al₂O₃ particles are ~0.4 μm in

diameter; SiC whiskers are ~0.6 μm in diameter and 10-80 μm in length) and the three-dimensional network formation of whiskers in a green compact.¹²

This paper presents research on the effects of two processing schemes (i.e., with and without a polymer coating on the nonsinterable particles) on the densification of a bimodal packing system; SiC powder dispersed in an Al₂O₃ matrix served as the model system. Submicrometer SiC particles similar in size to the Al₂O₃ particles were used in this study to more clearly observe the effects of a polymer coating on densification. To carefully estimate the effects of void spaces, or "gaps," formed by burning off polymer coatings from SiC particles (and thus to test the concept of "shrink-fitting") on densification, the following points must be examined:

- the effects of a polymer coating on densification during sintering (i.e., whether or not a polymer coating on the second-phase material increases densification)
- the effects of the gap volume on the extent of densification during sintering
- the effects of such characteristics of gaps as their thickness on the green compact microstructure (e.g., the pore-size distribution)
- the selectivity of the coating or adsorption of polymers on the nonsinterable second-phase particles (e.g., SiC)

The concept on which this study was based is schematically represented in Fig. 1.

II. EXPERIMENTAL METHOD

A. Powders

The Al₂O₃ powder used in this study was Reynolds RC-172 DBM without MgO additives (Reynolds Metals Co., Bauxite, AR); a size-classified¹³ portion

having particle diameters between 0.3 and 0.5 μm was used. The impurity analysis, performed by the inductively coupled plasma (ICP) technique, showed that the major impurity in the Al_2O_3 was silicon (220 ppm). The SiC powder used in this study was Fujimi GC #10000 (α -SiC; Fujimi Kenmazai Kogyo Co., Ltd., Nagoya, Japan). The mean SiC particle diameter, determined by photon correlation spectrometry (Coulter Counter Model N4, Coulter Electronics), was 0.61 μm in an OLOATM1200/hexane suspension.¹⁴ Particle-size distributions were obtained by counting a total of 650 particles in scanning electron micrographs (Model S-530, Hitachi, Ltd.). About 90% of the particles had diameters between 0.1 μm and 0.8 μm ; the number average diameter was 0.48 μm .

B. Processing and characterization

Al_2O_3 -SiC powder composites were prepared using two different processing schemes: consolidation with and without a polymer grafted onto the SiC particles. Five different processing methods were used to prepare the composites: two for the polymer-coated SiC particles and three for the uncoated particles. For all processing methods, SiC concentrations from 0 to 15 wt% were used.

In the two methods used for preparing composites with a polymer coating on the SiC particles, either a polymethylmethacrylate/polystyrene copolymer (PMMA/PS; MW 270,000, Polysciences, Warrington, PA) or silanized polystyrene (MW 250,000) was used as the grafting polymer. The silanized polystyrene was prepared by Friedel-Crafts alkylation of the corresponding polystyrene with para-chloromethylphenyltrimethoxysilane.^{12,15} Both infrared and NMR spectroscopy indicated that phenyl groups in the polystyrene had been alkylated with benzyltrimethoxysilane groups; the ICP

analysis of silicon in the polymer indicated that one in every forty phenyl groups in the silanized polystyrene was alkylated.^{12,15}

The SiC dispersion was sterically stabilized with 20 wt% polymer (with respect to the weight of SiC) in toluene. A SiC packing density ~35% of theoretical was obtained by allowing the dispersion to sediment under the force of gravity.

To prepare the SiC for mixing with Al₂O₃, the SiC dispersion was sonicated and tumbled for 48 h to ensure a good dispersion, then briefly centrifuged, and the supernatant discarded to minimize adsorption of excess polymer on the Al₂O₃ upon mixing. The SiC suspension was redispersed by adding toluene and sonicating. The resulting SiC powder suspension was mixed with an Al₂O₃/toluene suspension stabilized with 8 wt% oleic acid (with respect to the weight of Al₂O₃).

The following three methods were used to prepare composites without a polymer coating on the SiC particles. In the first, OLOA™1200 (6 wt% with respect to the total weight of the powders; OLOA/lubricating mineral oil 50/50 solution, Chevron Chemical Co., Richmond, CA) was used as received to stabilize an Al₂O₃-SiC mixed suspension in toluene. In the second method, OLOA™1200 was again used to stabilize an Al₂O₃-SiC mixed suspension, but in hexane.¹⁴ The dispersion/sediment test showed that both the Al₂O₃ and SiC powders are stable in an OLOA™1200/hexane (or toluene) solution, attaining ~35-40% of theoretical packing density. Studies of the stability of carbon black in an OLOA™1200/nonaqueous medium^{16,17} suggested that a combination of steric stabilization and electrostatic interparticle repulsion (by a charge separation mechanism via proton transfer) plays an important role in the stabilization of powder in an OLOA™1200/nonaqueous medium.

In the third method for preparing composites without a polymer coating, the SiC dispersion was stabilized with 5 wt% of octadecyltrichlorosilane (C-18 chlorosilane; Petrarch Systems, Bristol, PA) in toluene. Fourier transform infrared spectra of the SiC powder treated with C-18 chlorosilane showed strong absorbances near 3000 cm^{-1} . These absorbances are associated with C-H stretching vibrations, and indicate that the C-18 chlorosilane remained attached to the SiC surface. The dispersion/sediment test in toluene showed that 5 wt% of the C-18 chlorosilane makes the suspension very stable, for a minimal amount of dispersant in the suspension. After sonication and tumbling for 48 h, the SiC powder/C-18 chlorosilane suspension was mixed with an Al_2O_3 /toluene suspension stabilized with oleic acid (8 wt% with respect to the weight of Al_2O_3).

Each of the Al_2O_3 -SiC mixed dispersions was colloid-pressed at 53.79 MPa (7800 psi) using a laboratory press and 0.20- μm filters to cover the porous metal frits used in the press.¹⁸ Disc-shaped green compacts ~2.0 cm in diameter and 0.75-0.80 cm thick were obtained. After the compacts were dried, the organic materials were burned out at 550°C for 2 h in air (heating rate $\sim 8^\circ\text{C}/\text{min}$). The percent theoretical density of the green compacts was estimated from the sample mass and dimensions determined by a micrometer; only perfectly disc-shaped compacts were used. The green-compact density was cross-checked with the results obtained by an intrusion experiment using a mercury porosimeter (Autopore II 9220, Micromeritics).

The green compacts were packed with SiC powder in a graphite crucible. Sintering experiments were conducted at 1550°C for 1.5 h in a graphite tube resistance furnace with a flowing, high-purity argon atmosphere. The heating rate to the firing temperature was $\sim 15^\circ\text{C}/\text{min}$. The pore-size

distributions of the green compacts and fired samples were obtained by mercury porosimetry; approximately one gram of sample was used for each mercury porosimetry experiment. Fig. 2 outlines the general experimental procedure used in this study.

Thermal gravimetric analysis (TGA 7 Thermogravimetric Analyzer, Perkin-Elmer) was used to examine the relative adsorption of polymer (PMMA/PS) and organic dispersant (oleic acid) on the Al_2O_3 and SiC powders. To prepare the powder/polymer dispersions for analysis, separate batches of Al_2O_3 and SiC powders were tumbled in toluene with 20 wt% of PMMA/PS for 48 h. Similarly, to prepare powder/organic dispersions, Al_2O_3 and SiC powders were tumbled in toluene with 8 wt% oleic acid. The dispersions were centrifuged and redispersed in toluene again, and the resulting dispersions were filtered before drying.

To examine the effects on densification of the amount of adsorbed polymer on SiC, three batches of polymethylmethacrylate (PMMA) having different molecular weights ("very high MW", "medium MW", "low MW"; Aldrich Chemical Co., Inc., Milwaukee, WI) were used as the adsorbing polymers. Each SiC dispersion was prepared with 20 wt% of a PMMA of a characteristic molecular weight. Three Al_2O_3 -SiC green compacts were obtained by the processing method outlined previously for composites with polymer-coated SiC particles. The amount of PMMA still adsorbed on the SiC after redispersion was determined by thermal gravimetric analysis. The amounts of "very high MW", "medium MW," and "low MW" PMMA adsorbed per gram of SiC were 59 mg, 26.5 mg, and 24.2 mg, respectively. The extent of densification during sintering (change in percent theoretical density) was found to correlate directly with the amount of PMMA adsorbed on SiC.

III. RESULTS AND DISCUSSION

A. Characterization of green compacts

To accurately estimate the effects on densification of a gap between each SiC particle and the surrounding Al₂O₃ matrix, the porosity associated with the Al₂O₃ matrix region should be the same for both coated and uncoated green compacts. Thus, after polymer burnout the densities of green compacts processed with polymer-coated SiC particles should be lower than the densities of green compacts processed without polymer coatings, due to the gap between each SiC particle and the surrounding Al₂O₃ matrix in the polymer-derived samples (Fig. 1). As shown in Fig. 3, the experimental results for the processing routes do show that the densities of the polymer-derived samples were lower than the densities found for the uncoated samples.

The average thickness of the gap between each SiC particle and the surrounding Al₂O₃ matrix can be estimated from the difference in green density between coated and uncoated compacts. The following two assumptions were made to estimate this thickness from the data on green compact densities after organic burnout:

1. For green compacts, the porosity associated with the Al₂O₃ matrix region is the same for both coated and uncoated compacts.
2. For simplicity's sake, both Al₂O₃ and SiC particles in a green compact can be treated as spherical particles with their characteristic radii.

With the above two assumptions, the following equation for the average thickness of the gap, t , can be derived (see Appendix):

$$t = r_s(u-1)$$

where r_s is the average radius of the SiC particles; u is defined in the Appendix. Taking $0.50 \mu\text{m}$ as the average diameter of the SiC particles, the average gap thickness can be estimated from the data shown in Fig. 3. The estimated average thickness is approximately 20 nm for 5 wt% or more SiC (Fig. 4), which is about 8% of the particle radius for the SiC powder used in this study. The substantially higher gap thicknesses found for lower weight percentages of SiC are probably due to inaccuracies introduced in the estimation of green compact densities.

The root-mean-square of the length of linear polymers, $\langle r^2 \rangle^{1/2}$, can be roughly viewed as the mean diameter of the polymer chain. For many common carbon-backbone polymers, this is given by $0.06M^{1/2}$, in nanometers, where M is the molecular weight.¹⁹ If this equation is used to estimate the theta thickness of the grafted, silanized polystyrene or adsorbed PMMA/PS (each with a molecular weight of ~250,000), a gap thickness of 30 nm is predicted. The slightly smaller gap thickness of 20 nm estimated from green density data presumably reflects compression of the polymer adsorbed in the green compact due to colloidal pressing, a change in polymer environment (as toluene was replaced by air in the drying process) in the gap region during drying, and resulting changes in polymer configuration on the SiC surface.

Fig. 5 shows pore-size distributions in the region of the most frequent pore radius for five green compacts containing 10 wt% SiC after organic burnout. As shown in Fig. 5, the most frequent pore radius for polymer-coated compacts is slightly (~3 nm) higher than the most frequent pore radii found for uncoated compacts, which probably indicates disturbances in the green microstructure introduced by the gap between each SiC particle

H. Jang AFOSR/1988 Al_2O_3 -SiC: EFFECTS OF POLYMER COATING ON SiC
and the surrounding Al_2O_3 matrix. The differences in pore-size distribution between the polymer-coated compacts and the C-18 chlorosilane-derived compact support this hypothesis because the processing conditions (e.g., the dispersion medium (toluene) and the dispersant for Al_2O_3 (oleic acid)) were the same in both cases; only the dispersant for SiC differed (polymer vs C-18 chlorosilane).

Fig. 6 further elucidates the effects of a polymer coating on the green body microstructure by comparing the pore-size distributions of two Al_2O_3 -SiC (10 wt%) composites with and without a polymer coating on the SiC particles (silanized polystyrene and C-18 chlorosilane, processed as above) to that of pure Al_2O_3 dispersed with 8 wt% oleic acid in toluene. The overlap region between the polymer-coated (curve 2) and the uncoated composite compacts (curve 3) is designated "OR". This overlap region in the pore-size distribution should correspond to the porosity characteristics associated with the Al_2O_3 matrix region which is not affected by SiC particle dispersion in the composites. This conclusion is clearly supported by the fact that the most frequent pore radius for the pure Al_2O_3 compact (curve 1) is exactly that radius corresponding to the peak of the overlap region, "OR", in Fig. 6. Thus the area to the left of the "OR" region in the pore-size distribution of the polymer-coated compact (curve 2) should reflect a perturbation (i.e., a shift to larger pore diameters) in the green microstructure introduced by the dispersed SiC particles and by the gap between each SiC particle and the surrounding Al_2O_3 matrix.

Thermal gravimetric analysis (TGA) was used to examine the relative adsorption of polymer (PMMA/PS) and organic dispersant (oleic acid) on the Al_2O_3 and SiC powders. The TGA results (Fig. 7) clearly show that PMMA/PS

H. Jang AFOSR/1988 Al_2O_3 -SiC: EFFECTS OF POLYMER COATING ON SiC

adsorbs selectively on SiC particles, whereas oleic acid adsorbs more strongly on Al_2O_3 particles. The selective surface affinities of PMMA/PS and oleic acid for SiC and Al_2O_3 , respectively, must be taken into account to accurately examine the effects of gaps left between SiC particles and the Al_2O_3 matrix on densification (Fig. 1). The strong, selective adsorption of PMMA/PS on SiC can be viewed as the interaction of the ester functional group (of the PMMA unit in PMMA/PS) with the silanol site on the surface of the oxidized SiC powder in a neutral solvent used here (e.g., toluene). Fowkes and Mostafa's work²⁰ on the interaction of PMMA with a silica filler in a neutral solvent supports this conclusion.

Finally, the homogeneity of SiC distribution in two green compacts was examined by energy dispersive spectroscopy (EDS). Ten spots per sample were examined on a PMMA/PS-coated sample and on an OLOA™1200/hexane-derived sample (10 wt% SiC); the area examined per spot was $120 \mu\text{m}^2$. The average estimated SiC content of the PMMA/PS-coated sample was 10.7 wt% (standard deviation 1.51%); the average estimated SiC content of the OLOA™1200/hexane-derived compact was 10.9 wt% (standard deviation 1.84%). Neither sample showed appreciable SiC segregation during colloidal consolidation.

B. Effects of a polymer coating on densification

Fig. 8 shows sintering results as a function of SiC content for composites fired at 1550°C for 1.5 h. The following two facts are clear from these results: 1) the composites processed with polymer-coated SiC consistently have higher densities than those processed without polymer coatings for SiC concentrations above 3 wt%, and 2) as the SiC powder concentration in both types of composites increases, densification decreases rapidly. Fig. 9 illustrates densification during sintering in

terms of change in percent theoretical density. These results clearly demonstrate that composites processed with polymer-coated SiC undergo more densification than those processed without a polymer coating on the SiC. As the SiC powder concentration increases, differences in the fired densities of the coated and uncoated samples increase.

The x-ray powder diffraction patterns of three Al_2O_3 -SiC composites were also examined. The first composite (15 wt% SiC) was a PMMA/PS-coated sample. The second and third samples (20 wt% SiC) were derived, respectively, from an aqueous suspension at pH 10.5 without any organic dispersant or from an aqueous solution of polyvinylpyrrolidone. For all three samples, only peaks associated with α - Al_2O_3 and SiC were observed. No evidence for the formation of crystalline mullite, $3\text{Al}_2\text{O}_3:2\text{SiO}_2$, was observed.¹² The SiC powder used to pack the composites was also examined by x-ray powder diffraction. Only peaks associated with SiC were detected. Composites with a low SiC loading (< 6 wt%) turned dark grey upon firing. This effect was greatest for pure Al_2O_3 and decreased with increasing SiC loads. Previous work on Al_2O_3 -SiC whisker composites¹² suggests that the grey color of the composites is due to elemental carbon from the graphite crucible; carbon in the sintering atmosphere of the graphite tube furnace may inhibit sintering.

The pore-size distributions of fired composites containing 10 wt% SiC (Fig. 10) clearly show that the composites containing polymer-coated SiC are less porous and have smaller pore radii than the "uncoated" composites. The most frequent pore radii for the polymer-coated and the uncoated samples are approximately 75 nm and 125 nm, respectively. Therefore, the uncoated samples underwent more extensive pore coarsening during sintering than did the polymer-coated samples (i.e., 90 nm vs 40 nm).

More concrete evidence for the effect of polymer coatings on densification was obtained from data on the density of fired composites using several polymers with different molecular weights. In Fig. 11, the percent theoretical density (open circles) and the change in percent theoretical density (filled circles) during the sintering of 10 wt% SiC composites were plotted as a function of the weight in grams (for three PMMA molecular weights and one PMMA/PS molecular weight) of polymer adsorbed per gram of SiC. An approximately linear correlation between the change in percent theoretical density (or the density of the fired composites) and the amount of adsorbed polymer would indicate that the volume of the gap between SiC particles and the surrounding Al_2O_3 matrix does indeed affect densification. A semiquantitative analysis for the correlation actually obtained can be made by adopting the following two assumptions:

1. The chain segment density of the polymer is uniform throughout each gap region in a green compact before polymer burnout.
2. For a given weight fraction of SiC, shrinkage of the coated composite (ΔV_c) is the sum of the following:

$$\Delta V_c = \Delta V_{uc} + V_g \quad (1)$$

where ΔV_c and ΔV_{uc} are the changes in volume for a unit mass of the coated and uncoated composites, respectively, and V_g is the volume of the gap.

Equation 1 can be considered true as long as the following is also true:

$$\Delta V_c < (\Delta V_m)_{th} \quad (2)$$

where $(\Delta V_m)_{th}$ is the change in volume of the matrix during its transition from the green state to a fully dense state. Equation 2 indicates that there is a limit to the density increase possible for a coated composite, and that the density increase is dependent on V_g .

Based on Assumption 1, the amount of polymer adsorbed on a SiC particle (W_p) can be written:

$$W_p = \rho_p V_g \quad (3)$$

where ρ_p is the chain segment density of adsorbed polymer in the gap region. Substituting Equation 3 into Equation 1 yields:

$$\Delta V_c - \Delta V_{uc} = W_p / \rho_p \quad (4)$$

which predicts that the difference in volume change between coated and uncoated composites during densification should be proportional to the amount of polymer adsorbed on SiC particles for composites containing a given weight fraction of SiC, assuming that ρ_p is a constant for the polymers studied.

A plot of $\Delta V_c - \Delta V_{uc}$ values for this study (calculated from the data in Figures 3 and 8 for ΔV_{uc} and Figure 11 for ΔV_c) against W_p did reveal an approximately linear relationship (Fig. 12) at concentrations below 0.04 g polymer per gram of silicon carbide. The decrease in slope of the plot at high W_p values suggests that a limit probably exists to the increase in density that can be achieved by increasing the amount of adsorbed polymer.

VI. SUMMARY

It has been shown that composites processed with a polymer coating undergo more densification than do those processed without a polymer coating. The densification during sintering (i.e., the change in the

percent theoretical density) is approximately proportional to the amount of polymer adsorbed on SiC, suggesting "shrink-fitting" of the Al_2O_3 matrix into the gap region.

The pore-size distribution in polymer-coated green compacts showed a shift to larger pore diameters in the green microstructure from the pore-size distribution in uncoated compacts. This is due to the dispersed SiC particles and the gaps between SiC particles and the surrounding Al_2O_3 matrix. The estimated average thickness of each gap is approximately 20 nm.

REFERENCES

1. A. G. Evans, "Considerations of Inhomogeneity Effects in Sintering," J. Am. Ceram. Soc., 65 [10], 497-501 (1982).
2. F. F. Lange and M. Metcalf, "Agglomerate Motion and Cracklike Internal Surface Caused by Differential Sintering," J. Am. Ceram. Soc., 66 [6], 398-406 (1983).
3. R. Raj and R. K. Bordia, "Sintering Behavior of Bimodal Powder Compacts," Acta metall. 32 [7], 1003-19 (1984).
4. G. W. Scherer, "Viscous Sintering of a Bimodal Pore Distribution," J. Am. Ceram. Soc., 67 [11], 709-15 (1984).
5. R. K. Bordia and R. Raj, "Analysis of Sintering of a Composite with a Glass or Ceramic Matrix," 69 [3], J. Am. Ceram. Soc., C-55-C-57 (1986).
6. C. H. Hsueh, A. G. Evans, and R. M. McMeeking, "Influence of Multiple Heterogeneities on Sintering Rates," J. Am. Ceram. Soc., 69 [4], C-64-C-66 (1986).
7. C. H. Hsueh, A. G. Evans, R. M. Cannon, and R. J. Brook, "Viscoelastic Stresses and Sintering Damage in Heterogeneous Powder Compacts," Acta metall. 34 [5], 927-36 (1986).
8. L. C. De Jonghe, M. N. Rahman, and C. H. Hsueh, "Transient Stresses in Bimodal Compacts during Sintering," Acta metall. 34 [7], 1467-71 (1986).
9. T. J. Garino and H. K. Bowen, "Deposition and Sintering of Particle Films on a Rigid Substrate," submitted for publication in J. Am. Ceram. Soc.

10. R. K. Bordia and R. Raj, "Sintering Behavior of Ceramic Films Constrained by a Rigid Substrate," J. Am. Ceram. Soc., 68 [6] 287-92 (1985).
11. G. W. Scherer and T. J. Garino, "Viscous Sintering on a Rigid Substrate," J. Am. Ceram. Soc., 68 [4] 216-20 (1985).
12. S. Barclay, J. Fox, and H. K. Bowen, "Processing of Pressureless-Sintered SiC Whisker-Reinforced Al_2O_3 Composites"; submitted for publication to J. Mat. Sci.
13. P. Nahass, R. L. Pober, and H. K. Bowen, "Semicontinuous Classification of Ceramic Powders," submitted for publication in Adv. Ceram. Mat.
14. B. Bishop and H. K. Bowen, "Dispersion and Packing of SiC Powders," presented at the 88th Annual Meeting of the Am. Ceram. Soc., May 1986 (Abstract #41-BP-86).
15. M. Green, T. Kramer, M. Parish, J. Fox, R. Lalanandham, W. Rhine, S. Barclay, P. Calvert, and H. K. Bowen, "Chemically Bonded Organic Dispersants"; accepted for publication in Advances in Ceramics.
16. R. J. Pugh, T. Matsunaga, and F. M. Fowkes, "The Dispersibility and Stability of Carbon Black in Media of Low Dielectric Constant. 1. Electrostatic and Steric Contributions to Colloidal Stability," Colloids and Surfaces, 7, 183-207 (1983).
17. R. J. Pugh and F. M. Fowkes, "The Dispersibility and Stability of Carbon Black in Media of Low Dielectric Constant. 2. Sedimentation Volume of Concentrated Dispersions, Adsorption and Surface Calorimetry Studies," Colloids and Surfaces, 9, 33-46 (1984).
18. R. H. Heistand, II, Y. Oguri, H. Okamura, W. C. Moffatt, B. Novich, E. A. Barringer, and H. K. Bowen, "Synthesis and Processing of Submicrometer Ceramic Powders"; p. 492 in Science of Ceramic Chemical Processing, Proceedings of the Second International Conference on Ultrastructure Processing of Ceramics, Glasses, and Composites (Feb. 25 - Mar. 1, 1985, Palm Coast, FL). Edited by L. L. Hench and D. R. Ulrich, John Wiley & Sons, 1985.
19. D. H. Napper, Polymer Stabilization of Colloidal Dispersions; p. 12. Academic Press, New York, NY, 1983.
20. F. M. Fowkes and M. A. Mostafa, "Acid-Base Interactions in Polymer Adsorption," Ind. Eng. Chem. Prod. R&D, 17 [1], 3-7 (1978).

APPENDIX

The following equation can be written for the volume of a green compact, per unit mass:

$$V_c = V_{uc} + V_g \quad (1)$$

where V_c is the volume of a green compact processed with polymer-coated SiC particles, V_{uc} is the volume of a green compact processed with uncoated SiC particles, and V_g is the total volume of gaps between SiC particles and the surrounding Al₂O₃ matrix per unit mass of green compact. The difference in green density between uncoated and coated compacts of unit mass ($\Delta\rho$) can be written:

$$\Delta\rho = \rho_{uc} - \rho_c = [V_{uc}^{-1} - V_c^{-1}] = V_g (V_{uc}(V_{uc} + V_g))^{-1} \quad (2)$$

The assumption that the particles are spherical gives the following equation for the weight fraction of SiC in a green compact, f_s :

$$f_s = N_s \frac{4\pi r_s^3 \rho_s}{3} \quad (3)$$

The subscript "s" indicates SiC. Thus, r_s is the characteristic radius of a SiC particle, ρ_s is the density of crystalline SiC (3.16 g/cm³), and N_s is the number of SiC particles in an Al₂O₃-SiC green compact of unit mass.

Using Equation 3, the following can be written for the total volume of gaps per unit mass of a green compact:

$$V_g = (4\pi/3)(R^3 - r_s^3)N_s = (f_s/\rho_s)[(R/r_s)^3 - 1] \quad (4)$$

where $R = r_s + t$, t being the average thickness of the gaps. Substituting Equation 4 into Equations 1 and 2 and rearranging yields:

$$t = r_s(u - 1) \quad (5)$$

where

$$u = [\rho_s(\rho_{uc} - \rho_c)(f_s \rho_{uc} \rho_c)^{-1} + 1]^{1/3} \quad (6)$$

Therefore, the average thickness of the gaps, t , can be estimated by inserting experimental values of ρ_c and ρ_{uc} for various values of f_s in Equation 6, and substituting the value found for u into Equation 5.

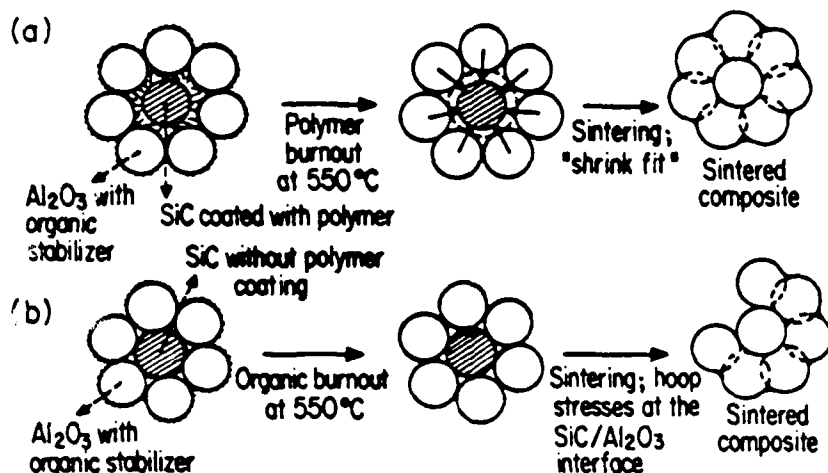


Figure 1. Schematic representation of two densification routes for Al_2O_3 -SiC composites: a) composite with polymer grafting, and b) composite without polymer grafting.

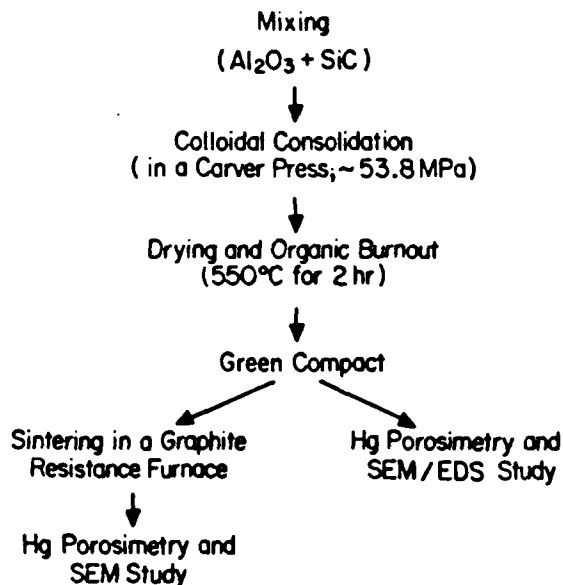


Figure 2. Flow chart of the experimental procedure used in this study.

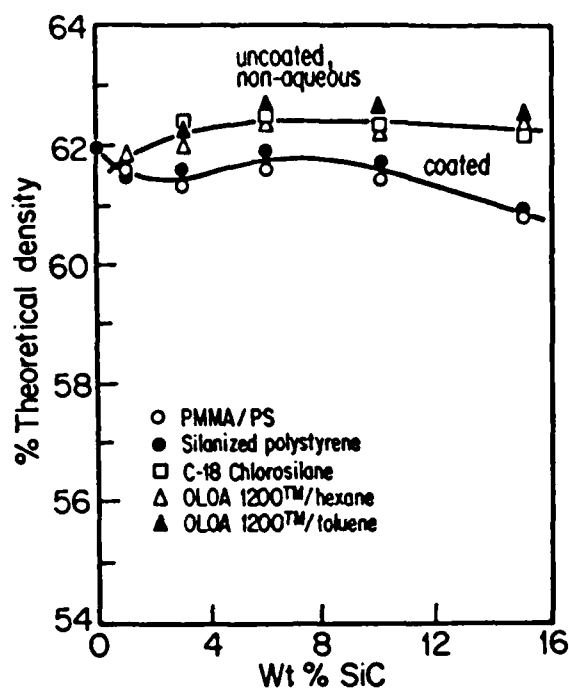


Figure 3. Green compact density as a function of SiC content for Al_2O_3 -SiC composites processed seven different ways.

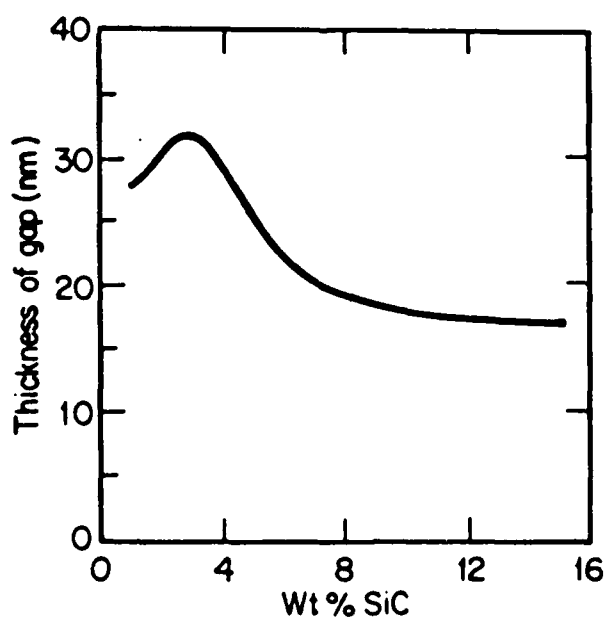


Figure 4. Average gap thickness between a SiC particle and the surrounding Al_2O_3 matrix as a function of wt% SiC in a green compact.

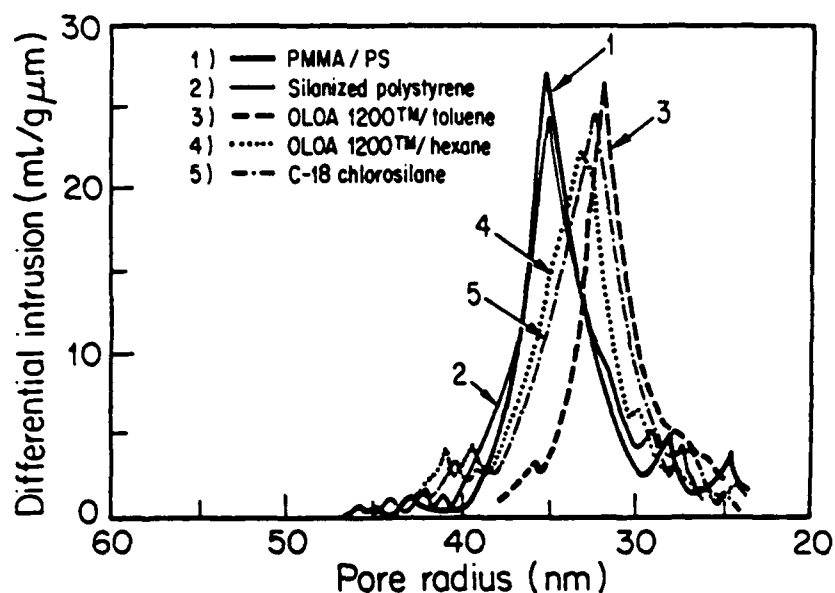


Figure 5. Pore-size distributions of green compacts containing 10 wt% SiC in the region of the most frequent pore radius.

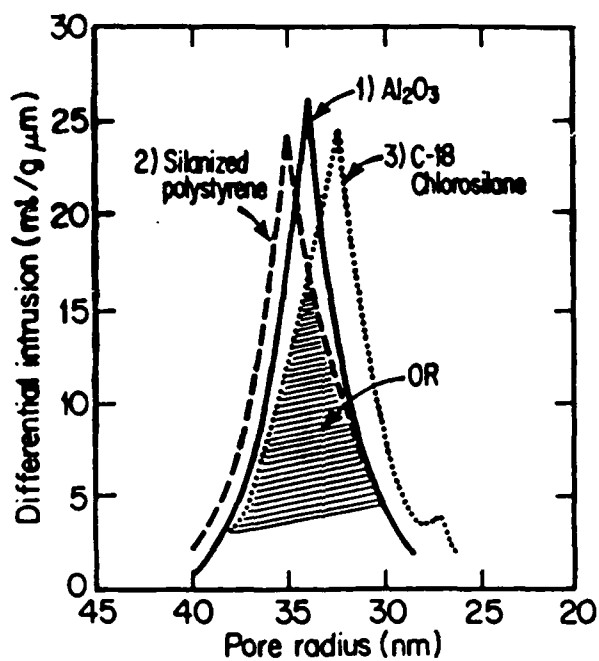


Figure 6. Pore-size distributions of three green compacts processed in nonaqueous suspensions: pure Al_2O_3 , and Al_2O_3 - (10 wt%) SiC composites processed with and without a polymer coating on the SiC particles.

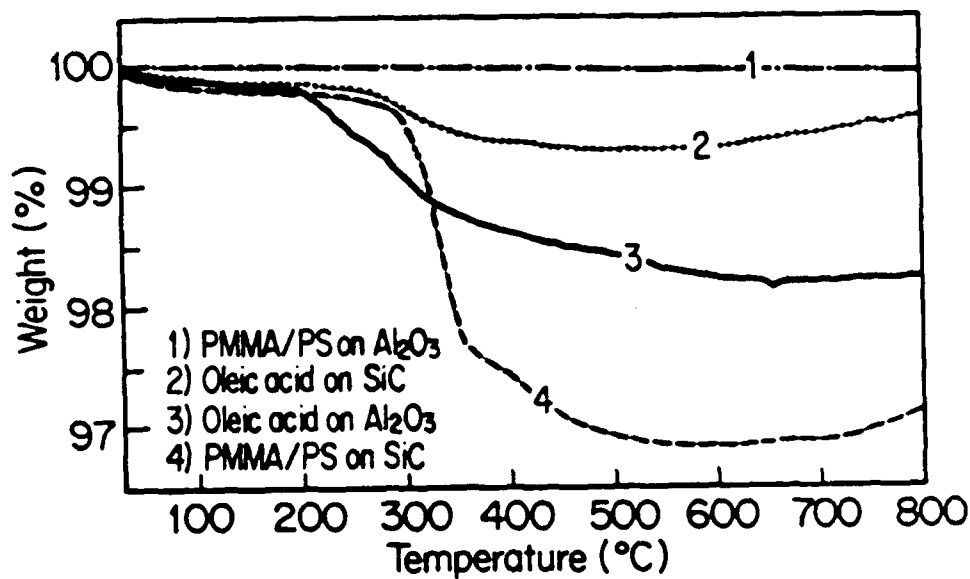


Figure 7. TGA curves for PMMA/PS and oleic acid adsorbed on SiC and Al_2O_3 powders.

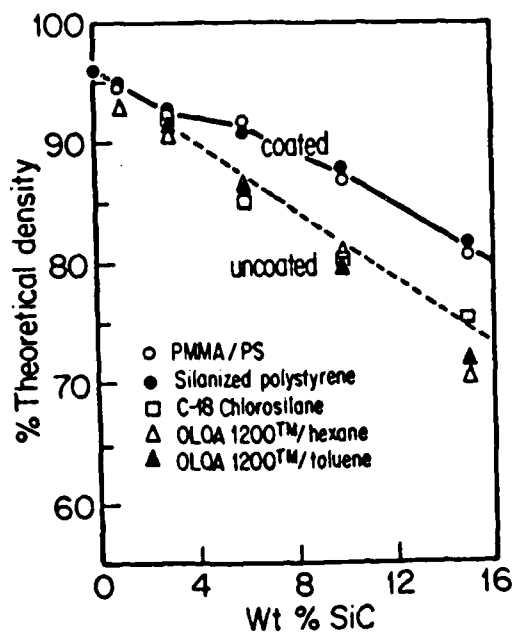


Figure 8. Percent theoretical density vs wt% SiC for various Al_2O_3 -SiC composites fired at 1550°C for 1.5 h at a heating rate of $15^\circ\text{C}/\text{min}$.

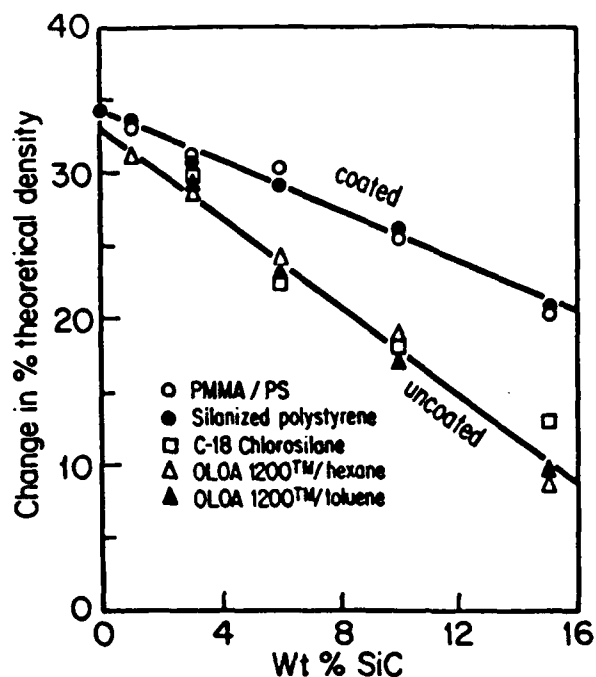


Figure 9. Change in the percent theoretical density of Al_2O_3 -SiC composites fired at 1550°C for 1.5 h vs wt% SiC.

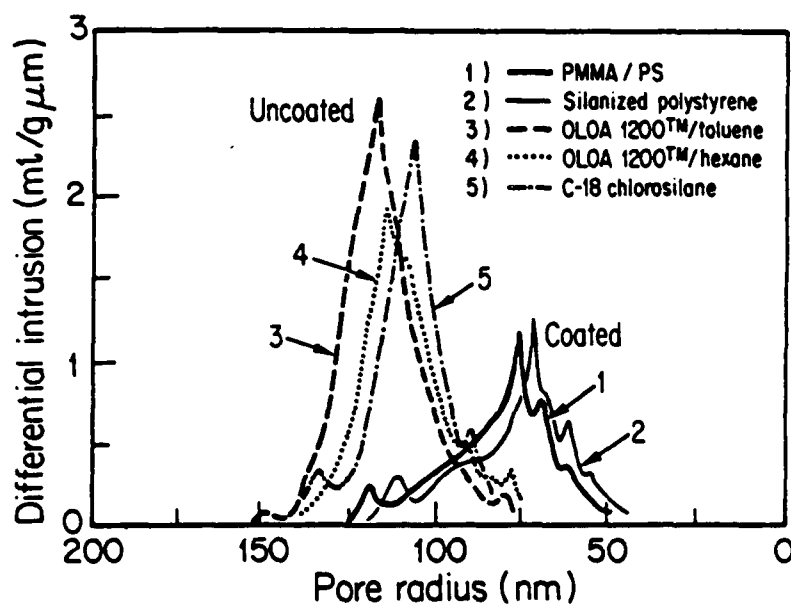


Figure 10. Pore-size distributions of fired Al_2O_3 -SiC composites containing 10 wt% SiC.

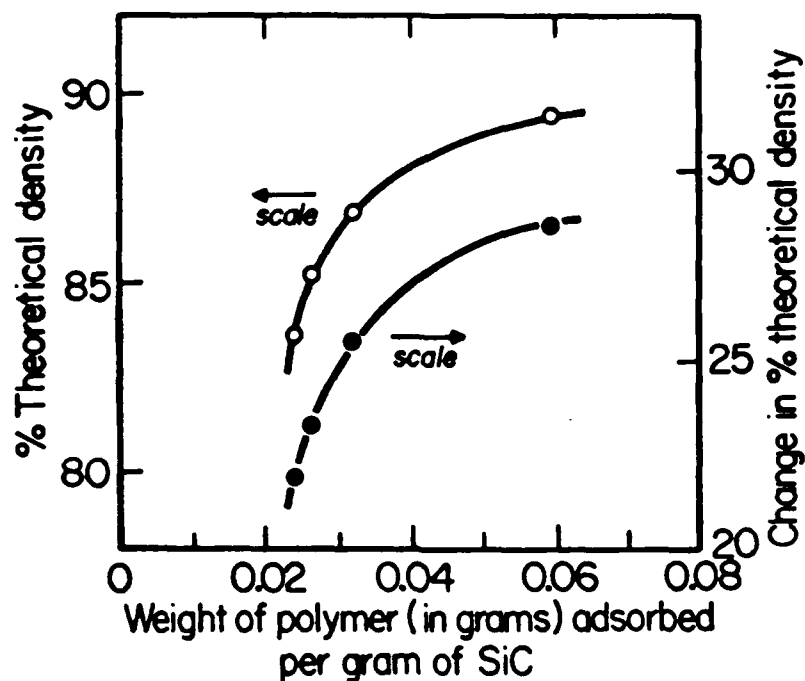


Figure 11. Percent theoretical density and change in percent theoretical density during sintering for 10 wt% SiC composites vs amount of polymer (in grams) adsorbed on SiC powder. (Composites fired at 1550°C for 1.5 h).

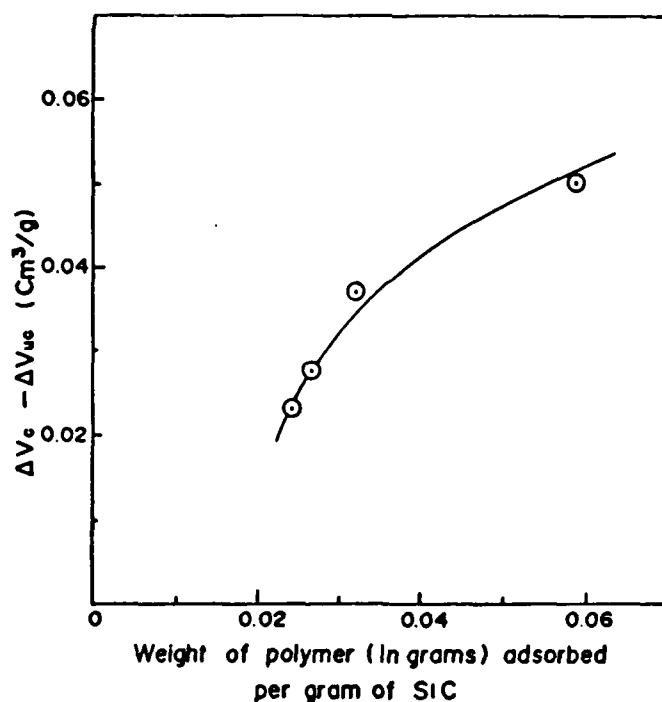


Figure 12. $(\Delta V_c - \Delta V_{uc})$ as a function of polymer (in grams) adsorbed on SiC powder.

DENSIFICATION OF Al_2O_3 -SiC POWDER COMPOSITES:
II. MICROSTRUCTURAL EVOLUTION AND DENSIFICATION

Hyun M. Jang

ABSTRACT

Microstructural evolution and densification kinetics of Al_2O_3 -SiC powder composites were studied using two different SiC powders. Examination of the microstructural evolution of Al_2O_3 -fine SiC powder composites showed three well-defined stages of densification: the first was characterized by constant pore size and no grain growth; the second involved rapid pore coarsening and grain growth; the third was characterized by pore shrinkage and slow grain growth. Studies of the densification kinetics of Al_2O_3 -coarse SiC powder composites exhibited two stages of densification: in the first stage there were no significant differences in densification rate between pure Al_2O_3 compacts and composites; in the second stage, however, differences in densification behavior between pure Al_2O_3 compacts and composites became pronounced.

I. INTRODUCTION

Heterogeneities in a powder compact typically densify at rates different than that at which the matrix phase densifies, inducing transient stresses within the sintering compact. These stresses cause particle rearrangement, resulting in pore development. Part I of this paper¹ documented the proposal and testing of one possible approach for efficiently densifying composites in which nonsinterable particles are uniformly dispersed in a sinterable matrix. The study showed that Al_2O_3 -SiC powder composites processed using polymer-coated SiC particles sintered to higher densities than did composites processed without polymer-coated SiC particles.

The main purpose of the present study is to examine 1) the microstructural evolution and 2) the densification kinetics of Al_2O_3 -SiC powder composites. To examine the microstructural evolution during densification, a number of equivalent green composites prepared from fine SiC powder were fired for various lengths of time. Pore-size distributions

and microstructures of the fired composites were then examined to provide detailed information supplementing the previous study.¹ In the present study, the densification kinetics of the Al_2O_3 -coarse SiC composites were monitored by dilatometer.

II. EXPERIMENTAL METHODS

The Al_2O_3 powder used in this study was Reynolds RC-172 DBM without MgO additives (Reynolds Metals Co., Bauxite, AR), size-classified² to a particle diameter range from 0.3 μm to 0.5 μm .

Two kinds of SiC powder were used in this study: Fujimi GC #10000 (α -SiC; Fujimi Kenmazai Kogyo Co., Ltd., Nagoya, Japan) served as the "fine" powder and Lonza UF-05 (Swiss Aluminium Ltd., Switzerland) served as the "coarse" powder. The Fujimi powder had a surface area of $\sim 16 \text{ m}^2/\text{g}$, as determined by the BET method. Inspection of a scanning electron micrograph (SEM) showed about 90% of the particle diameters to be between 0.1 and 0.8 μm , with an average diameter of 0.48 μm .¹ The Lonza powder's surface area was $\sim 5 \text{ m}^2/\text{g}$. As received, $\sim 13 \text{ wt}\%$ of the powder's particles were finer than 1 μm . These were removed by dispersing the Lonza powder in an OLOA™1200/hexane solution by sonication and allowing the coarse particles to settle from the suspension by gravity. The sediment was washed five times with pure toluene and dried at 90°C . The mean particle size of the Lonza powder sediment (the "coarse" powder in this study) was found to be $\sim 3 \mu\text{m}$. Fourier transform infrared spectroscopy indicated that the fine Fujimi powder had more oxidized (SiO_2) surfaces than did the coarse Lonza SiC powder.

The Al_2O_3 -Fujimi SiC composites (10 wt% SiC) were used to study microstructural development during densification. Composites were

H. Jang AFOSR/1988 Al_2O_3 -SiC: MICROSTRUCTURAL EVOLUTION, DENSIFICATION prepared by one of two processing schemes: consolidation with or without a polymer grafted onto the SiC particles. Three different processing methods were used to prepare the composites: one for the polymer-coated SiC particles and two for the uncoated particles.

To prepare composites with the polymer-coated SiC particles, the SiC dispersion was stabilized with a 20 wt% poly(methylmethacrylate)/polystyrene copolymer ("PMMA/PS," MW 270,000; Polysciences, Warrington, PA).

Two methods were used to prepare composites without a polymer coating on the SiC particles. In the first method, OLOA™1200 (6 wt% with respect to the total powder weight of a 50/50 mixture of OLOA™ to mineral oil; Chevron Chemical Co., Richmond, CA) was used to stabilize a suspension of Al_2O_3 and SiC powders in toluene. In the second method, the SiC dispersion was stabilized with 5 wt% octadecyltrichlorosilane ("C-18 chlorosilane"; Petrarch Systems, Bristol, PA) in toluene.

All of the Al_2O_3 -SiC dispersions were then colloid-pressed at 53.79 MPa (7800 psi). After binder burnout at 550°C for 2 h, the composites were embedded within SiC powder in a graphite crucible. Sintering experiments were performed in a graphite resistance furnace under a flowing high-purity argon atmosphere. The furnace was heated from room temperature to 1200°C at an average rate of 45°C/min. After sintering, pore-size distributions of the fired composites were determined by mercury intrusion experiments using a mercury porosimeter (Micromeritics Autopore II 9220; Micromeritics Instr. Corp., Norcross, GA). Fracture surfaces of the sintered composites were observed by scanning electron microscope (Hitachi Model S-530; Hitachi Ltd., Tokyo, Japan).

The processing and characterization methods used for the Al_2O_3 -Fujimi SiC composites were the same as those described in Part I of this paper.¹

Alumina-Lonza SiC composites containing selected volume fractions (0, 3, 8, and 15 vol%, based on theoretical density) of SiC powder were used to study the densification kinetics. The composites were prepared with PMMA/PS polymer grafted onto the SiC particles as described above. Densification behavior was continuously monitored by dilatometer (Netzsch 402E; Netzsch-Gerätebau GmbH, Exton, PA) under a flowing hydrogen (4%) - argon (96%) atmosphere to provide a reducing atmosphere and avoid oxidation of the SiC. In a preliminary experiment conducted under high-purity argon, the SiC powder oxidized and mullite formed. Since the maximum temperature of the dilatometer furnace is 1550°C, sintering was carried out at 1500°C.

III. RESULTS AND DISCUSSION

The sintering results as a function of firing time for composites containing 10 wt% Fujimi SiC powder are shown in Figure 1. An average heating rate of 20°C/min was used between 1200°C and 1700°C. The start of the firing time was arbitrarily chosen to be the time at which the sample temperature reached 1300°C. The results clearly demonstrate that over the entire course of densification, composites containing polymer-coated SiC were consistently more dense than composites processed without polymer-coated SiC.

Figure 2 shows the change in the most frequent pore radius as a function of firing time for three series of compacts processed with and without polymer coatings. From the results, it is evident that pore-size evolution takes place in three well-defined stages. The first stage of densification (0-15 min firing time) is characterized by a constant pore size. The most frequent pore radius in compacts at this stage is

essentially the same as that in the green body; however, the pore-size distribution broadens slightly as densification proceeds from ~60% of the theoretical density of the green compact to ~75%. Scanning electron micrographs of polymer (PMMA/PS)-derived samples (Figs. 3a and 3b) show neck growth but essentially no grain growth at this stage.

The second stage (~15-40 min firing time) is characterized by rapid pore coarsening, from ~35 nm to ~150 nm; the pore-size distribution also broadens significantly. Scanning electron micrographs (Figs. 3c and 3d) of samples prepared using polymer-coated SiC particles indicate that the rapid pore coarsening is accompanied by rapid grain growth. A comparison of Figure 3c with Figure 3b indicates that the transition period between Stages 1 and 2 is also characterized by a significant broadening in the grain-size distribution.

In the second stage, densification apparently involves a shrinkage mechanism by which the Al_2O_3 matrix densifies away from the SiC particles, coarsening the pores between the SiC particles and the surrounding Al_2O_3 matrix, and therefore generating little tensile stress at the interface. The pore coarsening observed at the second stage of sintering in the Al_2O_3 -Fujimi SiC composites (Fig. 2) may have something to do with this.

The last stage of densification (~40-120 min firing time) is characterized by pore shrinkage. Figure 2 clearly shows that the rate of pore shrinkage in this third stage is slower than that of pore coarsening in the second stage. Although grain growth steadily continues, the growth rate is significantly reduced at this stage (Figs. 3e and 3f). Differential sintering probably produces transient stresses in the third stage as the Al_2O_3 matrix begins to densify around the nonsinterable SiC particles. Thus, the much smaller values observed for the most frequent

pore radius in the polymer-coated compacts as compared to those observed for the uncoated compacts (Fig. 2) suggest that the gap produced between a SiC particle and the Al_2O_3 matrix by a burned-out polymer coating reduces transient stresses at the interface, allowing more densification to occur before hoop stresses around the SiC particles halt sintering. The reasons for the slightly different pore shrinkage rates observed for the two uncoated compacts are not known at this time.

To more clearly observe under scanning electron microscope the effect of a non-sinterable second phase on tensile stress development at the particle-matrix interface, we prepared Al_2O_3 -SiC composites using Lonza SiC powder with an average particle size of 3 μm . This powder is almost an order of magnitude larger than the Fujimi SiC powder; it also has a smaller surface area and, consequently, less SiO_2 to inhibit sintering.⁵ The sintering models used for this study assume that the densification kinetics are dependent on the volume fraction of the nonsinterable inert phase, not on particle size; according to a recent publication⁶, however, particle size probably does affect sintering kinetics, this possibility was not investigated in this work.

Results of the densification kinetics determination for composites containing the selected volume fractions (f_v) of Lonza SiC powders are shown in Figure 4. In this study, the amount of SiC is given as the volume fraction of SiC in the composite so that the data can be analyzed by the Raj-Bordia model. Time $t = 0$ in Figure 4 represents the start of Al_2O_3 shrinkage; the sintering temperature (1500°C) was reached after $t = 20$ min. The densification process for both pure Al_2O_3 ($f_v = 0$) and the Al_2O_3 -SiC composites apparently has two well-defined stages in terms of density changes. No significant difference in densification rate between the Al_2O_3

compact and the composites appear in Stage I; at $f_v = 0.03$, however, the densification rate of the composite was faster, and at $f_v = 0.08$ and 0.15 , the densification rates were slower than that of the pure Al_2O_3 compact.

Dilatometric measurements of sintering kinetics often yield curves that can be described by the equation:

$$\Delta\rho = \Delta\rho_{\max}(1 - e^{-t/\tau}) \quad (1)$$

where $\Delta\rho = (\rho - \rho_g)/\rho_g$ and $\Delta\rho_{\max} = (1 - \rho_g)/\rho_g$; ρ_g is the relative density of the green compact, ρ is the time-dependent relative density, and τ is the time constant for sintering. Assuming that the sintering behavior of the Al_2O_3 -SiC composites at 1500°C is described by the above equation, the time constant τ can be estimated for composites containing different volume fractions of SiC powder. Equation 1 can be written as:

$$\ln(1 - (\Delta\rho/\Delta\rho_{\max})) = -(1/\tau)t \quad (2)$$

Figure 5 plots the left-hand side of Equation 2 against time for a green compact with a relative density ρ_g of ~ 0.61 . Again, the results show two distinct regions in terms of densification rate. Since the above two equations only apply for isothermal sintering conditions, the densification behavior can only be estimated for Stage II. In Stage II, differences in the time constants for the pure Al_2O_3 compact and the Al_2O_3 -SiC composites become pronounced.

According to Raj and Bordia,^{3,4} the time constant for a bimodal compact can be related to that for a pure compact (e.g., Al_2O_3) according to the following relationship:

$$\tau_o = 9\beta(4f_v + 9\beta)^{-1}\tau \quad (3)$$

where τ_0 and τ are time constants for the Al_2O_3 compact and the Al_2O_3 -SiC compact, respectively, and f_v is the volume fraction of the SiC phase. The parameter β is defined as the ratio of the creep rate in the matrix to the densification rate of the porous body. Generally, if $\beta > 1$, the sintering behavior follows the rule of mixtures and the time constant for sintering remains unchanged. If $\beta < 1$, however, the sintering rate becomes considerably slower than the rule of mixtures would indicate. It has been shown^{3,4} that the maximum value of the hoop stress generated at the particle-matrix interface is given by the expression:

$$\sigma_{\theta, \max} = (2-9\beta)(4f_v+9\beta)^{-1}p_0 \quad (4)$$

where p_0 is the intrinsic sintering pressure in the powder compact. Using Equations 2, 3, and 4, the three parameters τ , β , and $\sigma_{\theta, \max}$, which characterize densification behavior of composites, were estimated; these are shown in Table I.

Table I. Estimated τ , β , and $\sigma_{\theta, \max}$ values for Al_2O_3 composites containing a 0-0.15 volume fraction (f_v) of Lonza SiC, during the second stage of densification.

f_v	τ	β	$\sigma_{\theta, \max}$
0	35	∞	$-p_0$
0.03	75	0.01	$8.2p_0$
0.08	110	0.02	$8.2p_0$
0.15	170	0.02	$2.5p_0$

As expected, three points are clear from the analysis:

1. The time constant, τ , increases as the volume fraction of the SiC phase increases.
2. β is much less than 1 and is virtually independent of the volume fraction of SiC.
3. Tensile hoop stress exists at the SiC particle- Al_2O_3 matrix interface during isothermal sintering.

Judging from the data presented in Table I, the tensile hoop stress (the positive value of $\sigma_{\theta, \max}$) is significant in Stage II. A rapid increase in τ or $\sigma_{\theta, \max}$ in Stage II probably indicates that the Al_2O_3 matrix begins to densify around SiC particles at the beginning of Stage II or at the transition period between Stages I and II. This process, then, could reduce the pore region between each SiC particle and the surrounding Al_2O_3 matrix, ultimately increasing the tensile stress at the interface.

Figure 6 is an SEM of the fracture surface of a composite containing 8 vol% Lonza SiC powder after sintering for 60 min at 1500°C . The irregularly shaped, 2-3- μm particles are SiC; the regularly shaped, 0.2-0.5- μm particles in Figure 3c-f are also SiC particles. These micrographs indicate that when SiC particles are the same size as the matrix particles, the SiC is either incorporated into the matrix (e.g., the Al_2O_3 grain in the center of Figure 3c has almost engulfed a SiC particle) or remains on the grain boundaries. When the SiC particles are an order of magnitude larger than the Al_2O_3 particles, the SiC remains as a discrete second phase and is not incorporated into the Al_2O_3 grains until after significant grain growth. In this latter case, therefore, SiC particles are surrounded by Al_2O_3 grains and remain at the grain boundaries.

IV. SUMMARY

The microstructural evolution of Al_2O_3 -Fujimi SiC powder composites takes place in three well-defined stages. The earliest stage of densification is characterized by a constant pore size; scanning electron micrographs of compacts at this stage show essentially no grain growth. The second stage involves rapid pore coarsening and grain growth. The final stage of densification is characterized by pore shrinkage; also, although the grains grow steadily, their rate of growth is significantly slower in this stage than in the previous stage.

Studies of the densification kinetics of Al_2O_3 -Lonza SiC powder composites showed two densification stages. Differences in densification behavior between pure Al_2O_3 compacts and Al_2O_3 -SiC composites were pronounced only in the second stage.

REFERENCES

1. H. M. Jang, W. Rhine, and H. K. Bowen, "Densification of Al_2O_3 -SiC Powder Composites: I. Effects of a Polymer Coating on SiC Particles," submitted for publication to Am. Ceram. Soc. Bull.
2. P. Nahass, R. L. Pober, and H. K. Bowen, "Semicontinuous Classification of Ceramic Powders," submitted for publication to Adv. Ceram. Mat.
3. R. Raj and R. K. Bordia, "Sintering Behavior of Bi-Modal Powder Compacts," Acta Metall., 32 [7] 1003-19 (1984).
4. R. K. Bordia and R. Raj, "Analysis of Sintering of a Composite with a Glass or Ceramic Matrix," J. Am. Ceram. Soc., 69 [3] C-55-C-57 (1986).
5. S. Sumita and H. K. Bowen, "Effect of Foreign Oxides on Grain Growth and Densification of Sintered Alumina"; pp. 840-47 in Ceramic Transactions: Ceramic Powder Science II. Edited by G.L. Messing, E.R. Fuller, and H. Hausner. The American Ceramic Society, Inc., Westerville, OH, 1988.
6. M. W. Weiser and L. C. De Jonghe, "Inclusion Size and Sintering of Composite Powders," J. Am. Ceram. Soc., 71, C125-C127 (1988).

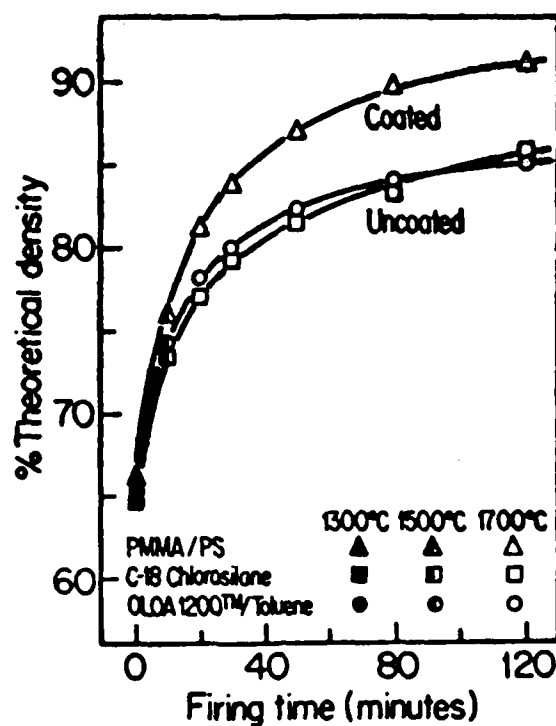


Figure 1. Percent theoretical density vs firing time for Al_2O_3 -Fujimi SiC (10 wt%) powder composites processed with and without a polymer coating on the SiC particles.

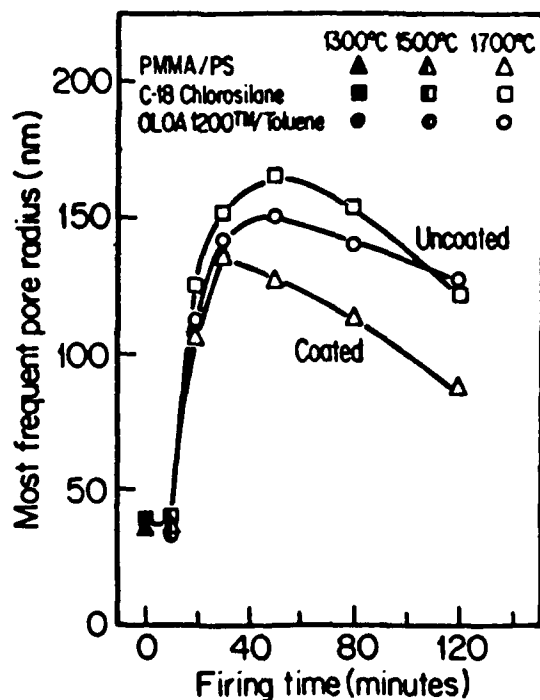
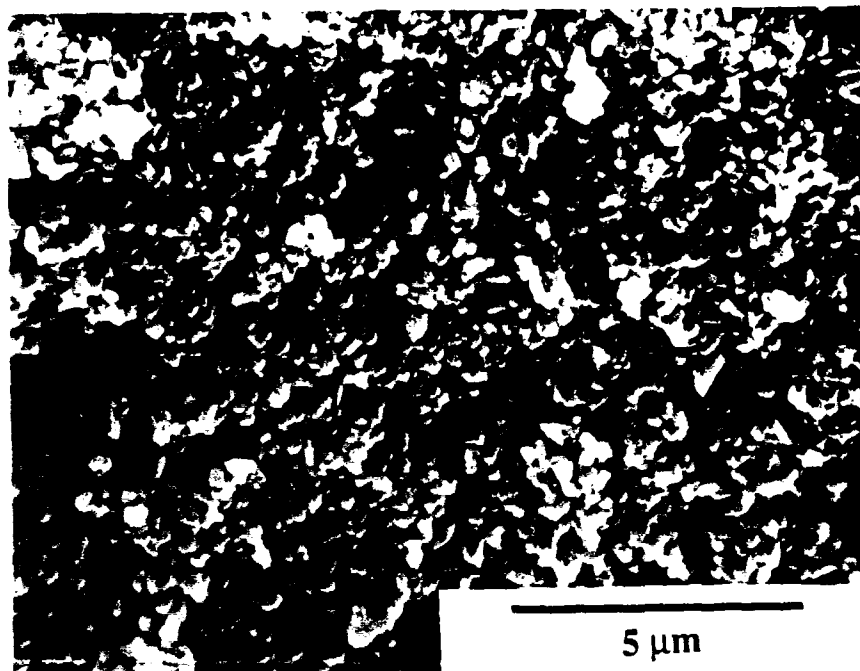
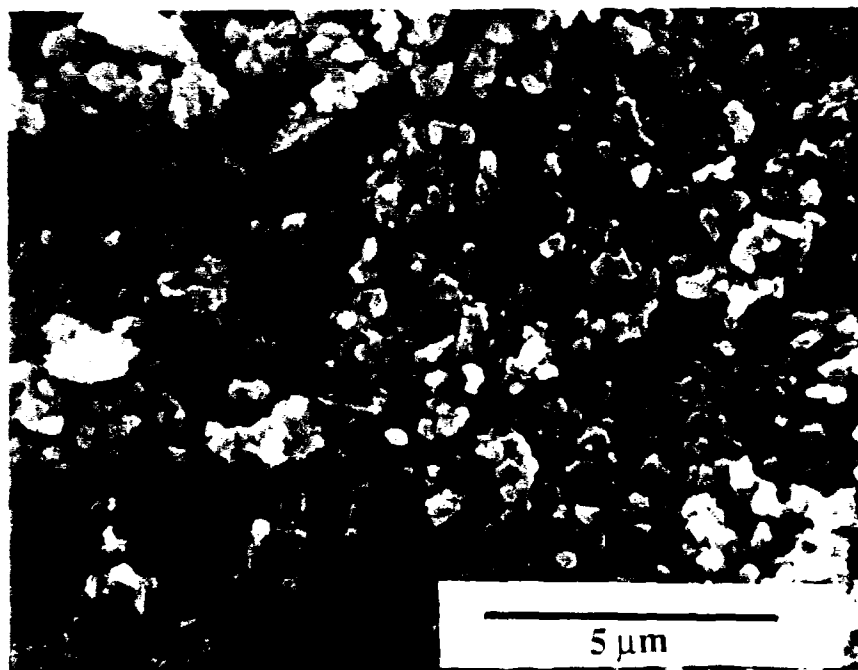


Figure 2. Most frequent pore radius vs firing time for Al_2O_3 -Fujimi SiC (10 wt%) powder composites processed with and without a polymer coating on the SiC particles.

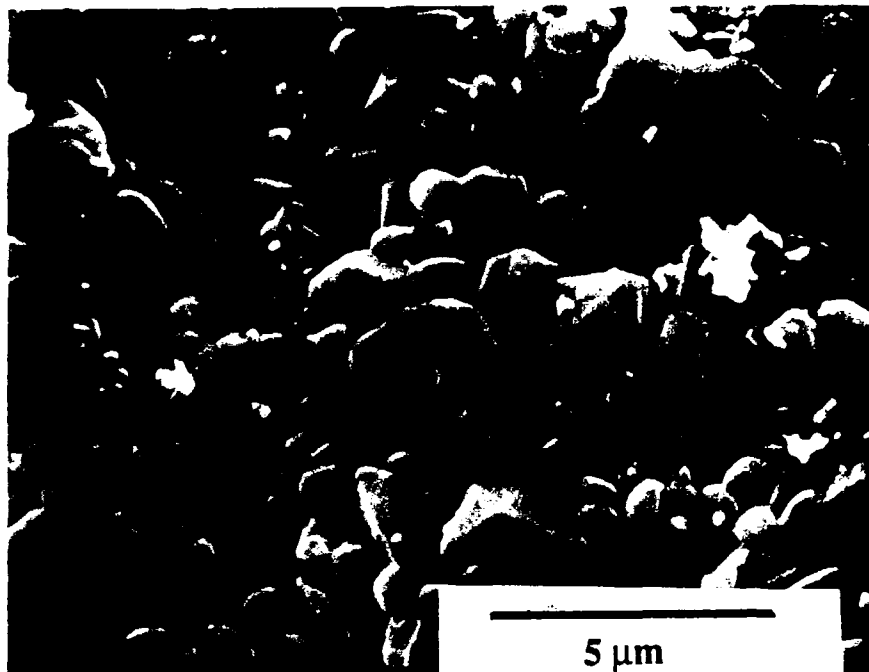


(a)



(b)

Figure 3. SEMs of fracture surfaces of Al_2O_3 -Fujimi SiC (10 wt%) composites at various stages of densification: after a) 0-min hold at 1300°C and b) 0-min hold at 1500°C .

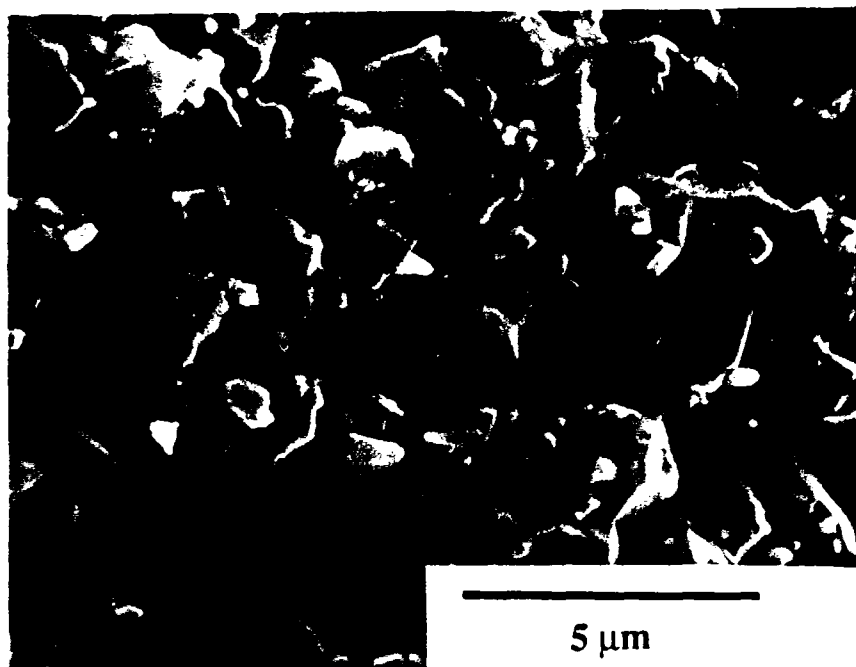


(c)

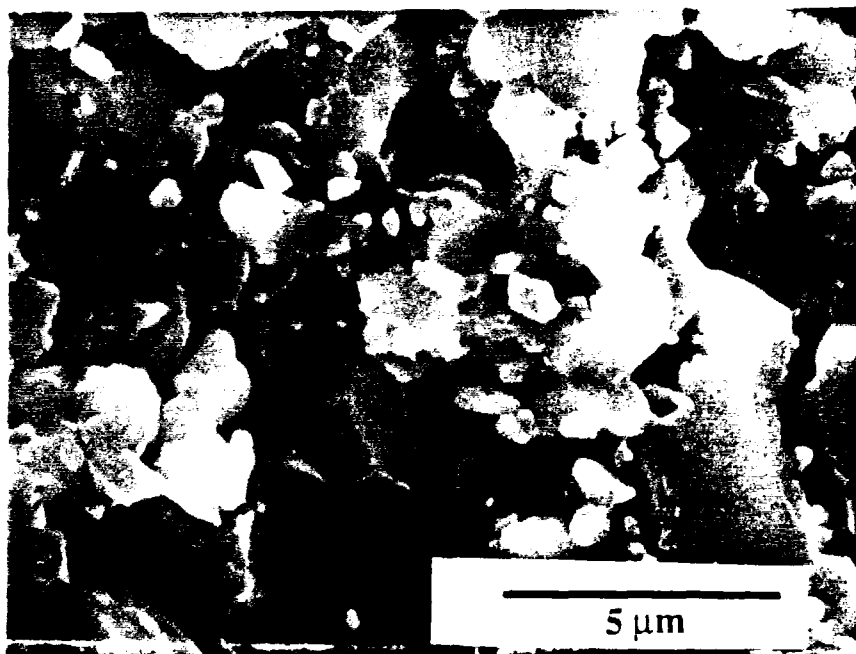


(d)

Figure 3 (cont'd). SEMs of fracture surfaces of Al_2O_3 -Fujimi SiC (10 wt%) composites at various stages of densification: after a c) 0-min hold at 1700°C and d) 10-min hold at 1700°C .



(e)



(f)

Figure 3 (cont'd). SEMs of fracture surfaces of Al_2O_3 -Fujimi SiC (10 wt%) composites at various stages of densification: after a e) 30-min hold at 1700°C and f) 100-min hold at 1700°C .

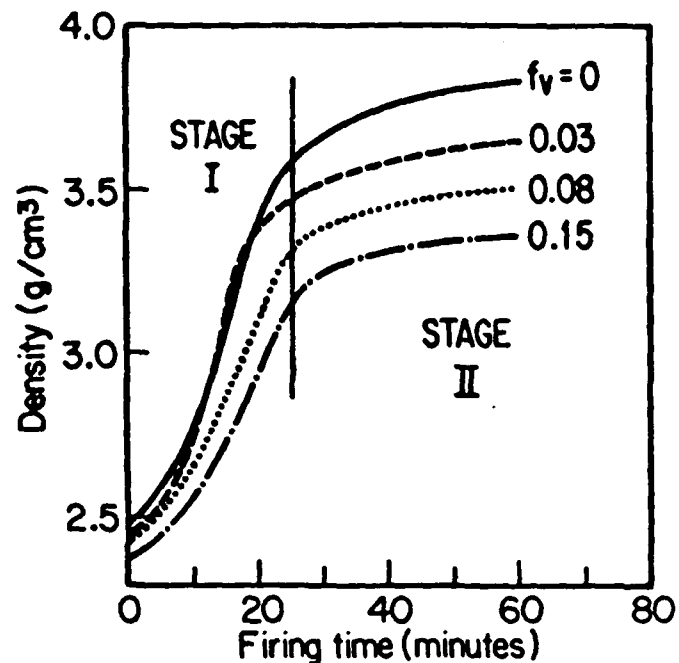


Figure 4. Sintered density vs firing time for Al_2O_3 composites containing a 0-0.15 volume fraction (f_v) of Lonza SiC. Note the two densification stages.

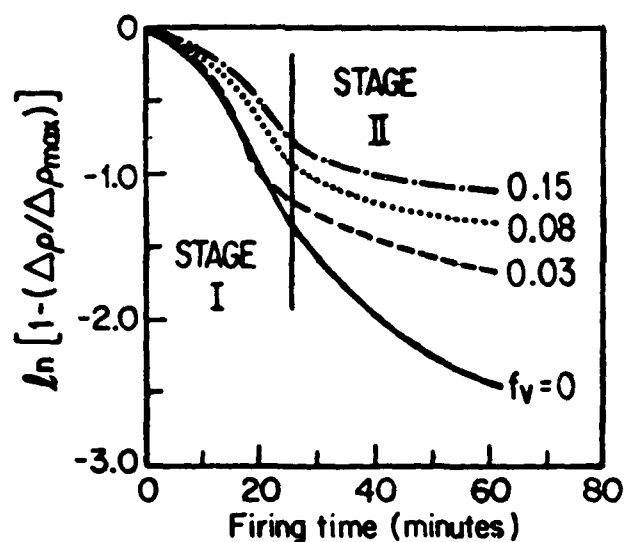


Figure 5. Plot of $\ln [1 - (\Delta\rho/\Delta\rho_{\max})]$ vs time for Al_2O_3 composites containing a 0-0.15 volume fraction (f_v) of Lonza SiC. Note the two densification stages.

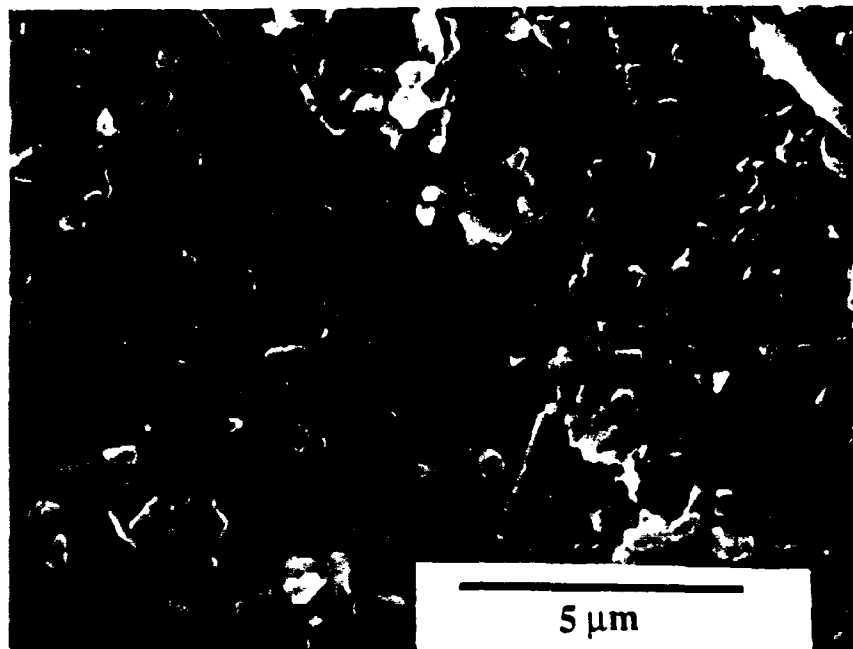


Figure 6. SEM of the fracture surface of a composite containing 8 vol% Lonza SiC powder after sintering for 60 min at 1500°C .

POWDER PROCESSING AND MICROSTRUCTURE DEVELOPMENT OF β -SiC

Bruce Bishop

ABSTRACT

Three aspects of β -SiC processing were investigated: dispersion, particle-size classification, and final-stage microstructure development. In conjunction with experiments described previously, the effect of OLOA®1200 on the charging of commercial β -SiC powder in low-dielectric-constant hydrocarbon media and the effect of the volume fraction of solids on the relative viscosity of SiC/OLOA/dodecane dispersions were investigated. The charging of particles, which imparts electrostatic barriers, was found to increase with OLOA concentration up to ~3.2 wt% OLOA by weight of powder, and increased with the amount of time allowed for OLOA and the particle surfaces to interact. This was directly compared to adsorption.

Particle-size classification of β -SiC powder dispersions in hexane stabilized with OLOA®1200 was performed using centrifugal separation. Average particle sizes could be reduced over successive classification runs and almost all large particles could be removed from small particle-size classes, but relative distribution breadths of the as-received and the finest classified material did not significantly differ.

The microstructural aspects of average grain size, grain-size distribution, and phase development were investigated for boron carbide- and carbon-doped as-received and classified β -SiC powders sintered at 2000°C and 2100°C. The average grain size for classified β -SiC powder compacts was smaller than that for as-received powder compacts when sintered at 2000°C, but on a relative scale was slightly greater. The higher densities of the classified-powder compacts were explained by the shifting of the pore/grain boundary separation threshold with grain size to produce higher densities at smaller grain sizes. Comparisons of initial particle-size distributions with final-stage grain-size distributions showed the size distributions to narrow during processing. This may not be unreasonable in the light of grain growth in porous compacts, but no supportive experimental evidence exists. At 2100°C, the parts transformed significantly to the alpha phases of SiC, and the microstructures consisted of plates and needles on the order of 100 μ m or larger. Classified-powder-part grain sizes were found to be smaller, on the average, than as-received powder-part grain sizes, possibly resulting in a more substantial 6H phase component than was evident in the as-received powder compacts, which consisted primarily of the 15R phase. At 2000°C, the cubic 3C phase was predominant; only a small increase in the alpha phase (probably 15R) was apparent.

INTRODUCTION

The processing of submicrometer ceramic powders utilizing colloidal suspensions to remove or minimize nonuniformities in starting green microstructures to improve the sintered microstructures has been an area of active research. In order for American private and governmental enterprises to compete in high-technology ceramics fields and keep pace with technological advances in areas such as high-performance aircraft and space exploration, improved ceramic properties through advanced processing are essential.

The following report is a detailed update on the progress achieved by this laboratory in processing β -SiC through nonaqueous dispersions to obtain fine-grained, high-density materials. Silicon carbide is one advanced structural ceramic with excellent high-temperature strength retention (Thummler, 1980) and good thermal-shock resistance (de Baisi, 1977), oxidation resistance (Dutta, 1984), and tribological properties (Miyoshi, Buckley, and Srinivasan, 1983). However, because of its low fracture toughness (Seshadri and Srinivasan, 1981), SiC is very sensitive to flaws. Consequently, to improve reliability, the flaw size and number must be reduced through advanced processing.

This report contains three sections. The first provides an update on β -SiC powder dispersion in low-dielectric-constant media. The second analyzes powder-size distributions obtained by centrifugal size classification of suspensions. The last reports on the microstructure development of sintered β -SiC with regard to grain size and distribution and phase analysis.

β -SiC POWDER DISPERSION IN LOW-DIELECTRIC-CONSTANT MEDIA

Introduction

The dispersion of colloids in nonaqueous, low-dielectric-constant media has been reviewed by Parfitt and Peacock (1978). Much of this information is relevant to the dispersion of β -SiC powder in hydrocarbon solvents with OLOA®1200 ("OLOA"), which has been a continuing topic of research in this laboratory (Bishop, 1986a). In general, such suspensions can be stabilized by steric and/or electrostatic repulsive forces. Steric repulsive forces are widely accepted and used in low-dielectric-constant media. Napper gives an excellent treatment of the subject (Napper, 1983). However, electrostatics meet with much more skepticism about their applicability to low-dielectric-constant media.

The confusion about electrostatics in low-dielectric-constant media stems from the inaccurate belief that ions cannot exist in such an environment. Ion formation with subsequent charging can occur when one type of ion is stabilized by a lyophilic moiety. This can happen when one ion is a small charged species (e.g., Na^+) that is attracted to a polar particle surface and the other is oil-soluble (e.g., di-2-ethylhexyl sulfosuccinate, which, together with Na, constitutes Aerosol OT). Another situation is when there is an acid/base interaction between the dispersant and particle surface such that proton transfer from the acid to the base occurs, with one ion desorbed from the surface and stabilized by a lyophilic chain or group (e.g., polyisobutylene succinimide on carbon black).

®Registered trademark of Chevron Chemical Co., San Francisco, CA.

Once a surface charge is established on the particles, there is some question as to how effective the repulsive mechanism is when the double-layer thickness is large (e.g., micron-scale). At low solids content, dispersion stability can be correlated with zeta potential (McGown, Parfitt, and Willis, 1965). However, at high solids concentrations, suspension stability is no longer a function of zeta potential. The solids content effect on dispersion stability for electrostatically stabilized suspensions in low-dielectric-constant media is very interesting.

Detailed studies made first by Albers and Overbeek (1959), then improved by Levine and co-workers (Chen and Levine, 1973; Feat and Levine, 1976) concluded that concentrated suspensions could not be stabilized by electric double-layer effects. Essentially, Albers and Overbeek found that extended double layers in concentrated suspensions with close particle-particle approach result in charged particles suspended in charged media, which lowers the repulsive barrier, decreasing stability. In an application of Levine's theory, Green and Parfitt (1986) analyzed the stability of concentrated nonaqueous titania dispersions and found that a pseudo secondary minimum in the interaction potential curve developed, which caused flocculation until the distance between flocs reached a point at which another secondary minimum occurred that structured the suspensions.

With this brief background on nonaqueous dispersions, two new experiments will be described relevant to the dispersion of β -SiC with OLOA in nonaqueous solvents. First, the effect of time and OLOA concentration on the charging of SiC by OLOA will be demonstrated; second, the effect of

solids contents less than 5 vol% on the relative viscosity of the SiC/OLOA/dodecane system will be described.

Summary of Previous Work

Research up to this point on the OLOA/ β -SiC/hydrocarbon system has shown that >3.15 wt% OLOA by weight of powder is required to disperse Betarundum Ultrafine β -SiC, which has a surface area of $18.3 \text{ m}^2/\text{g}$. The adsorption is quantitative up to ~2.8 wt% OLOA by weight of powder, then becomes incomplete but not zero when additional OLOA is added (Bishop, 1986a and 1986b). Based on the facts that adsorption is strong up to 2.8 wt% and the isobutylene polymer chain is very soluble in hexane, a steric barrier can be assumed to have been present. Molecules of OLOA have been shown to have a thickness of ~5 nm (Pugh, Matsunaga, and Fowkes, 1983). The rheology of the silicon carbide/OLOA/dodecane system above the dispersion point as a function of solids content changed from Newtonian to shear-thinning as the solids content increased from 5 to 30 vol%. Consequently, two issues need to be addressed: First, in addition to steric repulsion, how does charge in the system, if it is present, vary with time and OLOA concentration; and second, what is the nature of particle-particle interactions at solids contents below 5 vol%?

Experimental Background and Procedure

Zeta-potential measurements of particles in low-dielectric-constant media are very difficult and highly sensitive to impurities. Consequently, a new technique was used to measure charging in such systems. Measurement of acoustophoretic mobility is much easier than measurement of electrophoretic mobility, and because higher solids contents (as high as 50 wt%) can be used, solvent impurities play less of a role. In general,

measurement consists of ultrasonication of a dispersion of particles in a solvent. When an electric double layer surrounds each particle, the particles (assuming they have a higher density than the medium) move less as the sonic pressure wave passes through the dispersion than does the liquid. This causes the counter-ions to oscillate about the charged particles, resulting in an oscillating dipole. The resulting electric field can be detected by an antenna and correlated to mobility. This technique has been described in detail by Marlow, Fairhurst, and Pendse (1988).

Particle mobility was measured^{*} from 0 to approximately 4.5 wt% purified OLOA (see Bishop, 1985b for purification procedure) by weight of powder. This was accomplished by adding 12.8 wt% powder by weight of dispersion to hexane, then titrating the suspension with a concentrated OLOA/hexane solution. Two titrations were conducted; the step time was ~5 min in one case and 30 min in the other.

To study particle interactions, the relative viscosity of suspensions was measured from 1 to 5 vol%. The theoretical basis for this experiment was developed by Einstein (1906; 1911). Assuming 1) constant density and viscosity of a liquid medium, 2) low, laminar flow, 3) rigid spheres with no slippage at the liquid/sphere interface, 4) extreme dilution such that flow is unperturbed far from the spheres, 5) spheres large enough compared to solvent molecules that the liquid can be treated as a continuum, and 6) spheres small enough compared to the viscometer dimensions that wall effects can be ignored, the relative viscosity, η_R , of a suspension can be described by:

$$\eta_R = 1 + 2.5\phi \quad (1)$$

^{*}Pen Kem System 7000, Pen Kem, Inc., Bedford Hills, NY.

where ϕ is the volume fraction. If spherical particles are truly dispersed in a liquid due to repulsive forces, then little particle-particle interaction will occur at low solids content. Consequently, a plot of η_R versus volume fraction will be linear with a slope of 2.5.

Several factors in actuality are not considered in the theory, including polydispersity, solvation, and morphology. Polydispersity is not explicitly treated in Einstein's derivation because each particle is dealt with independently. Consequently, at the low concentrations at which the following experiment was conducted, polydispersity does not contribute to any deviation from Einstein's law.

Solvation of particles, whether in an aqueous or nonaqueous medium, increases the hydrodynamic volume of the particles. In the OLOA/SiC/dodecane system, it is known that the adsorbed dispersant acts as a solvation layer. In fact, Fowkes has reported the steric thickness of OLOA to be ~5 nm (Rugh, Matsunaga, and Fowkes, 1983). Therefore, the volume of particles added in the present study was less than the actual hydrodynamic volume. Not only do lyophilic chains on the particle surface affect solvation, they may also affect the rigid-sphere assumption, the degree of slip of the liquid at the particle surface, and the way solvent moves through the chains (i.e., by draining or not); the importance of these effects is unknown at this time.

Theory assumes spherical particles, which introduces inaccuracies in descriptions of SiC particles. At best, SiC particles are equiaxed chunks when less than a micrometer in size, and are usually irregularly shaped when greater than 1 μm with an axial ratio of >1 . Assuming that Brownian motion outweighs the orientation of irregular particles in stream lines of flow, the energy dissipation of tumbling irregular particles should be

higher than that occurring with spherical particles. From another perspective, a tumbling particle takes up a higher effective volume than a nontumbling particle. Both analyses find the viscosity to be higher than predicted, based on only the volume of the particles themselves. Consequently, nonspherical particles as well as solvation can lead to positive (higher-slope) deviations from Einstein's law.

For the experiment performed, suspensions containing 0.01, 0.02, 0.03, 0.04, and 0.05 volume-fraction solids by volume of dispersion were prepared in dodecane with 4 wt% purified OLOA by weight of powder as the dispersant. Samples were sonicated in a bath for 30 min, then tumbled for 64 h. After tumbling, samples were sonicated for 1-2 min in a bath before being measured. Care was taken to allow samples to cool to room temperature (20-21°C) after sonication because warm samples have much lower viscosities than cool samples. The samples were allowed to come to thermal equilibrium outside the viscometer first because the samples could then be shaken to remove any sediment which had formed during the cooling time. If a long equilibration time were allowed inside the viscometer, sedimentation would cause inaccurate results. Viscosity measurements were made twice on each of two samples at each concentration using a Haake Rotovisco RV-100 with a CV-100 measuring system (Haake Buchler Instruments, Inc., Saddle Brook, NJ) at 20°C. Viscosities were measured over an 8-min period of ramping up and back down from 0 s⁻¹ to 1000 s⁻¹ back to 0 s⁻¹. Viscosities were determined from the plots at 500 s⁻¹ on the ramp down to minimize sedimentation and thermal equilibrium effects. Relative viscosities were calculated by measuring the viscosities of supernatants of dispersions previously measured. Supernatants were prepared by centrifuging the dispersions at approximately 4500 G for 30 min.

Results and Discussion

The plot of relative acoustic mobility versus OLOA concentration is shown in Figure 1. In general, these curves indicate some charging of particles in the OLOA/SiC/hexane system. However, due to limitations of theory in nonaqueous systems for $\kappa a < 1$, where κ is the inverse of the double layer thickness and "a" is the particle radius, zeta potentials with their respective signs cannot be calculated. With respect to OLOA concentration, the amount of charging increases with concentration below the dispersion point -- the point at which the powder reaches a minimum hydrodynamic volume and the particles are dispersed. Varying the equilibration time produces three differences in sample charge. First, with a long step-time, a greater charge can be developed. Second, the maximum charge for the 30-min step-time curve occurs at about 3.2 wt% OLOA; the 5-min step-time curve does not maximize until closer to 4 wt%. Lastly, the longer step-time sample increases in charge from 0 to 3.2 wt% OLOA; the shorter step-time sample's charge does not start to increase until ~1.5 wt% OLOA.

These results indicate a dynamic equilibrium of dispersant adsorption on the solid/liquid interface. However, it was not determined whether the adsorption/desorption or charged ion adsorption model applied. Adsorption itself is time-dependent, requiring more than 24 h for the sample to come to equilibrium, though considerable adsorption does occur in less than 10 h. At approximately 4 wt% OLOA, 2-3 h were required to completely develop the electrostatic charge on an oxide pigment (Marlow, 1986) (no charging can occur without adsorption).

It is therefore not unreasonable to compare adsorption to mobility, knowing that practically all the dispersant is adsorbed, to about 2.5-3

wt%. After short periods of time, little dispersant would have adsorbed, and consequently even less would have desorbed. This results in little or no charging -- especially at low OLOA concentrations, where the driving force for dispersant adsorption (dispersant concentration in solution) is low. As a result, short step-time measurements can be considered as representing non-equilibrium conditions, while longer step-time measurements are certainly closer to equilibrium and seem to reflect an equilibrium situation.

In Figure 2, the relative viscosity of 4 wt% OLOA/Betarundum Ultrafine β -SiC/dodecane dispersions is plotted as a function of solids fraction by volume. The function is linear, with a correlation coefficient of 0.995; the equation describing the relative viscosity is:

$$\eta_R = 0.995 + 5.75\phi \quad (2)$$

where ϕ is the volume fraction. Because the equation is linear, particle interactions are at a minimum, indicating a highly dispersed system, and the combination of electrostatic and steric effects is quite effective at these solids loadings.

Although the intercept is basically correct, the slope is higher than predicted for the ideal case. Though the value of 5.75 is higher than 2.5, for real systems it is in the correct range of slopes (Overbeek, 1988). Two possible explanations for this deviation involve solvation and nonspherical morphology.

As described previously, steric barriers constitute an additional 9 vol% hydrodynamic volume. If this correction is made to the plot, the new equation becomes:

$$\eta_R = 0.995 + 5.23\phi \quad (3)$$

Although this new equation is not yet close to theoretical, the change illustrates the solvation effect. The actual amount of solvation in the system is unknown and the nonspherical nature of the particles -- especially large ones -- has not been quantitatively determined, making further corrections impossible, but it is quite evident that these two sources of deviation from theory are operable in the system.

Conclusions

Because of a unique interaction of a polyisobutylene succinimide dispersant (OLOA) with an acidic particle surface immersed in a nonpolar, low-dielectric-constant medium, a charge can be developed on particles in suspension. This charge is developed in a time-dependent manner due to the charging mechanism's relationship to adsorption and subsequent desorption. In these experiments, the type of surface (determining the isoelectric point) and its effect on charging with OLOA was not investigated. Under quasi-equilibrium conditions, the acoustic mobility reaches a maximum at the same point that low-solids-fraction suspensions become stabilized.

Based on relative viscosity as a function of solids fraction in dilute systems, there is little particle interaction; rather, particles tend to act independently. However, because of effects that do not fit the assumptions of the model (such as solvation and nonspherical particles), the reduced viscosity, $(\eta_R - 1)/\phi$, where ϕ is the volume fraction, is greater than 2.5.

Future Work

Experiments are presently in progress to further elucidate the characteristics of the electric double layer. First, electrophoresis

samples at 1.5, 3.5, and 4.6 wt% OLOA by weight of powder were prepared by centrifuging the 12.0 wt% powder dispersions and allowing some powder to remain in the supernatant. These samples will be run on a PenKem 3000 electrophoresis unit in order to determine electrophoretic mobilities and sign of charge. Zeta potentials will be calculated if the conductivities measured are high or low enough in a second set of samples which consist, respectively, of hexane, the supernatant of a hexane/5 vol% powder mixture, and actual and calculated (based on adsorption isotherm) supernatants of dispersions containing 4 wt% OLOA by weight of powder and either 1 or 5 vol% powder. If conductivity is very low, zeta potentials can be calculated by the Hückel equation ($\kappa a \ll 1$). If conductivities are high ($\kappa a \gg 1$), then equations used for aqueous colloids can be used. Moderate conductivities ($1 \leq \kappa a \leq 10$) coupled with large potentials (>25 mV), which are typical for low-dielectric-constant electrostatically charged colloids, do not have solidly based equations from which one can calculate zeta potential.

CENTRIFUGAL PARTICLE-SIZE CLASSIFICATION

Introduction

The tailoring of particle-size distributions for optimized processing and properties has been used in different aspects of ceramics (Brownell, 1976; Barringer et al., 1984). Centrifugal classification, which has been used in this lab, is one method for preparing powders with narrow particle-size distributions (Nahass, Poher, and Bowen, 1987). Preliminary results for the centrifugal classification of SiC were reported previously (Bishop, 1985a; 1986b). The purpose of this section is to describe in detail the particle-size distributions of selected particle-size ranges centrifugally separated from an as-received β -SiC powder.

Experimental Procedure

An 11 wt% Betarundum Ultrafine β -SiC powder (Ibiden Co., Ltd., Ogaki, Japan) dispersion was prepared in hexane using 8 wt% OLOA®1200 (Chevron Chem. Co., Oronite Additives Div., San Francisco, CA) by weight of powder as the dispersant. Selected particle-size ranges to be "cut" were >1.2, 0.8-1.2, 0.5-0.8, 0.3-0.5, 0.2-0.3, and 0.15-0.20 μm . The cut sizes were determined using the equation:

$$\text{Feed rate} = V/t = K\omega^2 r^2 (d_p - d_m) / (\eta \ln(y/x)) \quad (4)$$

where V = working volume, t = time, K = shape factor, ω = angular velocity, r = particle radius, d_p = particle density, d_m = media density, η = media viscosity, y = outside radius, and x = inside radius, as shown for the centrifuge-bowl geometry in Figure 3. Further details of the classification procedure have been discussed elsewhere (Nahass, Poher, and Bowen, 1987). After the hexane had been allowed to evaporate, the cuts were weighed, then analyzed by thermogravimetric analysis for dispersant concentration. Particle sizes were analyzed quantitatively by a sedimentation/optical transmission technique (Horiba Model CAPA-500, Horiba Instruments, Inc., Irvine, CA) and qualitatively by scanning electron microscopy.

Results and Discussion

Figure 4 shows the mass efficiency for the various cuts, corrected for dispersant weight. Overall, 92 wt% of the powder was recovered. For the first two cuts, more powder was recovered than had been predicted for those size ranges. For the last four cuts, less powder was recovered than was shown by the particle-size distribution. The reason for this can be seen

in the particle-size distributions for the as-received powder (Fig. 5) and the six cuts (Figs. 6-11), which are also represented numerically in Table 1.

Table 1. Percentage of particles by area in various size fractions for as-received and classified-powder fractions.

Size Fraction (μm)	Particles in Each Size Fraction for Each Cut (%)						
	As-Rec.	Cut 1	Cut 2	Cut 3	Cut 4	Cut 5	Cut 6
> 1.2	6.1	13.3	10.8	7.2	3.1	1.1	1.5
0.8-1.2	9.3	11.8	15.5	9.7	5.0	1.8	2.6
0.5-0.8	13.0	20.8	19.3	20.8	12.1	7.2	6.3
0.3-0.5	25.2	19.6	23.3	26.0	26.4	16.5	9.5
0.2-0.3	18.6	12.4	13.8	15.6	19.5	22.6	15.3
0.1-0.2	22.8	14.1	13.7	14.7	22.4	34.5	37.3
0.1-0	5.9	8.8	5.1	7.2	11.7	16.6	27.7

Each cut contained particles not only from the desired (calculated) particle-size range, but also from the other ranges. The inclusion of particles from other ranges in the first two cuts caused the last cuts to have fewer particles in their respective ranges, and consequently lower efficiencies.

Particles ending up in size fractions other than the ones in which they were calculated to be, could be caused by 1) an inaccurate geometric factor, 2) agglomeration, 3) particle interactions, 4) powder build-up in the centrifuge basket, 5) operator error, and/or 6) improper dispersion feed to the centrifuge. The geometric factor used with the modified

Stokes' equation was $2/9$ for spherical particles. However, each particle shape has its own geometric factor and, as can be seen in the photomicrographs (Figs. 2a-8a), the morphologies of the particles changed with size. Irregularly shaped particles are assigned a general geometric factor of $2/13$; using the spherical geometric factor for irregularly shaped particles would therefore cause the cut size to be underestimated by about 17%.

Agglomeration causes small particles to be separated out into the larger particle-size fractions. When two or more particles are flocculated together, their apparent hydrodynamic size increases and the agglomerate acts as a large particle with a density between that of the medium and that of the particles. The result is small particles in large particle-size fractions.

Particle interactions as large particles move toward the side of the basket and small particles flow up the fluid wall can cause improper powder separation. Large particles could trap smaller ones and force them toward the wall, thereby causing small particles to end up in the large particle-size fraction. Particle interactions could also hinder the movement of large particles toward the wall: assuming that the upward velocity of the particles is governed by the flow of liquid and is affected little by solids content, a reduced horizontal velocity vector due to particle interactions may allow large particles to be swept out of the centrifuge. Separation efficiency should increase with decreasing solids content. As the thickness of the powder layer on the inner side wall of the bowl increases, the distance a particle has to move before it hits this barrier decreases. Therefore, small particles, which travel to the top of the bowl and out, might not make it out after a powder layer has built up. With a

powder layer of 1 cm, the average particle size may be reduced by approximately 30%. The significance of this effect is questionable, however, based on independent research (Poher, 1988).

As always, operator error can be significant. With feed rates on the order of hundreds of milliliters per minute and dispersion volumes on the order of thousands of milliliters, run times must be on the order of tens of minutes. Start-up and shut-down, as well as feed rate and rpm fluctuations throughout the run, could be important determinants of particle-size distributions.

Lastly, the dispersion is fed into the centrifuge at the bottom of the bowl, toward the center, to minimize the amount of splashing. If any air is trapped in the dispersion, however, the bubbles could rise very rapidly up the fluid wall, possibly taking particles of all sizes with them.

As the above discussion indicates, many sources of error affect the average particle size and size distribution during classification; the relative effects of each source are unknown.

Close examination of the particle-size distributions reveals interesting variations. For the first cut, many coarse particles were removed from the powder (for each of the first three cuts, up to 2.4 area percent of the particles was contributed by particles greater than 2 μm in size). More than twice the area of particles greater than 1.2 μm in size was found in the first cut as compared to the original powder. Also, 30% more very fine particles (0.1-0.0 μm) were found in the first cut than in the as-received powder. This can be contrasted to the second cut, in which many very large particles were found, but not as many very fine particles were trapped. This is reflected in a larger average size for the second cut as compared to the first, but the average particle size for both cuts

was less than the calculated value because of the retained smaller particles. One possible reason for the decrease in retained small particles is that the powder concentration was reduced dramatically from the first run to the second because about one third of the powder was removed in the first cut.

From the second cut to the sixth, the cross-sectional area attributable to large particles in the three largest particle-size ranges generally decreased while the surface area of particles in the two smallest particle-size ranges increased. The bulk of the cut powders consisted of smaller particles as the cuts became finer: In the last cut, two-thirds of the particles were smaller than $0.2\ \mu\text{m}$. Consequently, the average particle size decreased from $0.42\ \mu\text{m}$ to $0.16\ \mu\text{m}$ in Cuts 2 and 6, respectively.

In Figures 5-11, the narrowing of the particle-size distribution to finer particle sizes is obvious. However, a more quantitative comparison of the relative distribution breadths requires the use of a statistical parameter such as the standard deviation. For skewed distributions such as those in Figures 5a-11a, linear averages and standard deviations are not the best forms of representation because they are based on normal distributions; the distributions presented in Figures 5a-11a are close to log normal (typical of most particle-size distributions), but are not symmetrically log normal. Preferable statistical expressions in such a case would be the geometric mean and deviation. These are more representative of the average and deviation of a skewed distribution. However, because of the unsymmetrical distributions, the original distributions could not be calculated from these two parameters only. The geometrical mean and standard deviation are useful only to compare the cuts.

The definitions of the geometric mean, d_g , and geometric standard deviation, σ_g , are as follows:

$$d_g = \prod_i d_i^{n.f._i} \quad (5)$$

$$\sigma_g = \exp\left\{\left[\sum_i n.f._i (\ln(d_g) - \ln(d_i))^2\right]^{1/2}\right\} \quad (6)$$

where \prod_i is the product over i intervals, with d_i the average diameter of the interval, and $n.f._i$ the respective number fraction. These equations are for number distributions of particles; they can be transformed to area distributions as follows:

Mean:
$$a_g = \prod_i a_i^{a.f._i} \quad (7)$$

$$(\pi/4)d_g^2 = \prod_i [(\pi/4)d_i^2]^{a.f._i} \quad (8)$$

$$d_g^2 = \prod_i d_i^{2(a.f._i)} \quad (9)$$

$$d_g = \prod_i d_i^{a.f._i} \quad (10)$$

Standard Deviation:

$$\sigma_g(\text{area}) = \exp\left\{\frac{[\sum_i a.f._i (\ln(a_g) - \ln(a_i))^2]^{1/2}}{2}\right\} \quad (11)$$

The 2 in the denominator of the argument of the exponential is included due to the fact that $\sigma_g = \sigma_g(\text{mass})$ for a log normal distribution, and in order to make this true for equations of the form reported above, the argument of the exponential must be divided by the number of dimensions being considered (e.g., 3 for mass) (Flint and Haggerty, 1988). The argument of the exponential for the $\sigma_g(\text{area})$ formula was therefore divided by 2.

$$\sigma_g(\text{area}) = \exp \left\{ \frac{[\sum_i \text{a.f.}_i (\ln[(\pi/4)(d_g^2)] - \ln[(\pi/4)(d_i^2)])^2]^{1/2}}{2} \right\} \quad (12)$$

$$\sigma_g(\text{area}) = \exp \left\{ \frac{[\sum_i \text{a.f.}_i ((\ln(\pi/4) + \ln(d_g^2)) - (\ln(\pi/4) + \ln(d_i^2)))^2]^{1/2}}{2} \right\} \quad (13)$$

$$\sigma_g(\text{area}) = \exp \left\{ \frac{[\sum_i \text{a.f.}_i (\ln(d_g^2) - \ln(d_i^2))^2]^{1/2}}{2} \right\} \quad (14)$$

$$\sigma_g(\text{area}) = \exp \left\{ \frac{([\sum_i \text{a.f.}_i (2\ln(d_g) - 2\ln(d_i))^2]^{1/2})}{2} \right\} \quad (15)$$

$$\sigma_g(\text{area}) = \exp \left\{ \frac{2[\sum_i \text{a.f.}_i (\ln(d_g) - \ln(d_i))^2]^{1/2}}{2} \right\} \quad (16)$$

$$\sigma_g(\text{area}) = \exp([\sum_i \text{a.f.}_i (\ln(d_g) - \ln(d_i))^2]^{1/2}) \quad (17)$$

These are the values reported as $d_{g,a}$ and $\sigma_{g,a}$ in Figures 5-11. For a point of reference on the standard deviations, a monosized particle-size distribution would have a value of 1.

Four points should be noted about the trend in standard deviations. First, the first cuts have broader particle-size distributions than does the as-received powder. Second, the fourth cut apparently has a broader distribution than do the second and third cuts. Third, the finest cut size has about the same breadth of particle-size distribution as the as-received powder. Fourth, the fifth cut has a slightly narrower particle-size distribution than the last cut.

Based on the previous discussion, the standard deviation of the first cut was expected to be the broadest. The first cut, run with the highest volume-fraction solids in the stock dispersion, was performed to remove the largest particles. Consequently, many of the largest particles were removed; at the same time, however, many of the smallest particles were also removed due to particle-particle interactions.

The breadth of the particle-size distributions decreased from the first cut to the fourth, after which it increased again. This change is an artifact of the way the standard deviation was calculated: for the as-received powder and the first three cuts, the smallest particle size measured was 0.10 μm ; for the last three cuts, the smallest size measured was 0.05 μm . The additional size interval was used for the standard deviations of the last three cuts to yield a more accurate number. However, this change made comparison with the large-sized powders questionable. If the standard deviations of the last three cuts are calculated the same way as those of the first cuts, then $\sigma_{g,a}$ for Cuts 4, 5, and 6 is 2.36, 2.21, and 2.40, respectively. For comparison throughout the cuts, these values make more sense but are not necessarily more accurate.

The reason the powder was classified in the first place was not only to decrease its average particle size but to narrow the distribution. A narrowed distribution would enhance densification and microstructural control (Yan, Cannon, Bowen, and Chowdhry, 1982; Barringer, Brook, and Bowen, 1984; Chapell, Ring, and Birchall, 1986). However, for this system, the finest cut size had about the same relative breadth as the starting powder even though the absolute particle-size distribution was different. The next-to-last cut, No. 5, was only slightly narrower. This was the

result of the average particle size's decreasing with classification at the same time the overall distribution was being narrowed. This can be seen rather well by a consideration of the last two cuts: the last cut had more particles less than $0.3\text{ }\mu\text{m}$ in diameter than did the fifth cut, and as a result had a smaller average particle size. However, the cuts had similar amounts (by area) of material far from their averages, which contributed significantly to the standard deviations. Since this material was further from the average for the last cut as compared to the fifth cut, the particle-size distribution for the last cut was broader; this assumes that the material measured at the largest sizes consisted of particles rather than agglomerates. No particles greater than $1\text{ }\mu\text{m}$ were observed by SEM, but the centrifugal analyzer measured many more particles than can be conveniently viewed under the microscope.

Conclusions

Fine powders with average particle sizes of $0.1\text{-}0.2\text{ }\mu\text{m}$ and 90% of the particles less than $0.5\text{ }\mu\text{m}$ were produced by centrifugal classification. Overall, powder retention in the system was greater than 90 wt%. However, the relative breadth of the particle-size distributions for the as-received and finest powders did not vary significantly. The lack of narrowing for the large-particle cuts was due to the retention of small particles in these cuts; the lack of narrowing for the small-particle cuts was due to small quantities of large particles in the small-to-average sized powders. These results may be attributed to inaccurate geometric factors, agglomeration, particle interactions, powder build-up inside the centrifuge, operator error, and/or improper dispersion feed to the centrifuge. It should be noted, though, that the larger cuts could be

narrowed if they were subsequently classified further both above and below the desired particle-size range.

Future Work

Future studies should include an investigation of this study's sources of error and their relative significance. Understanding these aspects could allow better classification at greater throughputs. In particular, an investigation of solids contents and dispersion qualities for different powders would be very useful in determining whether any narrowing of the particle-size distributions on a relative basis is possible with one series of classifications, or whether subsequently narrowing cuts above and below the desired particle-size range is necessary.

MICROSTRUCTURAL DEVELOPMENT OF β -SiC

Introduction

Parts (compacts) made from as-received and classified β -SiC powders doped with both 0.9 wt% B_4C and 2 wt% carbon from either polyphenylene (a polymeric carbon source) or carbon black were processed from OLOA®1200-stabilized suspensions and sintered under flowing argon at 2000°C and 2100°C in order to evaluate the powder suspensions and the effects of powder classification. With regard to densification, the classified-powder parts had higher densities than did the as-received powder parts, and the polyphenylene-doped parts had slightly higher densities than did the carbon-black-doped parts. Details on processing and sintered densities were reported previously (Bishop, 1987).

One reason for sintering the as-received and classified-powder parts was to observe changes in grain size through the sintering stage. Also, the issue of β - α phase transformations for different-sized powders is

critical to processing high-density β -SiC. The following discussion focuses on these two issues.

Experimental Procedures

Two of the three samples of each type (as-received Betarundum Ultrafine β -SiC powder (Ibiden Co. Ltd., Ogaki, Japan) doped with boron carbide (Callery Chemical Co., Callery, PA) and carbon black (Monarch 905; Cabot Corp., Billerica, MA) (ARCB); as-received β -SiC powder with boron carbide and polyphenylene (Polysciences Inc., Warrington, PA) (ARPP); centrifugally classified β -SiC powder doped with boron carbide and carbon black (CCCB); centrifugally classified β -SiC powder doped with boron carbide and polyphenylene (CCPP)) sintered at 2000°C and one of each type sintered at 2100°C were sectioned axially through the center and polished using, in succession, 9-, 6-, 3-, 1-, and 0.25- μ m diamond pastes. The 9- μ m paste was used to lap the samples flat; the samples were then polished for ~30 min with each successively finer-grained paste and checked to determine whether scratches from previous polishings had been removed.

The parts sintered at 2000°C were etched using a 50/50 weight ratio KOH/KNO₃ molten salt bath in a nickel crucible heated by a Meker-type, high-temperature gas burner. The salts were heated to their melting temperatures, then were allowed 15 minutes to reach the temperature of the gas burner after the melt had stopped bubbling. The parts were etched for a total of 15-30 s in 5-10-s intervals, after which the parts were observed by SEM to detect the presence of grain boundaries.

The carbon-black-doped parts sintered at 2100°C were etched using the molten salt bath system described above. Because the molten salt bath did not etch the 2100°C-sintered, polyphenylene-doped parts, these were boiled in Murakami's solution (1 part KOH, 1 part K₃Fe(CN)₆, 10 parts H₂O) for

3-5 h. Furthermore, for the 2000°C parts, the carbon-black-doped parts typically took shorter times to etch than did the polyphenylene-doped parts. One carbon-black-doped sample was etched in the Murakami's solution, and the observed microstructure was found to be practically identical to that obtained with another sample etched by the molten salt.

Grain sizes were measured from SEM photomicrographs of random areas from the interior of the 2000°C samples, taken at a magnification of 10,000x for the as-received powder samples and 8,000x for the classified powder samples. The photos needed to be contrast-enhanced before an attempt was made to perform a quantitative image analysis on the Magiscan 2 (Joyce Loebel Div., Vickers Ltd., Gateshead, England). Photos were photocopied and enlarged by 200%. The microstructures of at least four different areas were then traced onto tracing paper using a light table for illumination. Each tracing was then enhanced by darkening the grain boundaries and coloring in the pores and borders; this enhanced image was then reduced to the size of the original photomicrograph, cut out, and pasted on black paper. At least 445 grains were analyzed. The two-dimensional grain sizes were measured by area and their diameters deduced by assuming circles. These sizes were converted to three-dimensional ones using the Schwartz-Saltykov method, assuming a spherical geometry (Underwood, 1970). Even though the grains were not spherical, this assumption was made because 1) the aspect ratio for all samples was not large (~1.6) and 2) although the geometry of the starting powders was also not spherical, it was assumed to be so to determine the particle size by sedimentation/centrifugation. Geometric average sizes and standard deviations were calculated using the following equations:

$$d_g = \prod_i d_i^{a.f._i} \quad (1)$$

$$\sigma_g = \exp \left(\left[\sum_i a.f._i (\ln(d_g) - \ln(d_i))^2 \right]^{1/2} \right) \quad (2)$$

where \prod_i is the product over "i" intervals with d_i the average diameter of interval i, and $a.f._i$ the respective area fraction. These equations are for area distributions of particles.

X-ray powder diffraction was performed on both the powders and sintered samples that had been ground in a titanium carbide mortar and pestle. Ground samples were then washed in 8-M nitric acid for 64 h to remove any TiC, then rinsed in distilled water. Measurements were made on a Rigaku RU-300 powder diffraction unit at 50 kV, 200 mA, and 10° (2θ) per minute.

Results and Discussion

Photomicrographs representative of the four types of samples sintered at 2000°C are shown in Figures 12 and 13. The grain size of the as-received powder compacts is much larger than that of the compacts made of classified powder (Table 2). Also, few pores are apparent inside the

Table 2. Particle-size and grain-size distributions.

Material	$d_{g,a}$ (μm)	$\sigma_{g,a}$
As-received powder	0.32	2.32
Classified powder	0.16	2.26
ARCB, 2000°C	1.57	1.61
ARPP, 2000°C	1.70	1.61
CCCB, 2000°C	1.02	1.52
CCPP, 2000°C	1.04	1.60

grains of all the samples, indicating that pore/grain boundary separation did not occur to a great extent. The microstructures of all the samples appear to be more porous than the measured immersion densities would indicate, due, perhaps, to polishing and etching damage.

In Figure 14, the grain sizes of the compacts are plotted against their relative densities. The solid and dashed lines are replotted data from experiments using the same type of powder as the as-received powder in the present experiments, with doping levels that should make the samples practically equivalent (Li, 1987a). There is very good agreement between the two sets of data for the as-received powder. The densities reached by the classified powder are comparable to those obtained for as-received powder sintered at temperatures approaching 2100°C, at which there is considerably greater grain growth.

In order to determine whether the same diffusion mechanisms are operable in both the as-received- and classified-powder samples, the grain size divided by the initial particle size was plotted against sintered density (Fig. 15). This shifts the classified-powder compact grain-growth ratios up to those of the as-received material. Consequently, the diffusional processes in both types of samples are the same, as was anticipated.

Another aspect of Figure 15 is that the classified powder underwent relatively more grain growth than did the as-received powder. It had been hoped that classification would produce a narrower-size-distribution powder than the as-received material, and that this would suppress grain growth; the relative distribution breadth, however, did not significantly change as a result of the classification, and consequently relative grain growth

could not be suppressed by a significantly narrowed particle-size distribution. Another factor in the comparison of relative grain-growth ratios is green density. It has been shown that lower-green-density compacts of comparable powders have higher grain-growth ratios than do pellets of higher green density, when sintered to above 90% of theoretical (Barringer and Bowen, 1983). It is unclear, though, what the effect of different particle sizes would be when combined with differing green densities.

In order to explain the high density/smaller grain-size samples of the classified-powder compacts, the theory of pore/grain-boundary separation in the final stage of sintering was invoked. Assuming that pore movement is controlled by carbon-lattice diffusion, the grain-boundary migration and pore-migration rates in the final stage are equal when:

$$[1/G]D_l/M_b = 0.16[(\rho_0/1.5kT)/(\rho(1-\rho)^{0.5}\Omega)] \quad (3)$$

where G = grain size; D_l = the carbon lattice diffusion constant; M_b = grain-boundary mobility; ρ_0 = initial density; ρ = sintered density; Ω = atomic volume; k = Boltzmann constant; and T = temperature (Li, 1987b). Assuming that the sintered samples are at the threshold of pore/boundary separation, the value of D_l/M_b is about 1.5×10^6 dyne-s/cm. Based on this, the separation region is plotted against the grain size/density data in Figure 16. It can be seen that for smaller grain sizes, higher densities can be achieved before pore/grain-boundary separation occurs. This is one of the major advantages of classified SiC powder.

The size distributions of particles and grains (2000°C-sintered compacts) for the as-received and classified systems, respectively, are plotted in Figures 17 and 18. The effect of grain growth is quite obvious.

Also, the distribution of the particles is much broader than that of the grains, with the largest particles seemingly undergoing little grain growth compared to the smaller ones. Geometric standard deviations, along with the averages of the particle/grain-size distributions, are shown in Table 2.

Caution should be exercised in considering these distributions. Possible sources of error include failure to find the largest grains in the sintered material; polishing and etching damage, causing fewer small particles to be detected; inaccurate determinations of the largest particle sizes by the centrifugal particle-size analyzer; and the validity of comparing particle/grain-size distributions from centrifugal sedimentation of particles to three-dimensional grain size as determined from a microscopic examination of two-dimensional particle sections.

Literature comparing starting-powder particle-size distributions and final-stage grain-size distributions is sparse. Oel (1969), in his research of grain-growth laws via grain-growth rates in the final stage of sintering at steady state, plotted particle-size distributions as determined from SEMs against three-dimensional grain-size distributions as determined from SEMs of polished sections. Calculation of size distributions for MgO particles and the resultant grains after sintering at 1800°C for 20 min were very similar ($\sigma_{g, \text{ particles}} = 1.66$; $\sigma_{g, \text{ grains}} = 1.56$).

Data from Ikegami et al. (1978) on BaCl₂-doped MgO sintered to 80% of theoretical from a green density of 52% indicated no change in particle/grain-size distribution breadth over this density range; their data was derived from fracture surfaces and was not converted to three-dimensional data.

The only theory that predicts a narrowing of grain-size distribution in solid-state sintering was proposed by Tomandl (1980). Assuming a spherical geometry for grains in the final stage of sintering, calculations were made for materials with and without impurities. Without impurities at the grain boundaries, a steady-state distribution of grain sizes not very different in breadth from the initial grain-size distribution (not the particle-size distribution) was reached. These results are almost identical to those obtained by Kaysser et al. (1982), who calculated the theoretical steady-state distribution due to Ostwald ripening for the liquid-phase sintering of metal alloys. This is understandable, in that Tomandl's equations for the reduction of free energy are based on those for Ostwald ripening.

Tomandl's examination of the effects of impurities that do not diffuse well along grain boundaries (e.g., carbon on the grain boundaries of SiC) and that as a result slow not only the migration of grain boundaries but also grain growth, indicated that the grain-size distribution does not approach a steady state, but narrows over time. Theory also predicts a slowing in the grain growth, which is also one effect of carbon doping in SiC. Consequently, it may not be unreasonable for the grain-size distribution to narrow.

In the liquid-phase sintering of metal alloys, initial particle-size distributions have been reported to narrow (Riegger, Pask, and Exner, 1980). In this case, small grains become soluble in the liquid phase due to curvature effects, and plate out on larger grains. With the removal of small grains from the system, the distribution narrows. It is unlikely that any appreciable liquid phase appears during the sintering of β -SiC

doped with boron and carbon; consequently, any liquid-phase mechanisms would not be applicable.

However, elimination of small particles may be possible through grain growth in porous compacts. As reported by Greskovich and Lay (1972), particle-size differences can cause particles to coalesce after neck formation and dihedral angle equilibration but before significant densification. The driving force for this grain growth is the curvature of a grain boundary between particles of differing size because of dihedral-angle equilibration (Fig. 19). Since silicon and carbon grain-boundary diffusion in SiC is relatively fast compared to lattice diffusion, grain boundaries can be mobile even before densification occurs. Therefore, small particles could be eliminated, narrowing the grain-size distribution. However, because of possible error in the size distributions of particles and grains, and the lack of any supporting experimental evidence, no definitive statement can be made on the change of breadth in a particle-size distribution as particles change to grains and move into the final stage of sintering.

Another critical aspect of microstructure development in boron- and carbon-doped β -SiC is the β - α phase transformation, which typically occurs in the 1900-2100°C range, depending on impurities (Jepps and Page, 1981). In structural ceramics, significant amounts of transformed material in the shape of plates (needles on a planar surface) are detrimental to mechanical properties (Johnson and Prochazka, 1977). As a result, densification, grain growth, and the β - α phase transformation are competing processes in the sintering of β -SiC. In order to densify the material, coarsening needs to be suppressed and lattice diffusion enhanced. However, suppressing coarsening also enhances the transformation kinetics, and promoting lattice

diffusion enhances grain growth. Unless the material is hot-pressed in some manner by which the driving force for densification is enhanced, the driving force for grain growth not affected, and the driving force for phase transformation possibly reversed (Jepps and Page, 1981), sintering β -SiC doped with boron and carbon involves a compromise.

In this study, phase transformations in the classified- and as-received-powder compacts differed. At 2000°C, transformation was observed by SEM in only the sintered classified-powder compacts (Fig. 20). By XRD, the changes observed were an increase in the intensity of a shoulder on the higher 2θ side of the 100% β -SiC peak and an increase in intensity relative to the 100% β -SiC peak for peaks at $\sim 60^\circ$ and $\sim 72^\circ$ 2θ (Figs. 21 and 22). The X-ray diffraction pattern for the classified powder was obtained from powder taken from the fifth classification cut and not that of the sixth, which was used in processing: because practically all the 0.15–0.20- μm size-classified powder was used for processing and particle-size distribution determinations, the next smaller powder was used for X-ray diffraction pattern comparison.

An interesting feature of the platelets found in the microstructure of the classified-powder compacts is shown in Figure 20: because of a growth mechanism based on interfacial energies such that the α -SiC platelets grow within a β -SiC envelope, the alpha platelets are bonded directly to the beta matrix (Heuer et al., 1978). Consequently, the platelets would not impart any toughening to the compacts because of the strong interfacial bonding.

Sintering at 2100°C results in even more substantial transformation, as is evident from the optical photomicrographs of Figures 23 and 24, in which the microstructures are dominated by large α -SiC plates and needles.

The characteristic feather pattern (Johnson and Prochazka, 1977) is especially clear in Figures 23 and 24. Also, the sizes of the plates and needles are, in general, smaller for the classified-powder compacts than for the as-received-powder compacts. The XRD pattern of a compact sintered at 2100°C is much more complex than that of a compact sintered at 2000°C (Fig. 25). The phases detected were (using Ramsdell notation, in which a letter stands for the type of crystal structure (i.e., C for cubic, R for rhombohedral, H for hexagonal) and a numeral indicates the number of stacking layers in the unit cell) 3C, 15R, and 6H; no 4H phase was detected. The 3C phase is typically known as "beta" silicon carbide; all other hexagonal and rhombohedral polytypes are generically termed "alpha"-phase silicon carbide.

In a previous study of compacts sintered at 2000°C, the phase composition of boron- and carbon-doped β -SiC similar to the material used in the present experiments was reported to be ~90 vol% 3C and 10 vol% total of the 15R, 6H, and 4H phases (Williams et al., 1984). For Betarundum Ultrafine β -SiC under the conditions used in the present study, the major phase was 3C; a small amount of the alpha phase, probably 15R, was also present. The alpha phase was difficult to identify because of the small amount of the phase and the alpha peak overlap with the beta phase peak. Even though the X-ray patterns for both the as-received- and classified-powder parts showed small phase changes during sintering, only the microstructures of the classified-powder compacts showed the traditional long-needle grains.

The α -SiC needles (platelets in three dimensions) grow more readily in a matrix of smaller grains (Bocker, Landfermann, and Hausner, 1981), by exposing their low-energy basal plane to a coherent crystallographic plane

of β -SiC (Heuer et al., 1978). The edges of the plates then grow into a fine matrix. As with typical exaggerated grain growth, the driving force for platelet growth is not the size of the exaggerated grain (or plate, in this case) but that of the matrix. Consequently, the finer matrix obtained with the classified-powder compacts is more conducive to exaggerated grain growth through the β - α transformation than is the coarser matrix of the as-received powder compacts.

In a previous study of compacts sintered at 2100°C, the phase composition of boron- and carbon-doped β -SiC similar to the material used here was reported to be 60 vol% 3C, 15 vol% 15R, and 25 vol% 50/50 volume ratio of 6H and 4H (Williams et al., 1984). For the material in the present study, qualitative analysis of the as-received powder compacts revealed that 15R was the dominant phase and 6H a minor phase. Cubic β -SiC was also a minor constituent, judging from the XRD pattern and the fact that the microstructures contained few small equiaxed grains. For the classified-powder pellets, XRD showed more of the 6H phase than was apparent in the as-received powder samples, though the 15R phase was still a large constituent. Again, the amount of cubic phase was difficult to distinguish, though it must have been small, judging from the small amount of matrix material left.

This phase analysis is in qualitative agreement with a previous, quantitative, analysis made of a similar material (Williams et al., 1984). Two major differences between the analyses are that 1) the cubic phase did not seem to be retained as long in the sintered parts of the present study as was reported in the literature, and 2) the trend observed in both studies, of the 15R phase initially predominating, then being overtaken by the 6H phase, was controlled in the literature by changing the

temperature, while in the present study this trend was observed by changing the powder. Assuming the transformation to the 6H phase to have proceeded as far as it could go, the classified powder transformed more than did the as-received; this may have been due to the higher energy of the classified material, since both the as-received β -SiC powder and the transformed matrices are finer in structure than the as-received material.

The finer structures exhibited by the classified-powder samples sintered at 2100°C compared to those of the as-received-powder samples must have resulted from a greater number of nuclei per unit volume from which the β - α transformation could proceed. A greater number of growing plates would result in less beta material to be transformed per plate, and therefore a finer structure. However, the XRD patterns of the as-received and classified powders do not indicate a greater alpha content for the finer powder. This does not necessarily mean that there were not more stacking faults in the classified powder than in the as-received powder that could nucleate the transformation; it may be possible that, due to a lack of long-range order and/or a concentration below that detectable by XRD, these structures were not revealed.

Conclusions

The grain sizes of classified-powder compacts were smaller than those of as-received-powder compacts. When normalized to the initial particle size, the grain-growth ratio of both classified- and as-received-powder parts lie on the same curve of grain size/particle size versus sintered density, indicating no change in diffusion mechanism is produced by the difference in particle-size distribution. Also, the classified particle-size distribution provided no advantage with respect to relative grain

growth because the particle-size distribution breadth was equivalent to that of the as-received powder.

The grain-size distribution breadth narrowed when particles were sintered to the final stage, perhaps because grain growth in the porous compacts eliminated the smallest particles, narrowing the grain-size distribution. However, no other supportive experimental evidence exists, and because there were many possible sources of error in the present particle-size/grain-size distribution determinations, no conclusive statements can be made.

Alpha-SiC in boron- and carbon-doped β -SiC becomes more prominent as the sintering temperature is increased. Only a small increase in the alpha phase occurred at a sintering temperature of 2000°C in this study; a significant increase took place at 2100°C. Microstructurally, alpha platelets 20–60 μm in length that were bonded directly to the matrix grew at 2000°C in the finer beta matrix of the classified-powder compacts. At 2100°C, all microstructures showed excessive transformation, with plates and needles on the order of 100 μm in size; the classified-powder compacts had finer structures. The classified-powder compacts' smaller grain size when sintered to 2100°C may explain these compacts' greater transformation to the 6H phase, whereas the as-received material had less of the 6H phase and more of the 15R phase.

Future Work

The largest particles of both as-received and classified powders will be examined by SEM to determine whether the centrifugally measured particle sizes were correct or if the largest "particles" were actually agglomerates of particles.

REFERENCES

W. Albers and J.Th.G. Overbeek, "Stability of Emulsions of Water in Oil II. Charge as a Factor of Stabilization Against Flocculation," J. Colloid Sci., 14, 510-18 (1959).

E.A. Barringer and H.K. Bowen, "Effects of Particle Packing on the Sintered Microstructure"; in International Inst. for the Science of Sintering, Belgrade, Yugoslavia, 1983.

E.A. Barringer, R. Brook, and H.K. Bowen, "The Sintering of Monodisperse TiO_2 "; pp. 1-21 in Materials Science Research, Vol. 16. Edited by G.C. Kuczynski, A.E. Miller, and G.A. Sargent. Plenum Press, New York, NY, 1984.

E.A. Barringer, N. Jubb, B. Fegley, R.L. Pober, and H.K. Bowen, "Processing Monosized Powders"; pp. 315-33 in Ultrastructure Processing of Ceramics, Glasses, and Composites. Edited by L. Hench and D. Ulrich. John Wiley, NY, 1984.

B.A. Bishop, "Commercial SiC Powder Characterization, Dispersion, and Classification," CPRL Report #Q3, MIT, pp. 65-69 (1985a); "OLOA®1200 Purification," AFOSR Report, MIT, pp. 104-06 (1985b); "Commercial SiC Powder Dispersion by OLOA®1200," AFOSR Report, MIT, pp. 42-60 (1986a); "Dispersion and Classification of Commercial SiC," CPRL Report #Q4, MIT, pp. 80-86 (1986b); "Advanced Processing Techniques for Silicon Carbide," AFOSR Report, MIT, pp. 1-69 (1987).

W. Bocker, H. Landfermann, and H. Hausner, "The Influence of Powder Characteristics on the Sintering of α -SiC," Powder Metal. Intl., 13 [1] 37-39 (1981).

W.E. Brownell, Structural Clay Products; pp. 43-62. Springer-Verlag, Wein, 1976.

J.S. Chapell, T.A. Ring, and J.D. Birchall, "Particle Size Distribution Effects on Sintering Rates," J. Appl. Phys., 60 [1] 383-91 (1986).

C.S. Chen and S. Levine, "The Double-layer Interaction of Two Charged Colloidal Spherical Particles of a Concentrated Dispersion in a Medium of Low Dielectric Constant, I. Force Calculations," J. Colloid Interface Sci., 43 [3] 599-615 (1973).

V. de Baisi, "Ford Runs Uncooled Ceramic Turbine Engine at 2500°F," Gas Turbine World, pp. 12-18 (July 1977).

S. Dutta, "Sinterability, Strength, and Oxidation of Alpha Silicon Carbide Powders," J. Mat. Sci., 19, 1307-13 (1984).

A. Einstein, "Eine neue Bestimmung der Molekuldimensionen," Ann. d. Phys., 19, 289-306 (1906).

A. Einstein, "Berichtigung zu meiner Arbeit: 'Eine neue Bestimmung der Molekuldimensionen'," Ann. d. Phys., 34, 591-92 (1911).

G.R. Feat and S. Levine, "The Double Layer Interaction of Two Charged Colloidal Spherical Particles of a Concentrated Dispersion in a Medium of Low Dielectric Constant, III. Approximation of Perfectly Conducting Particles," J. Colloid Interface Sci., 54 [1] 34-44 (1976).

J.H. Flint and J.S. Haggerty, "A Model for the Growth of Silicon Particles from Laser Heated Gases," submitted for publication to Aerosol Sci. and Tech. (1988).

J.H. Green and G.D. Parfitt, "Charge Stabilization of Concentrated Dispersions in Apolar Media"; pp. 205-15 in Flocculation, Sedimentation, and Consolidation: Proceedings of the Engineering Foundation Conference. Edited by B.M. Moudgil and P. Somasundaran. Engineering Foundation, New York, NY, 1986.

C. Greskovich and K.W. Lay, "Grain Growth in Very Porous Al_2O_3 Compacts," J. Am. Ceram. Soc., 55 [3] 142-46 (1972).

A.H. Heuer, G.A. Fryburg, L.U. Ogbuji, and T.E. Mitchell, " β - α Transformation in Polycrystalline SiC: I. Microstructural Aspects," J. Am. Ceram. Soc., 61 [9-10] 406-12 (1978).

T. Ikegami, M. Tsutsumi, S. Matsuda, S. Shirasaki, and H. Suzuki, "Model of Densification with Simultaneous Grain Growth," J. Appl. Phys., 49 [7] 4238-41 (1978).

N.W. Jepps and T.F. Page, "The 6H-3C 'Reverse' Transformation in Silicon Carbide Compacts," Commun. Am. Ceram. Soc., 64 [12] C177-C178 (1981).

C.A. Johnson and S. Prochazka, "Microstructures of Sintered SiC"; pp. 366-77 in Ceramic Microstructures '76. Edited by R.M. Fulrath and J.A. Pask. Westview Press, Boulder, CO, 1977.

W.A. Kaysser, S. Takajo, and G. Petzow, "Particle Growth by Coalescence During Liquid Phase Sintering of Fe-Cu"; pp. 321-27 in Materials Science Monographs, Vol. 14. Edited by D. Kolar, S. Pejovnik, and M.M. Ristic. Elsevier Scientific Publishing Co., Amsterdam, 1982.

C.W. Li, "Microstructural Development During Sintering of Boron-Doped Beta SiC"; PhD Thesis, Massachusetts Institute of Technology, Department of Materials Science and Engineering, pp. 123-32 (June 1987a); p. 172 (June 1987b).

B.J. Marlow, D. Fairhurst, and H.P. Pendse, "Colloid Vibration Potential and the Electrokinetic Characterization of Concentrated Colloids," Langmuir, 4 [3] 611-26 (1988).

D.N.L. McGown, G.D. Parfitt, and E. Willis, "Stability of Non-Aqueous Dispersions, I. The Relationship Between Surface Potential and Stability in Hydrocarbon Media," J. Colloid. Sci., 20, 650-64 (1965).

K. Miyoshi, D.H. Buckley, and M. Srinivasan, "Tribological Properties of Sintered Polycrystalline and Single-Crystal Silicon Carbide," Am. Ceram. Soc. Bull., 62 [4] 494-500 (1983).

P. Nahass, R.L. Pober, and H.K. Bowen, "Semicontinuous Classification of Ceramic Powders," CPRL Report #76, MIT, pp. 1-20 (1987).

D.H. Napper, Polymeric Stabilization of Colloidal Dispersions. Academic Press, London, 1983.

H.J. Oel, "Crystal Growth in Ceramic Powders"; pp. 249-72 in Materials Science Research, Vol. 4. Edited by T.J. Gray and V.D. Frechette. Plenum Press, New York, 1969.

J.Th.G. Overbeek, private communication, June 1988.

G.D. Parfitt and J. Peacock, "Stability of Colloidal Dispersions in Nonaqueous Media"; pp. 163-226 in Surface and Colloid Science, Vol. 10. Edited by E. Matijevic. Plenum Press, New York, 1978.

R.L. Pober, MIT; private communication.

R.J. Pugh and F.M. Fowkes, "The Dispersibility and Stability of Carbon Black in Media of Low Dielectric Constant, 2. Sedimentation Volume of Concentrated Dispersions, Adsorption and Surface Calorimetry Studies," Colloids and Surfaces, 9, 33-46 (1984).

R.J. Pugh, T. Matsunaga, and F.M. Fowkes, "The Dispersibility and Stability of Carbon Black in Media of Low Dielectric Constant, 1. Electrostatic and Steric Contributions to Colloidal Stability," Colloids and Surfaces, 7, 183-207 (1983).

H. Riegger, J.A. Pask, and H.E. Exner, "Direct Observation of Densification and Grain Growth in a W-Ni Alloy"; pp. 219-33 in Materials Science Research, Vol. 13. Edited by G.C. Kuczynski. Plenum Press, New York, 1980.

S.G. Seshadri and M. Srinivasan, "Estimation of Fracture Toughness by Intrinsic Flaw Fractography for Sintered Alpha Silicon Carbide," Commun. Am. Ceram. Soc., 64 [4] C69-C71 (1981).

F. Thummler, "Sintering and High Temperature Properties of Si_3N_4 and SiC"; pp. 247-77 in Materials Science Research, Vol. 13. Edited by G.C. Kuczynski. Plenum Press, New York, 1980.

G. Tomandl, "Statistical Theory of Particle Growth in Crystalline Ceramics Without Liquid Phase"; pp. 61-75 in Materials Science Research, Vol. 13. Edited by G.C. Kuczynski. Plenum Press, New York, 1980.

E.E. Underwood, Quantitative Stereology; pp. 119-23. Addison-Wesley Publishing Co., Reading, MA, 1970.

R.M. Williams, B.N. Juterbock, C.R. Peters, and T.J. Whalen, "Forming and Sintering Behavior of B- and C-Doped α - and β -SiC," Commun. Am. Ceram. Soc., 67 [4] C62-C64 (1984).

M.F. Yan, R.M. Cannon, Jr., H.K. Bowen, and U. Chowdhry, "Effect of Grain Size Distribution on Sintered Density," Mat. Sci. and Eng., 60, 275-81 (1983).

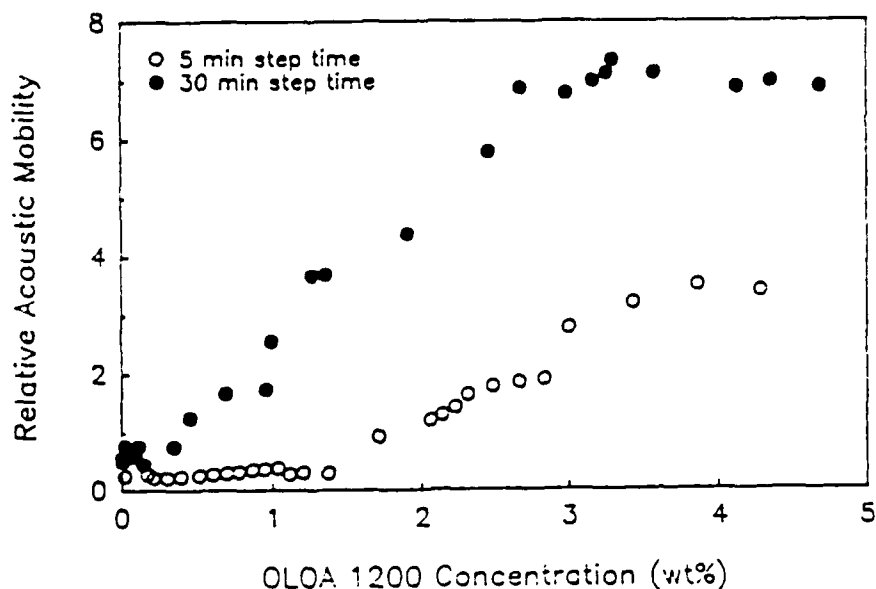


Figure 1. Relative acoustic mobility as a function of OLOA concentration for two different step-times.

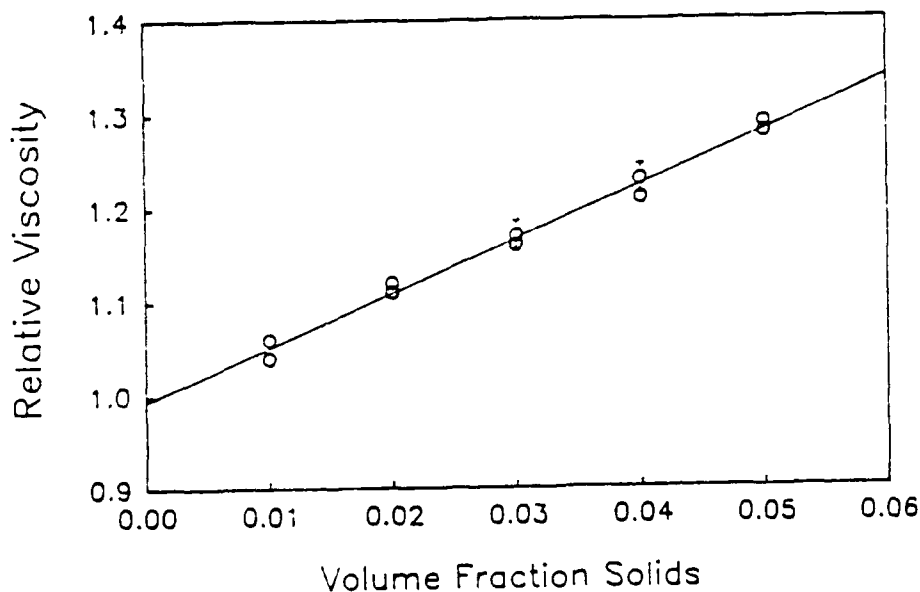


Figure 2. Relative viscosity versus volume-fraction solids for the OLOA/SiC/dodecane system.

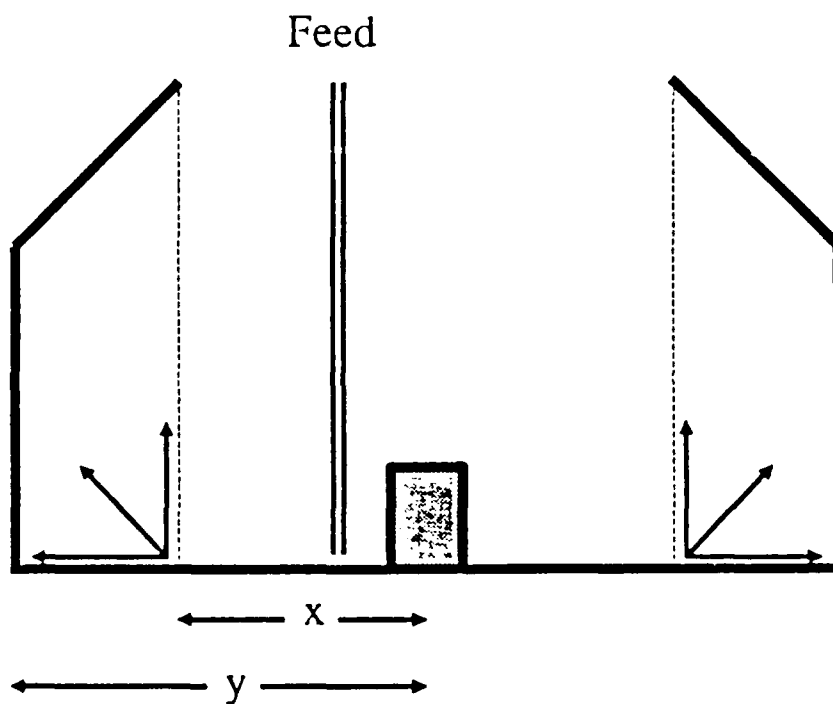


Figure 3. Centrifuge-bowl geometry for the centrifugal particle-size classifier.

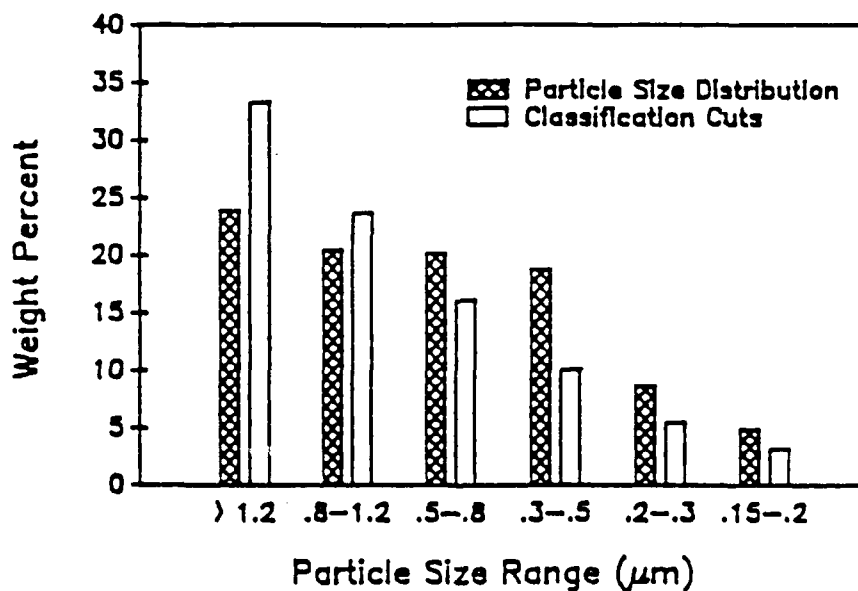
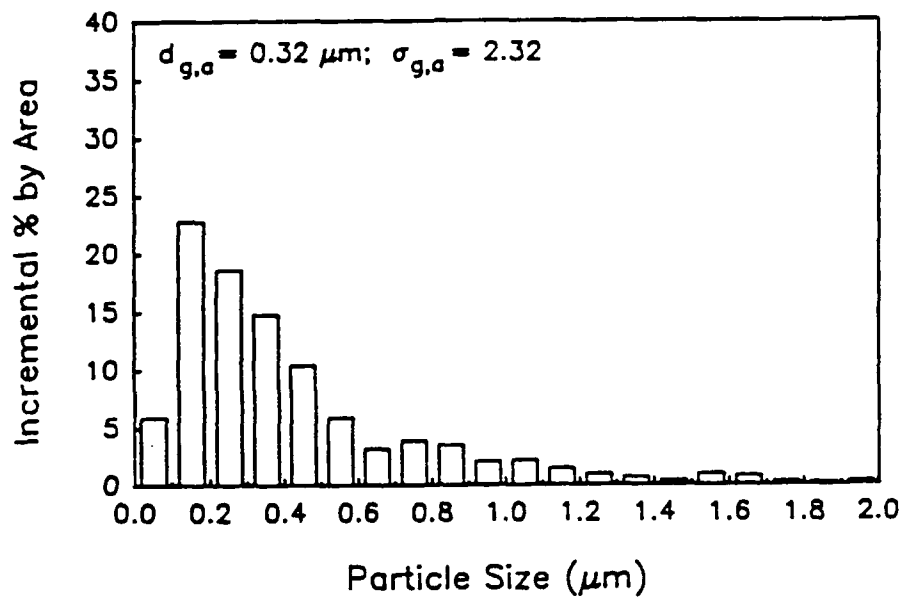
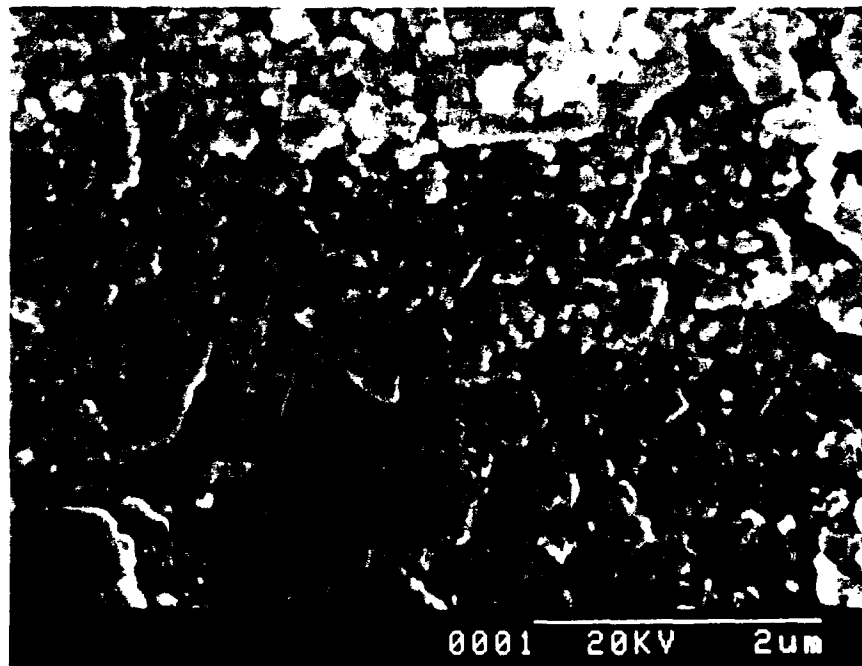


Figure 4. Classification efficiency as reflected in weight percent collected vs. weight percent present in particle-size classification cuts.

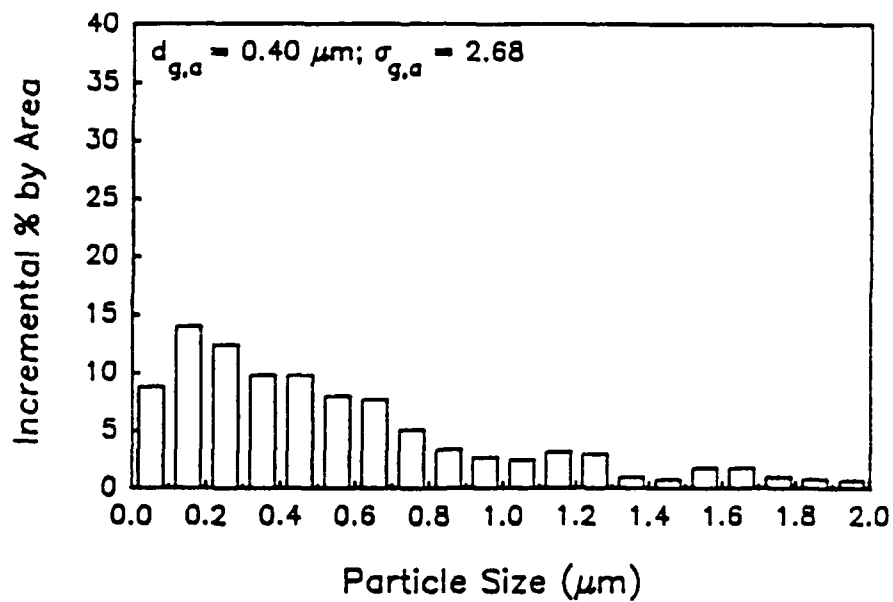


(a)

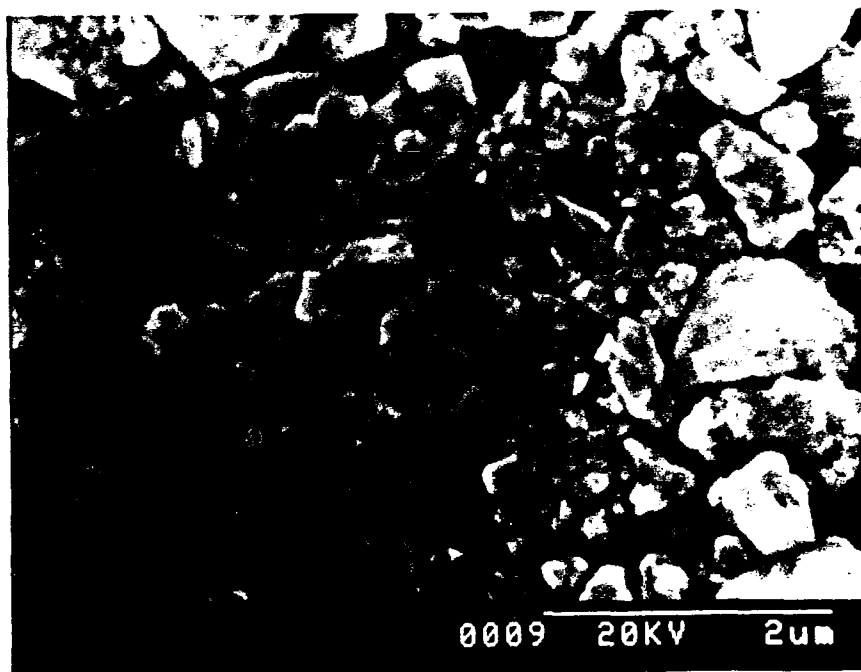


(b)

Figure 5. a) Particle-size distribution of as-received Betarundum Ultrafine β -SiC powder, with b) accompanying photomicrograph.

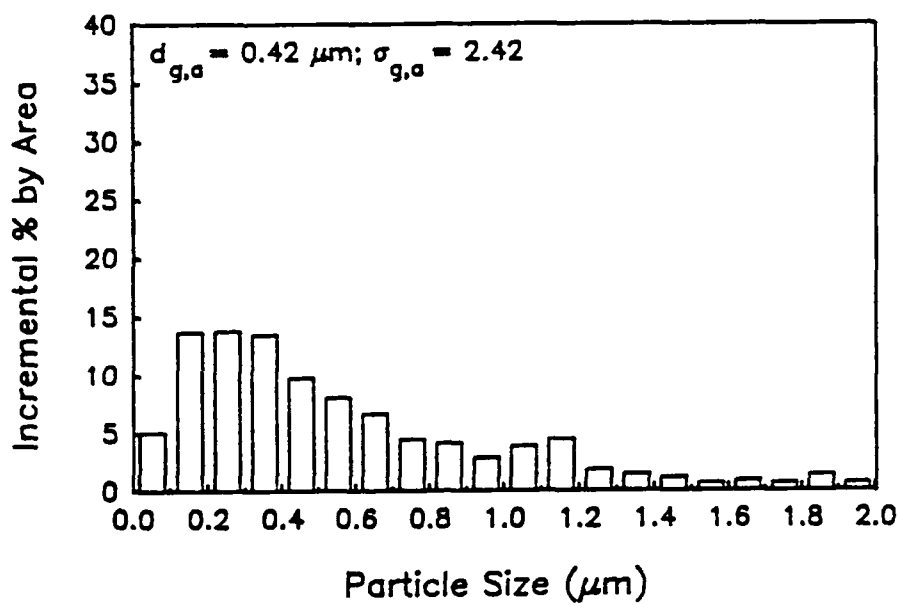


(a)



(b)

Figure 6. a) Particle-size distribution of Cut 1 ($>1.2 \mu\text{m}$), with
b) accompanying photomicrograph.

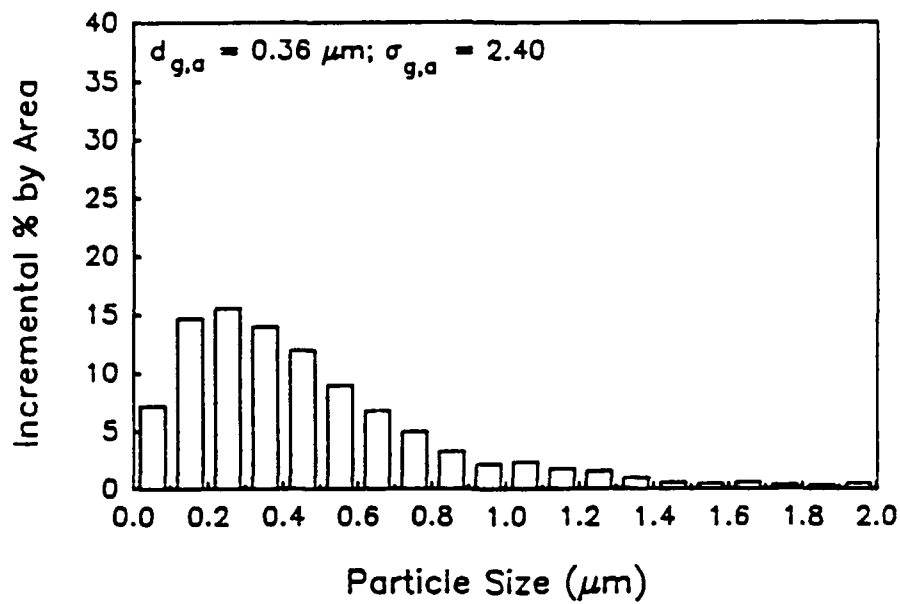


(a)

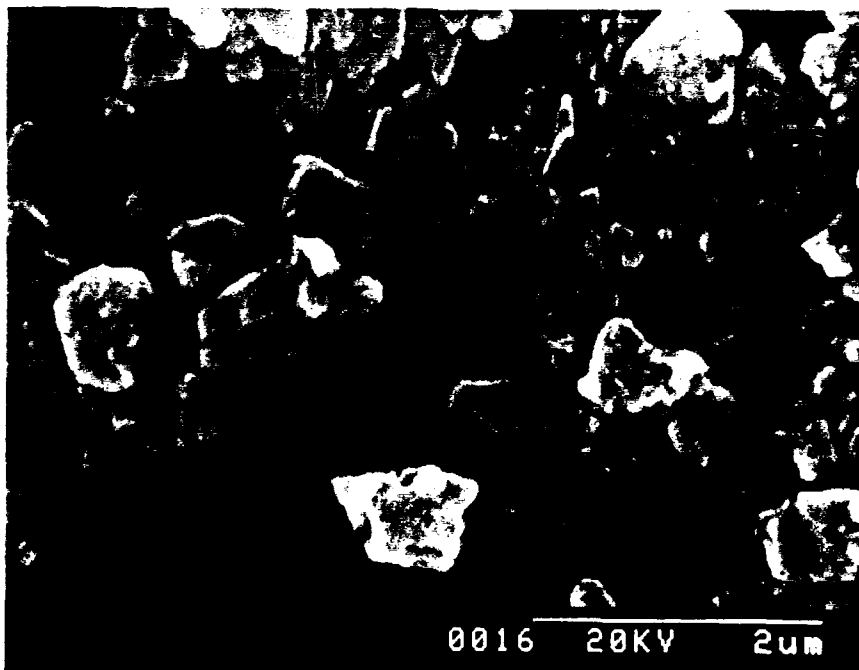


(b)

Figure 7. a) Particle-size distribution of Cut 2 (0.8-1.2 μm), with
b) accompanying photomicrograph.

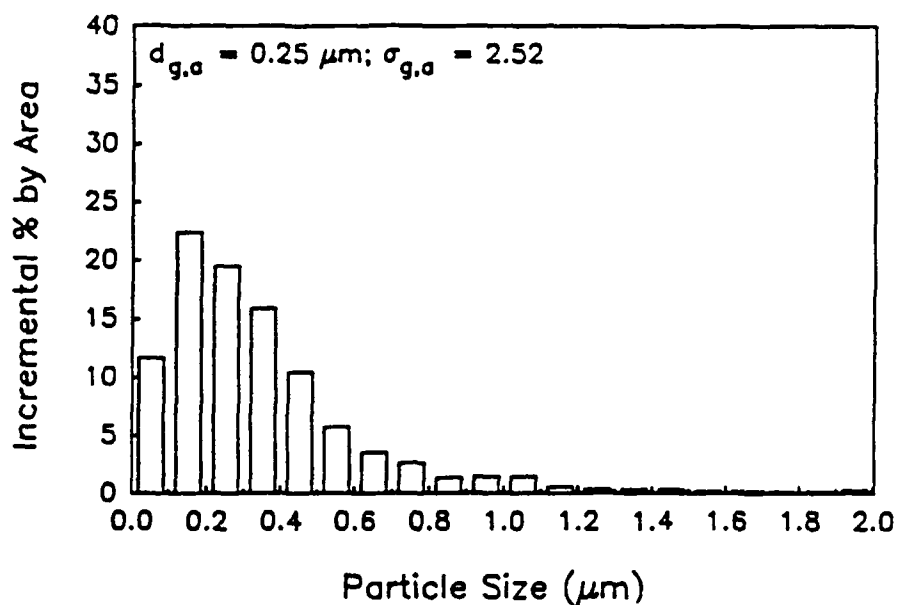


(a)

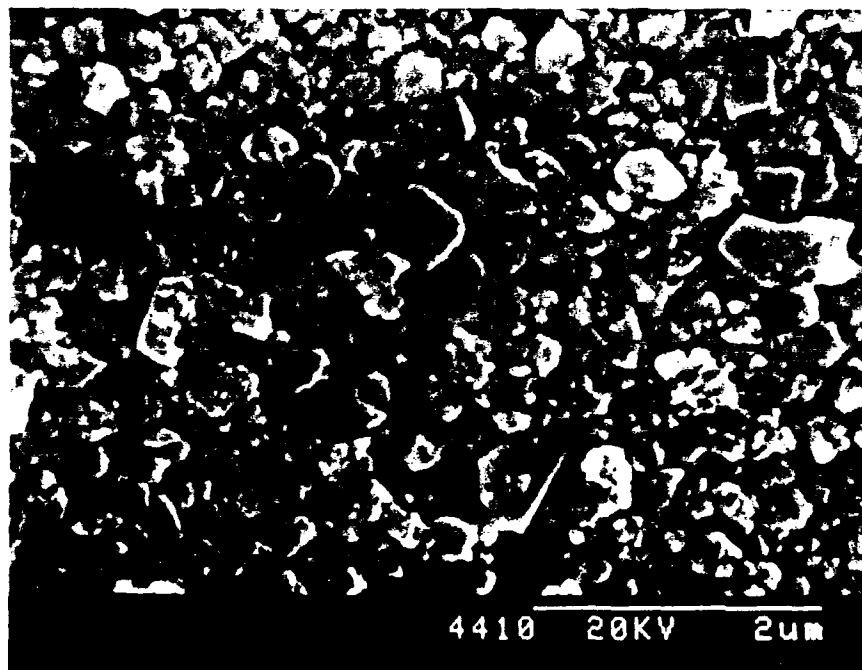


(b)

Figure 8. a) Particle-size distribution of Cut 3 (0.5-0.8 μm), with
b) accompanying photomicrograph.

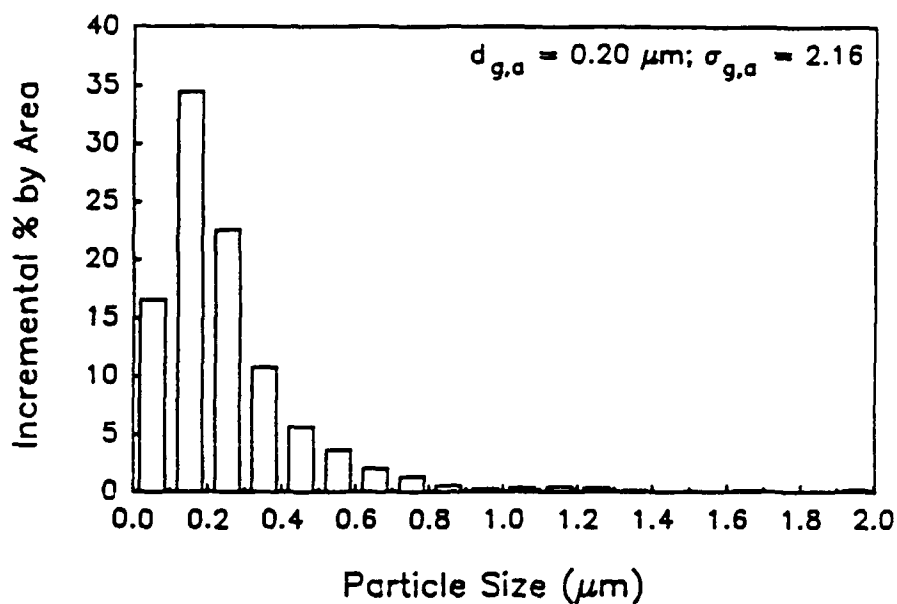


(a)

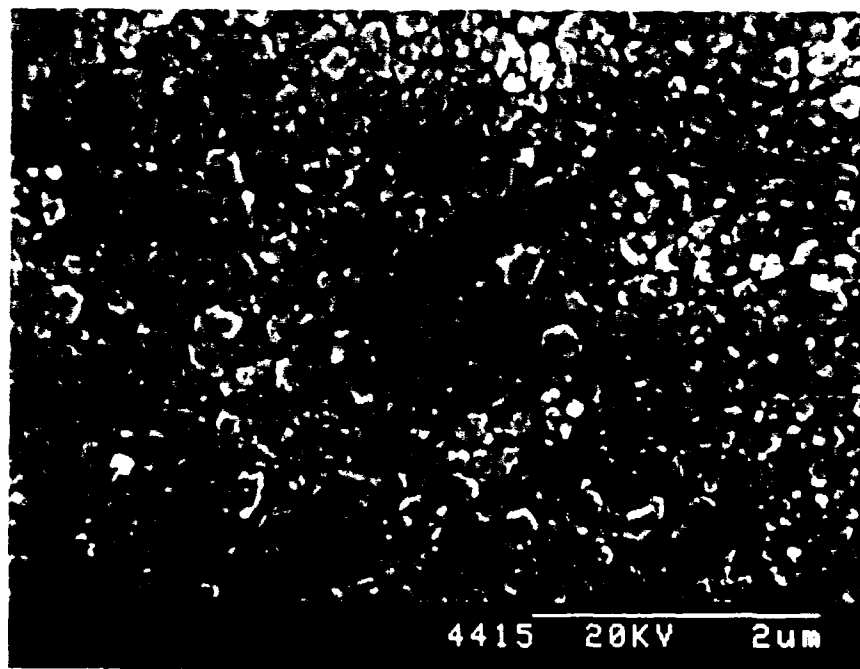


(b)

Figure 9. a) Particle-size distribution of Cut 4 (0.3-0.5 μm), with
b) accompanying photomicrograph.

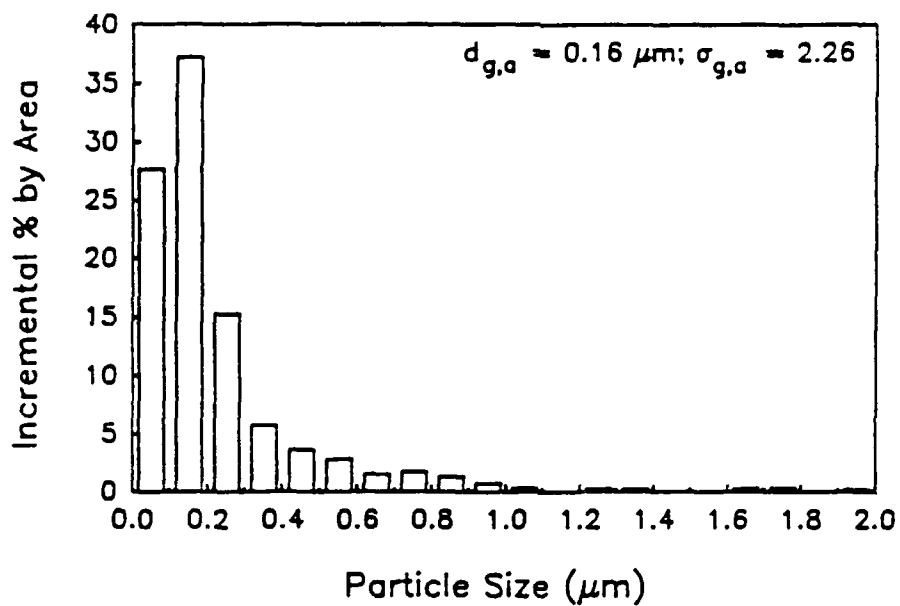


(a)

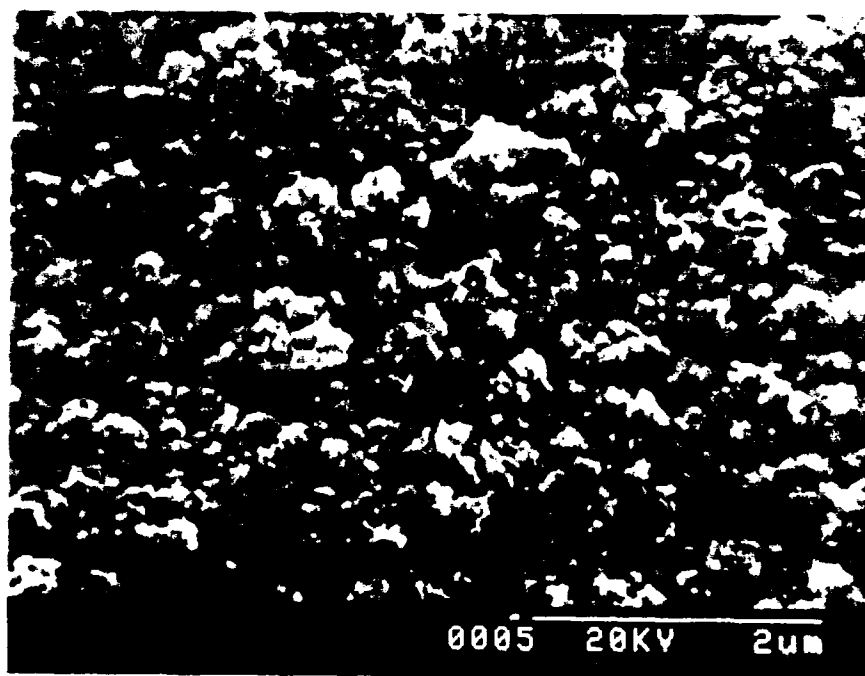


(b)

Figure 10. a) Particle-size distribution of Cut 5 (0.2-0.3 μm), with
b) accompanying photomicrograph.



(a)



(b)

Figure 11. a) Particle-size distribution of Cut 6 (0.15-0.20 μm), with
b) accompanying photomicrograph.

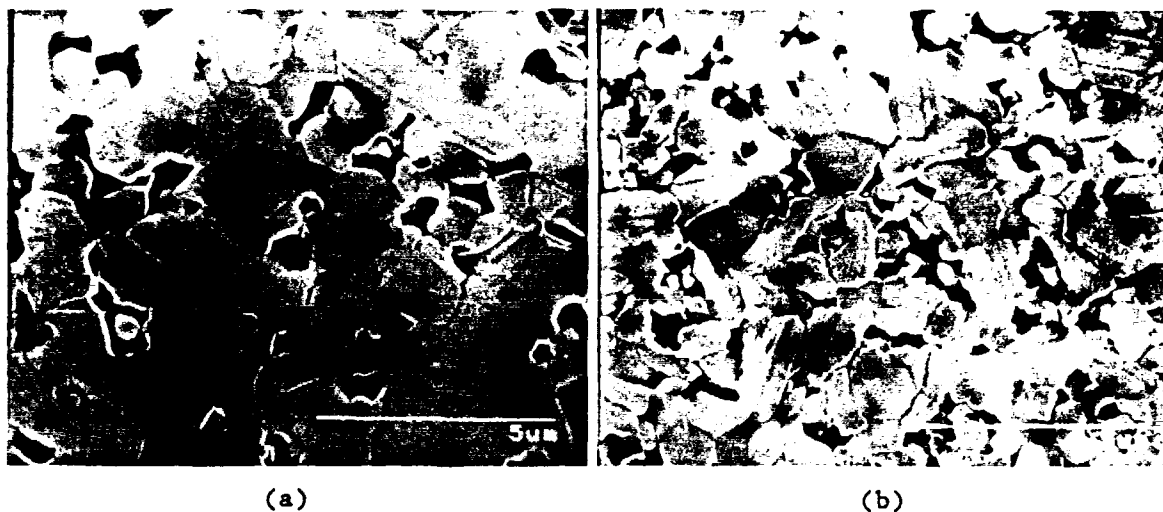


Figure 12. 2000°C-sintered microstructures of a) as-received β -SiC compacts and b) size-classified β -SiC powder compacts doped with B_4C and carbon black.

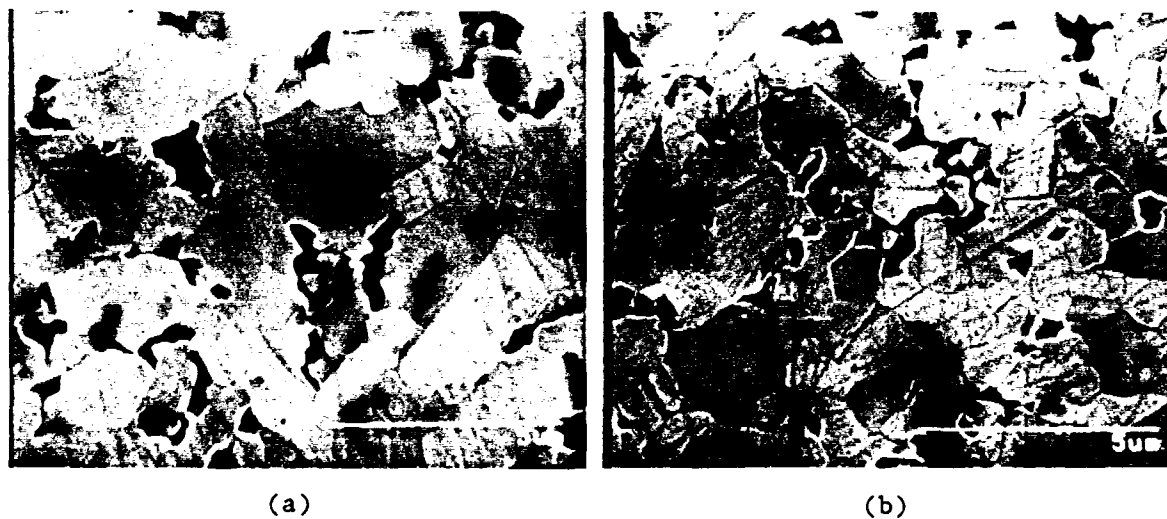


Figure 13. 2000°C-sintered microstructures of a) as-received β -SiC compacts and b) size-classified β -SiC powder compacts doped with B_4C and polyphenylene.

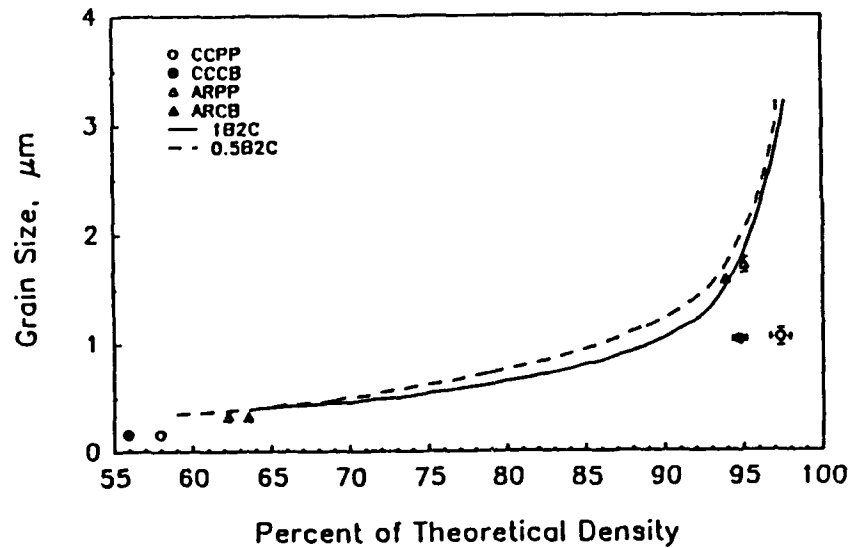


Figure 14. Grain size versus sintered density for the as-received and classified-powder compacts (2000°C) from this experiment and the 0.5 wt% boron-, 2 wt% carbon-doped and 1.0 wt% boron-, 2 wt% carbon-doped Betarundum Ultrafine β -SiC compacts of Li (1987a).

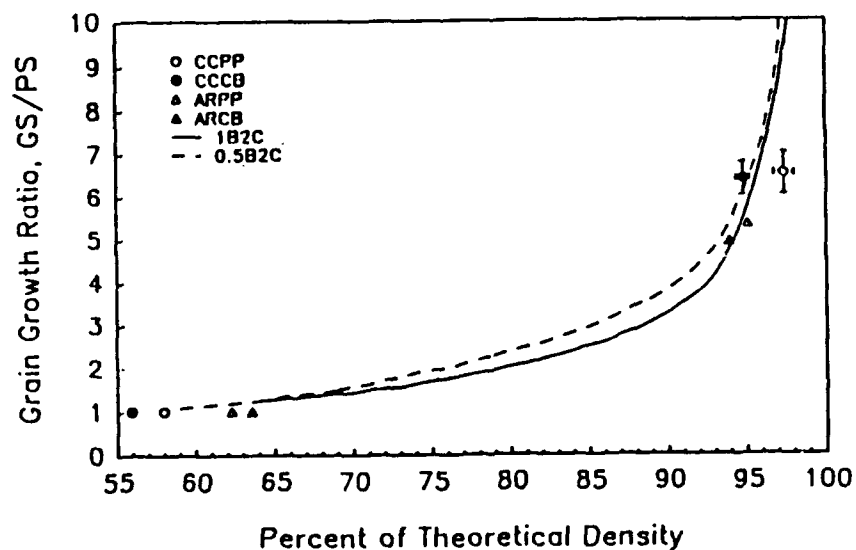


Figure 15. Grain-size ratio (GS/PS) versus sintered density for the as-received and classified-powder compacts (2000°C) from this experiment and the 0.5 wt% boron-, 2 wt% carbon-doped and 1.0 wt% boron-, 2 wt% carbon-doped Betarundum Ultrafine β -SiC compacts of Li (1987a).

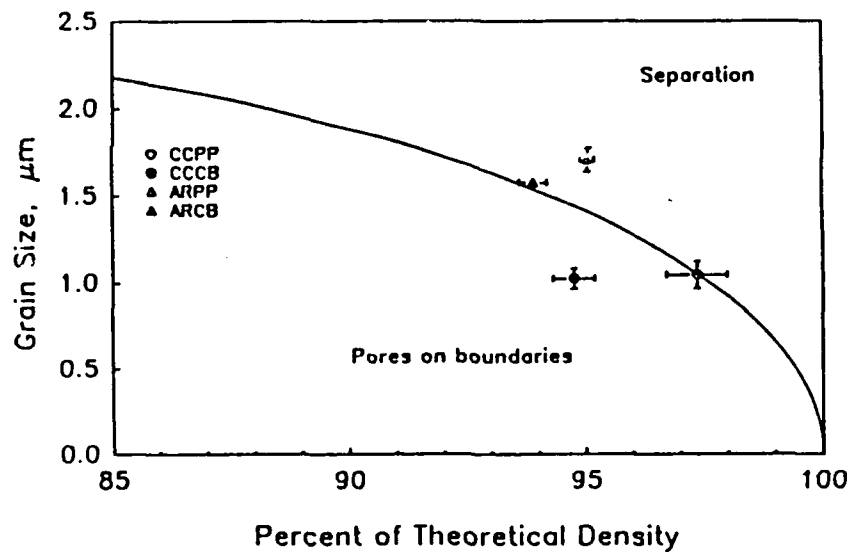


Figure 16. Grain size versus 2000°C-sintered density for as-received and classified-powder compacts, with separation threshold calculated from the data.

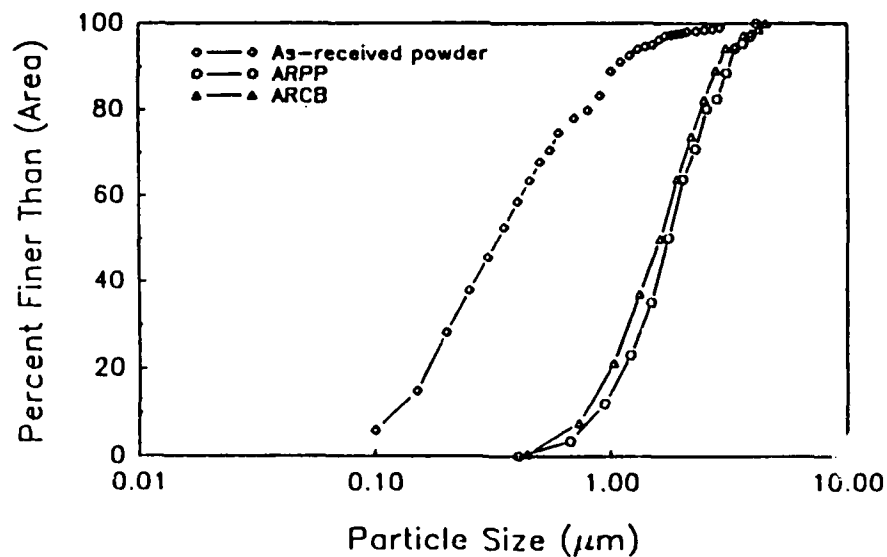


Figure 17. Particle-size distribution for as-received powder and grain-size distributions for as-received compacts doped with B_4C and either carbon black or polyphenylene sintered at 2000°C.

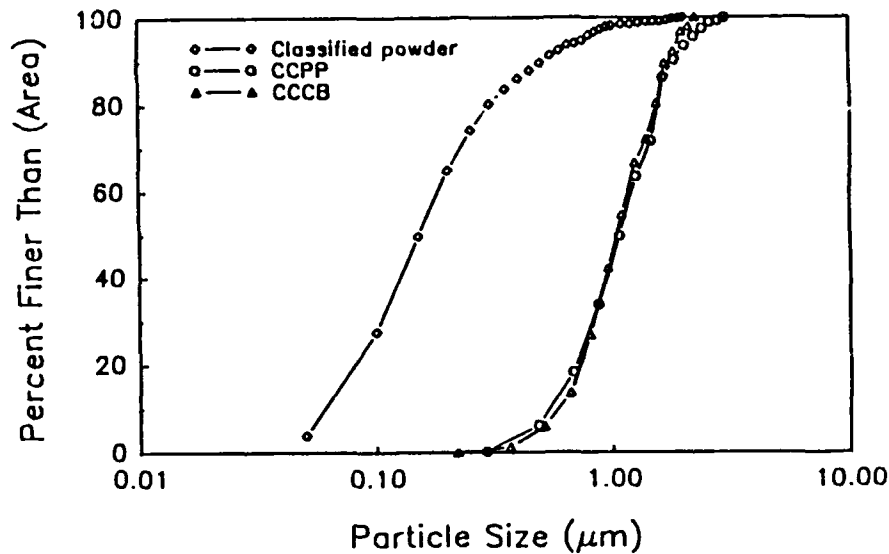


Figure 18. Particle-size distribution for classified powder and grain-size distributions for classified-powder compacts doped with B_4C and either carbon black or polyphenylene sintered at $2000^\circ C$.

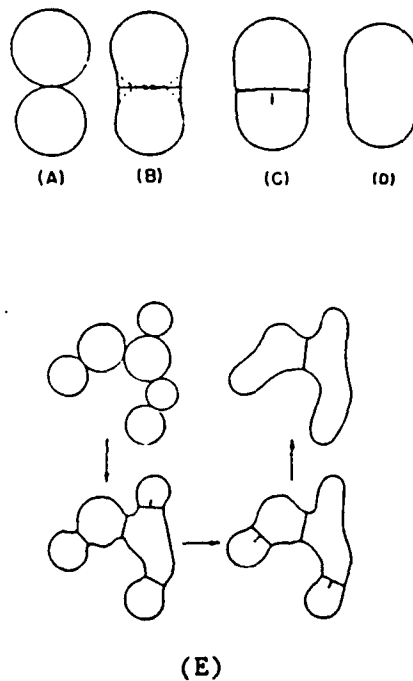
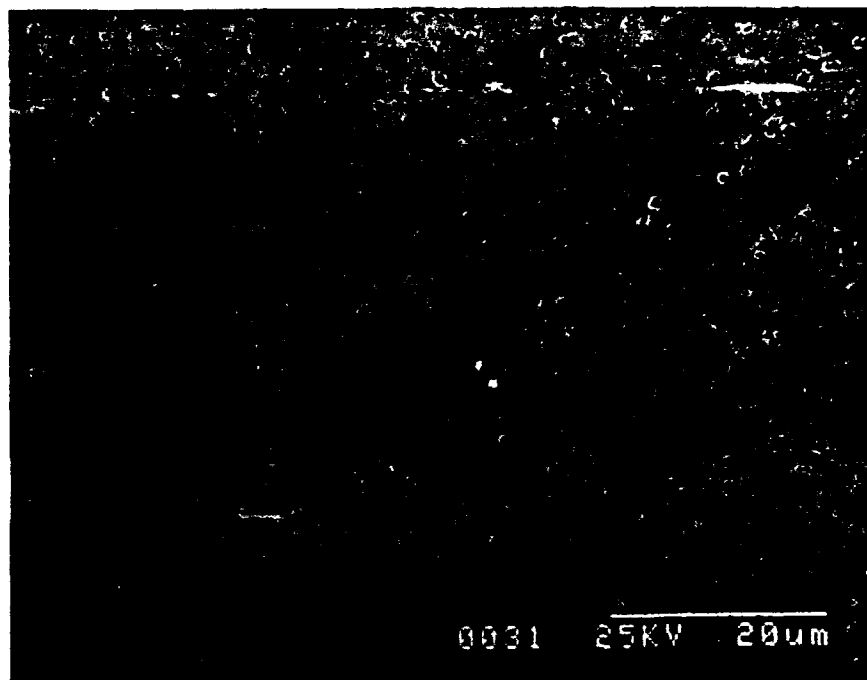
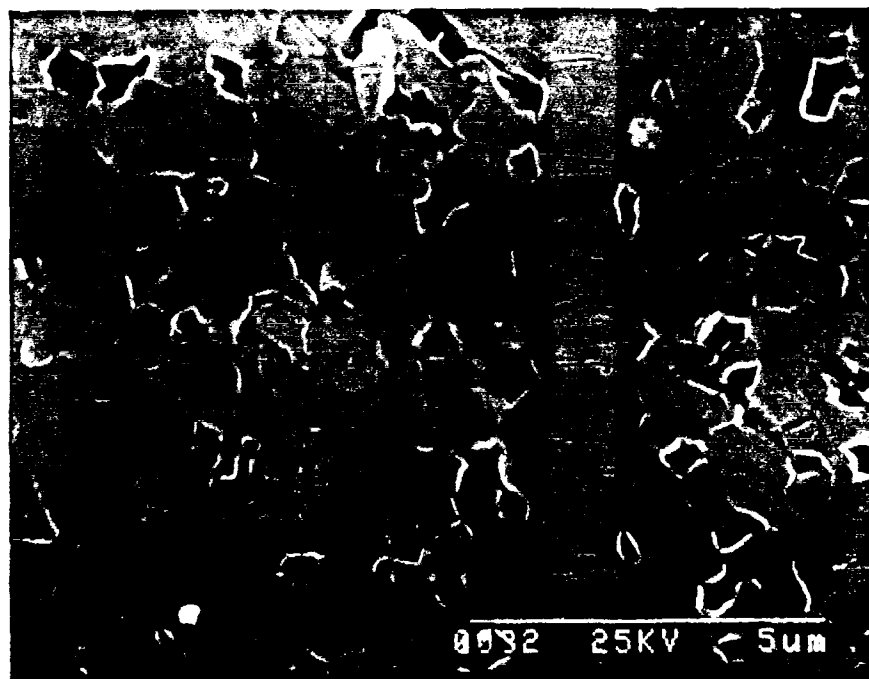


Figure 19. Schemata of grain growth in porous compacts due to grain-boundary curvature induced by dihedral-angle equilibration: a) Particles of slightly different size in contact, b) neck growth between contacting particles, c) grain boundary migrating away from contact plane, and d) grain growth; e) grain growth in a cluster of particles by surface diffusion (Greskovich and Lay, 1972).

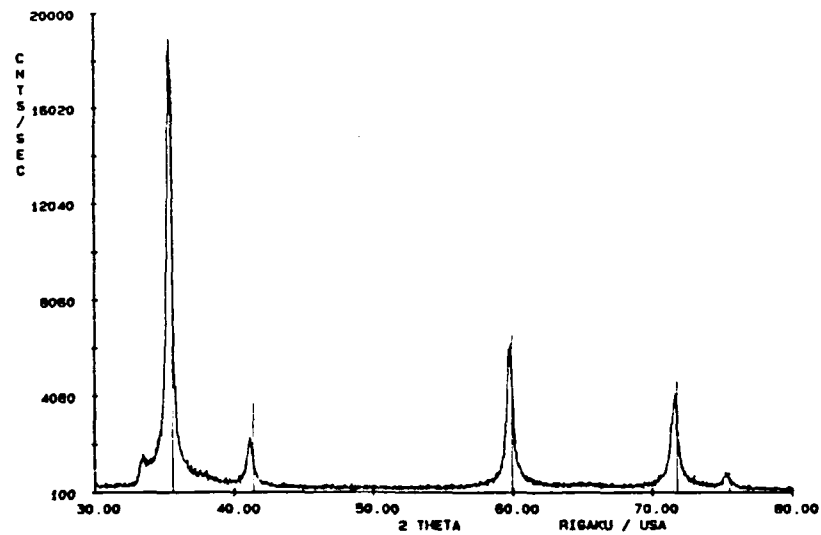


(a)

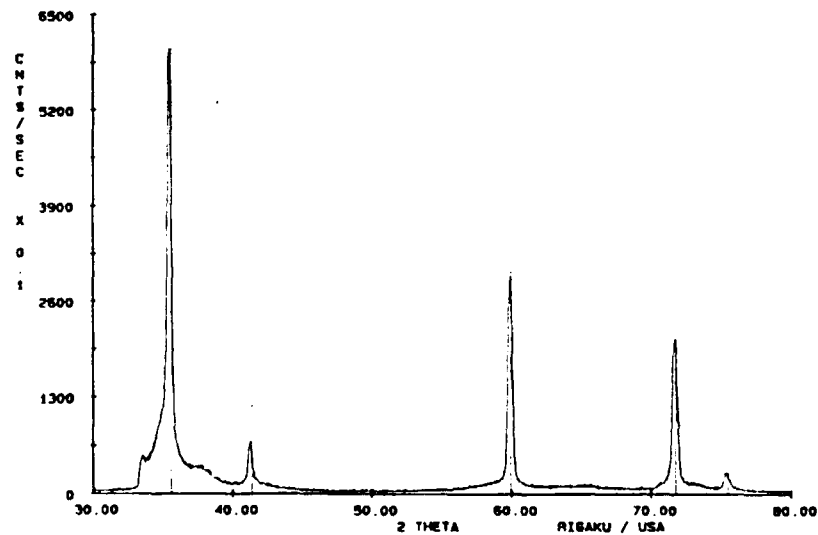


(b)

Figure 20. 2000°C-sintered microstructure of a classified-powder compact showing a) 20-60- μm alpha platelets in the beta matrix and b) bonding of a platelet to the matrix by means of the beta envelope.

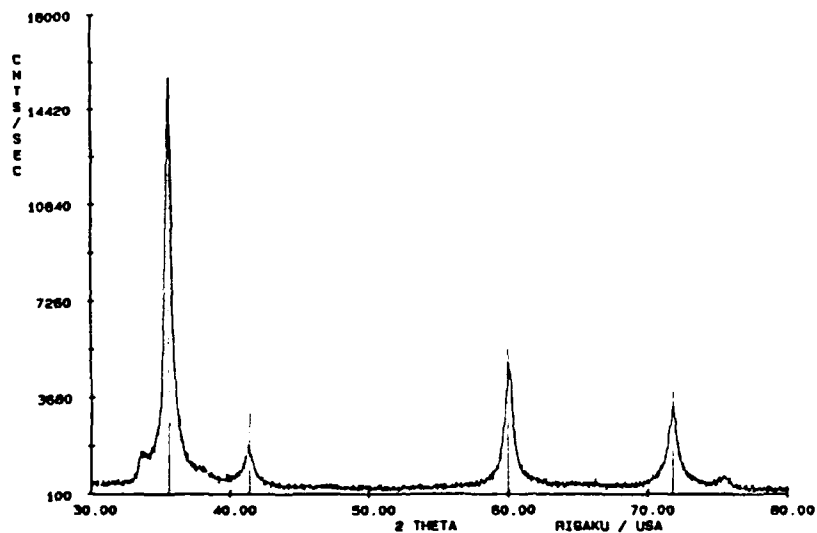


(a)

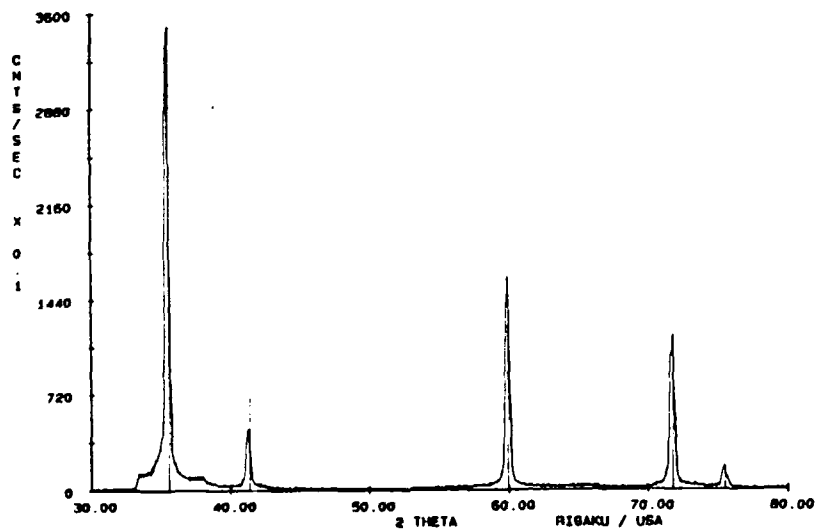


(b)

Figure 21. X-ray powder diffraction patterns of a) as-received powder and b) as-received powder compact sintered at 2000°C.



(a)



(b)

Figure 22. X-ray powder diffraction patterns of a) 0.2-0.3- μm classified powder and b) 0.15-0.20- μm classified powder compact sintered at 2000°C.

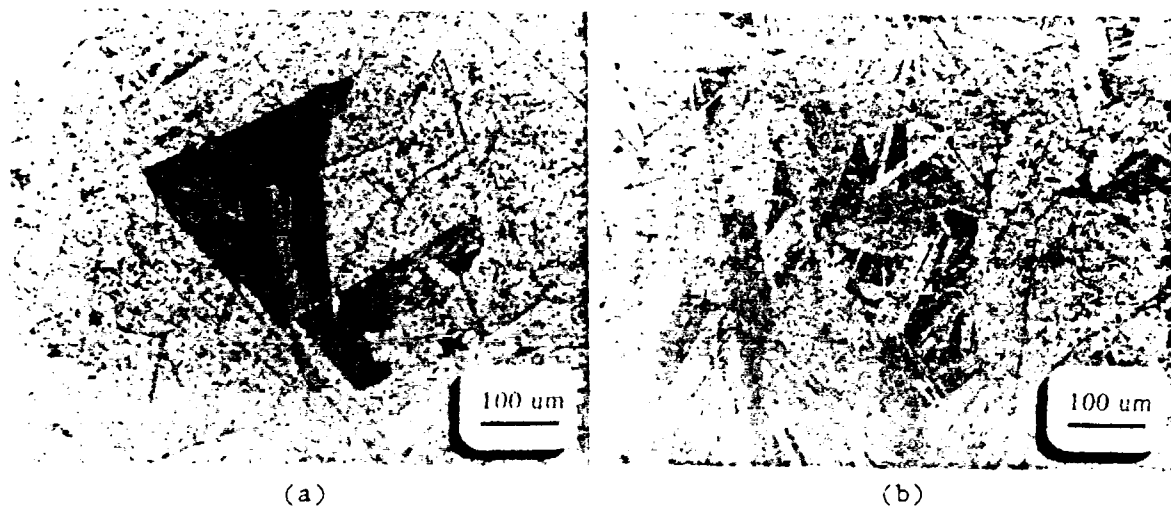


Figure 23. 2100°C-sintered microstructures of a) as-received and b) classified-powder compacts doped with 0.9 wt% B_2O_3 and 2 wt% carbon black.

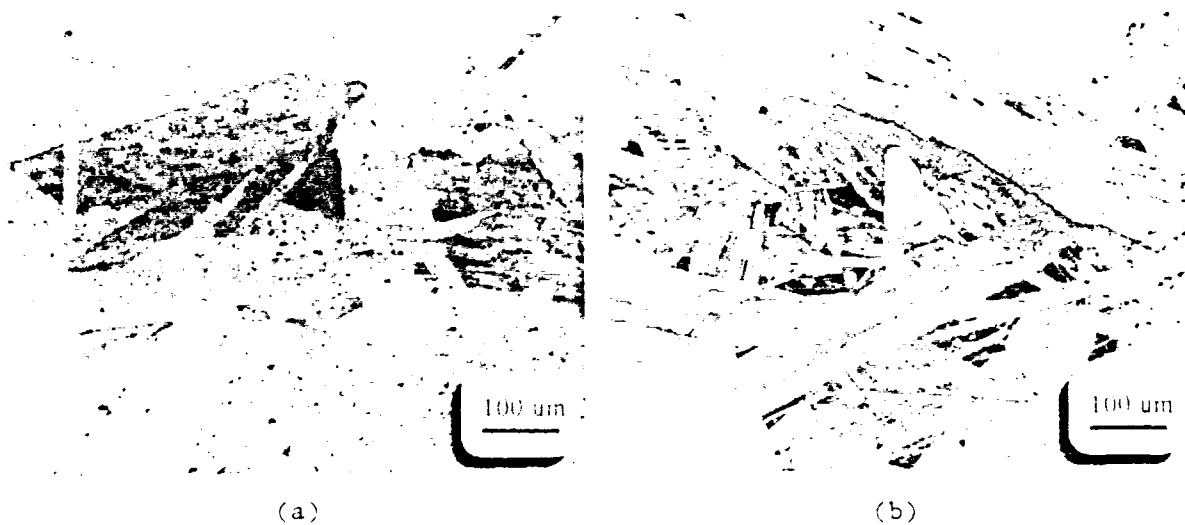
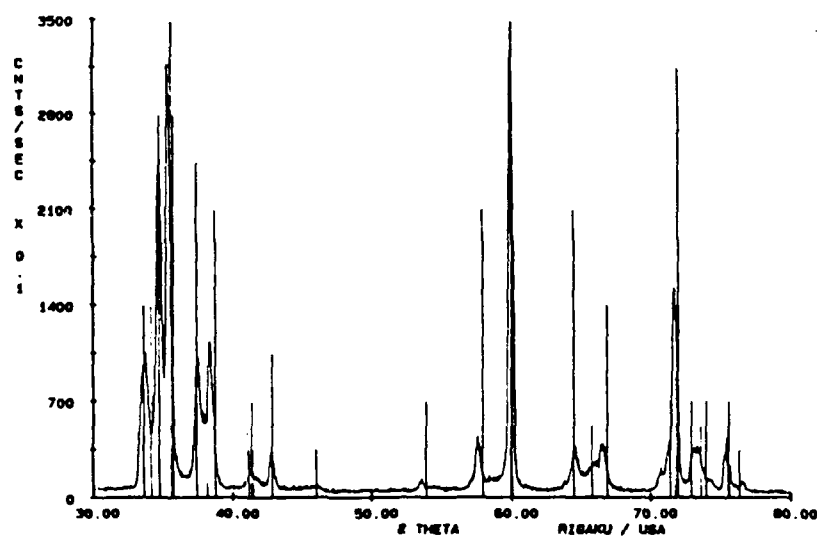
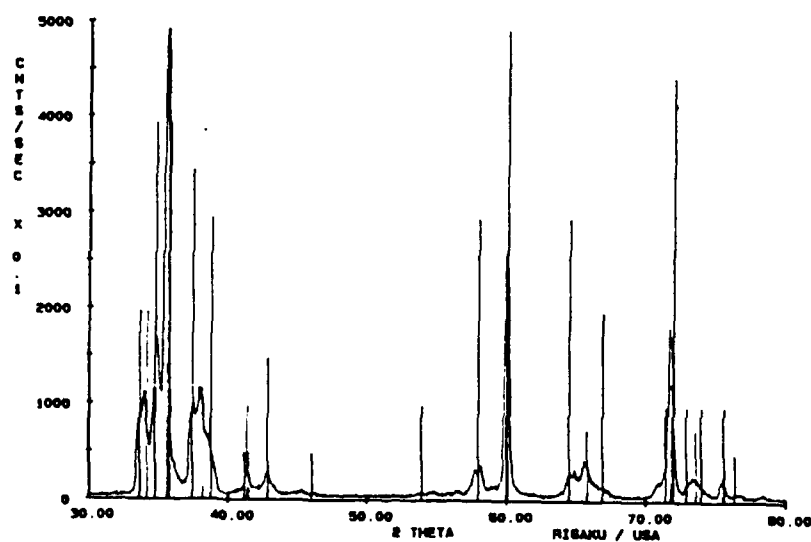


Figure 24. 2100°C-sintered microstructures of a) as-received and b) classified-powder compacts doped with 0.9 wt% B_2O_3 and 2 wt% carbon in the form of polyphenylene.



(a)



(b)

Figure 25. X ray powder diffraction patterns of a) as-received and b) classified-powder compacts sintered at 2100°C.

SINTERING SiC POWDER USING ORGANOSILICON POLYMERS AS BINDERS

Mark Spotz

ABSTRACT

Compacts containing β -SiC powder, B_4C , OLOA®1200 dispersant, polyphenylene, and either PMMA, polycarbosilane (Nicalon™), or a vinyl polysilane (Union Carbide Y-12044) were uniaxially pressed, pyrolyzed, and sintered at 2000-2100°C/30 min. Green pellets were subjected to a range of pressures so that sintering could be studied as a function of packing density. The organosilicon pyrolysis products did not enhance densification rates as expected. Pyrolyzed compacts containing Nicalon™ pyrolysis products contained higher oxygen levels (~1-3 wt%) than did pyrolyzed PMMA compacts, even though handling in air had been minimized. This fact may be partly responsible for inferior densification in some samples; when this extra oxygen was counterbalanced by additional free carbon, however, densification was quite similar for the Nicalon™ and PMMA systems. For the Nicalon™ and Y-12044 batches, pyrolytic residues provided up to 9 wt% of the total SiC. With corresponding initial polymer contents of up to ~21 wt% of powder, the batches displayed varying compaction behavior, with the Nicalon™ system providing the best intergranular bonding. In related experiments, a variety of wetting behaviors was observed for these polymers on pure powder compacts during the initial stages of pyrolysis (up to 400°C). These observations indicate that satisfactory wetting probably occurred for the SiC/Nicalon™/OLOA® mixture during initial softening and pyrolysis.

INTRODUCTION

One reason for incorporating organosilicon polymers into the processing of SiC and Si_3N_4 powders has been that these polymers pyrolyze to leave residues containing SiC and/or Si_3N_4 , and thus can increase the ceramic density of the pre-sintered compact. Increased densification rates should then result during sintering. This goal, as well as the associated diminution of volatile decomposition products, has guided prior work using these polymers as binders (Yajima, Shishido, and Okamura, 1977; Wiseman, 1984; Schwartz and Rowcliffe, 1986; Mutsuddy, 1987). One objective of the research is to determine whether sintering is enhanced. This report presents results of an experiment in which SiC powder was dry-pressed, pyrolyzed, and sintered using either conventional or organosilicon binders.

In related experiments, wetting behavior was observed for various organic and organosilicon materials placed on unfired SiC powder compacts.

EXPERIMENTAL PROCEDURE

The primary experiment was designed to examine SiC sintering densification as a function of powder packing, using either conventional or organosilicon binders. A procedure of mixing all constituents in suspension, extracting the solvent, granulating, and dry-pressing was selected both to facilitate control over unfired compositions and to conveniently provide a range of packing densities with which to test sintering performance. The following materials were used:

- Betarundum Ultra-Fine β -SiC (Ibiden Co., Ltd., Ogaki, Japan); specific surface: $18.3 \text{ m}^2/\text{g}$; Lot #0127.
- High-purity, submicrometer B_4C (Gallery Chemical Division, MSA Corp., Pittsburgh, PA); specific surface: $72 \text{ m}^2/\text{g}$; Lot #1890-75-3.
- Nicalon[™] uncured polycarbosilane (Dow Corning Corp., Midland, MI); Lot #PL-79.
- Y-12044 vinylic polysilane (Union Carbide Corp., Specialty Chemicals Div., Sistersville, WV); Lot #50911030586.
- Poly(methyl methacrylate) #18,224-9 (Aldrich Chemical Co., Milwaukee, WI); Lot #18/0285KL.
- Polyphenylene #7022 (Polysciences, Inc., Warrington, PA); Lot #51351; also HA-43 resin (Hercules, Inc. Research Center, Wilmington, DE).
- OLOA[®]i200 succinimide dispersant (Chevron Chemical Co., Oronite Additives Div., San Francisco, CA); Lot #86ARS-007.

Two series of samples were prepared. For the first, one batch each was prepared of SiC powder and one of the following binders: PMMA, polycarbosilane (Nicalon[™]), and vinylic polysilane (Y-12044). The quantity of Nicalon[™] or Y-12044 added was ~21 wt% of SiC powder, to provide ~9 wt% of the total SiC after sintering. The mixtures also contained B_4C powder

(1 wt% of total SiC after sintering), as-received OLOA®1200 succinimide dispersant (consisting of 49 wt% succinimide, 51 wt% mineral oil; succinimide content was 4.5 wt% of SiC powder plus 18 wt% of B₄C to disperse the respective powders), and polyphenylene to adjust excess carbon to 2 wt% of the total SiC after sintering.

A second series was prepared to examine the effect of a lower polymer content, representing conditions under which the polymer pyrolysis product might act more efficiently at low concentrations, rather than as a major batch constituent contributing to SiC packing density. For this series, one batch was prepared with PMMA (6.2 wt% of SiC powder) at 2 wt% (with respect to total SiC after sintering) targeted excess carbon; three batches were prepared with Nicalon™ (5.8 wt% of SiC powder) at different carbon levels (0, 2, and 4 wt% targeted excess carbon; polyphenylene carbon source). This series also contained B₄C powder (1 wt% of total SiC after sintering) and refined OLOA®1200 (90±5 wt% succinimide; succinimide content was 3.5 wt% of SiC powder plus 18 wt% of B₄C); the OLOA®1200 was refined by the differential separation technique (Bishop, 1985).

Each batch was prepared according to the following procedure. First, the dispersant and polymers were dissolved in reagent-grade toluene. SiC and B₄C powders were added and the resulting mixture was stirred 12 h. The batch was then ultrasonicated at low power for 2-5 min, and subsequently magnetically stirred while the toluene was extracted by vacuum distillation. The nearly dried mixture was removed from its flask, broken into chunks, and dried at 70°C for 16 h in a vacuum; the polysilane batch was afterwards cured under gettered argon at 200°C for 2 h to solidify the liquid Y-12044. The batch was then ground with a mortar and pestle into granules and subsequently stored.

The first series was prepared in air; the second series was handled under nitrogen throughout preparation except when the powders (pre-dried at 180°C for 3.5 h in vacuum) were added, the samples pressed, and the pellet dimensions measured (~8 h total). In some cases the pressed pellets were stored overnight in a dessicator before being loaded into the pyrolysis furnace.

Each batch provided material for about 15 pellets. Pellets were dry-pressed in either a 12.7-mm die (first series) or a 19.0-mm die (second series) at pressures ranging from 18 to 280 MPa (2500-41,000 psi). The corresponding SiC powder packing densities for the pressed compacts ranged from 35 to 50% of the theoretical density (T.D.). The samples were pyrolyzed under gettered argon to 1000°C, then sintered at 2000°C or 2100°C for 30 min in a carbon-tube furnace purged with gettered argon.

The SiC packing density and theoretical constituent volume fractions were calculated for each pellet from the compact's starting composition, weight, and dimensions as measured after pressing, pyrolysis, and sintering, by a method similar to that used by Schwartz, Rowcliffe, and Blum (1988). Two separate SiC packing parameters were calculated: the relative density after pyrolysis contributed by the powder alone, and that contributed by both the powder and the binder residue. An example of these calculations for a Nicalon™ batch is given in Table 1.

Densities of sintered pellets were determined using volumes obtained both by directly measuring the pellets' dimensions and by applying Archimedes' method. For the latter method, the pellets were sprayed with an acrylic coating to prevent intrusion before being submersed in water. The volumes as measured by dimension and by submersion agreed to within 2%.

Table 1. Calculation of constituent volume fractions for a sample containing SiC powder, B₄C powder, polyphenylene (PP), dispersant (OLOA®1200), and Nicalon™ polycarbosilane.

BEFORE PYROLYSIS	Mass Frxn	Density (gcm ⁻³)	Mass (g)	Vol. (cm ³)	Vol. Fraction
SiC	0.7539	3.21	0.4131	0.1287	0.4673
B ₄ C	0.0083	2.4	0.0045	0.0019	0.0069
PP	0.0045	1.1	0.0025	0.0022	0.0080
OLOA	0.0721	0.91	0.0395	0.0434	0.1576
Nicalon	0.1612	1.12	0.0883	0.0789	0.2865
<u>Porosity</u>	--	--	--	<u>0.0203</u>	<u>0.0737</u>
Total	1.0000	--	0.5480	0.2754	1.0000

AFTER PYROLYSIS	Pyro. Yield	ρ (gcm ⁻³)	Mass (g)	Vol. (cm ³)	Vol. Fraction
SiC	1.0	3.21	0.4131	0.1287	0.5138
B ₄ C	1.0	2.4	0.0045	0.0019	0.0076
PP res.	0.80	1.95	0.0020	0.0010	0.0040
Extra mass ^a	--	1.95	0.0180	0.0092	0.0367
Nic. res.	0.60	2.2	0.0530	0.0241	0.0962
<u>Porosity</u>	--	--	--	<u>0.0856</u>	<u>0.3417</u>
Total			0.4906	0.2505	1.0000

^a Unaccounted additional mass, arbitrarily assigned as carbon.

Chemical analyses were performed on compacts pyrolyzed to 1000°C. Prior to analysis, the pellets were ground into powder with a porcelain mortar and pestle; aluminum analyses were therefore obtained to determine contamination from the porcelain. Silicon, boron, and aluminum were analyzed by inductively coupled plasma (ICP) techniques (Model 5500, Perkin-Elmer ICP, performed at Galbraith, Inc., Knoxville, TN). Carbon was measured by an inorganic oxidation technique (Model CR-12, Leco Corp., performed at Galbraith, Inc.). Hydrogen was analyzed by an organic oxidation technique (Model 800 CHN Analyzer, Leco Corp., performed at Galbraith, Inc.). Oxygen was analyzed by fast-neutron activation (IRT Corp., San Diego, CA).

The undistinguished sintering behavior of the compacts containing organosilicon polymers raised the question of whether the additives had not wet the powder, thereby potentially affecting the distribution of additives in the compacts during the early, fluid stages of pyrolysis. This hypothesis was tested, at least for the initial stages of pyrolysis, by observing the apparent wetting of the various constituents placed on compacts of pure β -SiC powder (Betarundum Ultra-Fine) that had been pressed at 70 MPa (10,000 psi). The following materials were tested: purified OLOA®1200 (chunk), Y-12044 (droplet), PMMA (powder), Nicalon™ (solid chunk), Nicalon™ mixed with as-received OLOA®1200 (porous chunk), and two organic liquids -- oleic acid and mineral oil (both from Borden and Remington, Everett, MA). The purified OLOA®1200, refined using the differential-separation procedure (Bishop, 1985), contained $\sim 10 \pm 5$ wt% residual mineral oil. Each test material was placed on top of a compact under ambient conditions, then heated in a tube furnace under gettered argon to various temperatures. The softening/wetting behavior was observed by raising the furnace shell for periods brief enough to prevent excessive temperature swings.

RESULTS

Wetting and Penetration

The range of wetting and penetration behaviors for the various materials placed on SiC powder compacts was quite interesting; the results are summarized in Table 2. The oleic acid and mineral oil upon application quickly spread and were fully absorbed into the compacts under the forces of capillary action and/or gravity. The Y-12044 droplet upon application slowly formed an apparent contact angle θ of $70-85^\circ$; under argon, the Y-12044 drop remained unchanged at 60°C but was fully absorbed

Table 2. Apparent contact angles of designated additives against β -SiC powder compacts.

Additive	Temp ($^{\circ}$ C)	Contact Angle θ ($^{\circ}$)	Penetration
Oleic acid	25	~ 0	complete
Mineral oil	25	~ 0	complete
Y12044	25-60	70-85	negligible
	90	~ 0	complete
OLOA [®]	100	> 90	none
	125	~ 45	-
	180	< 30	-
	210	~ 0	complete
Nicalon	200	--	(softened)
	265	~ 135	(non-wetting)
	390	~ 135	none
Nicalon [™] /OLOA	210	~ 35	negligible

into the compact at 90° C. The purified OLOA[®]1200 softened to form a non-wetting sessile drop by 100° C, spread to form an apparent wetting angle of $\theta \sim 45^{\circ}$ at 125° C, formed a shallow puddle below 180° C, and was completely absorbed at 210° C. Wetting characteristics of the PMMA sample could not be evaluated because its evolving shape was apparently determined by its initial configuration (a small pile of loose powder sitting on the compact), bubble formation, and the sample's high viscosity.

The pure Nicalon[™] polymer behaved in a different manner from the mixture of Nicalon[™] and as-received OLOA[®]1200 (mixed in the same proportions as for the sintering experiment). The pure Nicalon[™] was effectively non-wetting. The chunks began to appear smoother from 200 to 220° C, then formed non-wetting, sessile drops below 260° C, and maintained an apparent contact angle of 125 - 140° throughout the range 320 - 390° C. The

Nicalon™/OLOA® sample softened and spread to form a shallow puddle below 210°C. The contact angle was finite and roughly 30-40°. Inspection of the contact interface after heating to 260°C revealed essentially no penetration.

Compaction and Pyrolysis Behavior

The compaction characteristics of the various SiC/binder batches differed, as evidenced by the compaction densities shown in Figure 1, for a 21 wt% initial polymer content. The Nicalon™ system exhibited the highest packing densities, the PMMA system the lowest. The compaction of all three batches exhibited linear behavior when plotted against log(MPa), but the Nicalon™ batch compaction appeared to plateau above 100 MPa.

During pyrolysis, the binder systems displayed different amounts of compact shrinkage. The volume shrinkages are shown in Figure 2 for pellets with a 21 wt% initial polymer content as a function of compaction pressure during dry-pressing. The Nicalon™ system displayed the greatest shrinkage; it is not clear whether this was due to capillary action or to some other effect. Although the regression slopes for Nicalon™ and PMMA are slightly negative, the shrinkages for the three binder systems are essentially independent of compaction pressure in the pressure range used in this experiment.

Fracture surfaces of the compacts with a 21 wt% initial polymer content were inspected by scanning electron microscopy both after pyrolysis and after sintering. Figure 3 shows a series of photomicrographs of pyrolyzed specimens at low magnification. Samples 3a, 3c, and 3e were pressed uniaxially at 70 MPa; Samples 3b, 3d, and 3f were subjected to various pressures in order to yield fairly constant mean powder packing densities of $45 \pm 1\%$ T.D. after pyrolysis.

The fractures clearly showed features arising from the original pressed granules. For all three binder systems in the first series, the granules apparently resisted deformation; this was attributed partially to the high initial binder level (~21 wt%). However, under higher pressures, the granule structures for PMMA and Nicalon™ deformed and bonded together to yield smoother fracture surfaces. For PMMA, a pressure of 280 MPa (40,000 psi) was required to significantly destroy the original granule character (Fig. 3d). The Nicalon™ binder system, however, showed superior deformation of and bonding between granules at 70 MPa (10,000 psi) (Fig. 3c). Granule deformation and bonding for the Y-12044 batch were extremely limited -- probably a result of the polymer's rigidity after curing, which had been done before pressing to eliminate tackiness.

Sintering

The relative densities of the sintered SiC compacts initially containing 21 wt% polymer were plotted against 1) SiC relative density contributed by the powder alone (Fig. 4a), and 2) SiC relative density contributed by the powder and the organosilicon binder residue (Fig. 4b). The results followed a general trend of increasing sintered density with increasing pyrolyzed packing density, as had been expected from the demonstrated effects of packing density on sintering kinetics (Barringer and Bowen, 1988). When plotted against pyrolyzed density for powder alone, the behavior observed for both organosilicon binders did not significantly differ from that observed for PMMA. However, when plotted against pyrolyzed density for all sources of SiC, the Nicalon™ and Y-12044 curves shifted to the right and, effectively, below the PMMA curve, if it were extrapolated to higher pyrolyzed densities.

Sintering results for samples with ~6 wt% initial polymer content for treatments of 2000°C/30 min and 2100°C/30 min are shown in Figures 5a and 5b, respectively. Two results are clear: 1) densification of the Nicalon™ compacts was sensitive to carbon concentration, and 2) at the same targeted carbon concentration, Nicalon™ compacts sintered less efficiently than PMMA compacts, but with extra added polyphenylene (4% excess batched carbon), they achieved equivalent performance.

Chemical analyses showed that oxygen content was higher by ~1-3 wt% in pyrolyzed Nicalon™ compacts as compared to pyrolyzed PMMA compacts. The elemental analyses are given in Table 3, and the calculated equivalent phase compositions are shown in Table 4. These results indicate that Nicalon™ compacts incorporated oxygen during processing. With a 6 wt% initial Nicalon™ content, the oxygen impurity exceeded the level expected (based on oxygen in the starting materials) by ~1.6 wt%; with a 21 wt% initial Nicalon™ content, the oxygen surplus was ~3.5 wt%. Tests have not yet shown whether the polycarbosilane coating the SiC particles reacted with oxygen and/or water prior to pyrolysis, or reacted with entrained O₂/H₂O during pyrolysis. Measurements of oxygen partial pressure (P_{O₂}) in the exhaust stream have shown the pyrolysis furnace to be capable of achieving extremely low oxygen levels (10⁻⁹ to 10⁻¹⁴ atm O₂).

The extra oxygen present in the pyrolyzed Nicalon™ compacts, assumed to be in the form of SiO₂, appears to be the reason that additional carbon was necessary to achieve sintered densities equivalent to those of PMMA compacts (Fig. 5). The data in Figure 4 are also presumably affected. It would appear desirable to re-examine the condition of high initial polymer content while minimizing exposure to oxygen.

Table 3. Elemental analysis of 1000°C pyrolyzed compacts; specified polymer's content: 21 wt% or 6 wt%; polyphenylene adjusted to give targeted free carbon content as noted (elements except oxygen analyzed by Galbraith, Inc.; oxygen content analyzed by fast-neutron activation, IRT Corp.).

Element	Nic [*] /21 wt% C / 2 wt%	Nic [*] /6 wt% C / 0 wt%	Nic [*] /6 wt% C / 2 wt%	PMMA/6 wt% C / 2 wt%
Silicon	65.31	66.60	65.46	67.65
Carbon	27.13	28.63	29.47	30.10
Hydrogen	0.72	0.19	0.29	0.16
Oxygen	4.60	2.38	2.69	1.62
Boron	0.56	0.62	0.55	0.53
Aluminum	<u>0.16</u>	<u>0.22</u>	<u>0.13</u>	<u>----</u>
	98.48	98.64	98.59	----

*Nicalon™

Table 4. Equivalent ceramic phases in pyrolyzed compacts, calculated from analyses in Table 3; totals normalized to 100 wt%.

Phase	Nic [*] /21 wt% C / 2 wt%	Nic [*] /6 wt% C / 0 wt%	Nic [*] /6 wt% C / 2 wt%	PMMA/6 wt% C / 2 wt%
SiC	89.00	93.64	91.53	94.52
Free carbon	0.73	0.80	2.32	1.57
Free silicon	0.00	0.00	0.00	0.00
SiO ₂	8.50	4.15	4.90	2.74
B ₄ C	0.73	0.80	0.71	0.68
Hydrogen	0.73	0.19	0.29	0.16
Al ₂ O ₃	<u>0.31</u>	<u>0.42</u>	<u>0.25</u>	<u>0.33</u>
	100.00	100.00	100.00	100.00

*Nicalon™

Fracture surfaces for pyrolyzed and pyrolyzed/sintered samples initially containing 21 wt% polymer are shown in the series of photomicrographs in Figure 6. The regions shown were located within well-packed granules. Samples 6a and 6b were separate pellets from the PMMA batch; Samples 6c and 6d were from the Y-12044 batch; Samples 6e and 6f were from the Nicalon[™] batch. The pyrolyzed microstructures within densely packed granules indicated uniform mixing of powder and polymeric constituents and appeared quite similar to the pyrolyzed powder/binder microstructures reported by others (Wiseman, 1984; Schwartz, Rowcliffe, and Blum, 1987).

The sintered microstructures shown in Figure 6 clearly exhibit structures typically associated with intermediate-stage densification of boron/carbon-doped β -SiC: equiaxed, cubic-phase grains, intergranular porosity, and some cases of accelerated grain growth (e.g., elongated grains in 6f). The size of the SiC grains, coupled with the apparent lack of intergranular material, suggests that the organosilicon pyrolysis products were incorporated into the grains.

CONCLUSIONS AND FUTURE WORK

The wetting behavior observed for the Nicalon[™]/OLOA[®] mixture, as opposed to pure Nicalon[™], on SiC powder compacts indicates that wetting can be affected considerably by the specific mixture of additives used in a batch composition. These results also suggest that satisfactory wetting for the SiC/Nicalon[™]/OLOA[®] batch mixture probably occurred during the initial stages of pyrolysis. The relatively large amount of pyrolysis shrinkage observed in the pellets containing Nicalon[™] is consistent with this tentative conclusion.

Of the binders utilized, the Nicalon[™]/OLOA[®] system produced the highest packing densities during pressing and the greatest degree of granule deformation and bonding for a given applied pressure. Y-12044 gave the worst compaction results, apparently due to its rigidity in the cured state. However, at lower binder levels and without curing, we might expect its compaction behavior to improve significantly.

Pyrolyzed compacts of the ~6 and ~21 wt% Nicalon[™] batches contained higher concentrations of oxygen than those predicted based on oxygen concentrations in the starting materials. This can be explained by assuming that the extra oxygen is associated with the polycarbosilane's sensitivity to oxidation and/or hydrolysis. Further studies are needed to determine whether Nicalon[™] reacts more readily with oxygen or water, and whether these reactions advance significantly during short exposures or during the subsequent reaction in the pyrolysis furnace. The planned studies include thermal gravimetric analysis (TGA) of polymer samples under controlled atmospheres, e.g., gettered argon, water-saturated argon, or dry air. The question of possible reactions between Nicalon[™] and the oxidized SiC powder surface will be explored using TGA and Fourier-transform infrared spectroscopy (FTIR).

SiC powder compacts containing the pyrolysis products of Nicalon[™] sintered as efficiently as compacts not containing these pyrolysis products, as long as sufficient carbon was present to reduce the additional SiO₂ formed from inadvertent contamination of the polycarbosilane during processing. The tentative conclusion is, however, that incorporating an organosilicon binder does not enhance the sintering kinetics of commercial β -SiC powder. Future sintering studies will re-examine the conditions of high initial polymer content while taking care to prevent oxygen incorporation.

In related experiments, the feasibility of incorporating either Nicalon™ or Y-12044 during colloidal pressing was demonstrated. This procedure is desirable since colloidal processing can result in denser, more uniformly packed green bodies than are possible with dry-pressing. These efforts will be continued to obtain comparative sintering data.

REFERENCES

E.A. Barringer and H.K. Bowen, "Effects of Particle Packing on the Sintered Microstructure," presented at the International Institute for the Science of Sintering, Belgrade, Yugoslavia, 1983, J. Appl. Phys. A., 45 [4] 271-75 (1988).

B. Bishop, "OLOA®1200 Purification," CPRL Report #Q5, MIT, pp. 25-27 (1985).

B.C. Mutsuddy, "Use of Organometallic Polymer for Making Ceramic Parts by Plastic Molding Techniques"; pp. 571-89 in High-Tech Ceramics. Edited by P. Vincenzini. Elsevier Science Publishers B.V., Amsterdam, The Netherlands, 1987.

K.B. Schwartz and D.J. Rowcliffe, "Modeling Density Contributions in Preceramic Polymer/Ceramic Powder Systems," J. Am. Ceram. Soc., 69 [5] C-106-C-108 (1986).

K.B. Schwartz, D.J. Rowcliffe, and Y.D. Blum, "Microstructural Development in Si₃N₄/Polysilazane Bodies During Heating," Adv. Ceram. Mat., 3 [4] 320-23 (1988).

M. Spotz, "Sintering SiC Powder using Organosilicon Polymers as Binders," CPRL Report #R14, MIT, pp. 116-21 (1988).

G.H. Wiseman, "The Development and Application of Polysilazane Precursors to Ceramics"; PhD Thesis. Dept. of Chemistry, MIT, pp. 291-310, Aug. 1984.

S. Yajima, T. Shishido, and K. Okamura, "SiC Bodies Sintered with Three-Dimensional Cross-Linked Polycarbosilane," Am. Ceram. Soc. Bull., 56 [12] 1060-63 (1977).

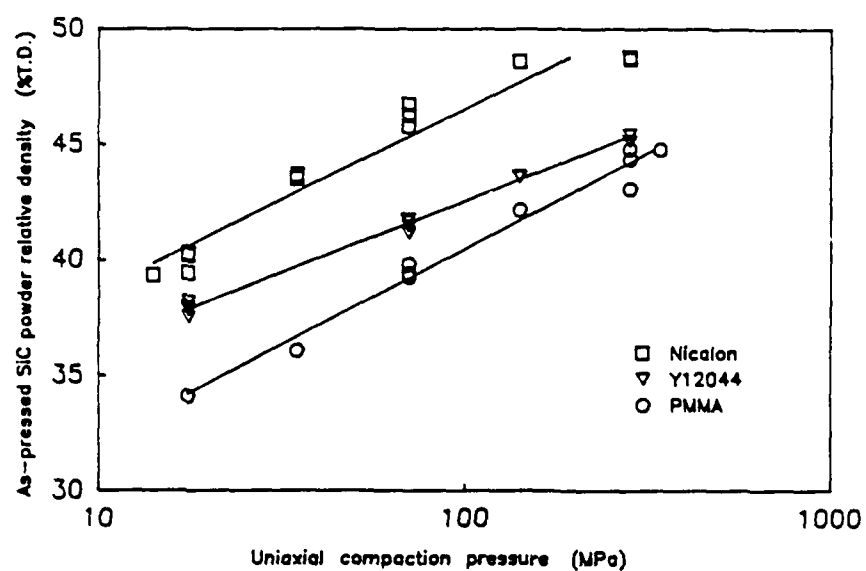


Figure 1. As-pressed SiC powder packing density (21 wt% batches) vs. uniaxial compaction pressure.

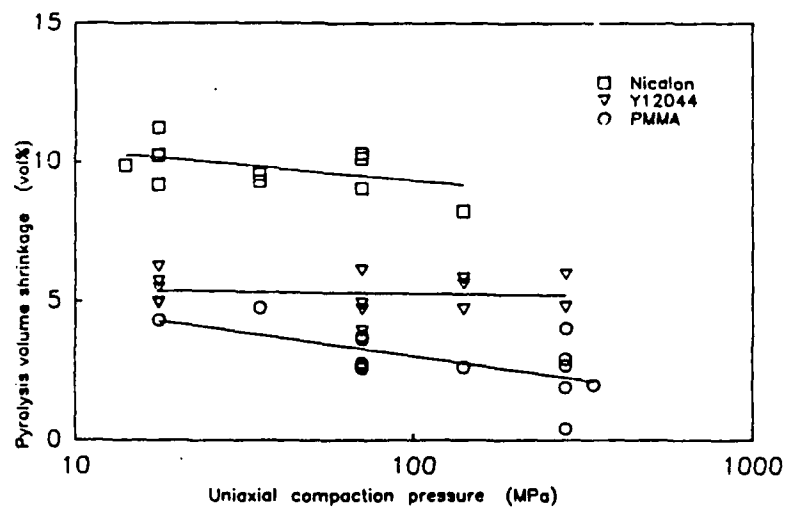


Figure 2. Volume shrinkage during pyrolysis (21 wt% batches) vs. uniaxial compaction pressure.

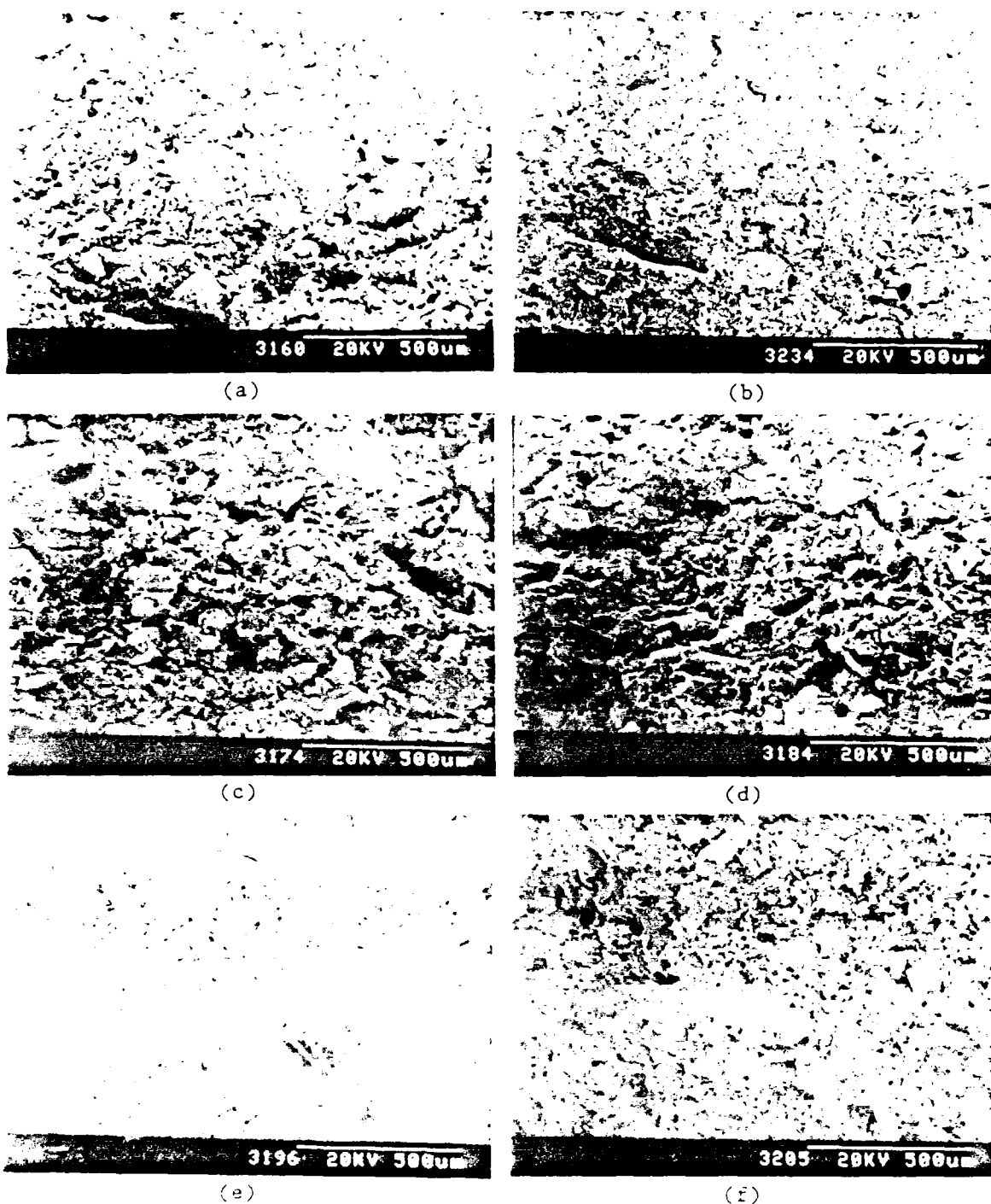
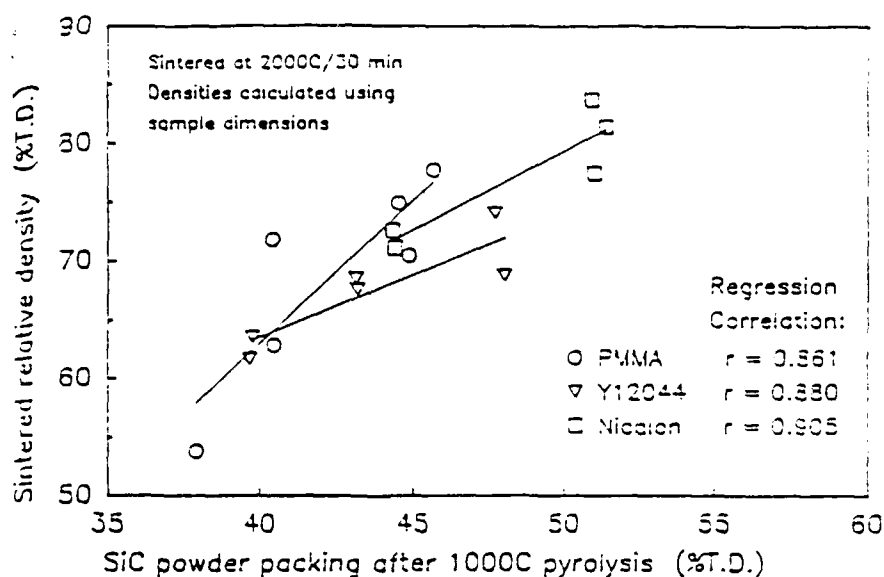
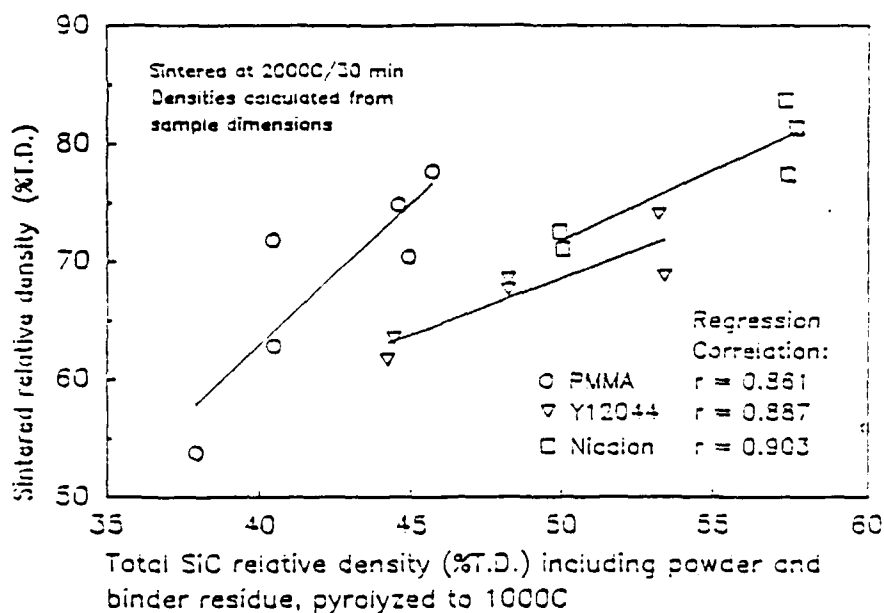


Figure 3. SEM of fracture surfaces of pyrolyzed SiC powder binder. Samples shown in (a), (c), and (e) were pressed at 70 MPa; samples shown in (b), (d), and (f) were subjected to different compaction pressures to achieve various developed packing densities of 45% T.D. Batches included (a)-(f): B-1, B-2, B-3, polyphenylene, and either PMA, Y-10, or Y-11. The fracture surfaces of the binder are shown in (a)-(f). The fracture surfaces of the binder are shown in (a)-(f). The fracture surfaces of the binder are shown in (a)-(f).

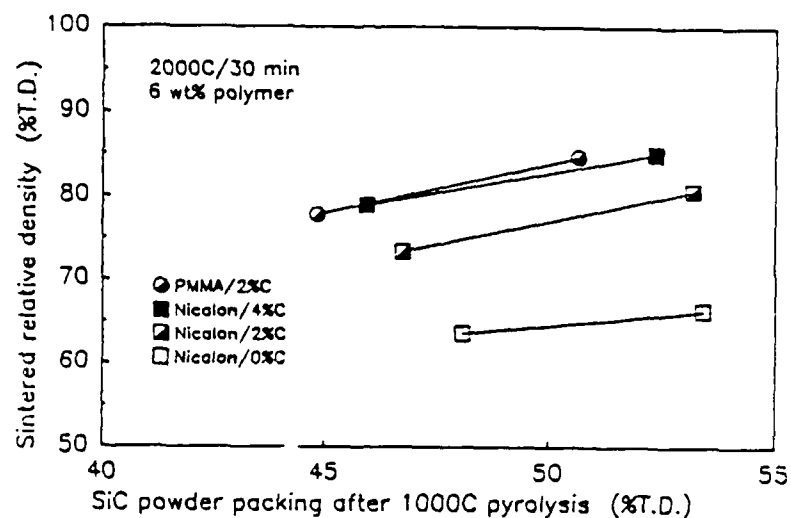


(a)

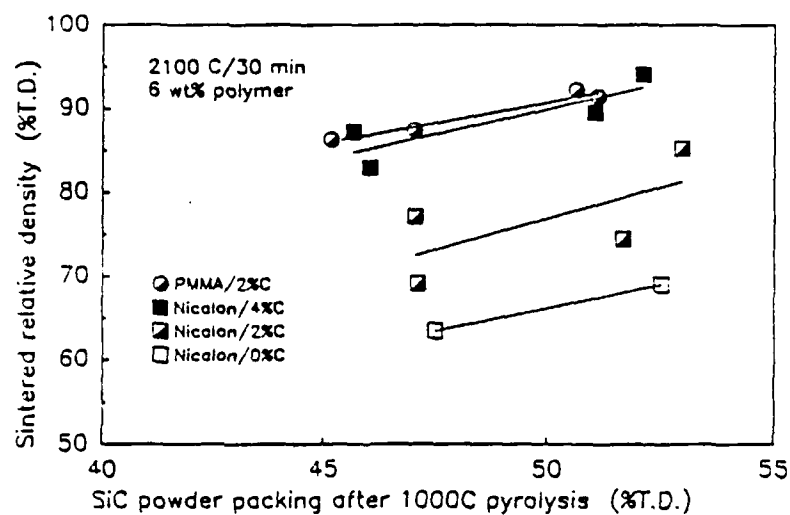


(b)

Figure 4. Sintered relative densities after 2000°C/30 min vs. pyrolyzed (pre-sintered) SiC packing densities calculated using a) just the SiC powder; b) both powder and binder pyrolysis product. Samples' initial polymer content was 21 wt% (powder basis).



(a)



(b)

Figure 5. Sintered relative densities vs. pyrolyzed (pre-sintered) SiC packing densities calculated using just the powder for samples sintered at a) 2000°C/30 min; b) 2100°C/30 min. Compacts contained β -SiC, B_4C , OLOA®1200, polyphenylene, and either Nicalon™ or PMMA at -6 wt% (powder basis). Carbon level was adjusted with polyphenylene.

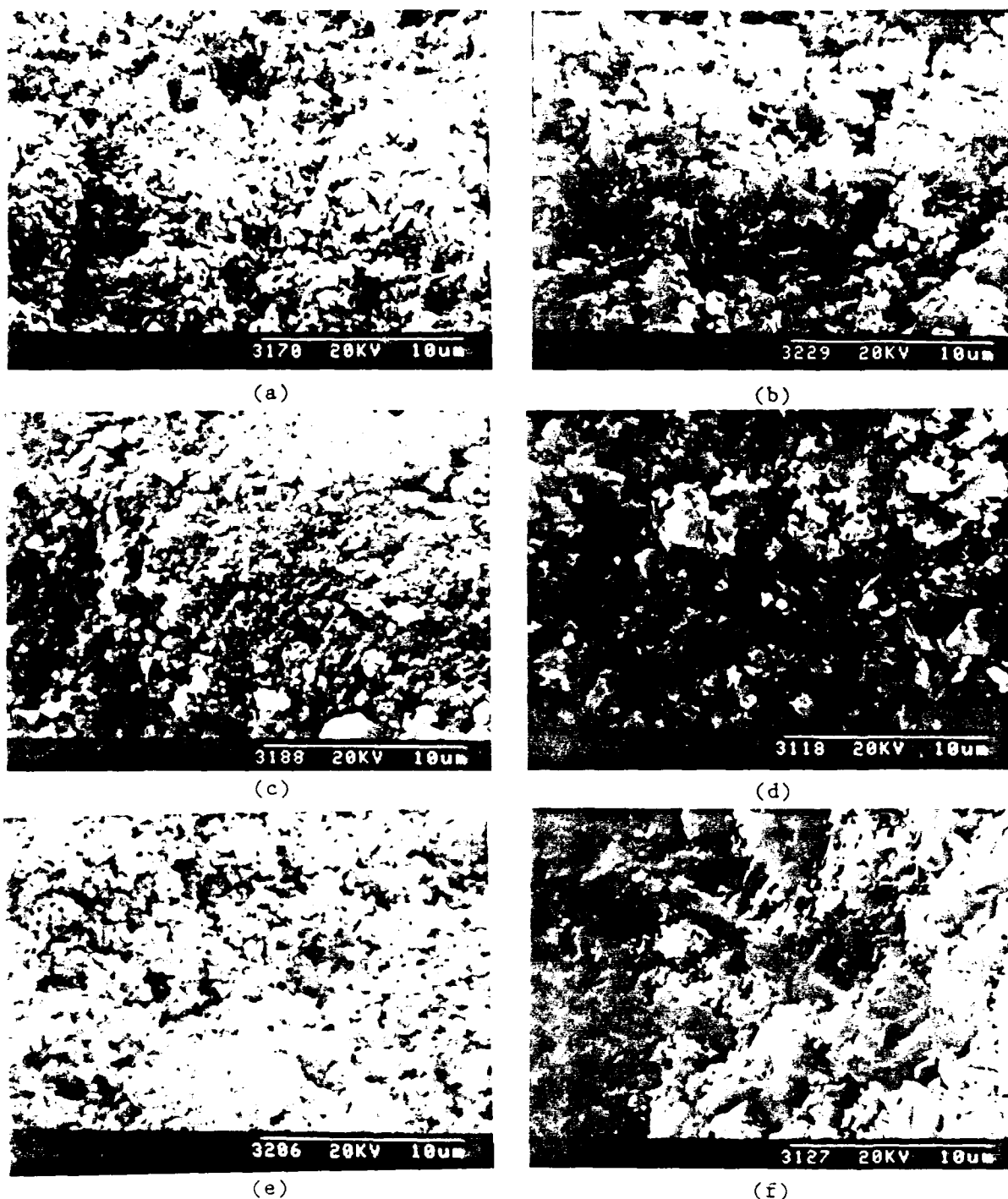


Figure 6. SEMs of fracture surfaces of pyrolyzed and sintered compacts. Samples shown in 6a, 6c, and 6e were pyrolyzed only; samples shown in 6b, 6d, and 6f were both pyrolyzed and sintered. Initial polymer content was ~21 wt% (powder basis). Polymer type and relative packing density (mean SiC powder packing density after pyrolysis) for each sample were: a) PMMA, 41.7% T.D., 180 MPa; b) PMMA, 44.9% T.D., 180 MPa; c) Y-12044, 45.8% T.D., 180 MPa; d) Y-12044, 43.0% T.D., 70 MPa; e) Nicalon, 44.8% T.D., 10 MPa; f) Nicalon, 44.8% T.D., 10 MPa.

III. RESEARCH PUBLICATIONS (8/1/85 - 12/31/88)

Published papers

E.A. Barringer and H.K. Bowen, "Effects of Particle Packing on the Sintered Microstructure," J. Appl. Phys. A, 45 [4] 271-75 (1988); presented at the International Institute for the Science of Sintering, Belgrade, Yugoslavia, 1983 (1988).

B.A. Bishop, M.S. Spatz, W.E. Rhine, H.K. Bowen, and J.R. Fox, "Sintering of Silicon Carbide Prepared from a Polymeric Precursor," pp. 856-63 in Ceramic Transactions: Ceramic Powder Science II. Edited by G.L. Messing, E.R. Fuller, Jr., and H. Hausner. The American Ceramic Society, Inc., Westerville, OH, 1988.

H.K. Bowen, "Advanced Ceramics," Sci. Am., 254 [10] 169-76 (1986).

H.K. Bowen, "Ceramic Superconductors," presented to the Committee on Science, Space, and Technology, U.S. House of Representatives, Washington, D.C., June 1987; published in Am. Ceram. Soc. Bull., 66 [8] 1191-96 (1987).

H.K. Bowen, "Reviving the 'We' Approach to Research," 1986 Scientist of the Year Lecture, address to I.R 100 Award winners; published in Research & Development, 28 [11] 62-64 (1986).

B. Fegley, Jr., P. White, and H.K. Bowen, "Processing and Characterization of ZrO_2 and Y-Doped ZrO_2 Powders," Am. Ceram. Soc. Bull., 64 [8] 1115-20 (1985).

M.K. Gallagher, W.E. Rhine, and H.K. Bowen, "Low-Temperature Route to High-Purity Titanium, Zirconium, and Hafnium Diboride Powders and Films"; pp. 901-06 in Ultrastructure Processing of Advanced Ceramics. Edited by J.D. Mackenzie and D.R. Ulrich. John Wiley & Sons, Inc., New York, 1988.

M. Green, T. Kramer, M. Parish, J. Fox, R. Lalanandham, W. Rhine, S. Barclay, P. Calvert, and H.K. Bowen, "Chemically Bonded Organic Dispersants"; pp. 449-65 in Advances in Ceramics, Vol. 21: Ceramic Powder Science. Edited by G.L. Messing, K.S. Mazdiasni, J.W. McCauley, and R.A. Haber. The American Ceramic Society, Inc., Westerville, OH, 1987.

A.R. Hardy, G. Gowda, T.J. McMahon, R.E. Riman, W.E. Rhine, and H.K. Bowen, "Preparation of Oxide Powders"; pp. 407-28 in Ultrastructure Processing of Advanced Ceramics. Edited by J.D. Mackenzie and D.R. Ulrich. John Wiley & Sons, Inc., New York, 1988.

R.H. Heistand, II, Y. Oguri, H. Okamura, W.C. Moffatt, B. Novich, E.A. Barringer, and H.K. Bowen, "Synthesis and Processing of Submicrometer Ceramic Powders"; pp. 482-96 (Chapt. 51) in Science of Ceramic Chemical Processing. Edited by L.L. Hench and D.R. Ulrich. John Wiley & Sons, New York, 1985.

R.J. Higgins, H.K. Bowen, and E.A. Giess, "Preparation and Sintering Behavior of Fine-Grained MgAl_2O_4 - SiO_2 Composites"; pp. 691-98 in *Advances in Ceramics*, Vol. 21: *Ceramic Powder Science*. Edited by G.L. Messing, K.S. Mazdinyani, J.W. McCauley, and R.A. Haber. The American Ceramic Society, Inc., Westerville, OH, 1987.

T. Ishii and H.K. Bowen, "Dispersion and Pressureless Sintering of Al_2O_3 - SiC Whisker Composites," pp. 452-59 in *Ceramic Transactions: Ceramic Powder Science II*. Edited by G.L. Messing, E.R. Fuller, Jr., and H. Hausner. The American Ceramic Society, Inc., Westerville, OH, 1988.

N.J. Jubb and H.K. Bowen, "The Processing of Monodisperse Boron-doped SiO_2 Particles," *J. Mat. Sci.*, 22 [6] 1963-70 (1987).

S. Kamiya and H.K. Bowen, "Microstructural Control of Al_2O_3 - TiO_2 Composites by Cyclic Annealing," pp. 978-88 in *Ceramic Transactions: Ceramic Powder Science II*. Edited by G.L. Messing, E.R. Fuller, Jr., and H. Hausner. The American Ceramic Society, Inc., Westerville, OH, 1988.

T. Kanai, W.E. Rhine, and H.K. Bowen, "Preparation of $2\text{ZrO}_2 \cdot \text{Yb}_2\text{O}_3$ Powder by Emulsion Techniques," pp. 119-26 in *Ceramic Transactions: Ceramic Powder Science II*. Edited by G.L. Messing, E.R. Fuller, Jr., and H. Hausner. The American Ceramic Society, Inc., Westerville, OH, 1988.

R.R. Landham, P. Nahass, D.K. Leung, M. Ungureit, W.E. Rhine, H.K. Bowen, and P.D. Calvert, "Potential Use of Polymerizable Solvents and Dispersants for Tape Casting of Ceramics," *Am. Ceram. Soc. Bull.*, 66 [10] 1513-16 (1987).

R.R. Landham, M.V. Parish, H.K. Bowen, and P.D. Calvert, "Organotitanate Dispersants for BaTiO_3 and Al_2O_3 ," *J. Mat. Sci.*, 22 [5] 1677-81 (1987).

W.C. Moffatt and H.K. Bowen, "Composite Ceramic Production by Precipitation of Polymer Solutions Containing Ceramic Powder," *J. Mat. Sci. Lett.*, 6 [4] 383-85 (1987).

W.C. Moffatt, P. Cortesi, P. White, and H.K. Bowen, "Alternative Processing Technologies for Alumina-Zirconia Composites"; pp. 1345-56 in *High Tech Ceramics*. Edited by P. Vincenzini. Elsevier Science Publishers BV, Amsterdam, The Netherlands, 1987.

W.C. Moffatt, P. White, and H.K. Bowen, "Production of Alumina-Zirconia Composite Ceramics by Nonsolvent Flocculation of Polymer-Containing Powder Dispersions," pp. 645-53 in *Ceramic Transactions: Ceramic Powder Science II*. Edited by G.L. Messing, E.R. Fuller, Jr., and H. Hausner. The American Ceramic Society, Inc., Westerville, OH, 1988.

P. Nahass and H.K. Bowen, "Precipitation of Titania in a Continuous-Flow Reactor with an Organic Base Stabilizer," *Mat. Sci. Eng.*, Vol. 100, 235-40 (1988).

A. Ochi, H.K. Bowen, and W.E. Rhine, "The Synthesis of Aluminum Nitride from Aluminum Hydride"; pp. 663-66 in the Materials Research Society Symposia Proceedings, Vol. 121: Better Ceramics Through Chemistry III. Edited by C.J. Brinker, D.E. Clark, and D.R. Ulrich. Materials Research Society, London, 1988.

Y. Oguri, R.E. Riman, and H.K. Bowen, "Processing of Anatase Prepared from Hydrothermally Treated Alkoxy-derived Hydrous Titania," J. Mat. Sci. 23, 2897-2904 (1988).

H. Okamura, E. Barringer, and H.K. Bowen, "Preparation and Sintering of Monosized Al_2O_3 - TiO_2 Composite Powder," J. Am. Ceram. Soc. Comm., 69 [2] C22-C24 (1986).

H. Okamura and H.K. Bowen, "Preparation of Alkoxides for the Synthesis of Ceramics," Ceram. Intl., 12 [3] 161-71 (1986).

A. Roosen, S. Sumita, and H.K. Bowen, "Powders, Interfaces, and Processing: Alumina as a Case Study"; pp. 433-46 in Materials Science Research, Vol. 21, "Ceramic Microstructures '86: Role of Interfaces." Edited by J.A. Pask and A.G. Evans. Plenum Publishers, New York, 1988.

Papers in press

P. White, B. Fegley, and H.K. Bowen, "Preparation of Zirconia-Alumina Ceramics from Narrow-Sized Powders," to be published in the Proceedings of Zirconia '86 Conference (September 1986, Tokyo). The American Ceramic Society, Westerville, OH, 1989.

B.A. Bishop and H.K. Bowen, "Suspension Processing of β -SiC Powders," to be published in the Proceedings of the Silicon Carbide Symposium (August 1987, Columbus, OH). The American Ceramic Society, Westerville, OH, 1989.

P. Cortesi and H.K. Bowen, "Continuous Coating of Alumina Particles with Alkoxide-Derived Zirconia Particles," to be published in Ceram. Intl.

R.A. Hay, W.C. Moffatt, and H.K. Bowen, "Sintering Behavior of Uniform-Size α -Alumina Powder," to be published in Mat. Sci. Eng.

H.M. Jang, W.E. Rhine, and H.K. Bowen, "Densification of Al_2O_3 -SiC Powder Composites: I. Effects of a Polymer Coating on SiC Particles," to be published in J. Am. Ceram. Soc.

H.M. Jang, W.E. Rhine, and H.K. Bowen, "Densification of Al_2O_3 -SiC Powder Composites: II. Microstructural Evolution and Densification," to be published in J. Am. Ceram. Soc.

H. Okamura, E.A. Barringer, and H.K. Bowen, "Preparation and Sintering of Narrow-Sized Al_2O_3 - TiO_2 Composite Powders," to be published in J. Mat. Sci.

R.E. Riman, R.R. Landham, and H.K. Bowen, "Synthesis of Uniform Titanium and 1:1 Ti Carboxy-Hydrosols by Controlled Hydrolysis," to be published in J. Am. Ceram. Soc.

A. Roosen and H.K. Bowen, "Influence of Different Consolidation Techniques on Green Microstructure and Sintering Behavior of Alumina Powders," to be published in J. Am. Ceram. Soc.

Submitted papers

W.C. Moffatt and H.K. Bowen, "Flocculation of Polymer-Containing Powder Dispersions by the Addition of Nonsolvents," submitted to the American Ceramic Society.

W.C. Moffatt and H.K. Bowen, "Thermal Processing and Properties of Highly Homogeneous Alumina-Zirconia Composite Ceramics," submitted to J. Mat. Sci.

W.C. Moffatt and B.E. Novich, "Continuous Processing of Composite Ceramic Powders," submitted to the American Ceramic Society.

P. Nahass, R.L. Pober, B.A. Bishop, and H.K. Bowen, "Semicontinuous Classification of Ceramic Powders," submitted to the American Ceramic Society.

A. Roosen and H.K. Bowen, "Powder Synthesis, Sintering Behaviour, and Annealing of Titania-Coated Alumina," submitted for inclusion in the Proceedings of the Powders Conference (November 1988, Berchtesgaden).

Papers in preparation

S. Kamiya and H.K. Bowen, "Mechanical Properties of Al_2O_3 - TiO_2 Composites Formed by Cyclic Annealing," to be submitted to the American Ceramic Society.

S. Kamiya and H.K. Bowen, "Processing and Microstructural Control of Al_2O_3 - TiO_2 Composites by Cyclic Annealing," to be submitted to the American Ceramic Society.

P. Nahass and B.E. Novich, "Surface Area of Continuously Processed TiO_2 Powder," to be submitted to J. Mat. Sci.

R.E. Riman, R.R. Whittle, W.E. Rhine, and H.K. Bowen, "Preparation and Structure of $\text{Sr}_2\text{Ti}(\text{OPr}^i)_8 \cdot 5\text{Pr}^i\text{OH}$," to be submitted to Inorg. Chem.

Y. Shindo, W.C. Moffatt, and H.K. Bowen, " Al_2O_3 - TiO_2 - ZrO_2 Composites," to be submitted to the American Ceramic Society.

C. Zing, W.E. Rhine, and H.K. Bowen, "Preparation of BaTiO_3 and SrTiO_3 Using a Water-in-Oil Emulsion Technique," to be submitted to J. Mat. Sci. Lett.

Reports

L.M. Barrett, "Annealing of Al_2O_3 -20% TiO_2 Below the Aluminum Titanate Transformation Temperature," B.S. thesis.

B.A. Bishop, "Suspension Processing of Silicon Carbide Using Multifunctional Organometallic Polymers"; PhD thesis proposal. Dept. Materials Science and Engineering, MIT, March 1986.

R.J. Higgins, "Preparation and Sintering Behavior of Fine-grained MgAl_2O_4 - SiO_2 Composites"; MS thesis. Dept. Materials Science and Engineering, MIT, June 1986.

T.J. McMahon, "Synthesis of Cordierite from Alkoxide Precursors"; MS thesis. Dept. Materials Science and Engineering, MIT, February 1987.

W.C. Moffatt, "Processing and Properties of Alumina-Zirconia Composite Ceramics"; ScD thesis. Dept. Materials Science and Engineering, MIT, June 1987.

R.E. Riman, "The Role of the Chemical Processing Variables for the Synthesis of Ideal Alkoxy-Derived SrTiO_3 "; PhD thesis. Dept. Materials Science and Engineering, MIT, February 1987.

M.S. Spatz, "Organometallic Polymers as Dispersants, Binders, and Sintering Aids for Silicon Carbide Powder"; PhD thesis proposal. Dept. Materials Science and Engineering, MIT, May 1986.

Patents

E.A. Barringer, B. Fegley, Jr., and H.K. Bowen, "Synthesis and Processing of Monosized Oxide Powders," US Patent No. 4,543,341 (1985).

W.C. Moffatt, "Ceramic Composite Production by Precipitation of Polymer Solution," Serial No. 07/000,208 (application filed 30 December 1986).